AN ABSTRACT OF THE THESIS OF

Jough-Tai Wang for the degree of Doctor of Philosophy in Atmospheric Sciences presented on November 21, 1986.

Title: An Observational Study of the Energetics and Dynamical Aspects of GATE Cloud Clusters.

Abstract approved: Redacted for Privacy

Thermodynamical and dynamical aspects of tropical cloud clusters are studied using data from the GARP Atlantic Tropical Experiment (GATE). The data set used in this study is a three-dimensional gridded set of upper-air analyses constructed by Ooyama and Chu (Hurricane Research Division, AOML/NOAA and SSEC-University of Wisconsin) for wind data and Esbensen (Oregon State University) for thermodynamic data. The energy and momentum budgets are estimated on the scale of large cloud clusters.

A strong upper-tropospheric heat source and middle-tropospheric drying are characteristic features of the mature stage of the observed cloud clusters. The heat source, moisture sink and the virtual heat flux for cloud clusters are larger than the corresponding quantities from GATE easterly-wave composites. The surface precipitation estimates produced from the vertically integrated moisture budget are consistent with direct observations.

From the momentum budget study, the following conclusions are drawn concerning the cumulus momentum effects. In the growing stage, the mesoscale and cumulus scale effect tends to: 1) provide a vertically integrated net sink for westerly momentum around the cluster center; 2) induce a convergent circulation in the lower layer. In the mature stage, the effects are to: 1) induce a divergent circulation in the upper layer and maintain a vorticity couplet pattern; 2) maintain a weak convergent circulation in the lower layer; and 3) cause a relatively weak easterly acceleration in the upper layer at the center. A hypothesis is postulated to illustrate the convective dynamical effects.

A simple barotropic non-divergent model was constructed to investigate the large-scale response to the hypothesized cumulus momentum forcing similar to that found in the GATE cloud-cluster momentum budget. The numerical results show that the cumulus momentum forcing is a plausible kinetic energy source for the mesoscale wavenumber spectrum. The sporadic nature of the convective mass flux does not have a significant effect on the large-scale dynamical response for physically realistic parameters in a barotropic non-divergent dynamical system.

An Observational Study of the Energetics and Dynamical Aspects of GATE Cloud Clusters

by

Jough-Tai Wang

A THESIS

submitted to

Oregon State University

in partial fulfillment of
the requirements for the
degree of

Doctor of Philosophy

Completed November 21, 1986

Commencement June 1987

APPROVED:

Redacted for Privacy

Professor of Atmospheric Sciences in charge of major

Redacted for Privacy

Chairman of Department of Atmospheric Sciences

Redacted for Privacy

Dean of Grad

Date thesis is presented 21 November 1986

Typed by Michelle Burrier for Jough-Tai Wang

To My Parents

ACKNOWLEDGEMENTS

My deepest appreciation is due my research advisor, Professor Steven K. Esbensen, for his invaluable guidance and stimulating suggestions through the course of this thesis work. He not only guided me into areas of new perspectives on contemporary research related to this thesis, but also provided the thermodynamic aspects of the data set. Sincere thanks goes to Professor W. Lawrence Gates for his interest, comments and encouragement during the writing of the thesis.

I would like to thank Professor Hua-Lu Pan for his pertinent comments and suggestions. Discussion with him on the momentum budget results was very fruitful. For their participation in various phases of my graduate program and helpful comments, I am grateful to Professors Jeong-Woo Kim, Ronald B. Guenther and Gene F. Craven.

I appreciate the assistance provided by Mr. Robert L. Mobley and Mr. William R. McKie, especially for their suggestions on efficient computer programming techniques and their help in developing graphical routines. I am also pleased to acknowledge my friends among the faculty, staff and students of the Department of Atmospheric Sciences and of the Climatic Research Institute, both at Oregon State University, for their help in various ways.

I also thank my wife, Quayin Hsieh, for her support, patience and understanding during the years of my graduate study at Oregon

State University.

This research was sponsored by the National Science Foundation under grants NSF ATM 82-13130 and ATM 84-14820.

TABLE OF CONTENTS

LIST OF FIGURES

Figure | Page

LIST OF TABLES

AN OBSERVATIONAL STUDY OF THE ENERGETICS AND DYNAMICAL ASPECTS OF GATE CLOUD CLUSTERS

CHAPTER 1. INTRODUCTION

In the early 1970's, the cumulus convection problem was identified as the single most important unsolved problem in the numerical modeling of climate. Since that time, much work has been devoted to understanding cumulus convection and its thermodynamical and dynamical effects on the large-scale environment.

In the tropics, the latent heat release associated with the convective events is regarded as a primary energy source for a variety of large-scale disturbances including the synoptic-scale disturbances (Riehl and Malkus, 1958). The interaction between the convective events and the large-scale disturbances can be described as cooperation between the clouds and the large-scale flow. The cumulus clouds supply the heat needed to drive the large-scale disturbance; the large-scale disturbance produces the moisture convergence needed to maintain the cumulus convection.

An example of cooperation between planetary-scale atmospheric phenomena in the tropics and the cumulus convection is the El Niño event. During an El Niño year, as demonstrated by Rasmusson and Carpenter (1982) and others, anomalous low-level convergence in the central part of the equatorial Pacific is accompanied by enhanced convection near the dateline, while sinking motion in the Western Pacific appears to suppress convection and the tropical cyclone

activity there (Chan, 1985).

The East Asia winter monsoon is another example of the interaction between planetary-scale atmospheric phenomena and convection. The monsoon is driven by the large thermal contrast between the equatorial heat source (in the 'maritime continent' of Borneo and Indonesia) and the immense region of cooling over northern China and Siberia. Chang and Lau (1980, 1982) showed that monsoon surges can sometimes lead to an intensification of convective activity in the maritime continent area. This increased convection, in turn, causes planetary-scale divergent outflow in the upper troposphere, enhancing the planetary-scale Walker and Hadley circulations that are associated with the monsoon.

Convection also plays an important role in the energetics of synoptic-scale tropical disturbance called easterly waves. These mid-tropospheric disturbances are the source of many tropical cyclones. Well developed cumulus clouds are not randomly distributed but are associated with regions of low-level mass convergence on the scale of waves (e.g., Malkus, 1960; Matsumoto et al., 1967; Reed and Recker, 1971; Ogura and Cho, 1973). Thompson et al. (1979), and Reed et al. (1971) concluded that in both the Western Pacific and the Eastern Atlantic, the largest amounts of rainfall occurred in and ahead of the wave trough where low-level convergence is greatest; smallest amounts were found in and ahead of the ridge. The large-scale environment in the easterly waves appears to have a controlling effect on the generation of convective clouds.

An even smaller scale of convective organization is the so-called "cloud-cluster" or mesoscale convective system. A cloud cluster appears on a satellite picture as a solid white mass (e.g., Fig. 1.1) produced through the merger of outflows from deep cumulonimbus clouds. Cloud clusters are a common feature of the convection near the ITCZ (Intertropical Convergence Zone) (Houze and Betts, 1981).

Fig. 1.2 shows schematically the time and space scales of the tropical disturbances from synoptic-scale waves to turbulence; planetary scale disturbances are not included in this figure. Cloud clusters represent a scale of motion distinct from the synoptic time scale of several days and mesoscale time scale of several hours; they appear to possess their own dynamical characteristics. Because of their ubiquity, size and relatively long time scale, the effects of the cloud clusters on the large-scale flow have become the subject of much investigation. One of the central objectives of GATE (Global Atmospheric Research Program, Atlantic Tropical Experiment) in 1974 was to study the structure of these cloud cluster disturbances and their effects on the large-scale circulation. Many researchers have used the observed data from GATE to study the detailed structure of cloud clusters and the convective events associated with them (summarized in Houze and Betts, 1981).

The large-scale thermodynamic and dynamical effects of cloud clusters having scales between synoptic scale waves and individual meso-scale features will be the main topic of this thesis. Before

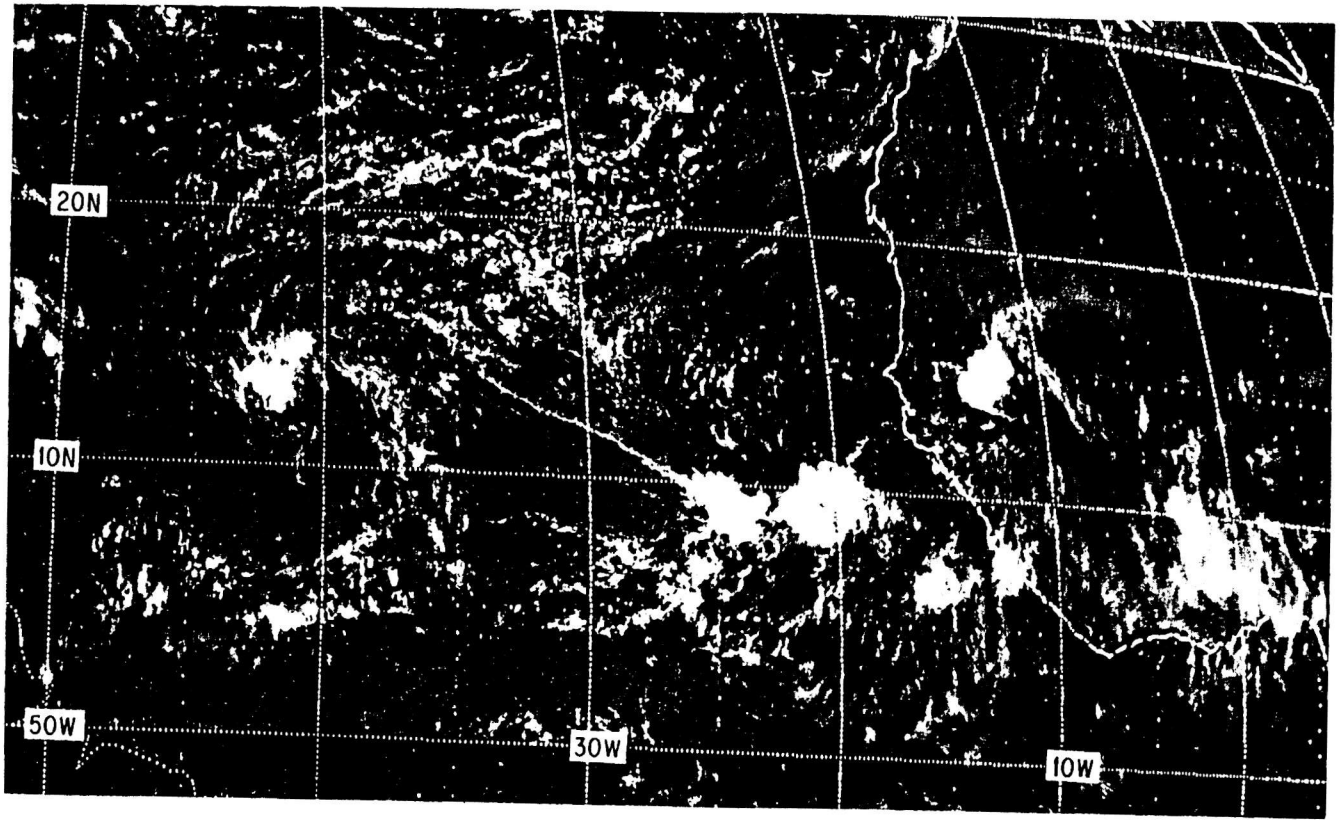

Figure 1.1. Visible satellite photograph showing tropical clouds ranging in size from small cumulus to large cloud clusters. Cloud clusters are evident by the large cirrus shields at 9°N 21°W, 7°N 16°W, 14°N 13°W. Photograph from the SMS-1 satellite is for 1130 GMT, 5 September 1974.

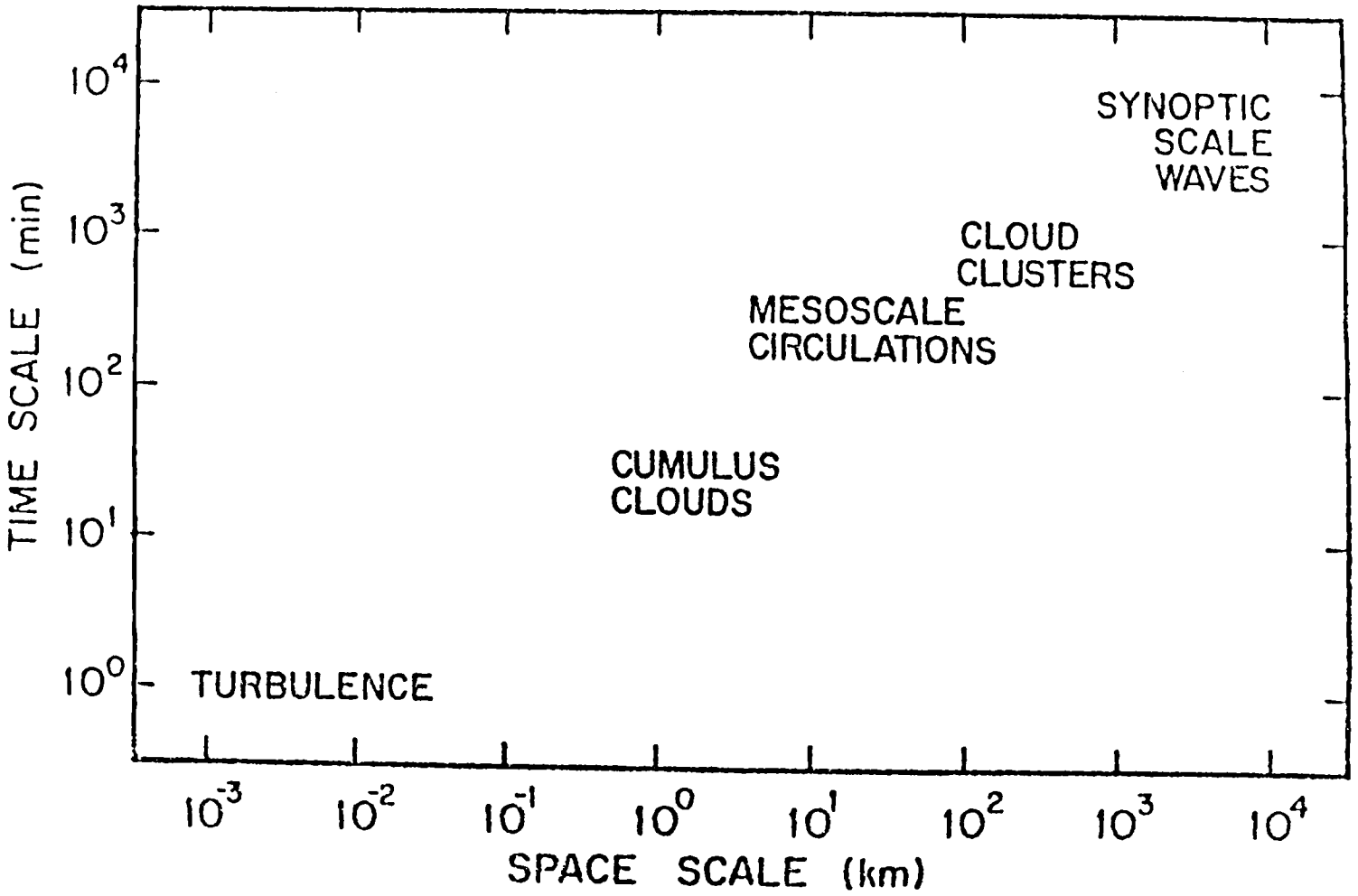

Figure 1.2. Relevant time and space scales of tropical disturbances (from Esbensen et al., 1982).

the outline of the thesis is presented, I will present a brief review of tropical convective systems.

1.1 What was known prior to GATE about convective systems

Prior to GATE, significant progress in the understanding of tropical convection had already been made. Riehl and Malkus (1958) stated that synoptic-scale disturbances may account for the bulk of the vertical energy transport in the atmosphere, and that individual cumulonimbus towers themselves in the tropics can accomplish most of the required energy transport. Since then, numerous thermodynamic budget calculations by various researchers (Gray, 1973; Yanai et al., 1973; Ogura and Cho, 1973) have supported the conclusions of Riehl and Malkus. These thermodynamic budget studies found that large unbalanced features occurred in areas where deep convection was present. To interpret these results, a number of diagnostic models have been proposed.

Yanai et al. (1973), Ogura and Cho (1973), and Nitta (1975) were among the pioneers in providing quantitative diagnostic models for the study of convection in the tropics that parallel the parameterization schemes for convection proposed by Ooyama (1971) and Arakawa and Schubert (1974). These cloud-ensemble models allow one to deduce the properties of convective clouds from observed large-scale budgets. The bulk properties of a tropical cloud cluster (such as vertical convective mass flux, excess temperature, and liquid water content of the clouds) are determined from a combination of 1) a model of a population of cumulus clouds which

exchange mass, heat, water vapor and liquid water with their environment through entrainment and detrainment, and 2) the observed large-scale heat and moisture budgets over a specified area containing the cloud cluster. The usefulness of the results from these diagnostic techniques or parameterization schemes depends on the extent to which the assumed cloud model actually describes the essential components of the cloud structure, as well as the accuracy of the observed large-scale budgets.

Only convective updrafts were explicitly included in the early diagnostic models (Yanai et al., 1973; Ogura and Cho, 1973). It was suggested that prognostic models using this type of parameterized cloud model might overestimate the subsidence between clouds, and hence, predict excessive warming (Johnson, 1976). Lack of convective downdrafts in these models was cited as a possible cause. Johnson (1976) and Nitta (1977) included convective-scale downdrafts in their models. Their results indicated that cumulus downdrafts compensate a large fraction of the cumulus updrafts and are thus an important part of the mass budget in tropical disturbances.

The knowledge of cumulus effects on the large-scale momentum budget is more limited. Palmen and Newton (1969) estimated the vertical transport of westerly momentum due to small scale eddies as a residual of the angular momentum equation, and suggested that momentum was transported downward. Holton and Colton (1972), using a linear diagnostic model, showed that the observed seasonal large-scale vorticity budget in the tropical upper troposphere can

have a significant budget residual, due to the imbalance between the generation of vorticity by the horizontal divergence and vorticity advection. Expressing the residual in the form of a damping mechanism, they concluded that the required decay time for the mean vorticity field should be on the order of one day. Based on such a short time scale, they speculated that the required process was the vertical transport of vorticity by deep cumulus convection.

Schneider and Lindzen (1976) referred to the effect of momentum change due to clouds as 'cumulus friction' and gave some justification to the original formulation from Ooyama (1971). That formulation implies in a gross sense that the mean vertical transport of horizontal momentum by convection over the depth of the atmosphere is down the vertical gradient. The resulting effect is thus to reduce the vertical shear.

The magnitude of the cumulus transport of momentum, in principle, can be estimated as the residual of the momentum budget equation. However, this computation of the momentum budget from observational data involves the evaluation of the large-scale horizontal geopotential gradient, which is difficult to measure reliably in the tropics. For this reason, the vorticity budget has been used extensively to study the cumulus momentum effect.

The observations of cloud clusters and the understanding of the cluster structure were also severely limited before GATE. Zipser (1969) found that the downdraft air to the rear of a cluster had very low moist static energy. This low moist static energy was

deduced to have come from the mid-troposphere in unsaturated downdrafts under the influence of rain. Chang (1970) clearly demonstrated the existence of westward propagating cloud systems (Fig. 1.3). Williams and Gray (1973) composited data in the vicinity of satellite-observed cloud clusters in the Western Pacific trade wind regime. From these composites Williams and Gray found that the cluster region possessed general upward motion in contrast to the clear areas in their surroundings in which the air was subsiding. However, the complete structure and life cycle of the cloud cluster and its interaction with the large-scale flow were not well understood.

1.2 GATE studies related to cloud clusters

During GATE in summer of 1974, a dense network of instrumented ships equipped with upper-air sounding equipment and quantitative weather radar were located over the eastern Atlantic Ocean. The ship network was supplemented by a fleet of research aircraft and a geosynchronous meteorological satellite. Thus, GATE provided an excellent opportunity to acquire first-hand observations of cloud clusters and other mesoscale convective systems. The GATE data set has already been examined by many researchers; some of the important findings and their implications are summarized here.

1.2.1 The structure of cloud clusters

One of the most important findings from the studies based on GATE data is the identification of the mesoscale organization of

Figure 1.3. Time longitude sections of satellite photographs for the periods 1 July-14 August 1967 in the 5-10°N latitude band of the Pacific. The westward progression of the cloud clusters is indicated by the bands of cloudiness sloping down the page from right to left (from Chang, 1970).

clouds imbedded in the cloud clusters. Mesoscale as well as cumulus scale vertical motions are important circulation features of cloud clusters (Houze, 1977, Leary and Houze, 1979).

The mesoscale cloud systems in GATE typically contained a band or line of deep convective cells with updrafts and downdrafts, and an anvil cloud in the middle and upper troposphere downwind of the convective band or line. Cloud clusters were generally found to have lifetimes of a day or less (Martin and Schreiner, 1981). This can be contrasted with the convective cells within the band or line; convective cells that grow and decay on a time scale of an hour, while the line itself may last up to 12 hours.

Houze (1977), Zipser (1977), and Betts et al. (1976) studied the squall-cluster system and found that it possesses, in addition to deep cumulonimbus towers along the leading edge, intense convective-scale downdrafts which occur in a narrow (10-20 km wide) heavy precipitation zone and a more gentle and broader (100-500 km wide) mesoscale downdraft beneath a precipitating anvil cloud to the rear of the active cumulonimbus towers. Cheng and Houze (1979) estimated from the GATE radar echo patterns that around 40% of the precipitation falls from the anvil region. The long duration of the stratiform light rain suggested that sustained upward motion on the mesoscale within the anvil provides the source of water substance.

Leary and Houze (1979) examined the structure and evolution of convection in the GATE non-squall cloud clusters which occurred on 5 September 1974, and found the mesoscale precipitation features

(MPF) appeared to be the primary entities of the tropical cloud clusters within which deep tropical convection occurs. Based on the similarity of the six MPF comprising the 5 September cloud clusters (squall clusters and some non-squall clusters contain just one MPF), they speculated that there existed a characteristic mesoscale organization of precipitation in tropical cloud clusters.

In their study of a squall-line cluster, Gamache and Houze (1982) showed that the anvil region is characterized by mid-level convergence, which feeds both a mesoscale downdraft below the anvil and a mesoscale updraft within the anvil cloud. They demonstrated the existence of the upward motion within the anvil cloud by obtaining quantitative profiles of the mesoscale vertical motions.

1.2.2 Diagnostic studies: Thermodynamic aspects

The observational evidence after GATE confirms that convective and mesoscale updrafts and downdrafts are characteristic features of tropical cloud clusters. Mesoscale rain areas were found to account for a significant fraction of the total precipitation in GATE (Cheng and Houze, 1979). The evidence also suggested that mesoscale precipitating systems may contribute importantly to the large-scale mass, heat and moisture transports (Leary and Houze, 1980). Attempts were made to include the observed mesoscale features in the diagnostic cloud model to represent the complete sub-grid scale cloud effect. Johnson (1980) constructed a cloud model which had mesoscale downdrafts and convective updrafts and downdrafts, to estimate the mesoscale contribution to the total

convective mass flux. The large-scale budgets used in his study were computed from easterly wave composites. Fig. 1.4 from Johnson (1980) demonstrates the potential importance of mesoscale downdrafts in the mass budget of a cloud cluster. It shows that the mass flux in mesoscale downdrafts is a significant fraction of the mass flux in convective updrafts.

Leary and Houze (1980) postulated an idealized mesoscale system with a precipitation pattern typical of mesoscale systems observed during GATE to study the effects of mesoscale updrafts in the anvil clouds. They found that the diagnostic profiles of vertical transports of mass and moist static energy were both qualitatively and quantitatively different from the results when the mesoscale effects were excluded. These results implied that the effect of mesoscale vertical air motions on cloud mass flux and net heating profiles should be considered in discussing the total convective effects.

However, the accuracy of these diagnostic models also depends on the observed budget results. Since the cloud cluster has its own life cycle on the order of 1 day, the thermodynamic budget on the easterly wave scale (time scale of 3 to 4 days) may not be able to reflect the characteristics of the tropical convection associated with this mesoscale organized event.

1.2.3 Diagnostic studies: Dynamical aspects

Studies using GATE data have also led to progress in understanding the dynamical effects of cumulus ensemble on the

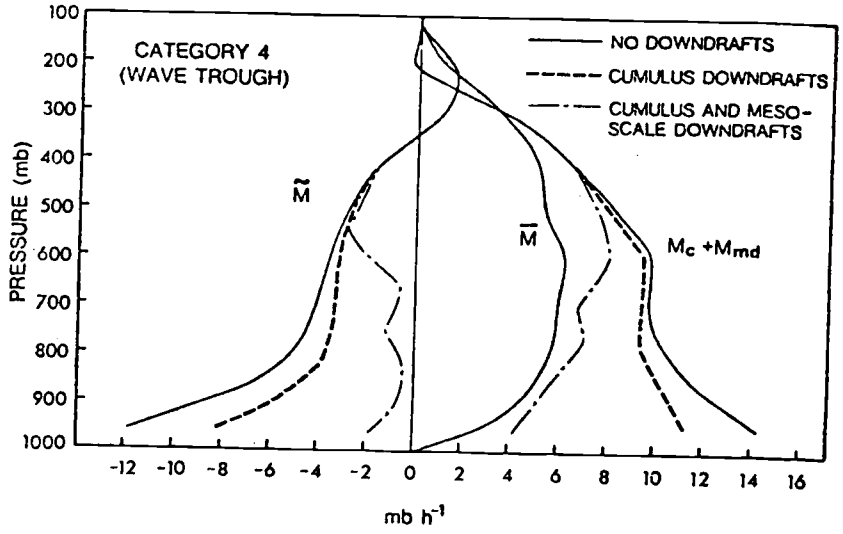

Figure 1.4. Environment mass flux $\tilde{M}$, mean mass flux $\bar{M}$ and net convective mass flux M_c+M_{md} for wave trough with and without downdrafts (from Johnson, 1980).

large-scale flow. Vorticity budget studies of easterly waves scale were performed by Shapiro (1978), Stevens (1979), Cho and Cheng (1980), and Esbensen et al. (1982). The vorticity residuals are complex, but generally show that at low levels, the convection acts as a sink of vorticity which opposes the amplification in a region of positive vorticity; while a convective vorticity source in the upper levels opposing the anticyclonic amplication.

Improvements in diagnostic models based on the vorticity equation were made by Cho and Cheng (1980), Shapiro and Stevens (1980) and Yanai et al. (1982). The general formulation of vorticity residuals (Z) from these diagnostic models may be written as

$$Z = \sum_i \delta_i(\eta_{\delta i}-\eta) + \eta \frac{\partial M_c}{\partial p} - M_c \frac{\partial \eta}{\partial p} - \hat{k} \cdot \nabla M_c \times \frac{\partial \underset{\sim}{V}}{\partial p} \qquad (1.1)$$

where $\eta_{\delta i}$, η, δ_i are respectively the vorticity detrained into the environment by the ith cloud ensemble, the large-scale vorticity averaged over an area, and the detrainment rate of the ith cloud. M_c is the vertical cumulus mass flux.

The four terms on the right-hand side are 1) the direct effect of the cloud ensemble due to the detrainment of excess absolute vorticity to the environment; 2) a divergent effect of the environment through the cloud entrainment and detrainment; 3) the vertical advection of mean vorticity by the cumulus-cloud-induced vertical circulation; and 4) the twisting of horizontal vorticity into the vertical direction due to the inhomogeneous spatial

distribution of the cloud population.

Tollerud and Esbensen (1983) were the first to investigate the horizontal structure of the upper-level vorticity residuals in the vicinity of GATE cloud clusters. They concluded that although the right-hand side of Eq. (1.1) had been shown to be a useful representation of the observed budget residuals in the lower and middle atmosphere, none of the terms could qualitatively describe the horizontal couplet pattern of vorticity budget residuals typically found in regions of strong shear. Furthermore, they suggested that better agreement could be achieved by formulating Z directly from parameterized cumulus momentum effects. Sui and Yanai (1984) tested this proposed formulation and verified that calculating Z from the curl of the parameterized cumulus momentum effects did a better job of explaining observed values of Z during GATE than the scheme shown in Eq. (1.1).

Esbensen et al. (1986) have recently explained why the formulation based on the cumulus momentum transports are superior in interpreting the observed horizontal vorticity residuals. The key point in their argument is that the vorticity dynamics of individual members of a cloud ensemble can be ignored when clouds are approximated as independent buoyant elements in a common large-scale environment.

Advances were also made in the understanding of the effects of clouds on the large-scale momentum budgets. Stevens (1979) analyzed the momentum budget on the easterly waves scale. The budget results showed that, depending on wave phase, the convection

tends to produce either sources or sinks of momentum at all heights.

Based on the aircraft data from GATE, Zipser et al. (1981) found that the horizontal winds normal to the rainband are strongly modified by the pressure-gradient force, while those parallel to the rainband are modified mainly through mixing. LeMone (1983) claimed that the vertical transport of horizontal momentum normal to a line of cumulonimbus observed during a GATE convective event was against the mean vertical momentum gradient, contrary to the predictions of mixing-length theory. From their numerical modeling study, Soong and Tao (1984) found that the vertical transport of v momentum (parallel to the rainband) was essentially the same in all the simulations they performed, even though the structure of the clouds was different in each of the runs. The u momentum (perpendicular to the rainband) is quite different in all of the simulations. These results imply that the mixing process alone may not be enough in describing the cumulus momentum effect.

1.3 Outline of the thesis

It is clear from our previous discussion, that a satisfactory theory which can describe adequately the cloud effects on the momentum field has yet to be formulated. In this thesis, I will attempt to compute the momentum budget of GATE cloud clusters and will construct a simple numerical model to study some key aspects of the large-scale response to the convective momentum forcing. The kinetic energy budgets of the observed and simulated flow

fields will also be examined.

Chapter 2 will discuss the observational data sets that are used in the observational portions of this study. The structure of thermodynamic variables associated with the cloud clusters, as well as the compositing scheme used in this study, are presented in Chapter 3. Chapter 4 discusses the heat and moisture budgets of five nonsquall cloud clusters observed during Phase 3 of GATE, while the momentum and kinetic energy budgets of these clusters discussed in Chapter 5. Chapter 6 uses a simple numerical model to study the large-scale upper tropospheric response to cumulus momentum forcing that is similar to that found in the observed cloud clusters. Conclusions and suggestions for further research are presented in Chapter 7.

CHAPTER 2. THE DATA SET

One of the primary reasons for locating the GATE ship array at 8.5°N and 23.5°W was to center it on the mean summer location of the eastern Atlantic ITCZ. In GATE, the approach of combining satellite, radar, and aircraft, with an exceptionally dense array of ships launching upper-air balloons was adopted to probe the convective cloud field. These data were supplemented by standard synoptic observations, surface-based cloud photography, and a variety of boundary layer measurements. Houze and Betts (1981) have summarized the observing method used in GATE. Each type of data collected contributed in a unique way to an understanding of the cloud fields.

Two data sets are used in this thesis: a set of gridded upper-air wind and thermodynamic data, and a set of gridded radiation data. The gridded wind data was analyzed by K. Ooyama (HRD-AOML/NOAA) and J.-H. Chu (SSEC, University of Wisconsin, Madison) from the upper air soundings. The gridded thermodynamic data was analyzed in a similar manner by S.K. Esbensen (Oregon State University). The radiation data were constructed by Cox and Griffith (Colorado State University) from satellite information. Here a brief discussion will be presented to describe the data set. More information can be found in Esbensen et al. (1982) and Tollerud (1983).

2.1 Gridded radiosonde wind and thermodynamic data

The GATE experiment was conducted from June to September 1974. The total period was broken down into three phases. Fig. 2.1 shows the GATE ship array during Phase III. Solid circles show the nominal A/B array ship positions and open circles show B-array ship positions.

The upper-air analyses are based on upper-air soundings from the GATE A/B and B ship arrays. The carefully edited upper-air soundings were statistically interpolated to a 1/2° x 1/2° latitude-longitude grid at 41 pressure levels from 1012 mb to 70 mb and at 3 hours intervals during 18 days (31 August-17 September) of GATE phase III.

A unique feature of this analyzed data set is the reduction of spatial aliasing through optimal statistical interpolation. Some of the important components of Ooyama's scheme are briefly described here. As summarized in Esbensen et al. (1982), a spectrally controlled interpolation scheme using cubic B-splines was used to produce time-height section for intership comparisons and data editing. The time-height sections from the series of upper-air soundings at each ship retained information on disturbances with periods $\geq$ 12 hours and vertical wavelengths $\geq$ 100 mb. Spatial interpolation of the time-height series was then performed using a modified version of the optimum statistical interpolation originally proposed by Gandin (1963).

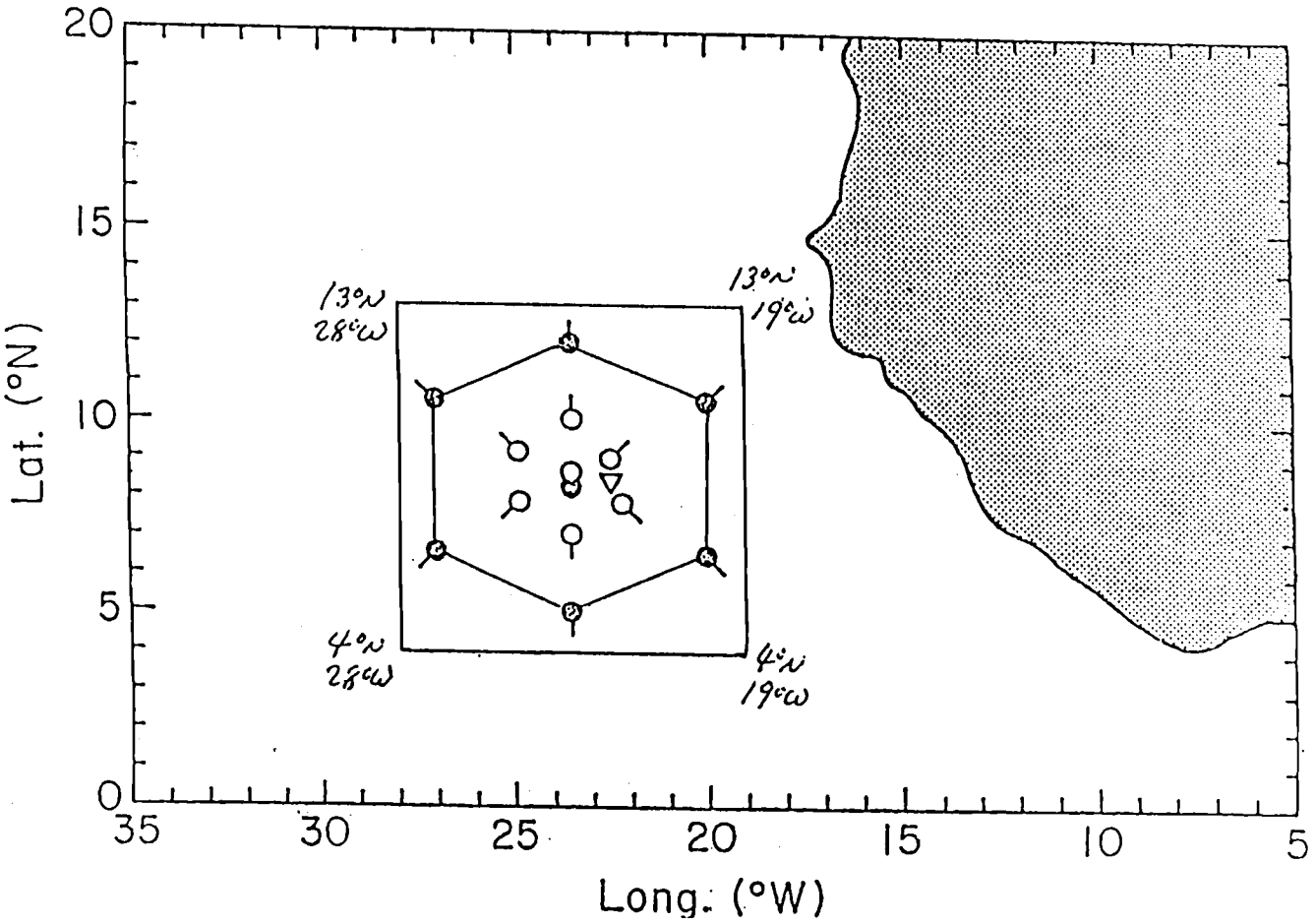

Figure 2.1. GATE ship array during phase III. Solid circles show the nominal A/B array ship positions and open circles show B-array ship positions. The open triangle gives the position of the ship Dallas.

The 8-day low pass filtered data from the time-height sections were chosen by Ooyama and Esbensen to define the so called 'norm' field. In preparation for the statistical interpolation of the deviations of the winds, temperature and relative humidity from the norm fields, a detailed analysis was performed on the level-by-level sample spatial variance and spatial correlation functions of the observed data. Using the cubic B-spline routines, the continuous correlation functions were objectively analyzed from the sample correlation functions constructed from observations at pairs of ships, under the assumption that the field was statistically homogeneous as far as the correlation function was concerned.

The correlation functions were then used to statistically interpolate deviations from the norm field to grid points. Cubic B-splines with a wavelength cutoff of 450 km were fitted to the gridded data. Fig. 2.2 shows the horizontal grid chosen by Ooyama and Esbensen for the representation of the interpolated values. Fig. 2.3 illustrates the vertical grid chosen for this archived set. In all, there are 41 analyzed pressure levels, with the grid intervals varying in depth to give adequate resolution in the upper and lower troposphere. The variables used in this study from the Ooyama and Chu wind data set are horizontal velocity and vertical velocity. The variables used from the thermodynamic data set from Esbensen are temperature and relative humidity. The data are available in 8-day lowpass (the norm field), 2 to 8 day and 12 h to 2 day period bands (see Fig. 2.4). Geopotential fields are deduced hydrostatically from the thermodynamic data set and will be

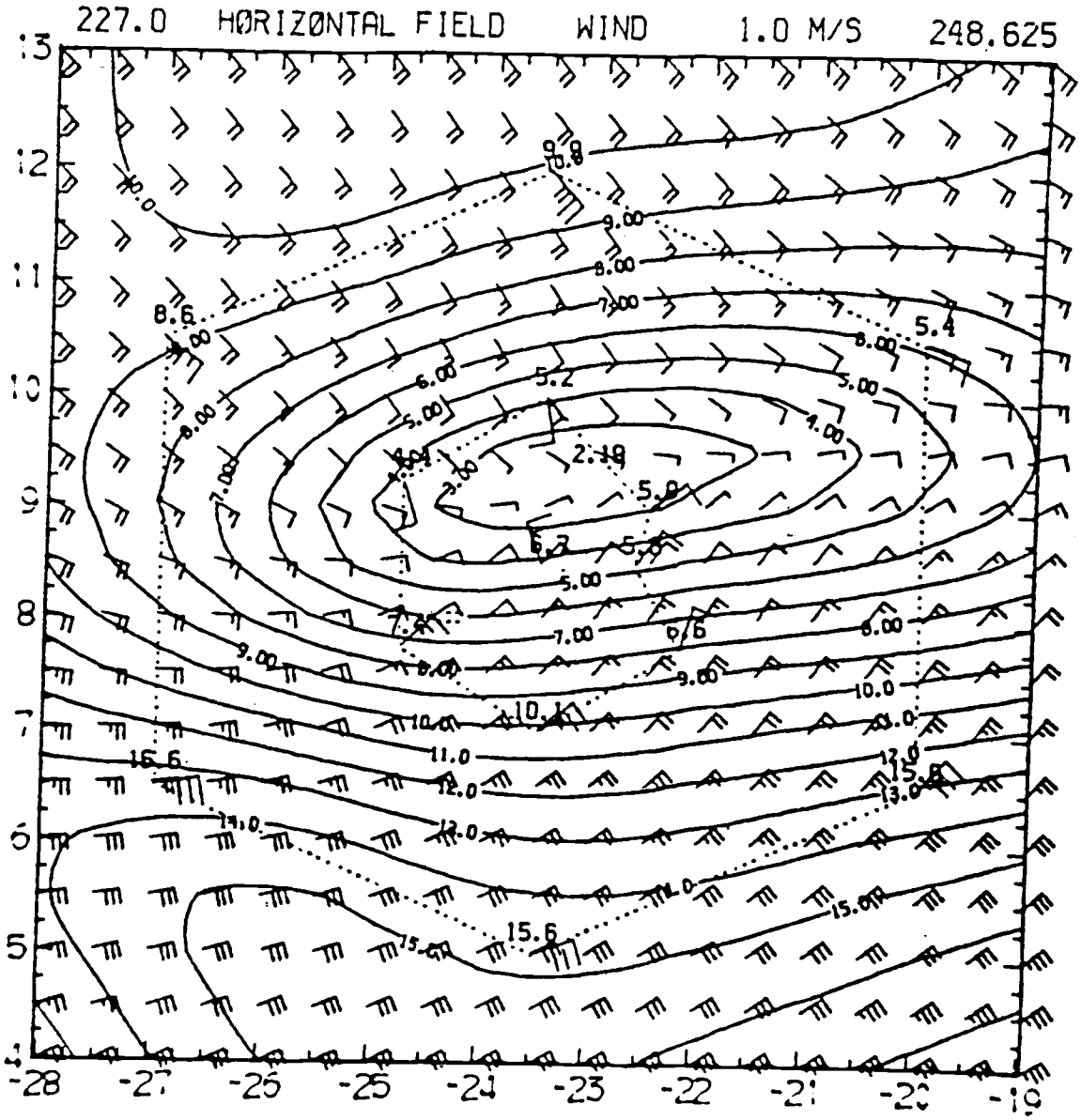

Figure 2.2. Horizontal domain in the analyses of wind and thermodynamic data chosen by Ooyama and Esbensen. This is a 19 by 19 horizontal grid.

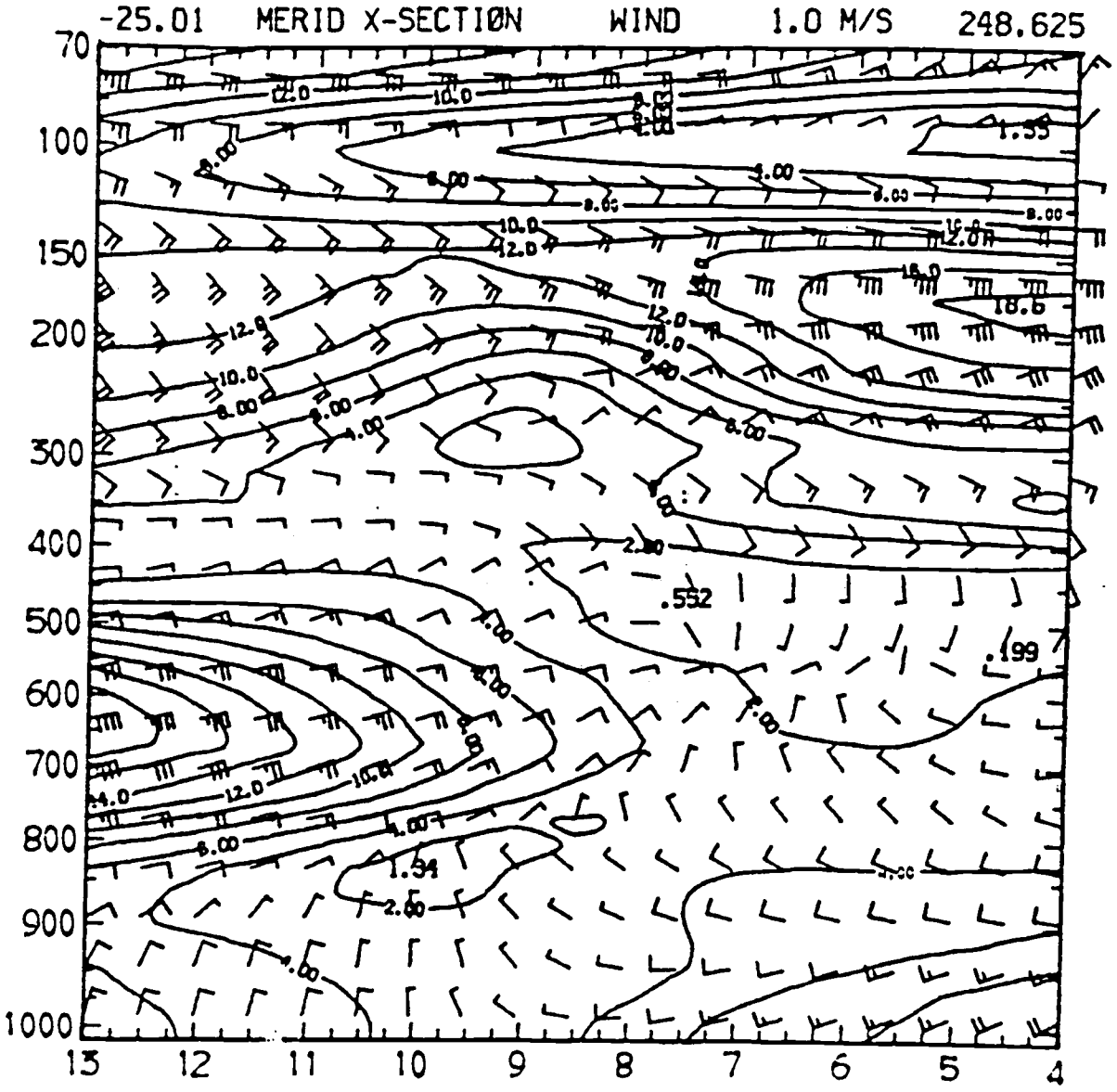

Figure 2.3. Meridional cross-section of windspeed at 25°W at 1500 GMT on 5 September 1974. There are 41 vertical levels in the data set.

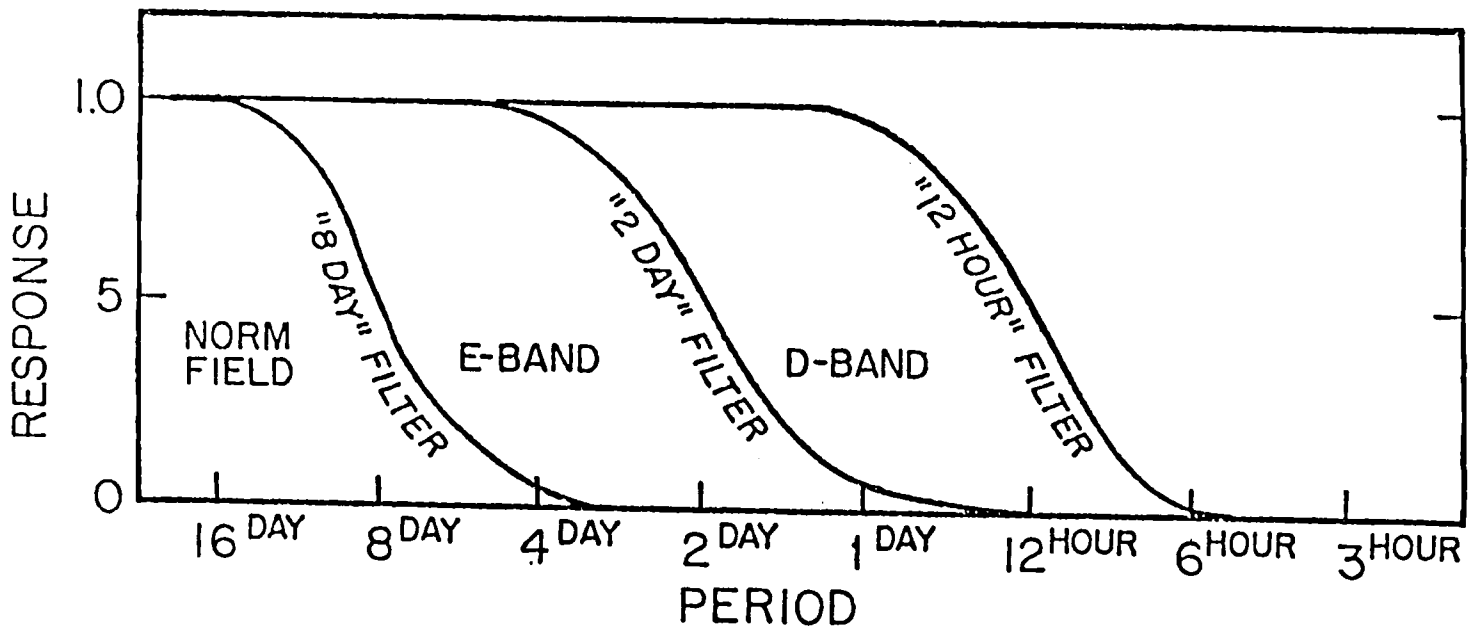

Figure 2.4. Frequency response functions of filters used in analysis of wind and thermodynamic data.

discussed in Chapter 5 along with the momentum and kinetic energy budgets.

2.2 Satellite-observed radiation data

During GATE, a geostationary meteorological satellite (SMS-1) gathered radiation data from the GATE area. These data were obtained at 15-to-30 minute intervals throughout the experiment and provided a detailed history of the development of cloud patterns over the GATE region. Based on this satellite-and radar-inferred cloud structure, Cox and Griffith (1979a) designed computational algorithms to generate the shortwave and longwave radiation divergence during Phase III of GATE. The average cloud-water content and two different basic types of clouds were prescribed to construct the radiative divergence profiles. Cloud-top pressure distributions were generated from SMS infrared brightness data observed over the entire GATE A/B array. This involved two steps. The first step was to convert the observed brightness to a cloudtop temperature by applying the Visible Infrared Spin-Scan Radiometer (VISSR) calibration routine. The second step was to associate the temperature at each cloudtop with a pressure by using the information from the previously-determined relationships of temperature versus pressure. The complete procedure has been described in Cox and Griffith (1979a).

The horizontal grid points at which Cox and Griffith chose to output their radiation data are the same as those at which the wind and thermodynamic data are stored. The domain of the radiation

data is slightly smaller than that of the gridded radiosonde sets, extending from 20°W to 27°W and from 5°N to 12°N. The averaging period is one hour and there are 10 vertical levels, while the time interval for the upper air data is every 3 hours. This data set included cloud-top percentage data, and radiative divergences of shortwave and longwave data. Shortwave and longwave divergences represent the radiative effect of that 100 mb layers with the exception of the value in the lowest layer which represents the layer from the surface to 1000 mb. Cloud-top percentage data for a given layer represent the percentage of the sky covered by cloud with cloudtops that fall within that layer. The cloud-top data are used to locate the anvil clouds associated with GATE cloud clusters in time and in space.

2.3 Characteristics and quality of the analyzed data set

The radiosonde data quality have been discussed by Ooyama and Esbensen (1977), Reeves et al. (1976), and Frank (1978). The characteristics of the gridded analyzed data set for wind and thermodynamic variables used in this study were documented and discussed in Esbensen and Ooyama (1983). Some of their findings are described here.

The domain of the spatial analysis extends over a nominally square area bounded by the approximate limits of 4°N and 10°N latitude and 19°W and 28°W longitude. However, the statistical measures of analysis quality for the E-band and D-band analyses deteriorate quickly outside the A/B hexagon, where the data have

been extrapolated rather than interpolated. Also the norm fields of winds, temperature and relative humidity become increasing dependent on the choice of boundary conditions outside the A/B hexagon. Therefore, the data outside the A/B array, particularly near the corners of the analysis domain, should be interpreted with caution.

The filters applied to the spatial correlation functions and to the statistically interpolated values in the E- and D- band data have an effective wavelength cutoff of 450 km. Thus, the analysis can resolve synoptic-scale features and the largest cloud clusters which have anvil clouds with horizontal dimensions on the order of 200 km.

In the lower troposphere, the diurnal variations of temperature and relative humidity are negligibly small (~0.1°C and 1%, respectively). However, in the upper troposphere relatively large diurnal variations (0.2°C~0.4°C) remain in the data. Fig. 2.5 shows the meridional cross section of the geopotential field, which is composited with respect to the time of day at 0300 GMT and 1500 GMT, through the center of the B array for the E+D band. The diurnal effect is on the order of 20 m^2/s^2 below 350 mb (or 2 m of geopotential height), but becomes quite large in the upper layers due to the diurnal temperature effect. To interpret the quantities as diurnal thickness changes, or composites of disturbances such as cloud clusters that may have a clear diurnal component in their time of occurrence, we have to be cautious.

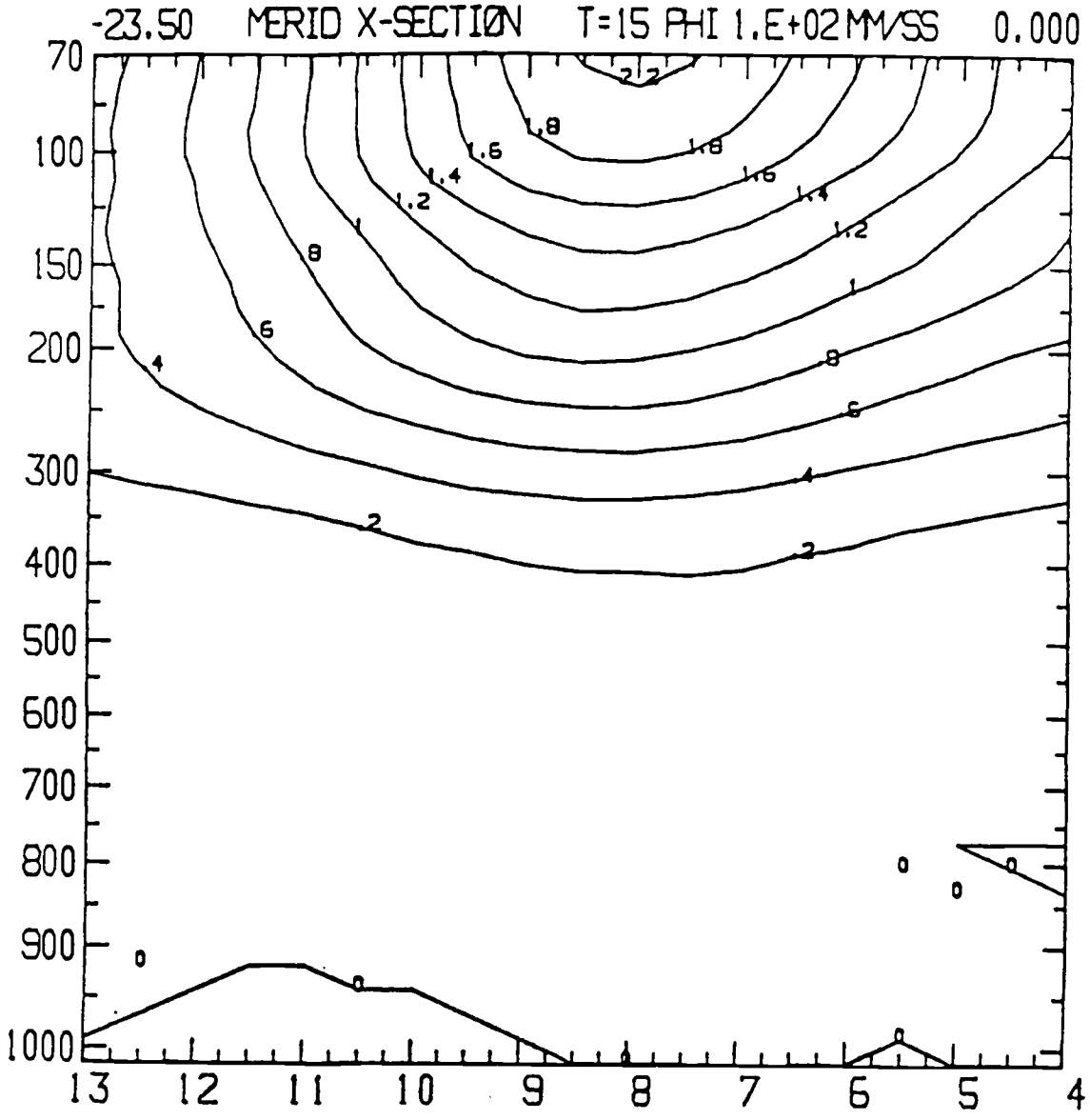

(a)

Figure 2.5. Meridional cross-section of anomalies of geopotential for the Phase III composite at (a) 1500 GMT and (b) 0300 GMT, with horizontal plots at 101 mb for (c) 1500 GMT and (d) 0300 GMT. Contour interval is 10 m^2/s^2.

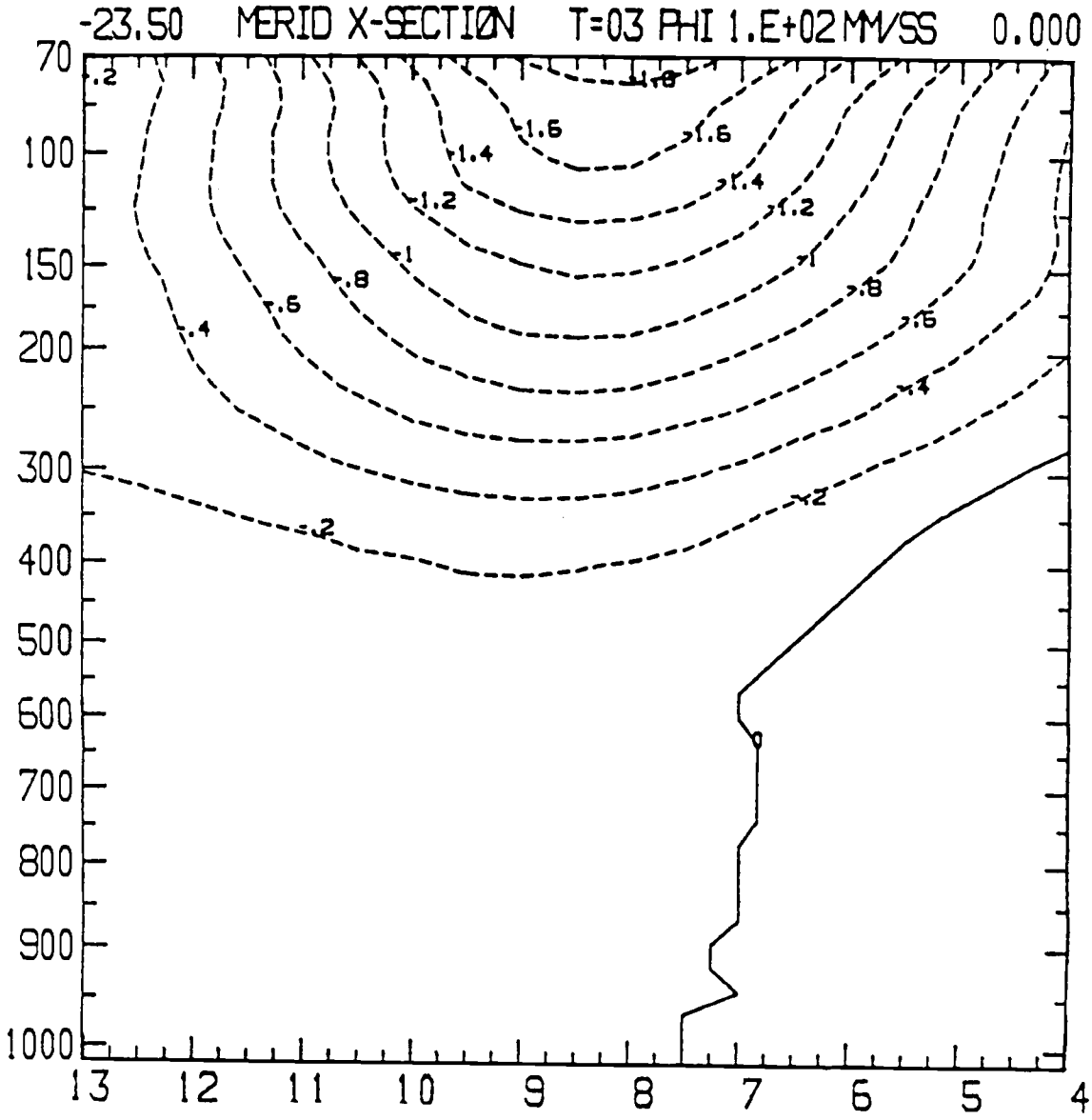

(b) 0300 GMT

Figure 2.5 (continued)

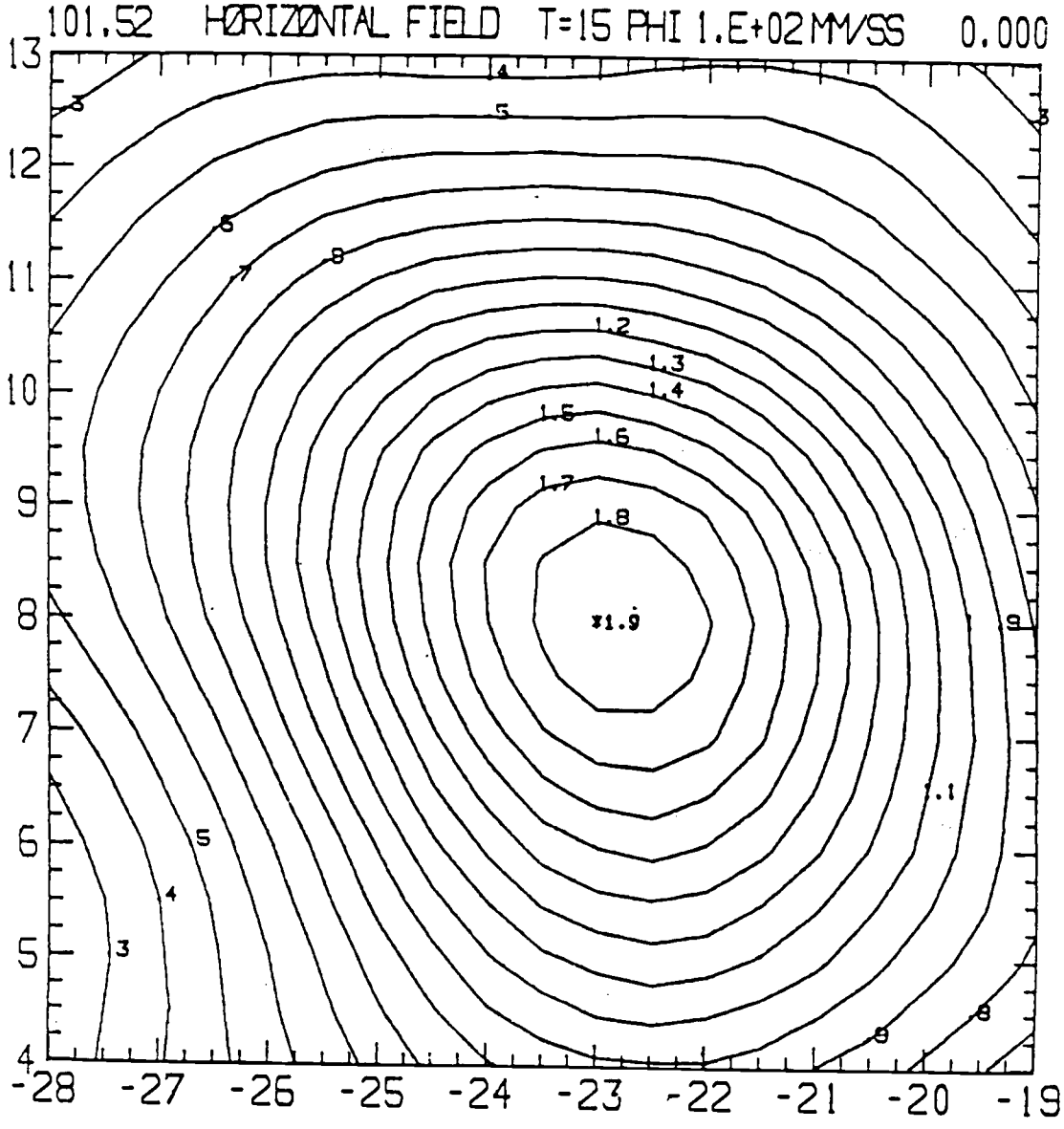

(c) 1500 GMT, horizontal plot

Figure 2.5 (continued)

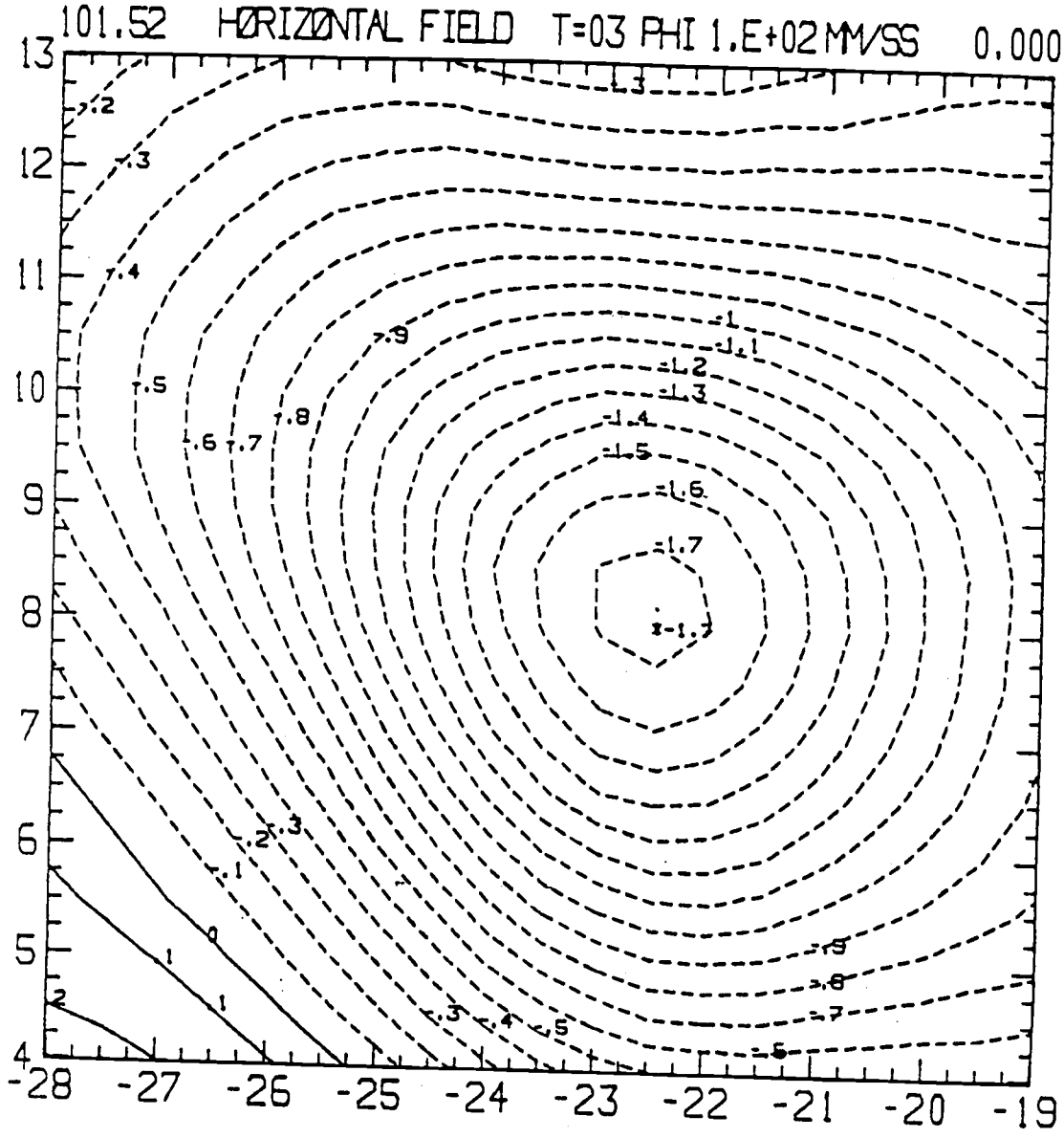

(d) 0300 GMT, horizontal plot

Figure 2.5 (continued)

CHAPTER 3. THERMODYNAMIC ANALYSIS ASSOCIATED WITH GATE CLOUD CLUSTERS

Houze and Betts (1981) concluded that in the ITCZ region, there were two types of cloud clusters, rapidly moving squall clusters, and slowly moving non-squall clusters. The majority of squall clusters formed and decayed over the West African continent. The cloud clusters sampled by the GATE ship array were predominantly non-squall clusters. The present study will focus only on the events involved with the non-squall cloud clusters (simply called cloud clusters in the latter part of this thesis). This chapter will discuss the methodology of the composite analysis, and summarize the characteristic features of the thermodynamic variables associated with the development of the cloud cluster.

3.1 Computation of anvil index and determination of stages for cluster development

Following Tollerud and Esbensen (1983), we identify the stage of cluster development from an indirect measure of the area covered by anvil clouds in large cloud clusters. The anvil index is determined based on the radiation data from Cox and Griffith (1979a). An anvil index is nonzero only when the data indicate that the tops of large convective clouds have reached the layer between 100 mb and 300 mb. The cloud-top percentages in the top two layers of the radiation data set are used in constructing the

index. The anvil index is set to 1 in each 1/2° by 1/2° grid area where 90% or more of the sky above 300 mb is covered by cloud, while all other gridpoints are assigned a value of zero. The hatched region in Fig. 3.1 identifies the area where the index is 1.

Based on these criteria, a time series of anvil index plots can be generated. Because of the limitation on the resolution of the wind and thermodynamic data set, only those anvils that persist in the satellite data for six hours or more and reach an approximate diameter of 200 km are identified as a cloud cluster.

The anvil index is used as an indicator of a cluster's stage of development. The life cycle of each cluster is broken into three stages: growing, mature, and dissipating. In the growing stage, the anvil first appears (that is, the index becomes 1 at some location in the vicinity of the cluster) and grows rapidly in size. During the mature stage the cluster anvil attains its greatest horizontal extent and remains approximately the same size. In the dissipating stage the anvil begins to break up and eventually disappears (the index at all gridpoints in the previous anvil region becomes zero).

The anvil index is also used to locate the cluster center, which is needed in the compositing procedure as discussed in the Section 3.2. The cluster center represents the centroid of the anvil cloud in the horizontal plane during the mature stage in which the cluster attains its greatest horizontal extent.

It is noted that although the definitions of life cycle stages

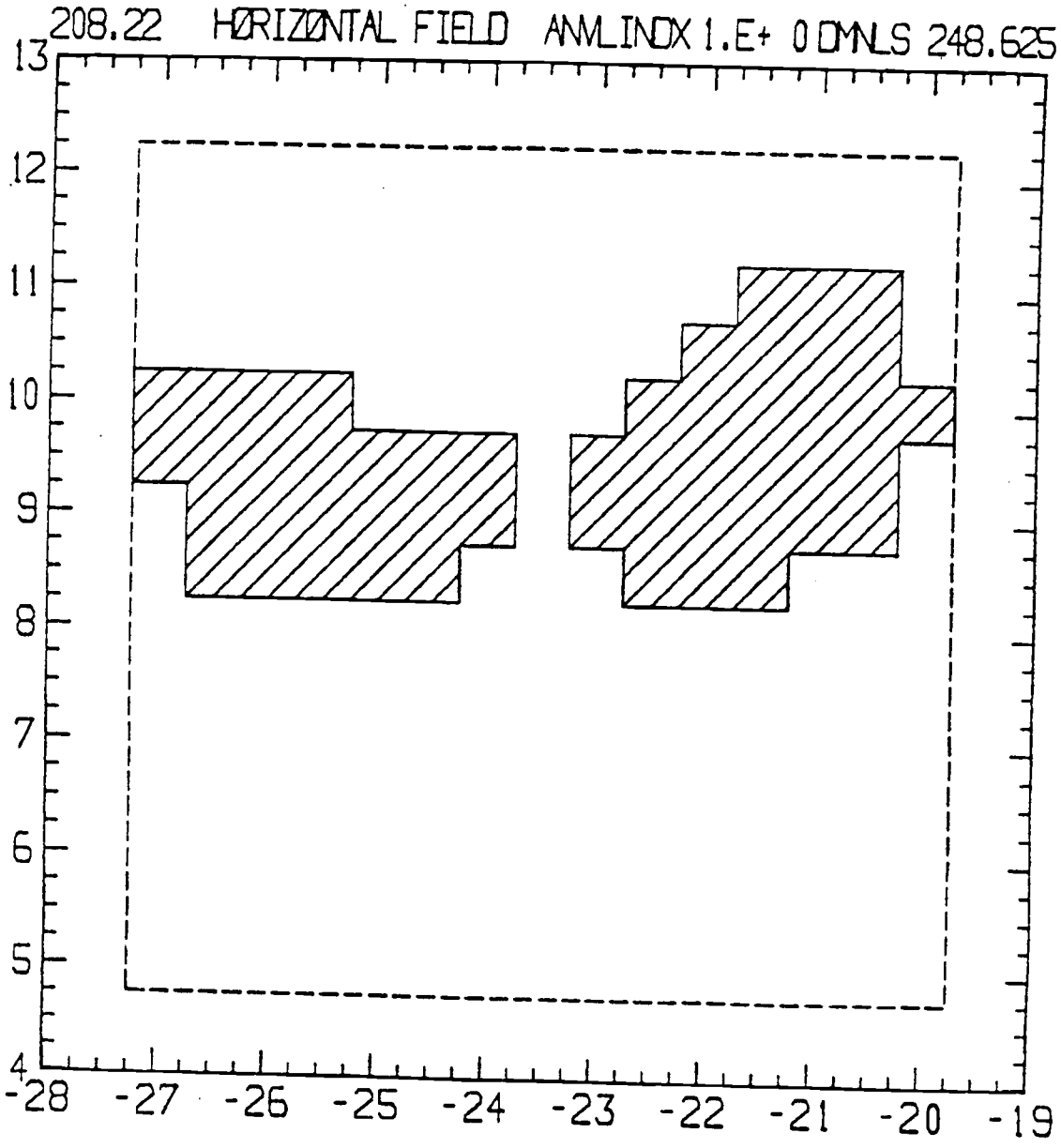

Figure 3.1. One example of the anvil index. The anvil index is used to determine the stages of the cluster development and the center of the cluster.

roughly parallel those of Leary and Houze (1979), exact correspondence should not be expected. The criteria used here are based upon satellite data which cannot resolve cloud features smaller than anvils, while the classification criteria of Leary and Houze (1979) are based on radar data which can resolve smaller-scale convective features. There is typically a 2-3 hour lag between the two classification schemes, with the beginning of the life stages determined here trailing those determined in the manner of Leary and Houze (1979).

3.2 The compositing procedure

During phase III of GATE, five cloud clusters were identified under the criteria described in Sec. 3.1. Table 3.1 and Fig. 3.2 from Tollerud and Esbensen (1983) show the time of occurrence, cluster center location, and the life cycle of slow-moving clusters and their relation to the easterly wave phase. The easterly wave phase categories used to produce Fig. 3.2 were determined by Thompson *et al.* (1979). It can be seen that the clusters' mature stage tends to occur during middle to late afternoon. Also, it can be seen that the slow-moving clusters intensify within or just before the wave trough and dissipate just behind it. These relationships between cluster development, time of day, and easterly-wave phase are in accordance with numerous other studies of GATE convective systems (Houze and Betts, 1981).

The compositing procedure consists of placing a 13 by 13 point rectangular composite grid over each cluster at each of the 41

Table 3.1 Slow-moving clusters included in composite.

Cluster No.	Date	Center Location, Mature stage
1	2 Sept. 1974	25°W, 8°N
2	5 Sept. 1974	21°W, 9.5°N
3	5 Sept. 1974	25°W, 9°N
4	16-17 Sept. 1974	21°W, 9°N
5	17 Sept. 1974	25°W, 10°N

Table 3.2. The life cycle of 5 September cluster (cluster no. 3 in Table 3.1).

Stage	GMT time	MT
growing	0900	52
mature	1500	54
dissipating	2100	56

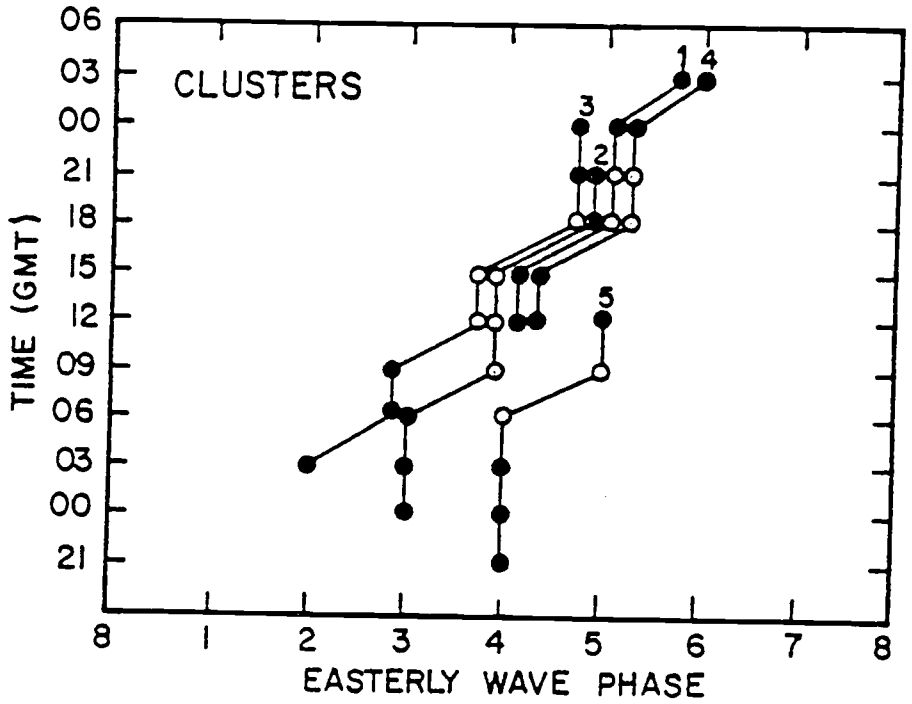

Figure 3.2. Life cycle of GATE phase III cloud clusters included in cluster composite. Open circles identify mature stage of each cluster. The chronology of easterly waves are from Thompson et al. (1979). Number on cluster life cycle lines correspond to numbers on Table 3.1 (from Tollerud and Esbensen, 1983).

pressure levels, with the composite grid axes oriented north-south and east-west. The grid intervals are approximately 1/2° latitude by 1/2° longitude. The composite grid center point is placed in each case at the cluster center, which is pre-determined from plots of the anvil index. Except for cluster 5, which was determined to have just one sampling time in the dissipating stage, two consecutive sampling times were available for each stage of each cluster. The resulting set of values are then averaged within each stage at each gridpoint in the three-dimensional composite grid volume. Fields thus composited include wind and thermodynamic variables, and terms for various budget equations.

To the extent that individual cloud clusters have similarity in terms of thermodynamic and dynamical variables, the compositing process may be regarded as summarizing the features of the observed non-squall cloud clusters. However, due to the small number of samples one has to be cautious in generalizing the results. From Table 3.1, we note that cluster 2 and cluster 4 (both are at the eastern part of the array) reach their mature stage, while cluster 3 and cluster 5 are only at their growing stage in the same time period. Hence, information at the mature stage in clusters 2 and 4 affects the eastern part of the composite array in the growing stage; extreme values tend to be shifted to the eastern part in the growing stage. In the other stages, this type of distortion does not occur.

3.3 Cloud cluster event on 5 September 1974

The 5 September cluster was among the largest in GATE and was well-sampled by a variety of instrument systems. This cloud cluster has been among the most extensively analyzed system within GATE. This section will describe the general synoptic situation of the 5 September 1974 cluster and its associated thermodynamic fields.

3.3.1 General synoptic setting

The general synoptic setting on 5 September was described in Leary (1979) and Ogura et al. (1979). Fig. 3.3 shows the sequence of cloud activity as seen in satellite infrared images from 3 September 1974 to 6 September 1974. The 5 September double cloud cluster is preceded by a fast-moving squall cluster over the GATE ship arrays. The eastern cluster appears slightly earlier than the ultimately more intense western cloud cluster. Both clusters form just west of the trough of a passing easterly wave. The eastern cluster forms around 2100 GMT 4 September at the edge of GATE A/B array, and moves westward to the location at 9°N, 21°W at 0000 GMT 5 September. The western cluster forms in the early morning of 5 September (while the eastern cluster is in its mature-dissipating phase), matures in the afternoon and dissipates at late afternoon. The stages of the western cluster life cycle have been identified as in Table 3.2. The western cluster is the main focus here.

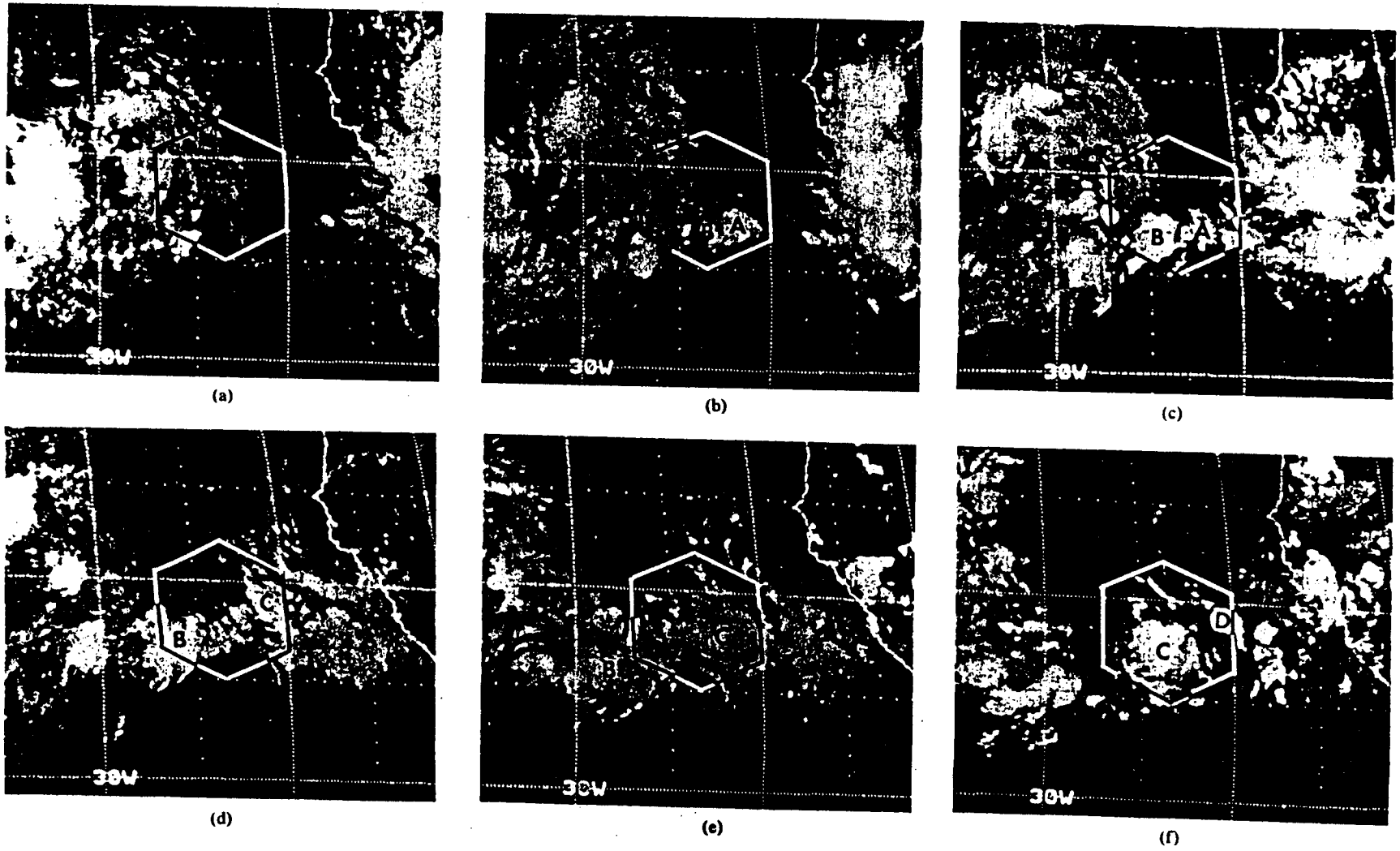

(a) (b) (c) (d) (e) (f)

Figure 3.3. The infrared satellite photography for the period from 1800 GMT 3 September 1974 through 1800 GMT 6 September. Six clusters are marked as A through F.

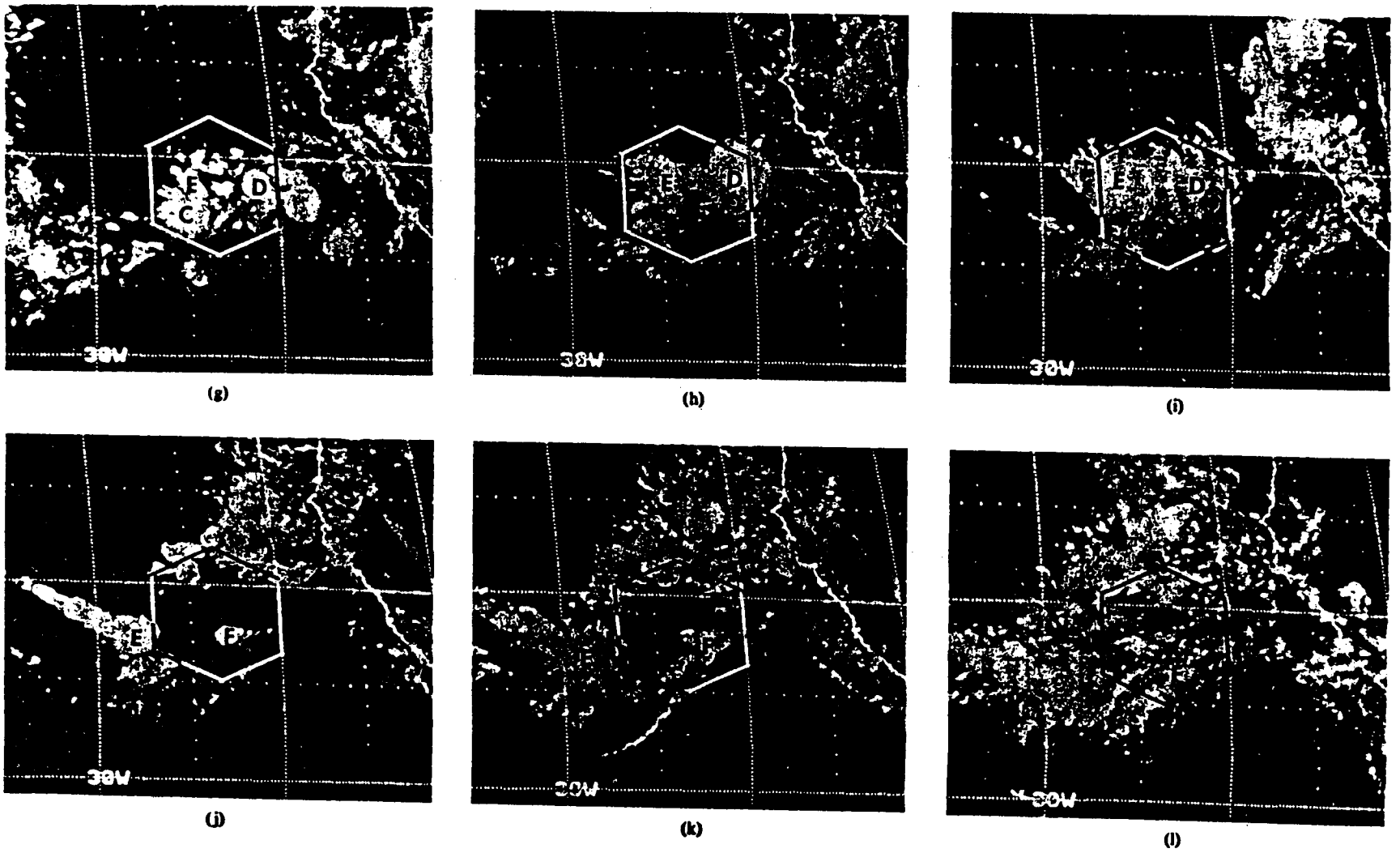

Figure 3.3 (continued)

3.3.2 The thermodynamic fields

Tollerud (1983) has discussed the wind structure of the 5 September cluster. He found upper-layer divergence coincided closely with anvil cloudiness, and reached its peak when convection was most intense and then decreased at a much slower rate. Strong divergence in upper layers still existed at 2100 GMT on 5 September after deep convection had ceased. The vertical structure of horizontal divergence in the growing stage is characterized by a near-surface convergent layer up to 850 mb and two divergent layers between 850-500 mb and 300-150 mb, with weak convergence in between. Upper-layer divergence became particularly large in the latter stage of the cluster, and the surface convergence decreased in intensity.

The vertical velocity went through a corresponding change. There was strong upward velocity in the lower layer in the growing stage and maximum upward velocity at 350 mb level in the mature stage. The vertical velocity in the dissipating stage in the upper layer was larger than that in the growing stage.

The norm fields (8-day low pass part of the data) of the temperature and relative humidity are one to two orders of magnitude larger than the perturbed part of these variables. To identify the change of temperature and relative humidity associated with the cloud cluster event, it is more revealing to present only the contribution from the perturbed part.

Figs. 3.4 and 3.5 show horizontal sections of relative humidity and temperature anomalies at four different pressure

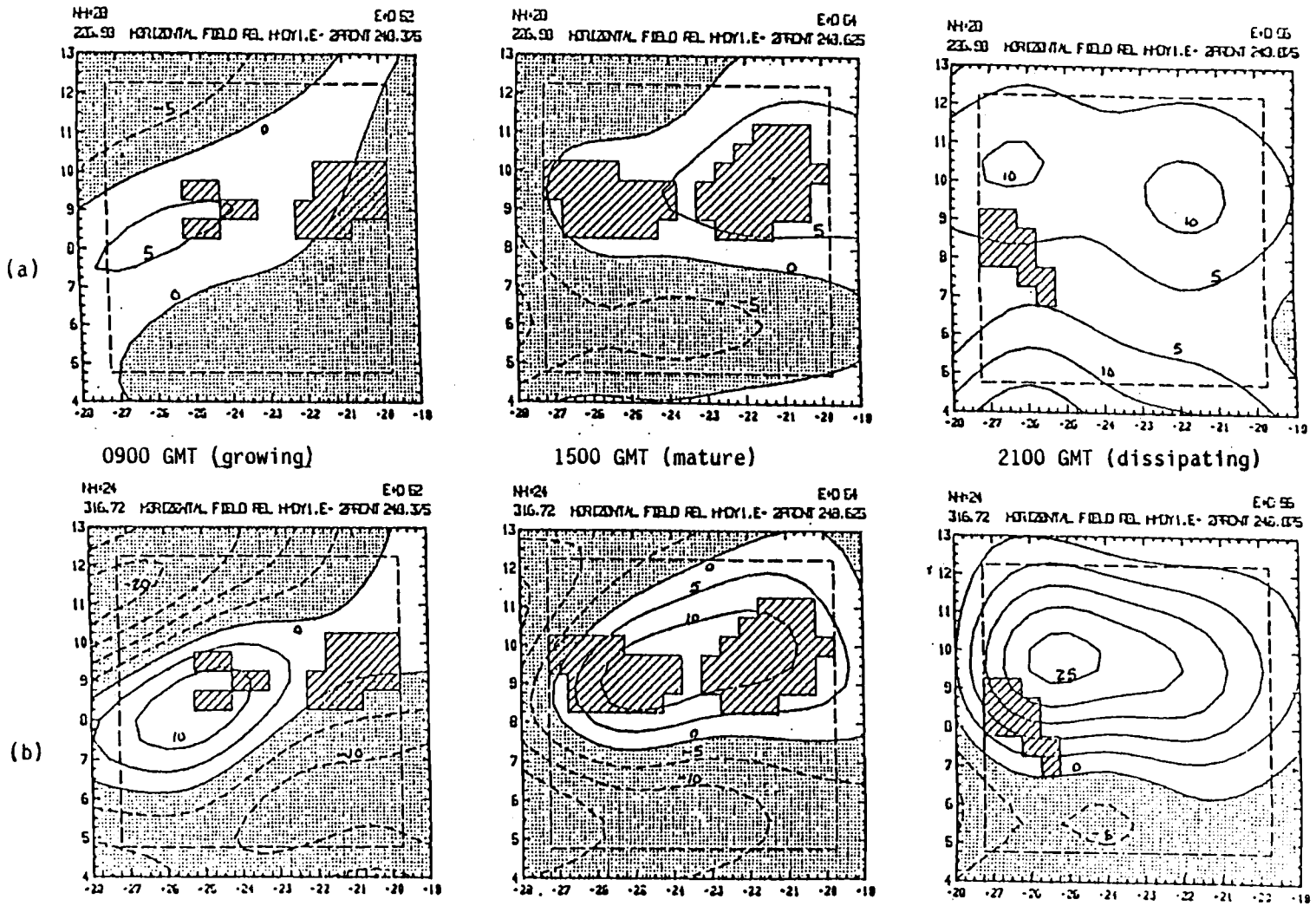

Figure 3.4. The horizontal contour plots of relative humidity deviations (E+D bands) during the life cycle of 5 September cluster at (a) 227 mb, (b) 317 mb, (c) 463 mb, and (d) 738 mb. Units are percent; contour interval is 5%.

(c)

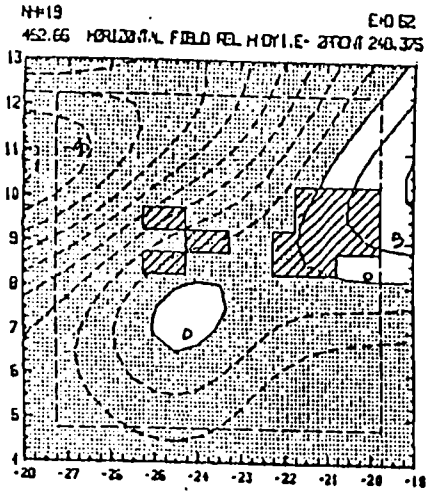

0900 GMT (growing)

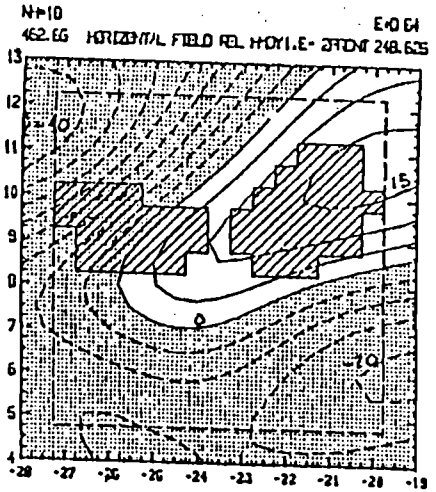

1500 GMT (mature)

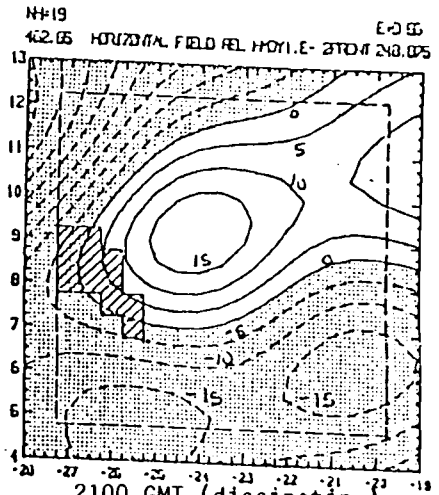

2100 GMT (dissipating)

(d)

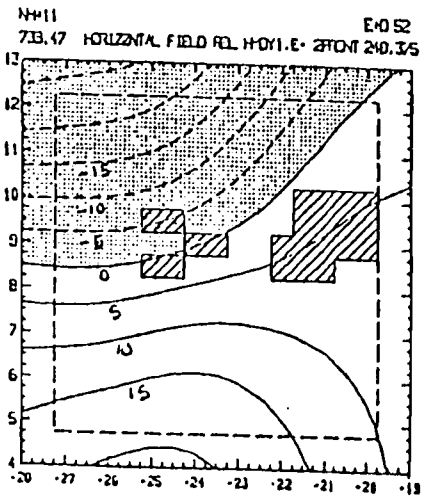

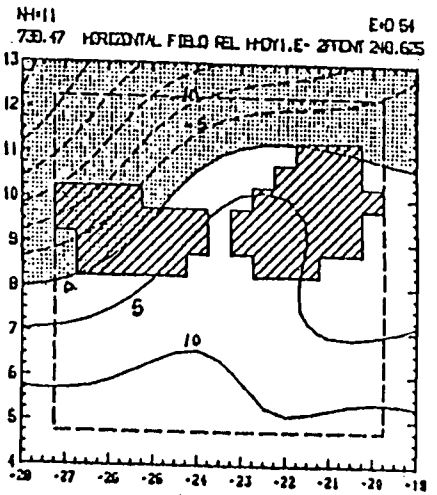

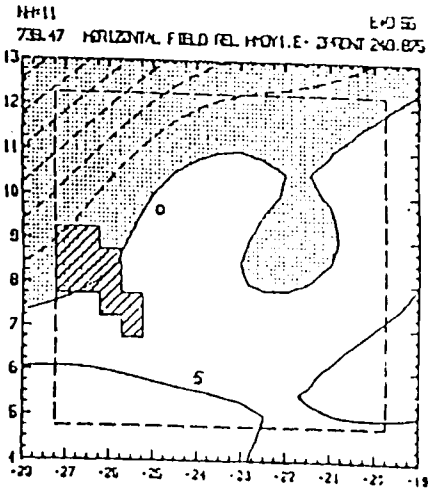

Figure 3.4 (continued)

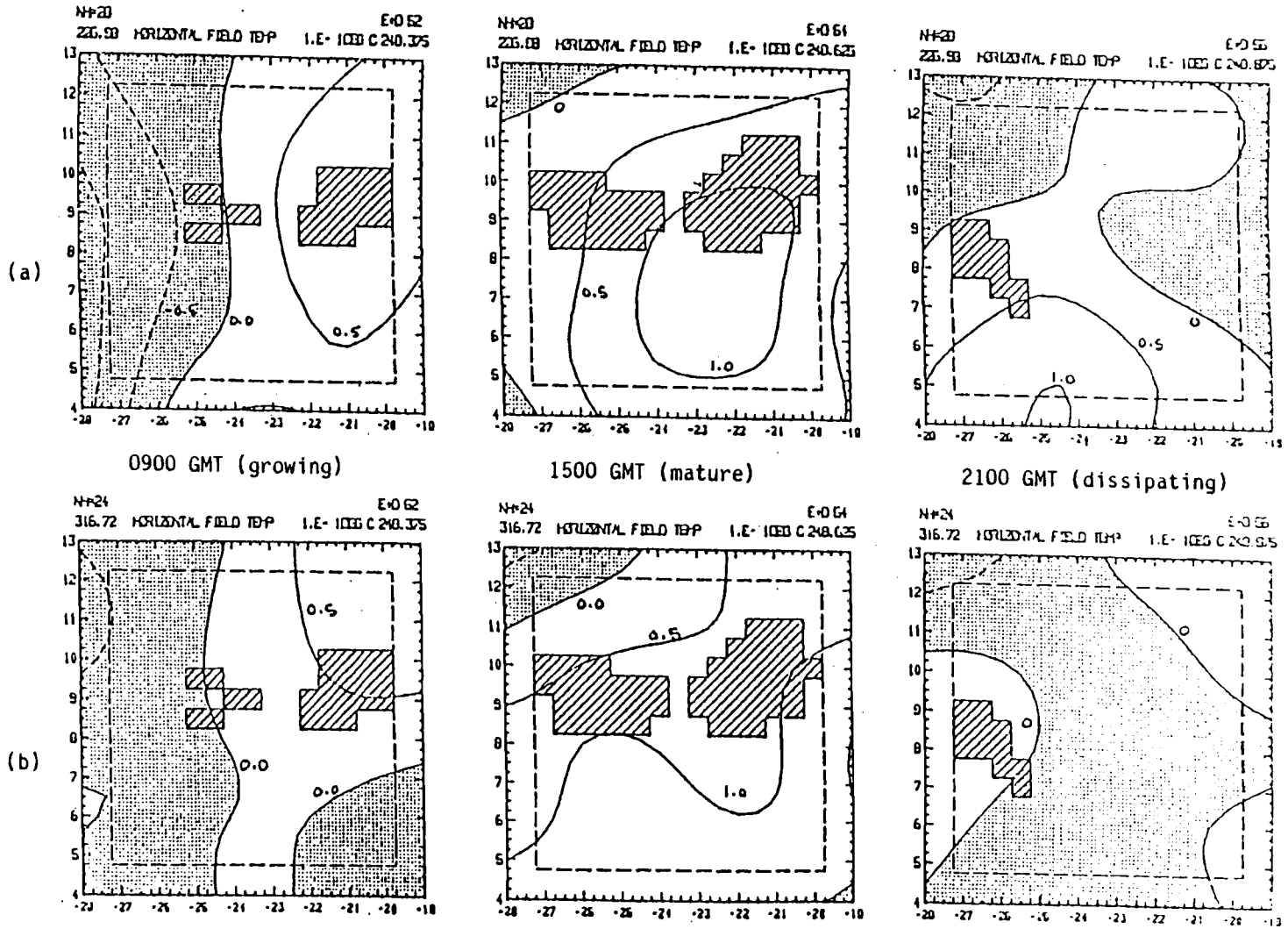

Figure 3.5. As in Fig. 3.4 except for temperature deviation. Units are °C; contour interval is .5°C.

(c)

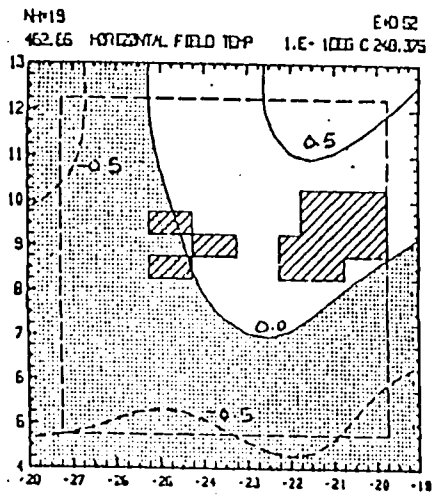

0900 GMT (growing)

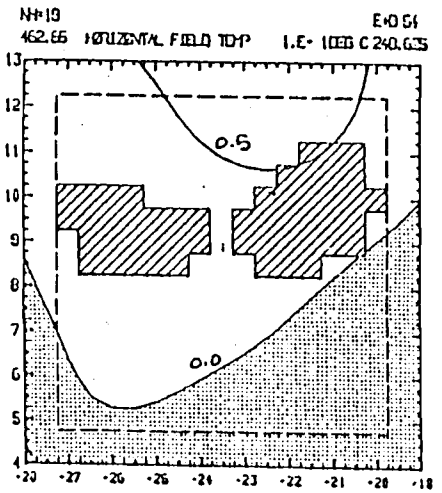

1500 GMT (mature)

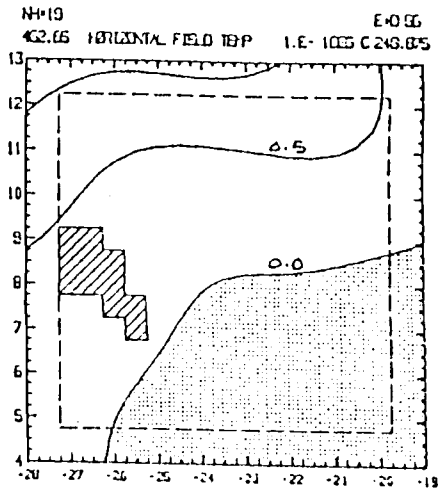

2100 GMT (dissipating)

(d)

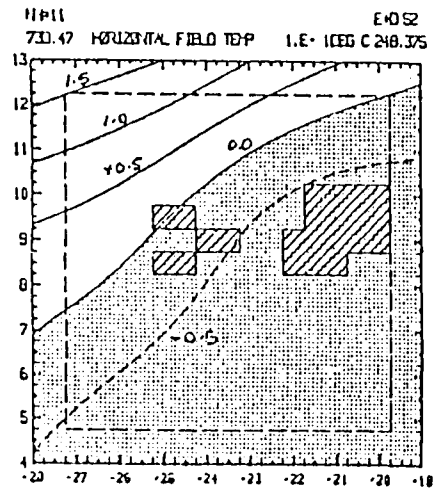

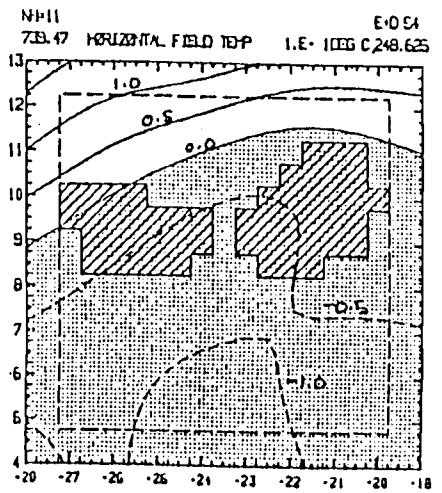

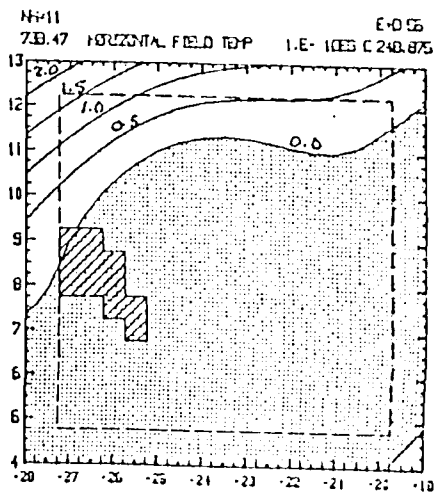

Figure 3.5 (continued)

levels during the life cycle of the 5 September cloud cluster. The features with periods greater than 8 days are not included, but easterly waves and cluster-scale features remain.

At upper levels relative humidity plots show a relative maximum situated within the anvil in the mature stage. The temperature is warmer in the mature stage than in other stages. The relative maximum of relative humidity and warming at upper layers suggest a moistening effect in the anvil region in the mature stage. This moistening effect is an indication of the water vapor that has been transported from lower layers through cloud-cluster-scale ascent or through the detrainment of water vapor by penetrating convection. Warming on the order of 0.5°C makes it difficult to judge whether the warming is simply a diurnal influence or an effect associated with the convection.

At 738 mb, the influence of easterly waves can be found, with warming and drying to the northwest and cooling and moistening to the southeast.

3.4 Composite results

Fig. 3.6 shows the meridional cross-sections of the anomalous relative humidity composite in the life cycle of the cloud cluster. In the growing stage, an easterly wave pattern dominates in the 650-800 mb layer. The order of magnitude of the anomaly is around 3% near the cluster center in the upper layers. In the mature stage, the anomaly increases and reaches around 10% at upper layers, while at the easterly wave level, the moistening extends

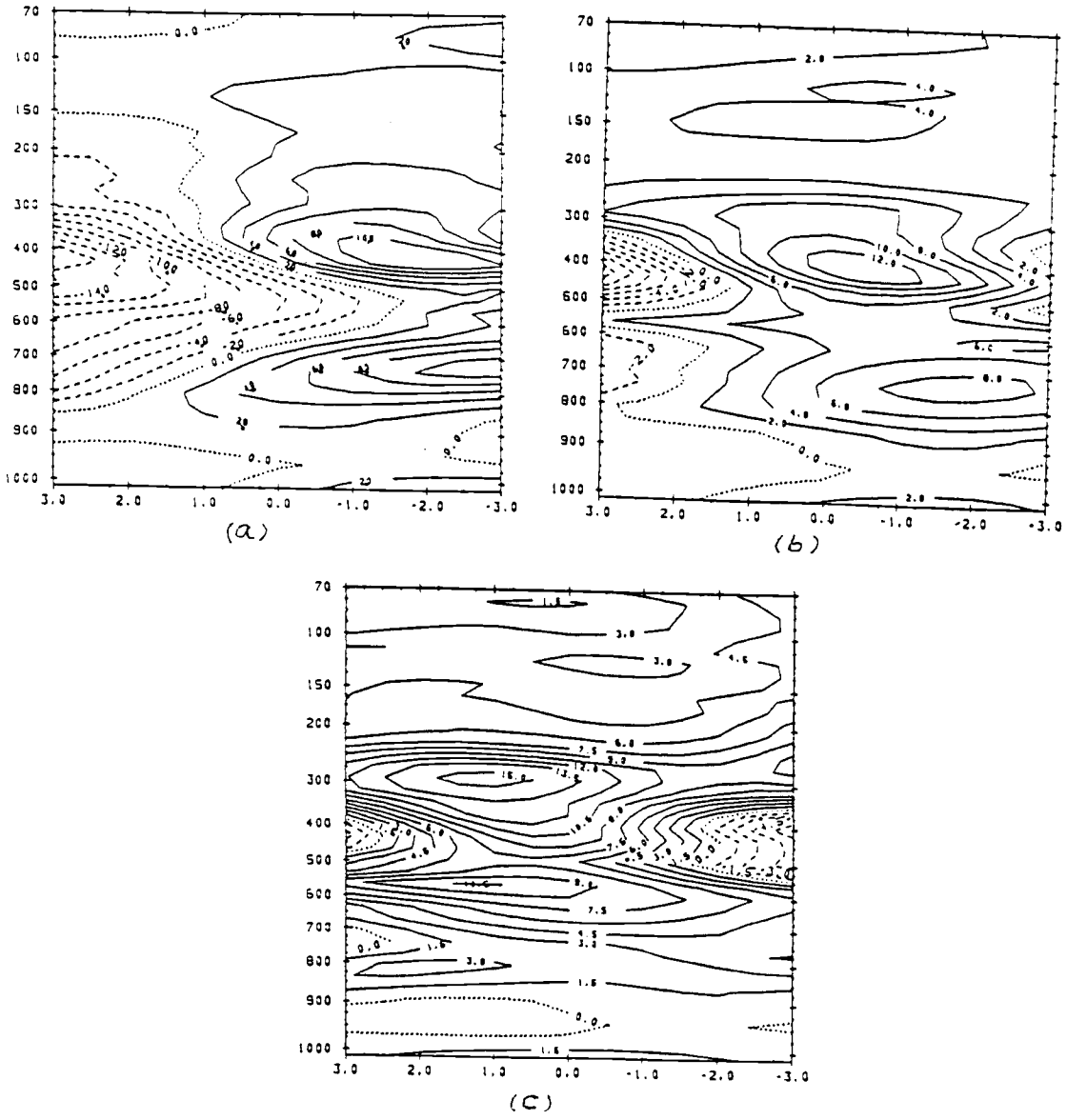

Figure 3.6. Composited meridional cross-section of relative humidity deviations (E+D bands) through the cluster center during (a) growing, (b) mature, (c) dissipating stages. Units are %; contour interval is 2%.

farther north. The anomaly is still large in the dissipating stage at upper layers. The corresponding temperature fields are shown in Fig. 3.7. In the mature stage, a clear warming at the 250 mb level on the order of 0.5°C is identified, while lower layers are still experiencing the influence of the easterly wave. Warming at the upper layer in the dissipating stage is on the order of 0.1°C. As pointed out in Chapter 2, the diurnal temperature effect at the upper troposphere layer is on the order of 0.2°C. Thus the warming at 250 mb on the order of 0.5°C may not be totally due to the cloud-cluster effect.

From Figs. 3.6 and 3.7 we may conclude that in the mature stage, relatively large warming and moistening effects occur near the cluster center region, with a relative humidity maximum at 400 mb and a warming maximum at 250 mb.

The differences of the temperature and moisture content between the dissipating and growing stages may reveal the contribution of the convection to the environment. Figs. 3.8 and 3.9 show the meridional cross-section of the total moisture content and temperature differences (8-day low pass data included, although the contributions are mainly from the perturbed part). Moistening occurs over about 750-200 mb, with the maximum moistening occurring around the 600 mb level (~1 g/kg). Drying dominates from the surface to 750 mb.

Temperature becomes warmer after the development of convection in the 250-450 mb layer, while cooling prevails in the lowest layer. This result is comparable with that of Frank (1978), in

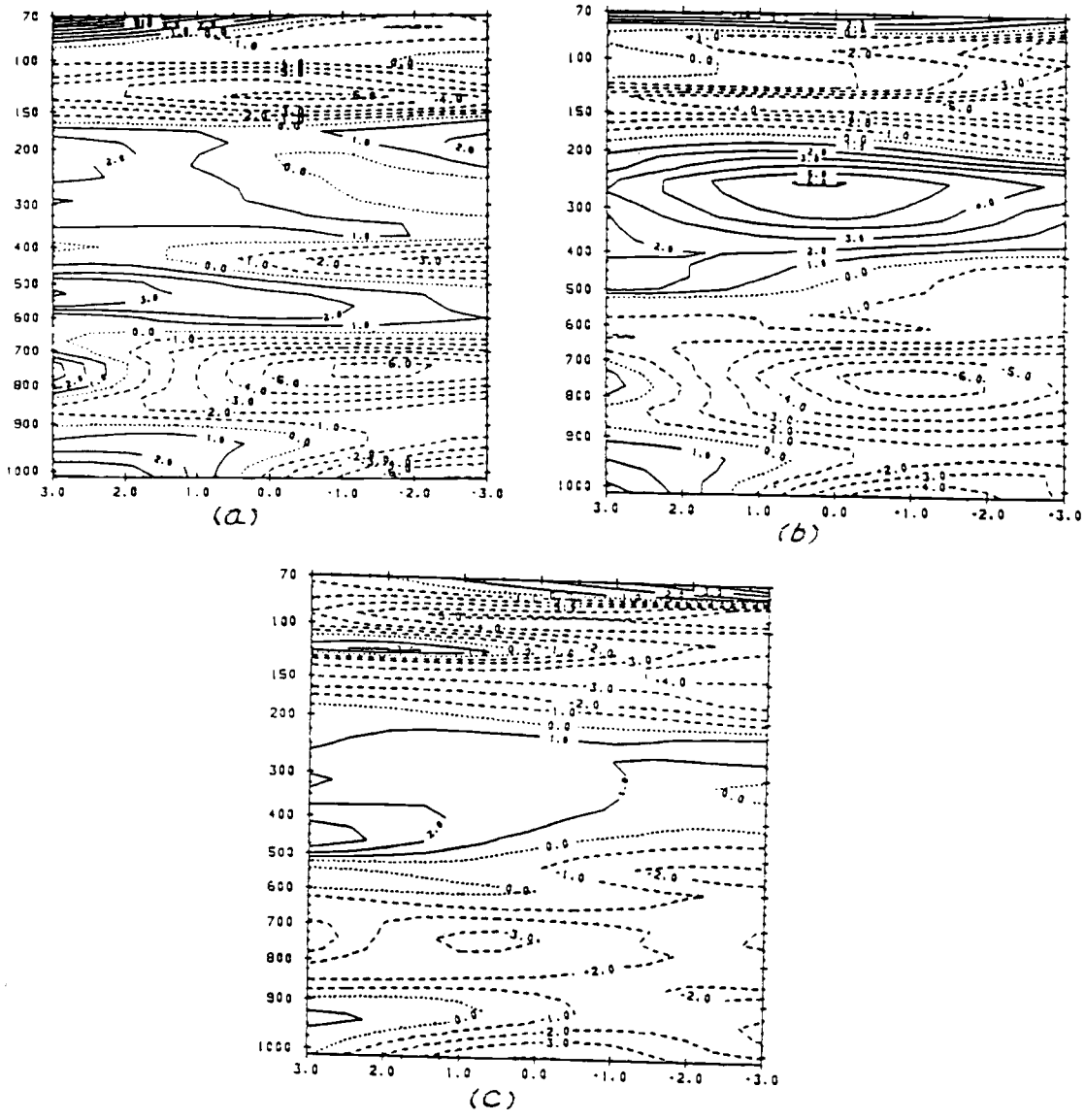

Figure 3.7. As in Fig. 3.6 except for temperature deviations. Units are 10^{-1} °C; contour interval is 0.1°C.

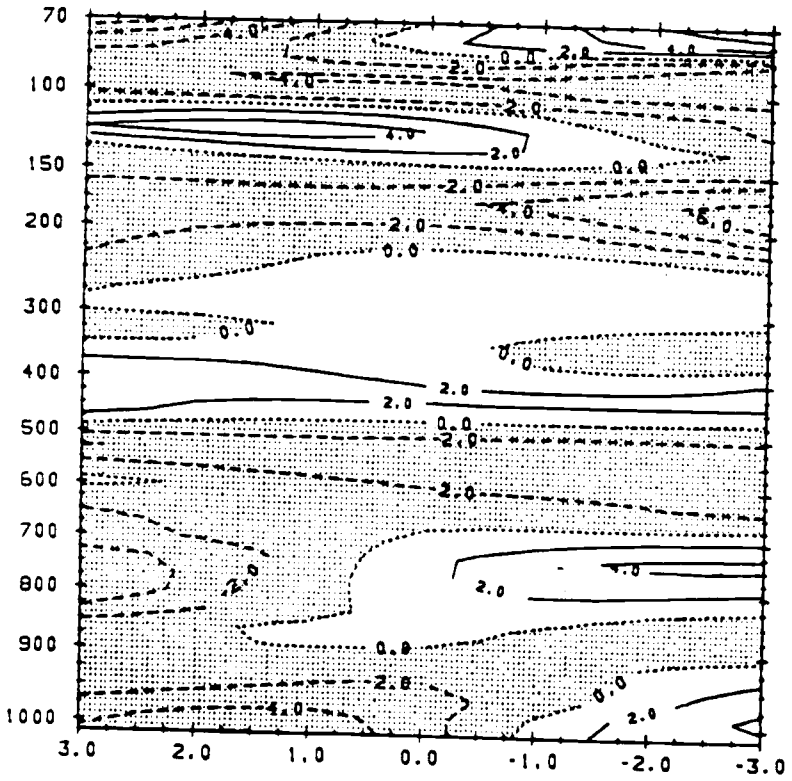

Figure 3.8. Meridional cross-section of moisture content difference between the composited dissipating and growing stages. Units are 10^{-4}; contour interval is $2x10^{-4}$.

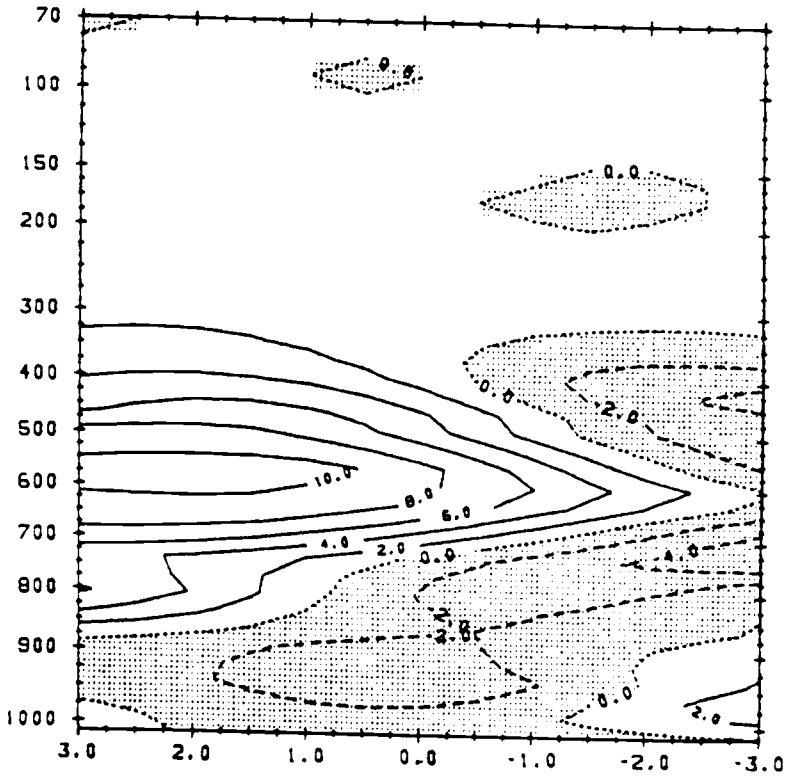

Figure 3.9. As in Fig. 3.8 except for the temperature difference. Units are 10^{-1} °C; contour interval is 0.2°C.

which a composite with the mean B-array data was used. Easterly waves still have influence on the 800-630 mb layer. Warming (cooling) occurs to the south (north), coupled with drying (moistening) to the south (north), indicating the advance of the wave trough out of this time period. Cooling occurring at 150-250 mb layer may be related to the development of the anvil cloud.

As stated in Chapter 1, one of the most important findings from the study based on GATE data is the identification of the mesoscale organization of clouds imbedded in the cloud clusters (Houze, 1977; Leary and Houze, 1979). Cloud clusters generally have lifetimes of a day or less. Within this period, it goes through a life cycle from growing stage to mature stage, and finally reaches the dissipating stage. It was also found that the convective updrafts and downdrafts, as well as the mesoscale updrafts and downdrafts, are an integral part of the cluster system (Houze and Betts, 1981).

The thermodynamic characteristics of the composite cloud cluster may thus be interpreted in terms of the convective and meso-scale updrafts and downdrafts associated with the clusters. The difference in the equivalent potential temperature ($\Delta\theta_e$), between dissipating and growing stages summarize the change of temperature and moisture content during the life cycle of the cloud cluster. As shown in Fig. 3.10, the $\Delta\theta_e$ values are negative in the lowest layer and of the order of 1°K, apparently due to the drying and cooling effects within that layer. This is consistent with the observations of Betts et al. (1976) and Zipser (1969,

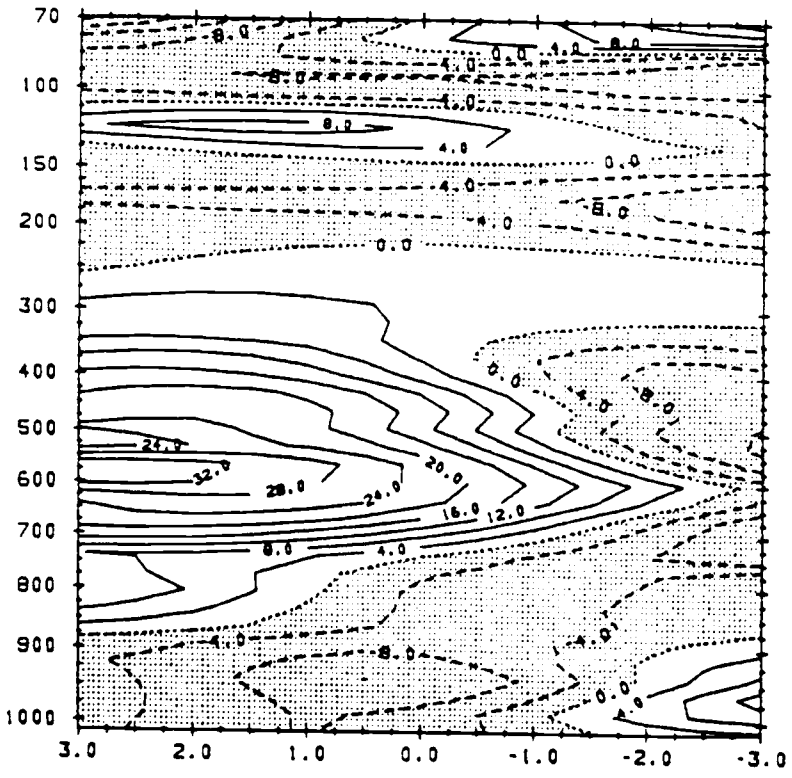

Figure 3.10. As in Fig. 3.8 except for equivalent potential temperature. Units are 10^{-1} °K; contour interval is 0.4°K.

1977), in which they report that the lowering of boundary layer θ_e in convective and meso-scale downdrafts. The $\Delta\theta_e$ values are positive in the layer between 300-750 mb, and are of the order of 2°K. These positive values are related to the moistening or the warming within that layer, which can be regarded as a net result of warming due to the transport and cooling associated with the mesoscale ascent. Another layer of positive $\Delta\theta_e$ is at 110-140 mb layer, which is solely due to the temperature increase there; this is probably related to the diurnal change of temperature. The reason for the temperature increase at 110-140 mb is not yet understood, although the negative $\Delta\theta_e$ at 150-250 mb may be due to the adiabatic cooling associated with mesoscale ascent.

We may summarize the change of moisture content and temperature after the development of convection as follows: Warming and moistening occur in the 250-450 mb layer. In the lowest layer, cooling and drying dominate. In the middle troposphere, the easterly wave has a large influence on the change of the temperature and moisture fields through the propagation of the wave through the area. More discussions on the thermodynamic effects of convection on the large-scale environment will be presented in Chapter 4.

CHAPTER 4. HEAT AND MOISTURE BUDGETS

In Chapter 3, the characteristics of the temperature, moisture and static stability fields, along with the change associated with the life cycle of cloud clusters, have been discussed. In this Chapter, the results of heat and moisture budget computations will be presented.

4.1 Budget equations

The heat and moisture budgets are cast in the commonly used form

$$Q_1 \equiv \frac{C_p}{(P_0/p)^\kappa} \left(\frac{\partial \bar{\theta}}{\partial t} + \underset{\sim}{\bar{V}} \cdot \underset{\sim}{\nabla} \bar{\theta} + \bar{\omega} \frac{\partial \bar{\theta}}{\partial p} \right) \tag{4.1}$$

$$Q_2 \equiv -L_v \left(\frac{\partial \bar{q}}{\partial t} + \underset{\sim}{\bar{V}} \cdot \underset{\sim}{\nabla} \bar{q} + \bar{\omega} \frac{\partial \bar{q}}{\partial p} \right) \tag{4.2}$$

where Q_1 and Q_2 are, respectively, the apparent heat source and the apparent moisture sink expressed in energy units. Here, p, $\underset{\sim}{\bar{V}}$, $\bar{\omega}$, $\bar{\theta}$, and $\bar{q}$ are the air pressure, the horizontal wind velocity, the vertical 'p' velocity, potential temperature and the specific humidity, respectively. The specific heat at constant pressure, C_p, and the latent heat of vaporization, L_v, are held constant. An overbar stands for the areal mean. Q_1 and Q_2 are explicitly calculated from the data set described in Chapter 2.

Using Q_1 and Q_2, the first law of thermodynamics and the

moisture continuity equation may be written in the approximated forms

$$Q_1 = Q_R + \frac{\partial}{\partial p}(gF_s) + L_v(c-e) + L_s(d-s) + L_f(f-m) \qquad (4.3)$$

$$-\frac{Q_2}{L_v} \equiv \frac{\partial}{\partial p}(gF_q) - (c-e) - (d-s) \qquad (4.4)$$

where Q_R is the radiative heating rate, and F_s and F_q are the vertical eddy flux of sensible heat and water vapor per unit mass. The variables c, e, f, m, d, and s are the condensation, evaporation, freezing, melting, deposition and sublimation rates, respectively. L_s, L_f, and L_v are the latent heat of sublimation, fusion and vaporization, respectively, with $L_s = L_f + L_v$.

Summing Eq. (4.3) and L_v^* Eq. (4.4), we obtain

$$Q_1 - Q_2 - Q_R \equiv \frac{\partial}{\partial p}(gF_h) + L_f(f-m+d-s) \qquad (4.5)$$

where $F_h = F_s + L_v^* F_q$. Eqs. (4.3)-(4.5) differ from early budget studies (e.g., Yanai et al., 1973) by the inclusion of phase transitions involving ice.

The virtual flux F_h^* at any pressure level is defined as

$$F_h^*(p) = \int_{70mb}^{p} (Q_1 - Q_2 - Q_R)\frac{dp}{g} \qquad (4.6)$$

$F_h^*(p)$ will differ from $F_h(p)$ during periods when the vertically integrated cloud-ice content above p is changing in a Lagrangian sense. However, since the effect of ice storage will be

on the order of Q_2/L_v, and since $L_f << L_v$, we expect that $F_h^*(p) \simeq F_h(p)$.

The application of the Q_1, Q_2, and Q_R to the study of convective effect on the large-scale flow can be illustrated by using a diagnostic cloud model. Following Yanai et al. (1973) we may write

$$Q_1 - Q_R = -M_c \frac{\partial \bar{S}}{\partial p} - Le \tag{4.7}$$

and

$$Q_2 = L M_c \frac{\partial \bar{q}}{\partial p} - L\delta(\bar{q}^* - \bar{q}) - Le \tag{4.8}$$

where δ is the rate of mass detrainment, M_c is the cumulus vertical mass flux, and $S = C_pT + gZ$ is the dry static energy. Eqs. (4.7) and (4.8) state that the thermodynamic effect of the cumulus clouds on the large-scale environment is a combination of induced compensating subsidence which warms and dries the cloud environment, detrainment of the water vapors which moisten the environment, and re-evaporative processes of the detrained cloud liquid water which cool and moisten the environment. The left-hand side of the equations are directly computed from the observed heat and moisture budgets, while the right-hand side are the approximate forms to represent the cloud effects. The cumulus mass flux M_c can be determined by combining Eqs. (4.7) and (4.8). Several calculations of Q_1 and Q_2 have been made for GATE. Some of the studies were based on the time and area mean methods which obviously cannot describe the transient effect of the cloud

clusters (Nitta, 1977; Albright et al., 1981; Cho, 1977). Some of the studies were on the easterly wave scale, where the wave period was 3 to 4 days, longer than the life cycle of cloud clusters (Thompson et al., 1979). Although the connection between the easterly wave trough and the maximum convective activity had been noticed, still the easterly wave trough composite studies cannot represent the budgets of the cloud-cluster-scale circulations, which have lifetimes around 1 day and space scales of ~200 km.

4.2 Results of the 5 September 1974 case

The clusters of 5 September were among the largest of GATE. The eastern cluster appeared slightly earlier than the more intense western cluster. Fig. 4.1 shows the meridional cross-sections of Q_1 through the center of that cluster in three different stages of its life cycle. The center for western clusters is determined as 9°N, 25°W. The result demonstrates that in the growing stage of the cluster, the maximum Q_1 (around 15°C/day) is near the cluster center at 850 mb. At this time, the stratiform anvil cloud has just started to build. In the mature stage, the maximum heating is at a higher level than in the growing stage with a rate of 21°C/day. The dissipating stage shows that the breakdown of the 400-500 mb layer maximum occurred in the mature stage. However, the heating around 500 mb still occurred at a rate of about 8°C/day.

The corresponding Q_2 (moisture sink) features are shown in Fig. 4.2. Q_2 already possessed relatively large values at lower

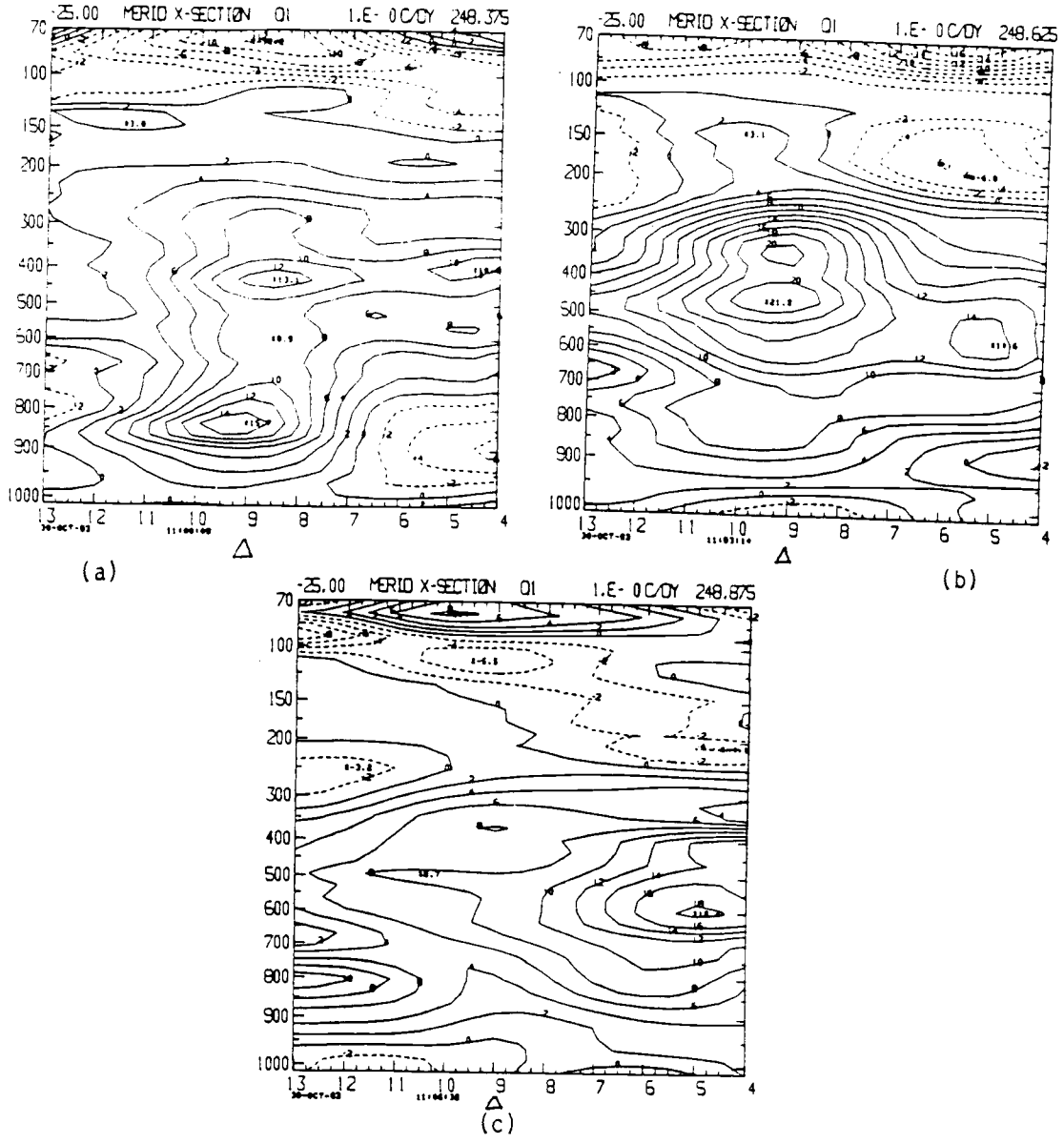

Figure 4.1. Meridional cross-section of the apparent heat source (Q_1) through the cluster center during the (a) growing, (b) mature, (c) dissipating stages of 5 September cluster. Units are °C/day; contour interval is 2°C/day. Δ indicates the cluster center.

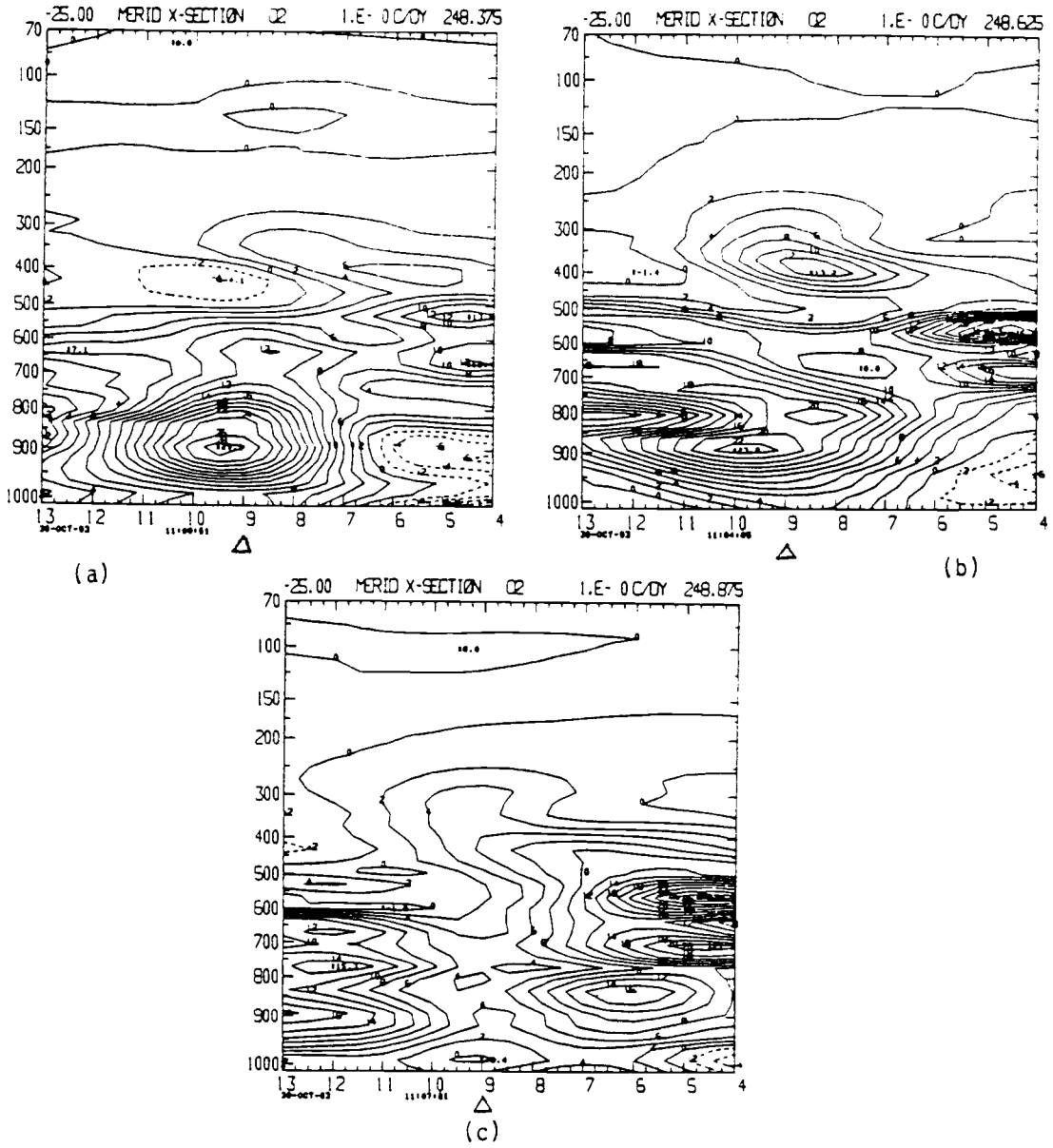

Figure 4.2. As in Fig. 4.1 except for the apparent moisture sink (Q_2).

levels in the growing stage. In the mature stage, a second maximum around 13°C/day is found at the 400 mb level. There is no clear maximum value near the center of the cluster in the dissipating stage. The Q_1 and Q_2 patterns are quite different. From Eqs. (4.3) and (4.4), it can be seen that either the virtual flux or Q_R are contributing to this difference. The same cross-sections for virtual flux are shown in Fig. 4.3. The general pattern of virtual flux is that it increases up to a certain level and then decreases upward. (Virtual flux has to be zero at the top of the model atmosphere by assumption.) In the mature stage, the rates of increase are more rapid than those in the growing stage. Maximum F_h* is 550 w/m^2 right at the cluster center around 650 mb. The energy depletion contributed by the virtual flux divergence in the layer between the surface and 600 mb is around 8°C/day. In the dissipating stage, the virtual flux at the lower layer (surface to 600 mb) looks much like a constant flux layer, and its contribution to the energy depletion is around 0.5°C/day between the surface and 600 mb.

The horizontal structures of the Q_1 and Q_2 fields are shown in Figs. 4.4 and 4.5 for the 705 mb and 430 mb levels. At the 705 mb level in the growing stage, because of the development of the eastern cloud cluster, the maximum heating and moisture sink tend to be in the eastern part of the array. In the mature stage, Q_1 has a maximum around the center of the B-array ship at lower levels (~705 mb), while Q_2 has a maximum of 18°C/day to the north of the cluster center. At the 430 mb level, the shift of the maximum

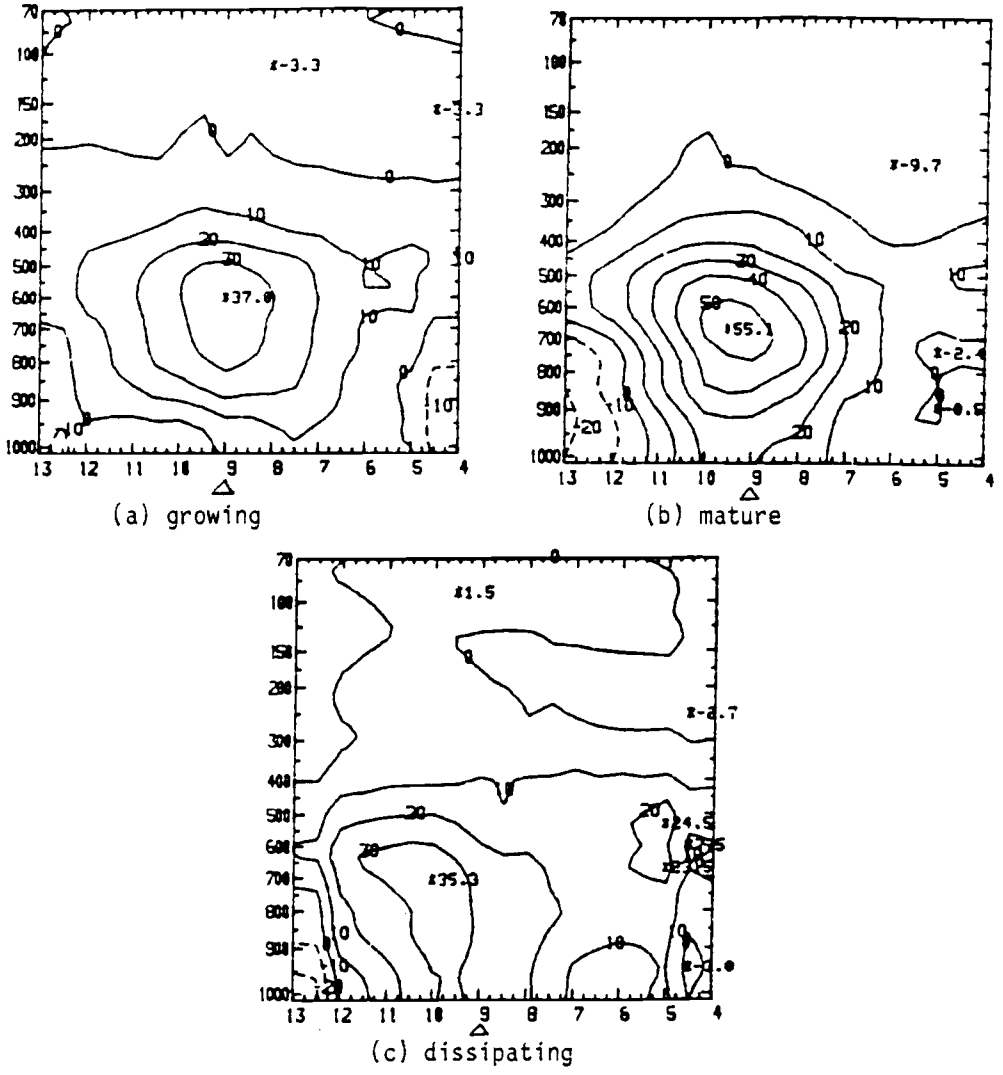

Figure 4.3. As in Fig. 4.1 except for virtual fluxes ($F_h^*(p)$). Units are 10 w/m^2 ; contour interval is 100 w/m^2 .

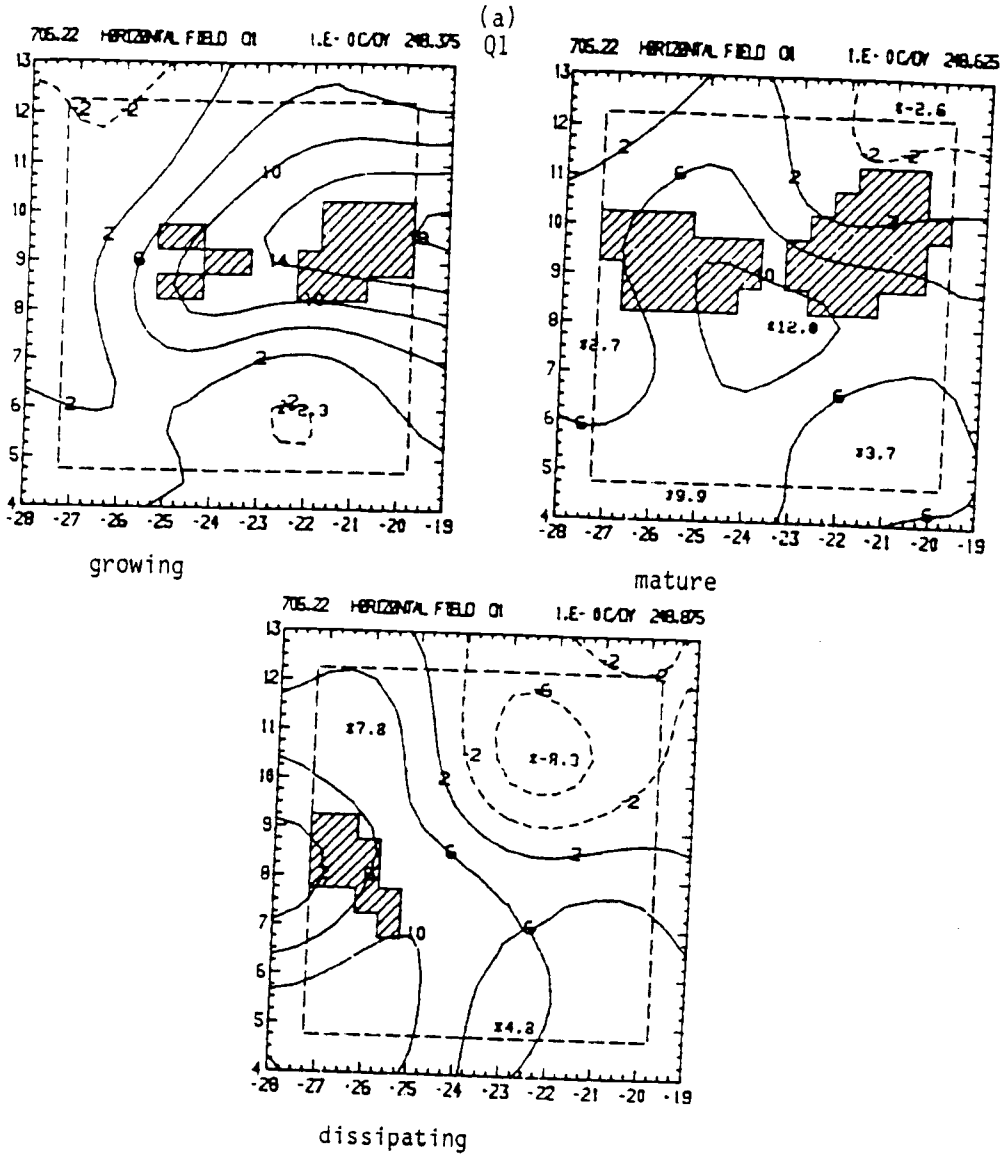

Figure 4.4. Horizontal plots of Q_1 (a) and Q_2 (b) during the life cycle of 5 September cluster at 705 mb. Units are °C/day; contour interval is 4°C/day.

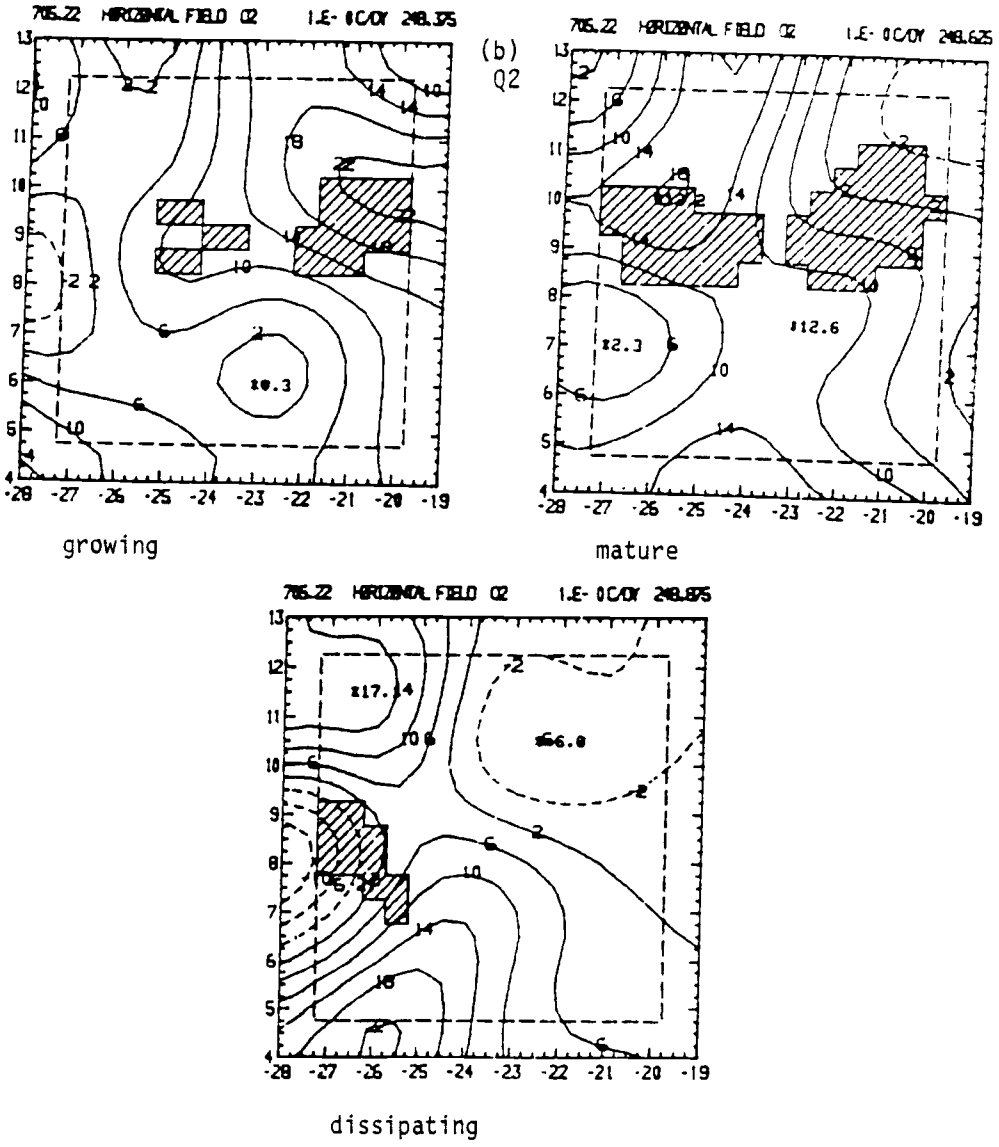

Figure 4.4 (continued)

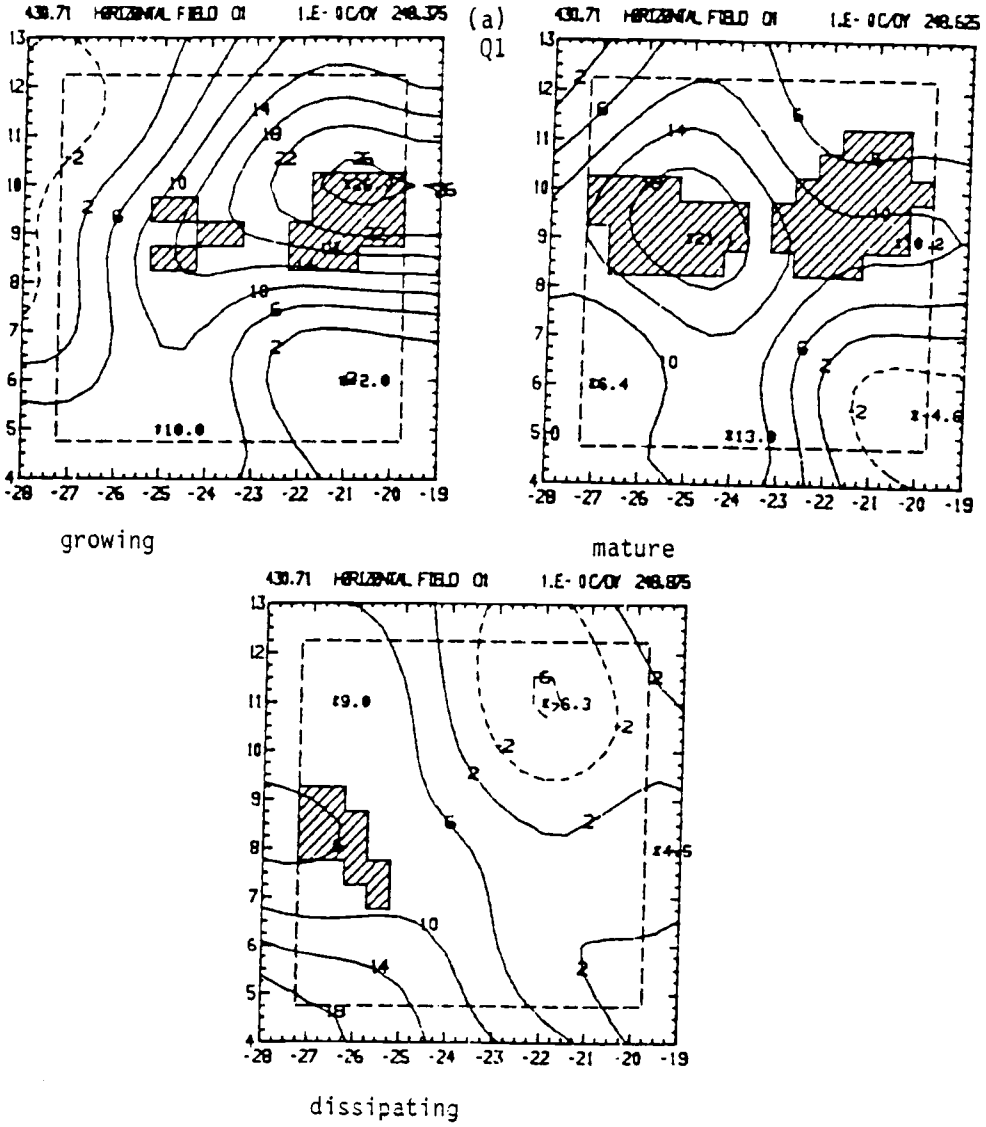

Figure 4.5. As in Fig. 4.4 except for 430 mb.

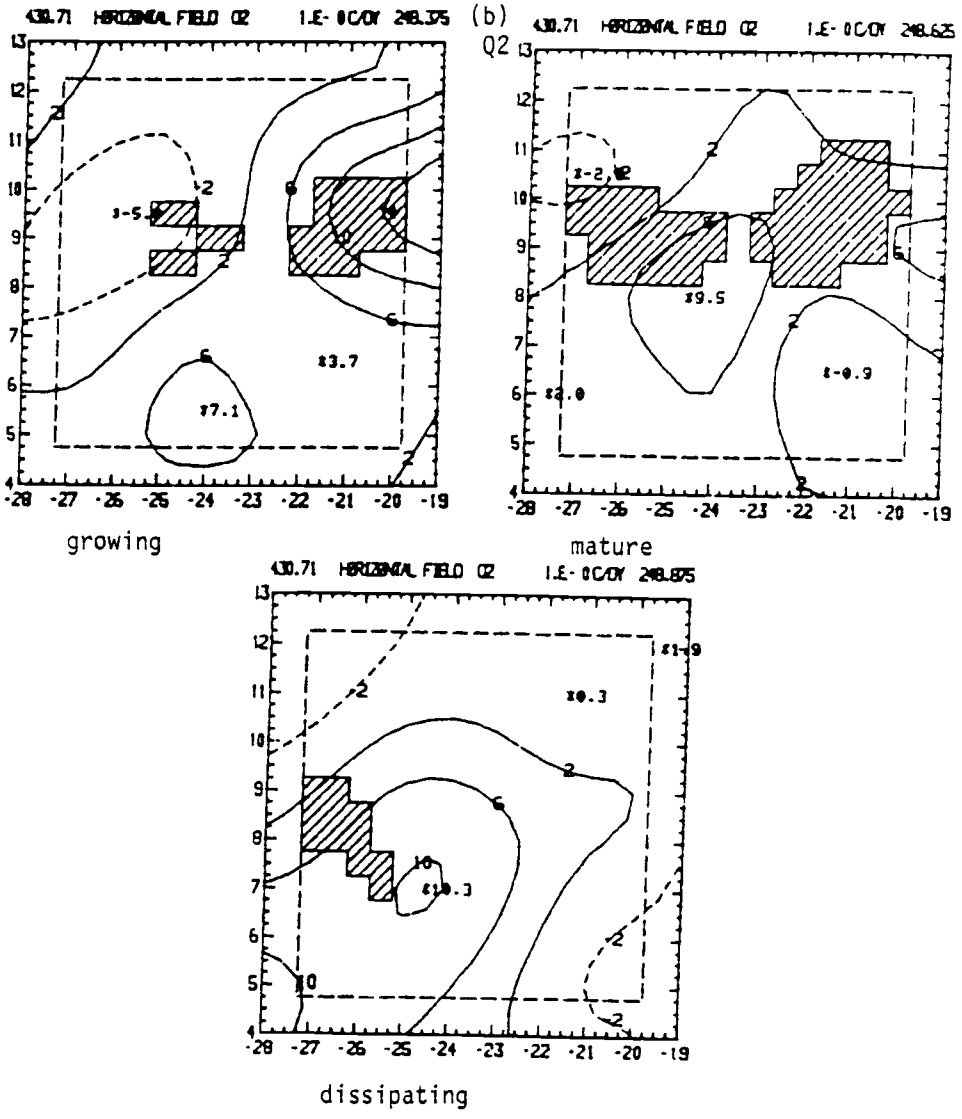

Figure 4.5 (continued)

heating from eastern clusters to western clusters along with each change of the stage of the clusters is quite clear. Q_2 at that level has much smaller values in comparison with those of Q_1. In the dissipating stage, the large values of Q_1 and Q_2 in the mature stage are replaced by much smaller values. For Q_2 at 705 mb, some relatively large values occurred around the edge of the ship array, which may be regarded as due to the deficiency in interpolated data outside the ship array rather than to real physical processes.

If Eq. (4.4) is vertically integrated from the top of the model atmosphere to the surface it becomes

$$\int_{70mb}^{sfc} \left[- \frac{\partial}{\partial p} (L_v g F_q) + L_v(c-e) + L_v(d-s) \right] \frac{dp}{g} \equiv \int_{70mb}^{sfc} Q_2 \frac{dp}{g} \qquad (4.9)$$

By assuming the vertically integrated deposition and sublimation are small or cancel each other, we have

$$P_0 - E_0 = \int_{70mb}^{sfc} \frac{Q_2}{L_v} \frac{dp}{g} \qquad (4.10)$$

where P_0 and E_0 are rates of surface precipitation and surface evaporation, respectively. So if E_0 can be estimated from some bulk aerodynamic formula, the P_0 distribution can be determined. Fig. 4.6 shows the surface distribution of $P_0 - E_0$ in the unit of mm/day for the growing, mature and dissipating stages. $P_0 - E_0$ can be interpreted as the net precipitation rate at the surface.

In the growing stage, the $P_0 - E_0$ has a maximum value around the center of the eastern cluster (~48 mm/day), since the cluster is fully developed there already. In the mature stage, maximum $P_0 - E_0$

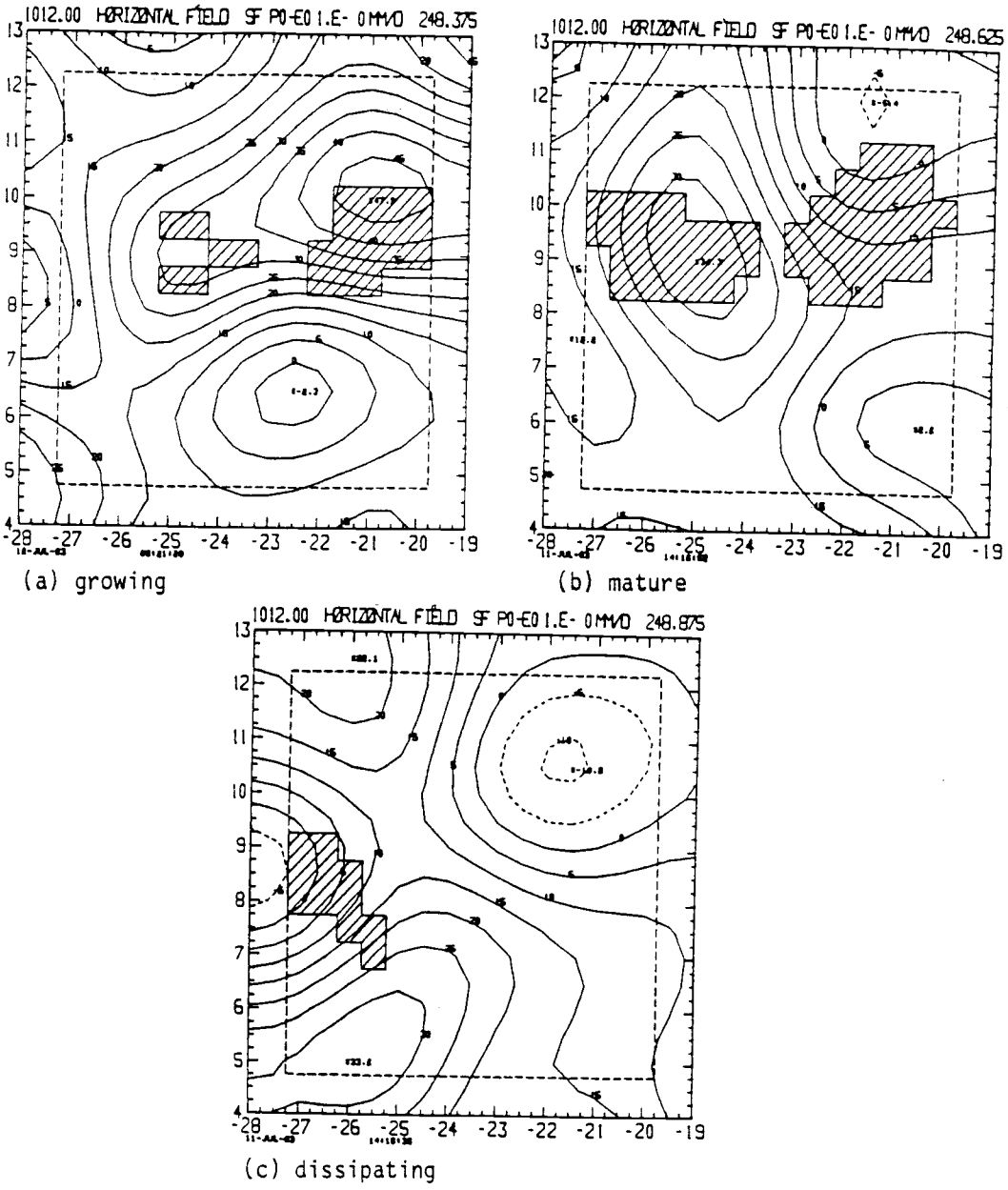

Figure 4.6. Horizontal plot of net surface precipitation ($P_0 - E_0$) during the (a) growing, (b) mature, (c) dissipating stages of the 5 September cluster. Units are mm/day; contour interval is 5 mm/day.

lies in the center of the western cluster (~34 mm/day). $P_0 - E_0$ in the dissipating stage has a different pattern, with no explicitly large value around the cluster center as in the other stages.

The Q_R data used here was constructed by Cox and Griffith (1979a), who already showed the maximum Q_R values for 5 September to be on the order of 2 to 3°C/day cooling (Cox and Griffith, 1979b).

4.3 Composite results of the heat and moisture budgets

Using the compositing procedure described in Chapter 3, we have composited the fields from the five non-squall cloud clusters. Because of the similarities between individuals cases, the compositing processes may be regarded as summarizing the important features of the individual clusters.

4.3.1 Q_1 and Q_2

The most remarkable result of the heat and moisture budget computations is that the composite life cycle of the budgets in the vicinity of the five large anvil clouds is very similar to that hypothesized for the individual MPFs, which are believed to be the basic units of deep convection in cloud clusters (Leary and Houze, 1979; Zipser, et al., 1981). It is not obvious that this should be the case since the radar data which is available for three of the five systems (2 September and the two systems on 5 September) show that the life cycles of the MPFs which combine to form a common

anvil cloud are not synchronous, and that there is interaction among the MPFs.

Figs. 4.7 and 4.8 present heat and moisture budget composites along north-south cross sections through the center of the composite non-squall system during its growing, mature and dissipating stages. In the growing stage, Q_1 increases rapidly with height below 850 mb and then more slowly to the maximum just above 635 mb. A secondary maximum appears just below 400 mb. Heating in excess of 4°C/day is confined mainly to the layer below 250 mb. Q_2 has one large maximum near 890 mb and shows that most of the apparent drying is confined below the 635 mb level in the growing stage.

In the mature stage, the maximum heating shifts upward by 200 mb to the 430 mb level. The values of the heating are larger than in the growing stage even at the level of the growing-stage heating peak near 635 mb. However, the vertical profile has undergone a very significant change. The lower-tropospheric peak of Q_2 remains about the same magnitude but shifts upward to the 770 mb level. A second drying maximum forms near the 530 mb level in the mature stage to give the Q_2 profile a clear double-peak structure.

This type of double-peak structure of Q_2 profile has been found in many studies (Yanai et al., 1973; Cho, 1977; Cho et al., 1979). Johnson (1984) attempted to explain this feature by suggesting that this Q_2 profile is merely a sum of two different physical processes, namely, physical processes on the cumulus scale and mesoscale. He argued that the warming and drying associated

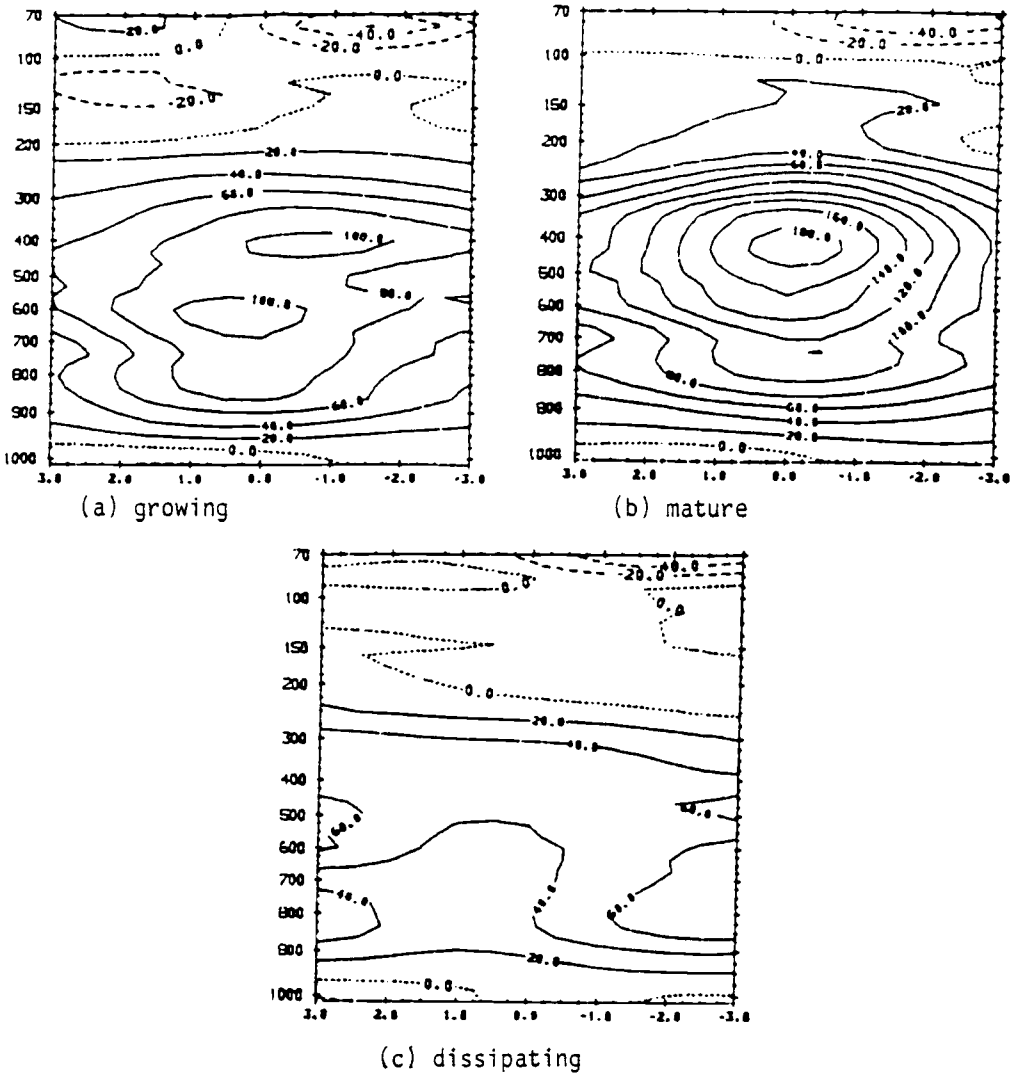

Figure 4.7. Meridional cross-section of Q_1 through the center of the composited cluster during the (a) growing, (b) mature, (c) dissipating stages. Units are 10^{-1} °C/day; contour interval is 2°C/day.

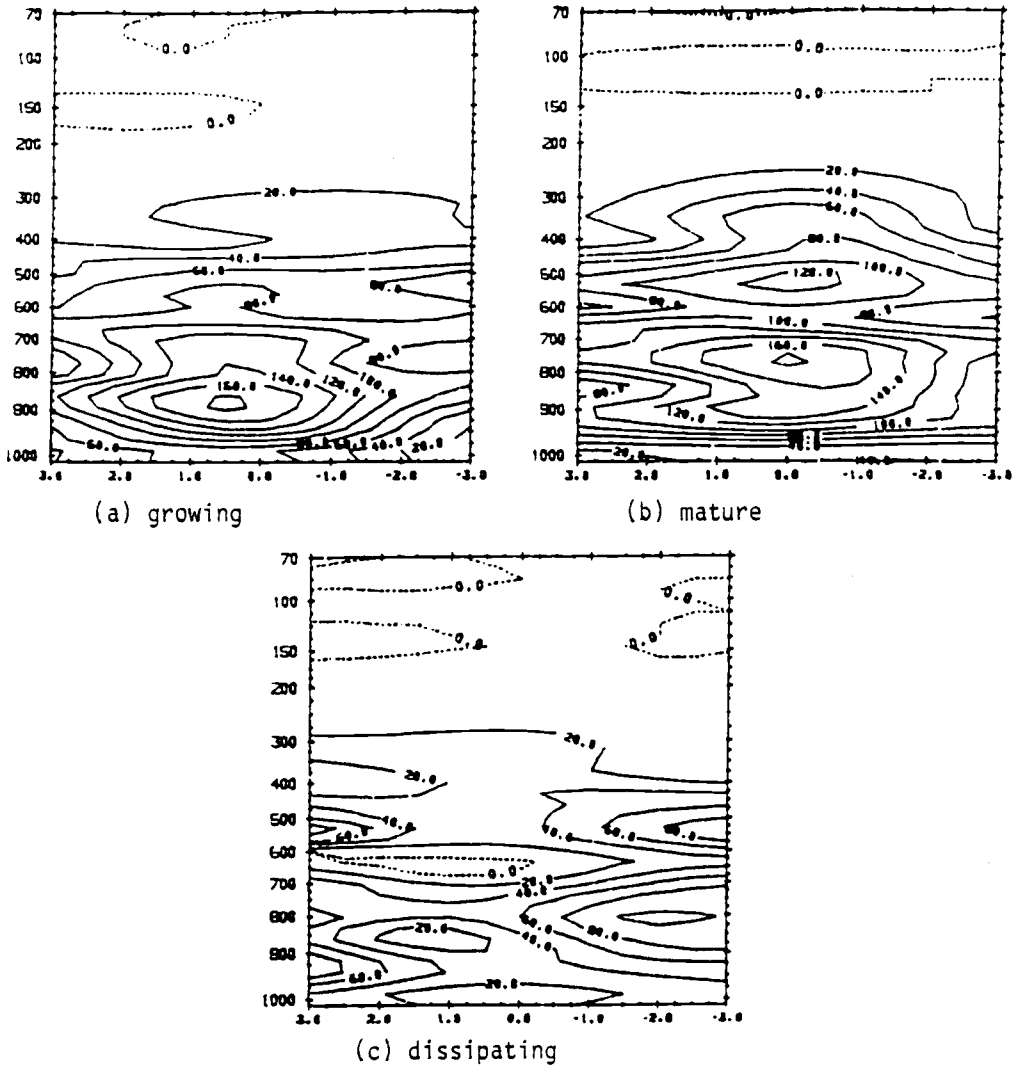

Figure 4.8. As in Fig. 4.7 except for Q_2.

with the subsidence, that compensates the upward cumulus mass flux, were the only contribution from the cumulus clouds. Johnson suggested that detrainment of hydrometeors was not important in modifying the large-scale Q_1 and Q_2 values. There was, however, ample evidence to suggest the importance of the cumulus cloud detrainment effect on the large-scale heat and moisture fields. Chen (1985) found that the GATE phase III mean detrainment rate and the cloud liquid water content were at a relative maximum at the 600 mb level. This indicates the potentially significant contribution from the cloud detrainment process. The detrainment of hydrometeors through the shallow clouds to moisten the large-scale environment is more plausible as the cause of the relative minimum Q_2 between two relative maxima Q_2 layers, as seen in the present study.

In the dissipating stage, the magnitudes of Q_1 and Q_2 decrease dramatically. A heating maximum of about 6°C/day can be seen near 400 mb. A layer of weak (~3.5°C/day) and relatively uniform heating exists from 600 to 850 mb. Below 865 mb the heating drops to very small positive values. The apparent drying in the lower troposphere remains near the 800 mb level while the apparent drying at upper levels continues to shift upward to near the 430 mb level. The minimum separating the two drying maxima is very abrupt at the 635 mb level.

Several interesting comparisons can be made with the heat and moisture budget results of other investigators. It was shown that all of the convective systems that have been included in our

composite occurred at or near the time of easterly wave trough passages (see Table 1 of Thompson et al., 1979). The composite results centered on the convective activity in this study show lower and middle tropospheric heat sources and moisture sinks during the growing and mature stages that are very similar to the values in the trough of the composite wave from Thompson et al. (1979). However, the strong upper-tropospheric heat source and the middle-tropospheric drying in the mature stage, as well as the sudden collapse of the drying at lower levels in the dissipating stage, do not appear in the wave composite.

Another interesting observation is that the convective system shown in Table 3.1 and Fig. 3.2 appears to be strongly influenced by the diurnal cycle. Growing stages tend to occur in the late night and early morning hours, mature stages occur in the middle of the day, and dissipating stages tend to occur in the afternoon and evening. This behavior of deep convection in GATE has been noted by many authors, including Albright et al. (1981) who computed Q_1 and Q_2 as a function of time of day for all three phases of GATE. The Q_1 values in the growing and mature stages of this composite cluster resemble the mid-day heating profiles of Albright et al. (1981) more strongly than they resemble the easterly wave trough profiles of Thompson et al. (1979); the heating is deeper for the diurnal and anvil-centered budgets, with a local maximum appearing in the 500 to 600 mb layer. Also, the moisture sink at midday more closely resembles the mature stage composite than it does the wave-trough composite.

The Q_1 value at the 430 mb level in the mature stage is around 16°C/day, while the local change of temperature at that level as described in Chapter 3 is only around 2°C/day. It indicates that the convective activity, as well as other large-scale advective processes are equally important in affecting the local change. Thus the relatively small temperature change is the results of a cancelling effect of various processes involved.

4.3.2 Q_R and $F_h^*(p)$

The data set produced by Cox and Griffith (1979a) has been used in two ways in this study. The gridded cloud-cover values are used to identify the anvil cloud area and to determine the life-cycle stages of the cloud clusters. The estimates of radiative heating (Q_R) are also used to evaluate the $F_h^*(p)$ from Eq. (4.6). The virtual flux is the sum of the sensible and latent heat fluxes. The convergence of the virtual flux represents the net convective effects. The convergence (divergence) of virtual flux corresponds to warming and drying (cooling and moistening).

The Q_R field estimated by Cox and Griffith is the net radiative convergence of each one hundred millibar layer from 100 mb to 1000 mb and from 1000 mb to the surface. Cox and Griffith (1979b) and Byrd and Cox (1984) investigated the horizontal structure of Q_R in three different layers (namely, 100-400 mb, 400-700 mb, and 700-1000 mb) with different time composites. In this section Q_R is composited in the same manners

described in Sec. 3.2. The composited Q_R field is converted to forty-one pressure levels to make it compatible with Q_1 and Q_2 estimates.

Fig. 4.9 shows the Q_R values along a north-south cross section through the center of the composite non-squall system during its life cycle. It is seen that, in the growing stage, most of the Q_R values are negative (except some small positive regions in the mature stage), with the maximum cooling occurring at the surface at the rate of 2.8°C/day. In the mature stage, the area around the center above 950 mb tends to have a relative maximum in the north-south direction. Due to the development of the anvil cloud in the mature stage, the profile is quite different from the other stages. Between 250-950 mb, Q_R becomes much larger relative to the growing and dissipating stages. The cooling rate around those layers is less than -0.5°C/day. Above the 250 mb level, there is a relatively strong cooling of about -2 ~ -3°C/day. Byrd and Cox (1984) found that in the 100-400 mb layer the largest radiative energy losses occur over the convective region, and suggested this might be due to the large radiative cooling at the cloud-top level. The vertical structure of Q_R presented here not only shows the cloud-top position and the associated large cooling, but also the relative warming within the anvil cloud regions due to the radiative effect.

In the dissipating stage, the structure of Q_R is somewhat similar to that in the growing stage. The relatively strong cooling is found around 500 mb.

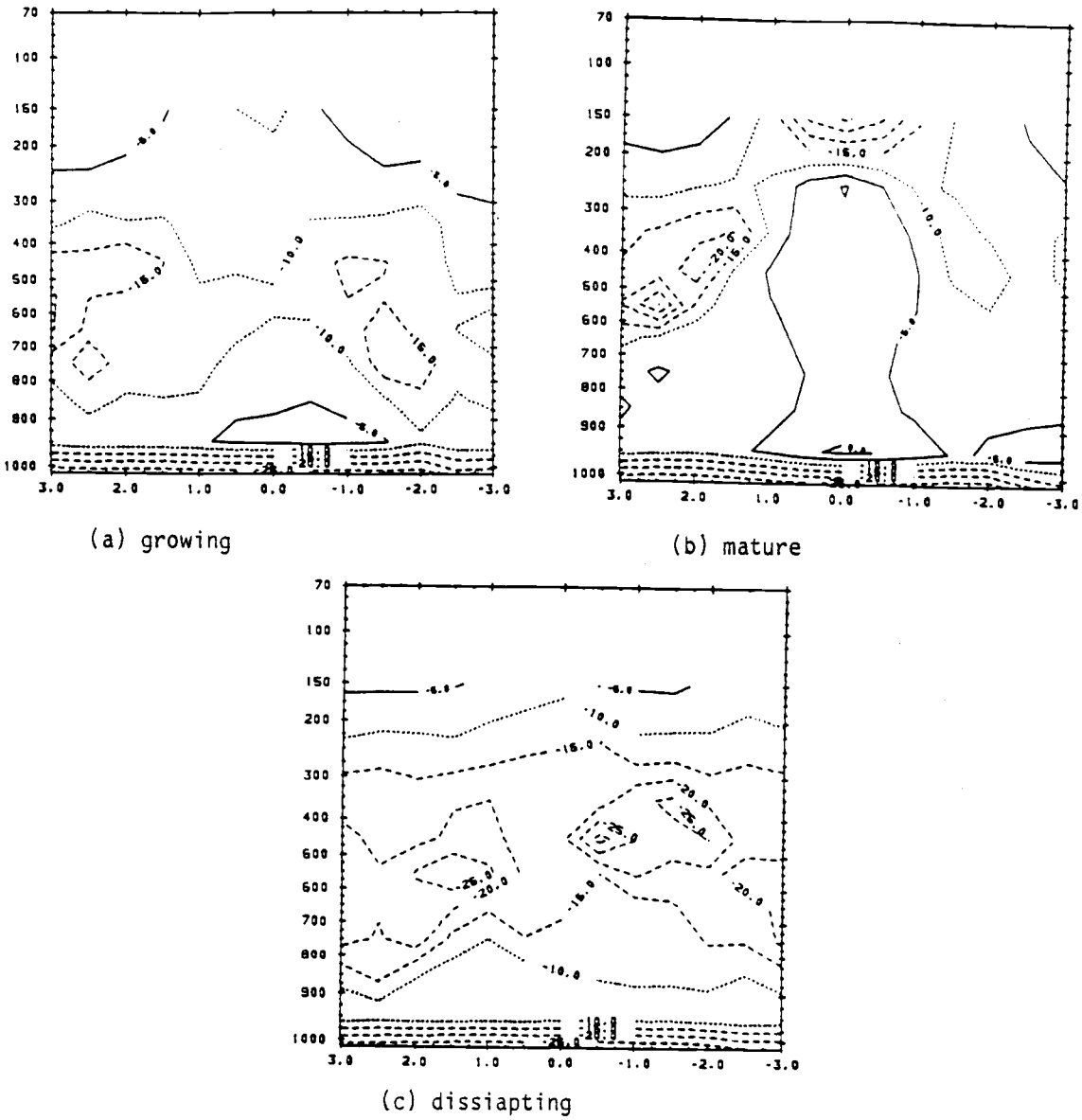

Figure 4.9. As in Fig. 4.7 except for radiative heating (Q_R). Units are 10^{-1} °C/day; contour interval is 0.5 °C/day.

The Q_R structure in the mature stage through the center of the cloud cluster is quite similar to those found at local noon time by Albright et al. (1981) for the GATE phase III mean values.

Fig. 4.10 shows the composite horizontal structure of Q_R in the 100-200 mb layer. In the mature stage, when the anvil cloud is fully developed, strong cooling at -2.5°C/day occurs near the cluster center, compared with 0.8°C/day cooling at other stages. Results for the 200-300 mb layer are shown in Fig. 4.11. The mature stage Q_R has a relative maximum heating around the center in contrast to the relative minimum possessed at other stages of that layer, apparently due to the existence of stratiform cloud.

The corresponding structures of $F_h^*(p)$ are presented in Fig. 4.12. In the growing stage, a flux maximum of 265 w/m^2 is found just above the 700 mb level at the center of the convective system. This maximum nearly doubles in magnitude to 451 w/m^2 in the mature stage. In the dissipating stage, the middle-tropospheric maximum disappears completely and is replaced by a constant flux layer extending from the surface to 725 mb.

At upper levels, virtual fluxes in excess of 100 w/m^2 are generally confined below the 400 mb level. However, in the mature stage, 100 w/m^2 fluxes can be found above the 300 mb level at the center of the system.

At the surface, the virtual fluxes are found to be much larger (~200 w/m^2) in the mature stage and dissipating stages than they are in the growing stage (~100 w/m^2). There is also an apparent shift in the zone of maximum virtual flux to the north as time

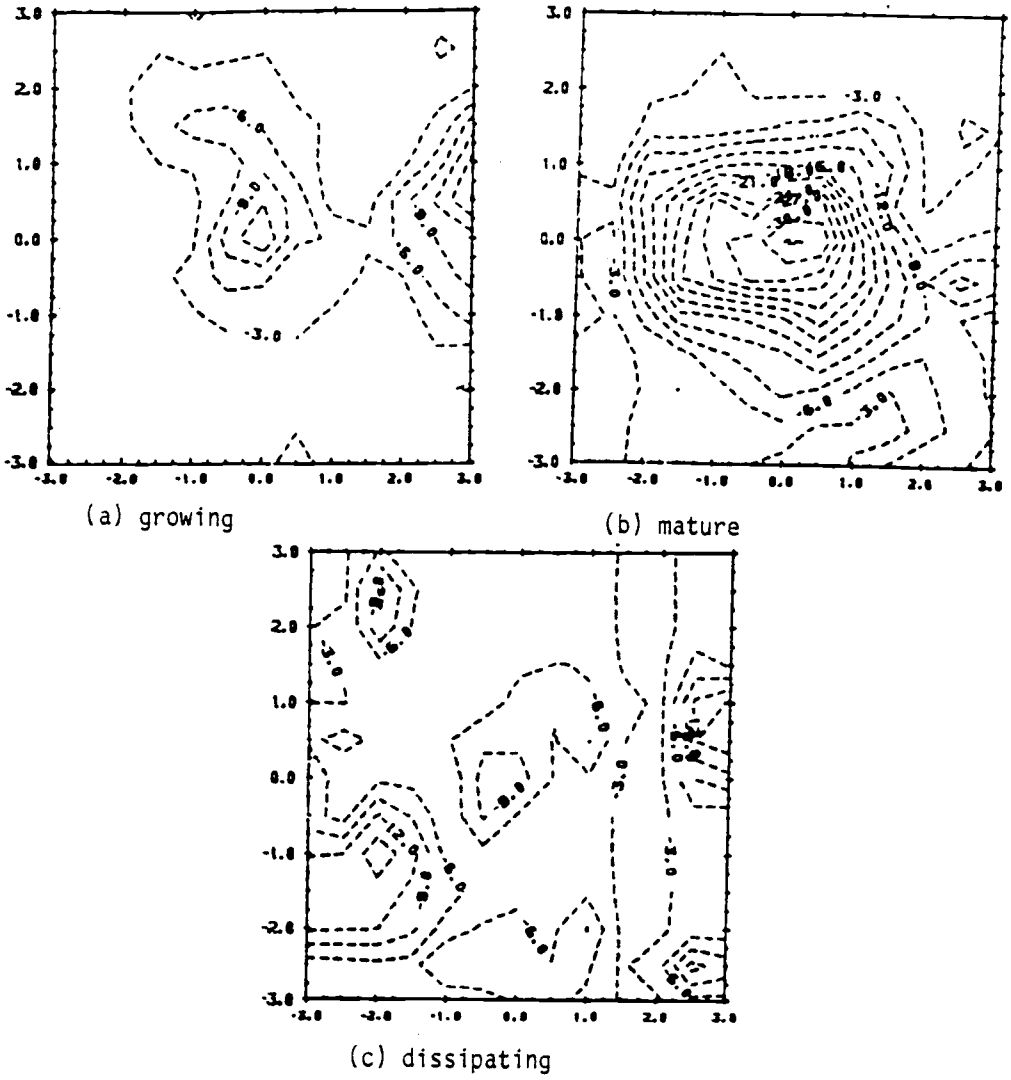

Figure 4.10. Horizontal structure of Q_R in 100-200 mb slab. (a) growing , (b) mature, (c) dissipating stage of the composited cluster. Units are w/mb/m^2 ; contour interval is 3 w/mb/m^2 .

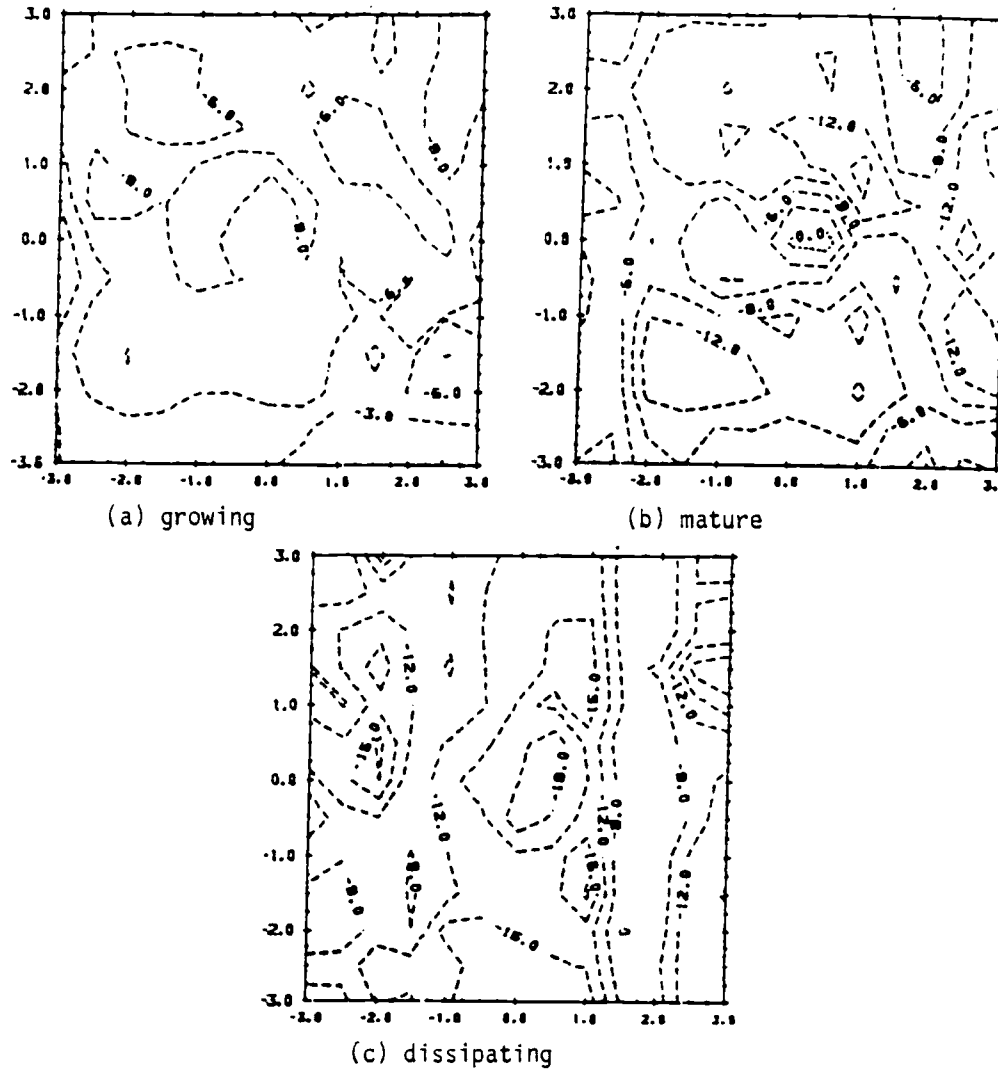

Figure 4.11. As in Fig. 4.10 except for 200-300 mb slab.

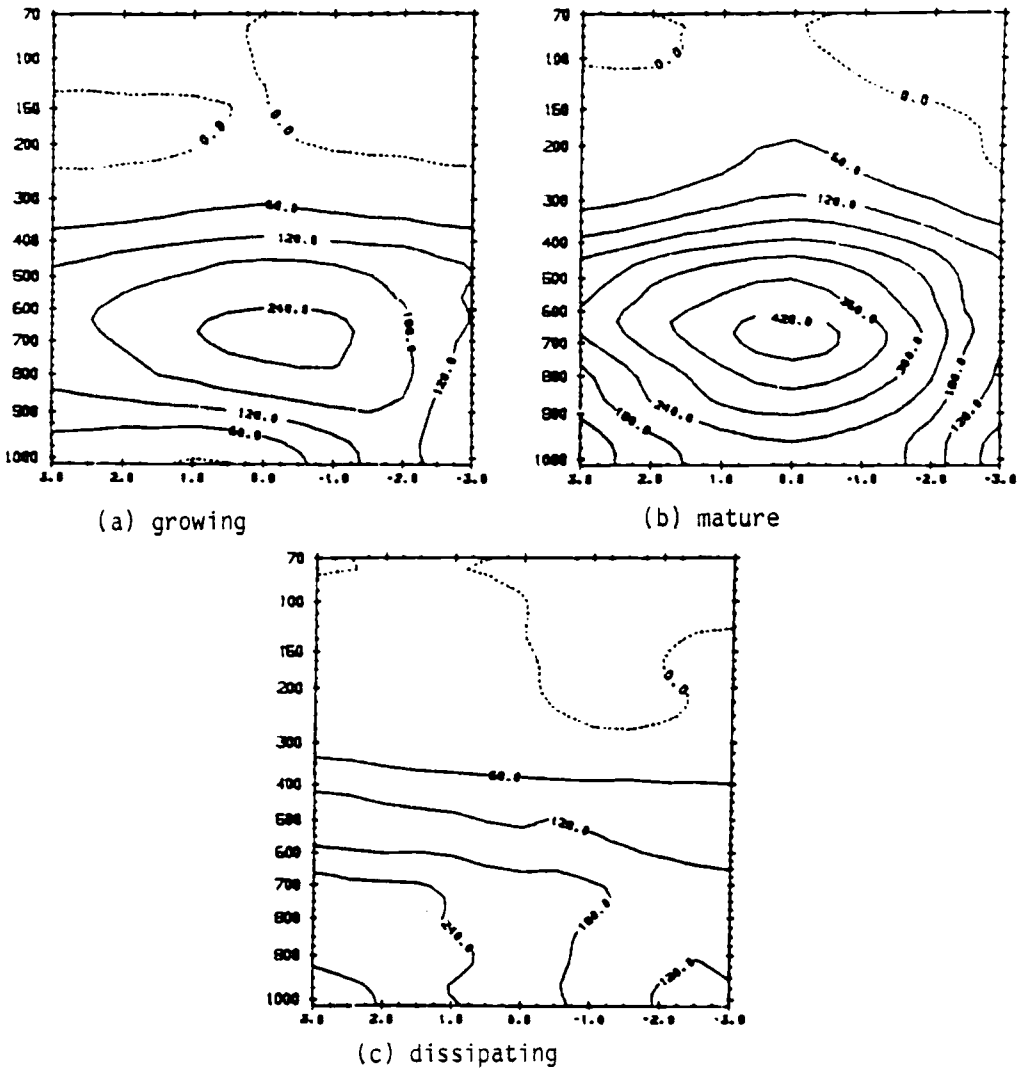

Figure 4.12. As in Fig. 4.7 except for $F_h^*(p)$. Units are w/m^2; contour interval is 60 w/m^2.

progresses.

From an easterly-wave composite, the $F_h^*(p)$ presented by Thompson et al. (1979) had a maximum value around 230 w/m^2 at 800 mb before the advance of the trough. Those values are smaller than the mature stage values in the present study. The convergence of the virtual fluxes estimated from Thompson et al. (1979) were on the order of 5°C/day in the trough region. They found that the thermodynamic energy in the lower layer (from surface to 800 mb) was depleted, while energy at the upper layer was increased at the same rate through the convergence of virtual flux. The virtual flux convergence estimated in the mature stage of this study is on the order of 10°C/day. The thermodynamic energy source exists at 700 mb and above, with an energy sink situated below 700 mb. Since the convergence of the virtual flux is a measure of the total convective effects, the resulting structure of this convergence suggests that thermodynamic energy has been transported upward by the convective effects, causing the stabilization of the large-scale environment as described by Arakawa and Schubert (1974). The virtual flux convergence estimated in the present study is almost twice as large as the easterly wave composite result from Thompson et al. (1979). This large difference indicates that more convective effects are realized on the scale of cloud cluster than on the easterly wave scale. So the budgets of heat and moisture over the GATE A/B area are dominated by disturbances smaller than the easterly waves.

The virtual flux is estimated from the integration of

$Q_1 - Q_2 - Q_R$ as in Eq. (4.6). The role of radiation in affecting the virtual flux convergence can be identified through the integration of $Q_1 - Q_2$. The flux estimated through this integration without radiative cooling is smaller than the virtual flux, although the patterns are similar to the virtual flux in the growing and dissipating stages. The bulge structure of relative maximum of virtual flux in the mature stage cannot be found in the estimation of this new flux. The Q_R is responsible for setting up the relative maximum of virtual flux in the upper troposphere.

These results suggest that the radiative heating/cooling may increase the convective activity in tropical cloud clusters. Whether the radiative cooling plays any role in initiating the cloud cluster scale of motion can't be determined in this budget study. However, it is noticed that some researchers have proposed that differential radiative heating/cooling in the cloud cluster region and its environment might be a mechanism in the development of a cloud-cluster-scale disturbance (Mcbride and Gray, 1980; Byrd and Cox, 1984).

4.3.3 The surface flux [$F_h^*(p_s)$]

To estimate the general reliability of the calculated budget results, the average surface values of $F_h^*(p)$ in different stages are computed and compared with the ship observations. The A/B and B scale ship observational data are used to estimate the surface sensible and latent heat fluxes using the bulk aerodynamic formula.

Table 4.1 shows the computed budget estimates and surface

Table 4.1. Mean surface flux of F_h^* determined from the budget results and the surface ship observations.

	Budget results (w/m^2)	Surface observations (w/m^2)
Growing stage	35.34	150.23
Mature stage	130.84	160.95
Dissipating stage	114.73	145.12

observations of $F_h^*(p)$ in the growing, mature, and dissipating stages. The budget estimate of surface flux reveals the large difference in F_h^* values between the growing and mature stages. On the other hand, the value in the dissipating stage being only a little smaller than the mature stage value. The mean surface observations change relatively little between the different stages of the non-squall cloud clusters life cycle, although the value in the mature stage is larger than that in the growing and dissipating stages.

Johnson and Nicholls (1983) have presented the horizontal structure of surface sensible and latent heat fluxes based on an observational case of squall line movement. Hourly data from four different ships were composited with respect to the center of squall line. Their results showed that the total fluxes in most areas are around 100-200 w/m^2. However, at the leading edge of the squall line, the values are around 300 w/m^2, with extreme values up to 500 w/m^2. In this study, the estimated and observed composited fluxes in most areas are around 50-150 w/m^2, with extreme values up to only 230 w/m^2. The observed horizontal distribution of the surface fluxes is composited using the average values of six hourly observations at the thirteen ships in the GATE ship arrays. Because the surface observations are highly influenced by a single event around the ship, the values in Table 4.1 show only for the areal mean.

Except in the growing stage, the budget estimates and the surface observations are reasonably close. The small computed

value of surface flux in the growing stage is due to negative F_h* to the northwest corner of the A/B array resulting from the Q_2 estimates.

Fig. 4.13 presents the vertically integrated $P_0 - E_0$ values during the life cycle of the cluster. In the growing stage, large $P_0 - E_0$ values are found toward the eastern boundary, which is due to the compositing process rather than the associated convective events. As discussed in Chapter 3, five individual clusters are included in the compositing. Two western clusters always start to develop after the eastern clusters are fully matured; in the growing stage of the compositing process, some information from those two eastern clusters (as they are in the mature stage already) will inevitably be included in the eastern part of the compositing grid. For the mature and dissipating stages, this type of distortion does not occur.

Thompson et al. (1979) estimated the $P_0 - E_0$ through the center of the GATE A/B ship array, and found that the order of magnitude of $P_0 - E_0$ was 30 mm/day when the convective activity was very active. The $P_0 - E_0$ through the cluster center for the individual case of the present study is on the order of 40 mm/day, which is larger than those estimated by Thompson et al. (1979). Large $P_0 - E_0$ values found in the composite cluster center indicate that large precipitation is associated with the cluster. The negative value in the dissipating stage suggests that strong surface evaporation may exist, and may be related to the recovering of the boundary layer at that stage.

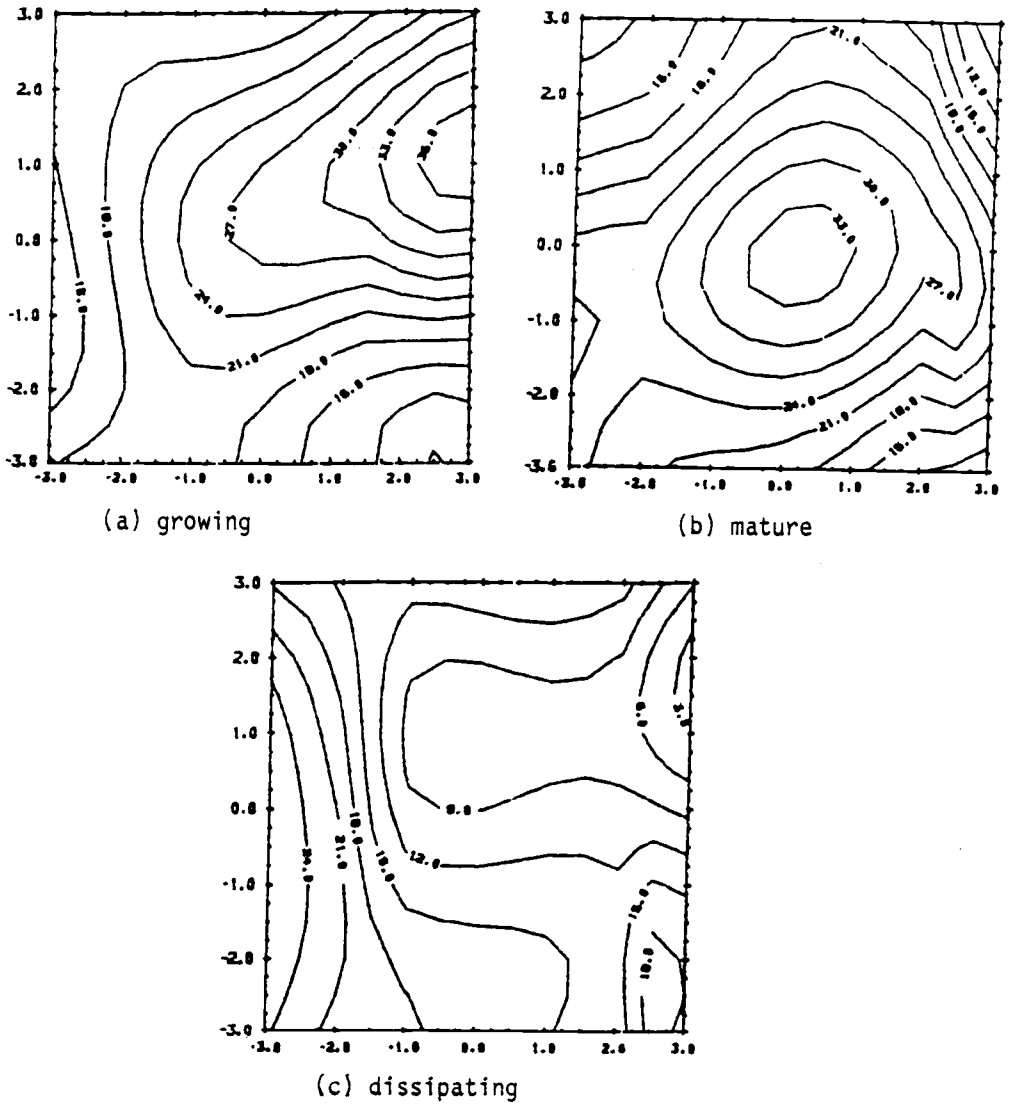

Figure 4.13. Net surface precipitation ($P_0 - E_0$) during the (a) growing, (b) mature, (c) dissipating stages of the composited cluster. Units are mm/day; contour interval is 3 mm/day.

In summary, the present heat and moisture budget studies reveal that the strong upper-tropospheric heat source and the middle-tropospheric drying in the mature stage, as well as the sudden collapse of the drying at lower levels in the dissipating stage, are characteristic features of the cloud cluster scale budget. The Q_1, Q_2 and F_h* values are larger than the easterly wave composite result. Large net precipitation is found near the cluster center in the mature stage, while some negative values found in the dissipating stage indicate a recovery of the boundary layer. On both the cloud-cluster-scale and easterly wave scale, the unresolved processes, namely the convective effects, always have a stabilizing effect on the large-scale environment.

CHAPTER 5. MOMENTUM AND KINETIC ENERGY BUDGETS

Cumulus clouds transport thermodynamic energy upward and thus gravitationally stabilize the large-scale environment. During this process, it is believed that some large-scale dynamical properties such as momentum are also affected by the cumulus processes. However, the detailed mechanisms of these dynamical interactions are not yet well known. Observational studies of the momentum balance in the tropics have been limited by the difficulty in measuring the horizontal pressure gradient accurately; only a few attempts to estimate the momentum budget residual have been made in convective situations. Stevens (1979) studied the momentum budget on the easterly wave scale and found that the large-scale budget had a significant imbalance, suggesting that sub-synoptic-scale circulation strongly affect the wave dynamics. He concluded that the apparent momentum sources were sufficiently complex that neither Rayleigh drag nor a simple vertical momentum exchange could be considered to be an adequate description of the cumulus momentum effects.

Some researchers have suggested that convective clouds can transport westerly momentum against the vertical gradient of mean wind (Nitta and So, 1980; LeMone, 1983; LeMone et al., 1984), in contrast to the traditional assumption of a down gradient mixing process (e.g., Palmen and Newton, 1969). Here, I will examine the momentum and kinetic energy budgets in the vicinity of a large cloud cluster to identify the convective contribution to the

large-scale momentum and kinetic energy budgets.

5.1 Momentum and kinetic energy budget equations

The equations which are used to estimate the momentum budgets may be written as

$$\frac{\partial \bar{u}}{\partial t} + \bar{u}\frac{\partial \bar{u}}{\partial x} + \bar{v}\frac{\partial \bar{u}}{\partial y} + \bar{\omega}\frac{\partial \bar{u}}{\partial p} - f\bar{v} = -\frac{\partial \bar{\phi}}{\partial x} + X \qquad (5.1)$$

$$\frac{\partial \bar{v}}{\partial t} + \bar{u}\frac{\partial \bar{v}}{\partial x} + \bar{v}\frac{\partial \bar{v}}{\partial y} + \bar{\omega}\frac{\partial \bar{v}}{\partial p} + f\bar{u} = -\frac{\partial \bar{\phi}}{\partial y} + Y \qquad (5.2)$$

where the notations are all traditional. X and Y are the momentum residuals which represent the contribution from the unresolved scale of motion to the grid-scale motion in the east-west and north-south directions, respectively, and include data analysis error.

The momentum residuals are computed as

$$X = \frac{\partial \bar{u}}{\partial t} + \bar{u}\frac{\partial \bar{u}}{\partial x} + \bar{v}\frac{\partial \bar{u}}{\partial y} + \bar{\omega}\frac{\partial \bar{u}}{\partial p} - f\bar{v} + \frac{\partial \bar{\phi}}{\partial x} \qquad (5.3)$$

$$Y = \frac{\partial \bar{v}}{\partial t} + \bar{u}\frac{\partial \bar{v}}{\partial x} + \bar{v}\frac{\partial \bar{v}}{\partial y} + \bar{\omega}\frac{\partial \bar{v}}{\partial p} + f\bar{u} + \frac{\partial \bar{\phi}}{\partial y} \qquad (5.4)$$

all the quantities on the right-hand side can be computed directly from the observed data set.

The kinetic energy equation may be derived from Eqs. (5.1) and (5.2). Multiplying Eq. (5.1) by $\bar{u}$ and Eq. (5.2) by $\bar{v}$, and summing the resulting two equations gives

$$\frac{\partial \bar{K}}{\partial t} + \bar{u}\frac{\partial \bar{K}}{\partial x} \bar{v}\frac{\partial \bar{K}}{\partial y} + \bar{\omega}\frac{\partial \bar{K}}{\partial p} = -\bar{u}\frac{\partial \bar{K}}{\partial x} - \bar{v}\frac{\partial \bar{K}}{\partial y} + \bar{u}\,X + \bar{v}\,Y \qquad (5.5)$$

where $K = 1/2(u^2+v^2)$. The data set needed to estimate these two budgets are the wind data and the geopotential height data described in Chapter 2. A description on how these geopotential height data were constructed is included in the Appendix A.

5.2 Momentum budget results

5.2.1 5 September 1974 cluster

Fig. 5.1 shows the north-south cross section of the 5 September clusters in the growing, mature and dissipating stages for the pressure gradient forces (PGF) in vector form. The results above the 150 mb level will not be discussed due to the relatively large diurnal influence on the temperature (and hence the geopotential) fields. In the growing stage around the cluster center, the 700 mb level of PGF (where the easterly wave is active) is characterized by large northwesterly acceleration, in contrast to the weak acceleration in the upper layer around 220 mb. Another large northwesterly acceleration is found to the south of the cluster center in the 200-300 mb layer. In the mature stage, the region of northwesterly acceleration in the 700 mb region becomes more northerly, while the region of weak acceleration in the upper layer extends to a larger area. In the dissipating stage, weak upper-layer accelerations in the mature stage change to relatively

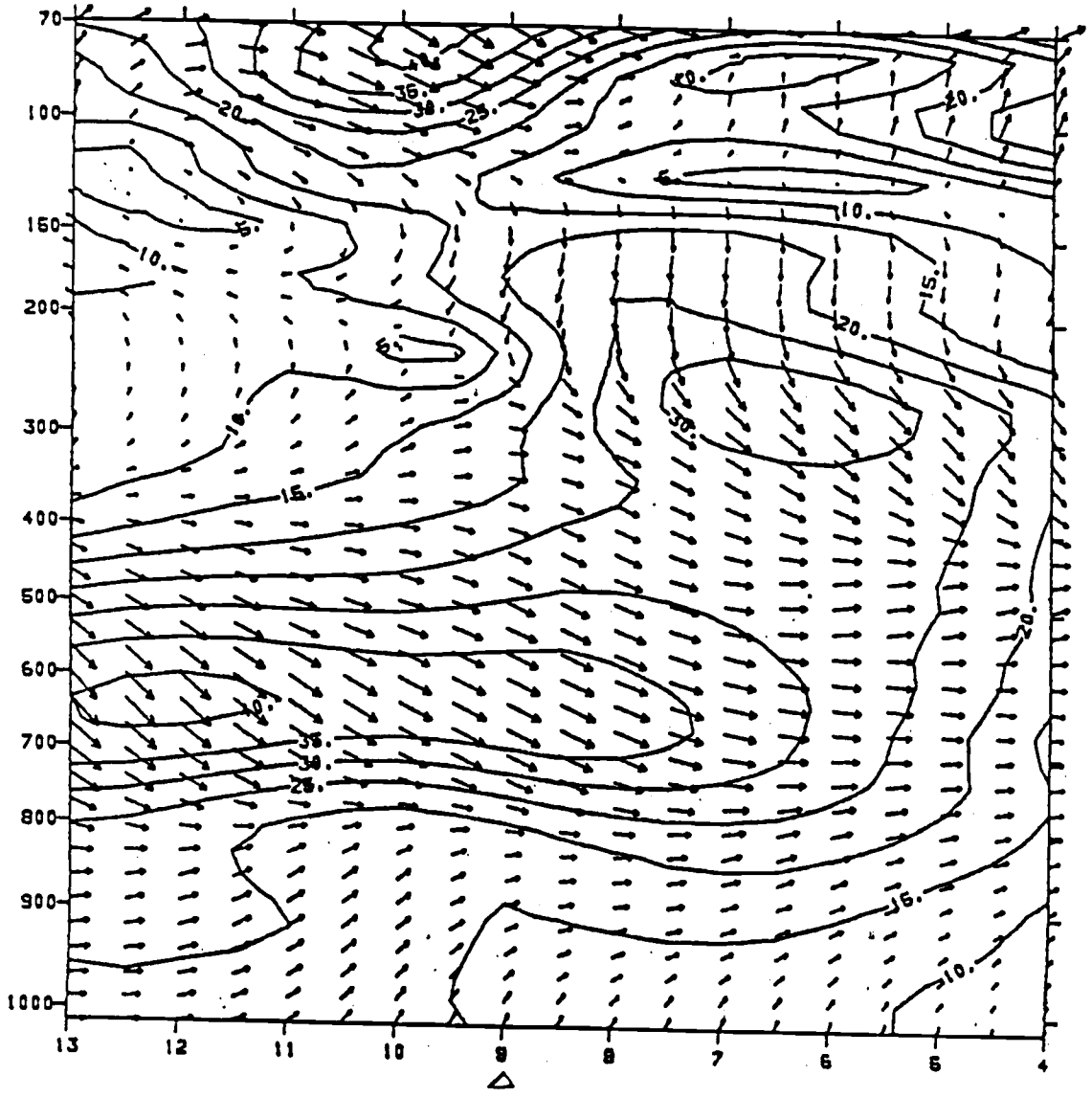

(a) growing

Figure 5.1. Meridional cross-section of the pressure gradient force (in vector form) through the cluster center during the (a) growing, (b) mature, (c) dissipating stages of the 5 September cloud cluster. Units are 5×10^{-5} m/s^2; contour interval is 10^{-5} m/s^2 for magnitude of the vector. Vector length is proportional to the magnitude. Δ indicates cluster center.

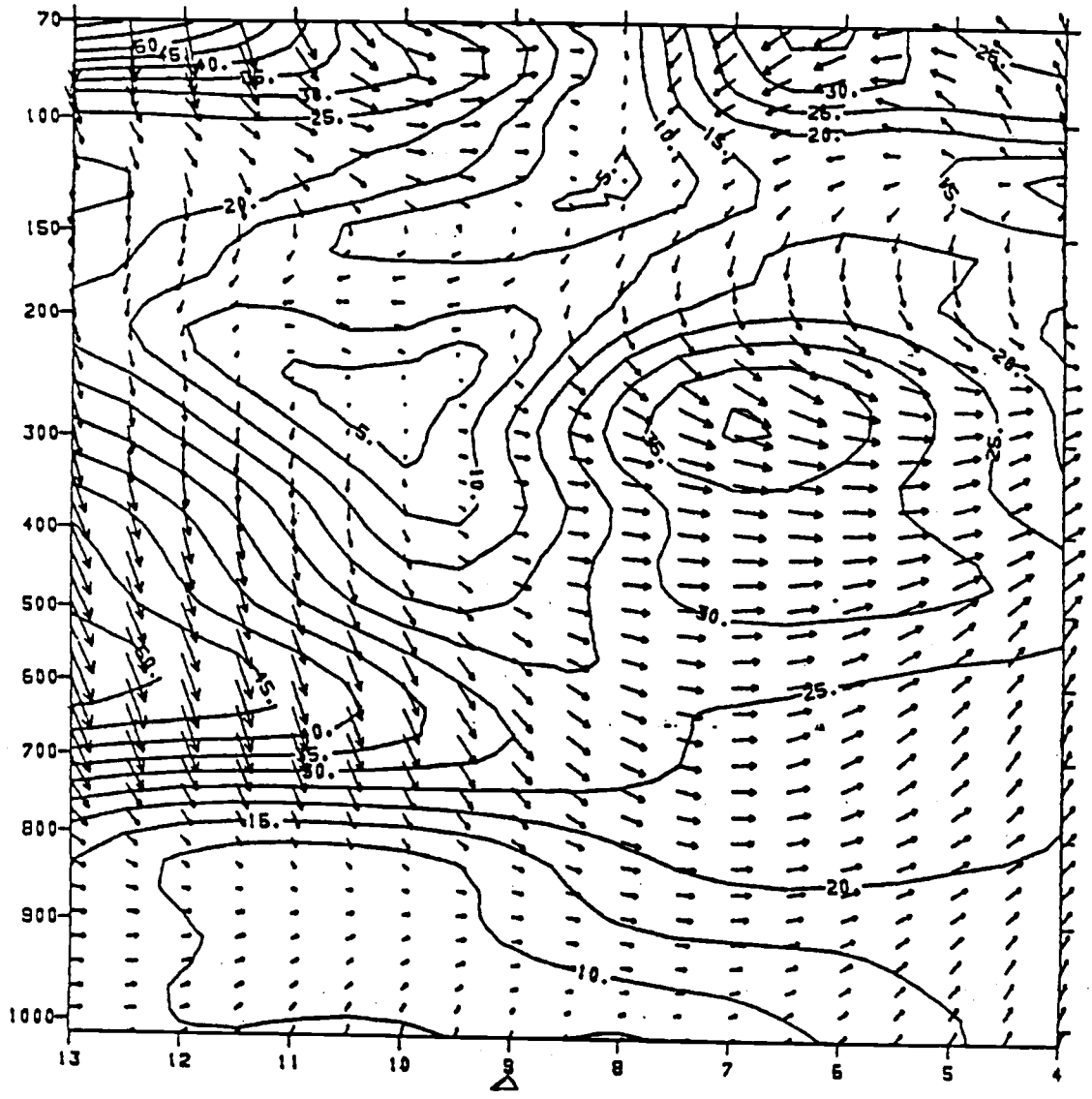

(b) mature

Figure 5.1 (continued)

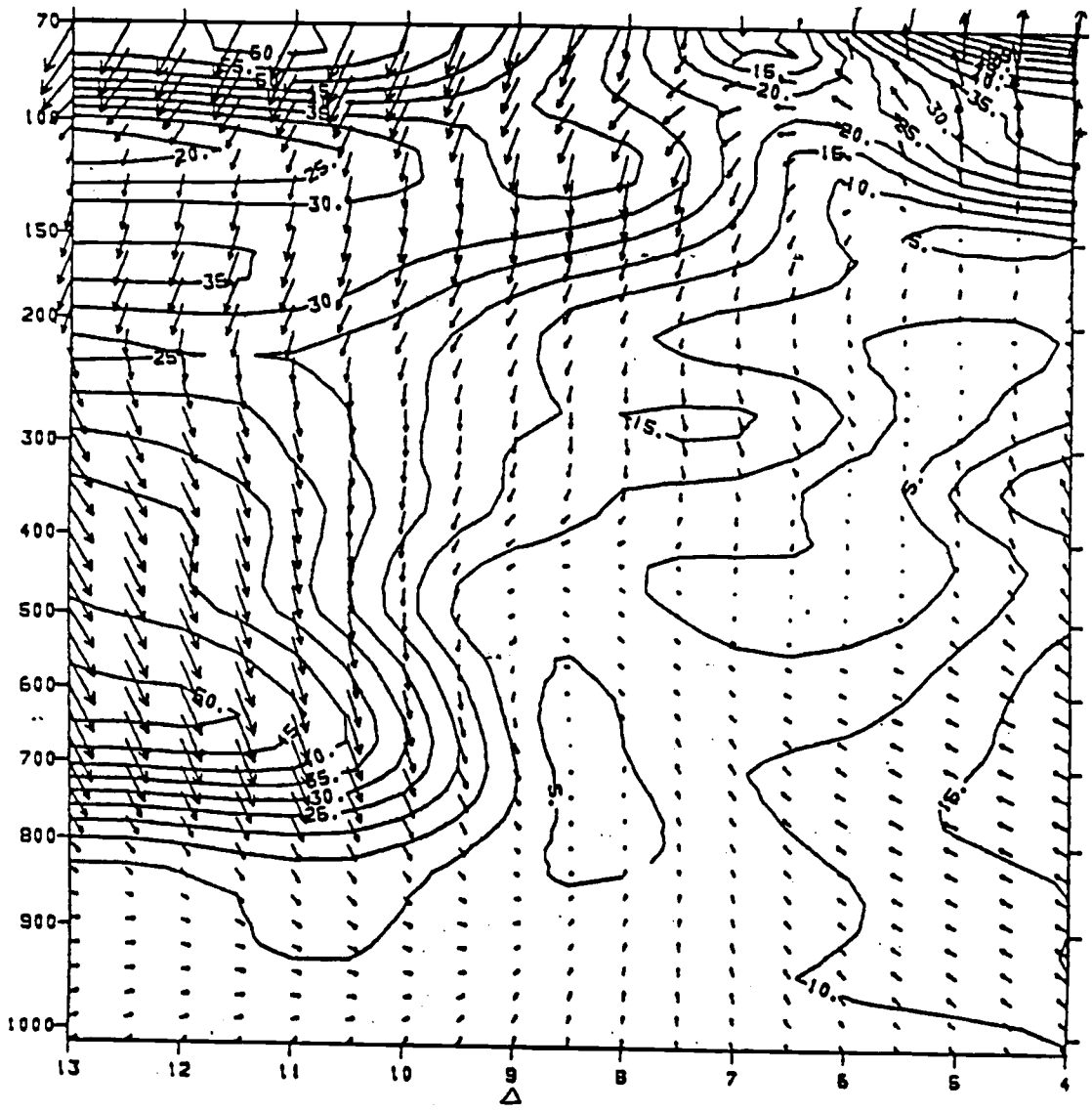

(c) dissipating

Figure 5.1 (continued)

large northerly acceleration near the cluster center. The weakening of the magnitude of the acceleration in the eastern part of the lower layer is also noted.

Fig. 5.2 shows horizontal plots of the PGF at 700 mb and 227 mb in different stages of the cloud cluster life cycle. Fig. 5.2a demonstrates that the 700 mb northwesterly acceleration is associated with the easterly wave trough approaching from the eastern part of the array in the growing stage. The movement of the easterly wave trough towards the west in the mature stage can be identified in Fig. 5.2b. Fig. 5.2c reveals the further advancement of the trough and the change of PGF associated with this trough movement at the 700 mb level. At the 227 mb level, Figs. 5.2d and 5.2e reveal that relatively high pressure situated in the area of the cloud cluster center causes the weak acceleration there and the flow that is accelerated out of this high pressure center; in the dissipating stage, northerly acceleration dominates in the cluster center.

Fig. 5.3 is the same as Fig. 5.1 except for the sum of total momentum change and the Coriolis force. Two regions of large northerly acceleration at the 700 mb (300 mb) level to the north (south) of the array are mainly due to the Coriolis effect. Near the cluster center in the 200-300 mb layer, the easterly acceleration is a minimum. In the mature stage, upper-layer northeasterly acceleration dominates to the south of the cluster center and southeasterly acceleration dominates to the north. At the 700 mb level, northwesterly acceleration prevails in the

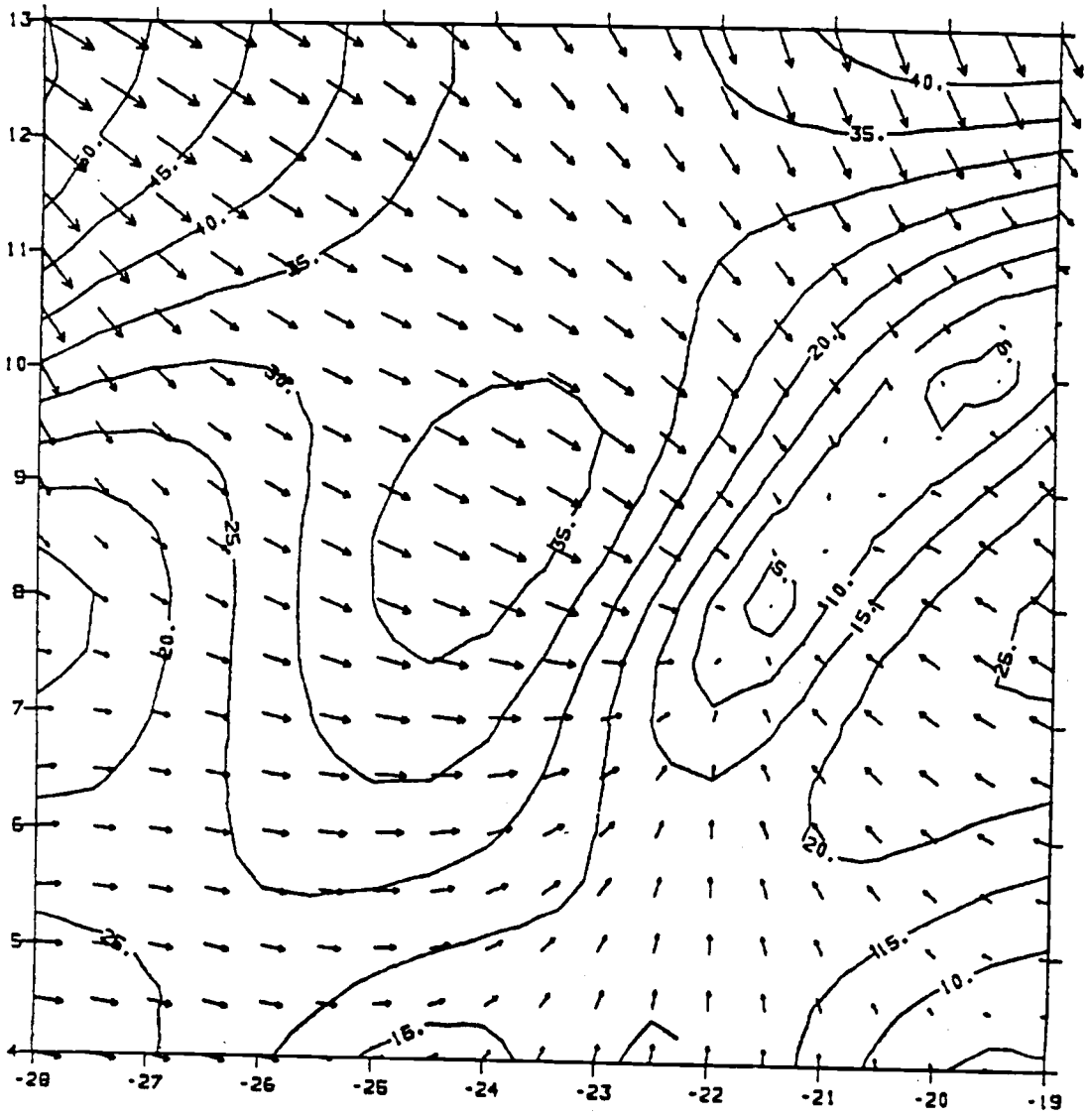

(a) growing, 705 mb

Figure 5.2. Horizontal plot of pressure gradient force during the (a) growing, (b) mature, (c) dissipating stages of the 5 September cluster at 705 mb. (d), (e) and (f) are the corresponding figures at 227 mb. Units are 10^{-5} m/s^2; contour interval is 5×10^{-5} m/s^2.

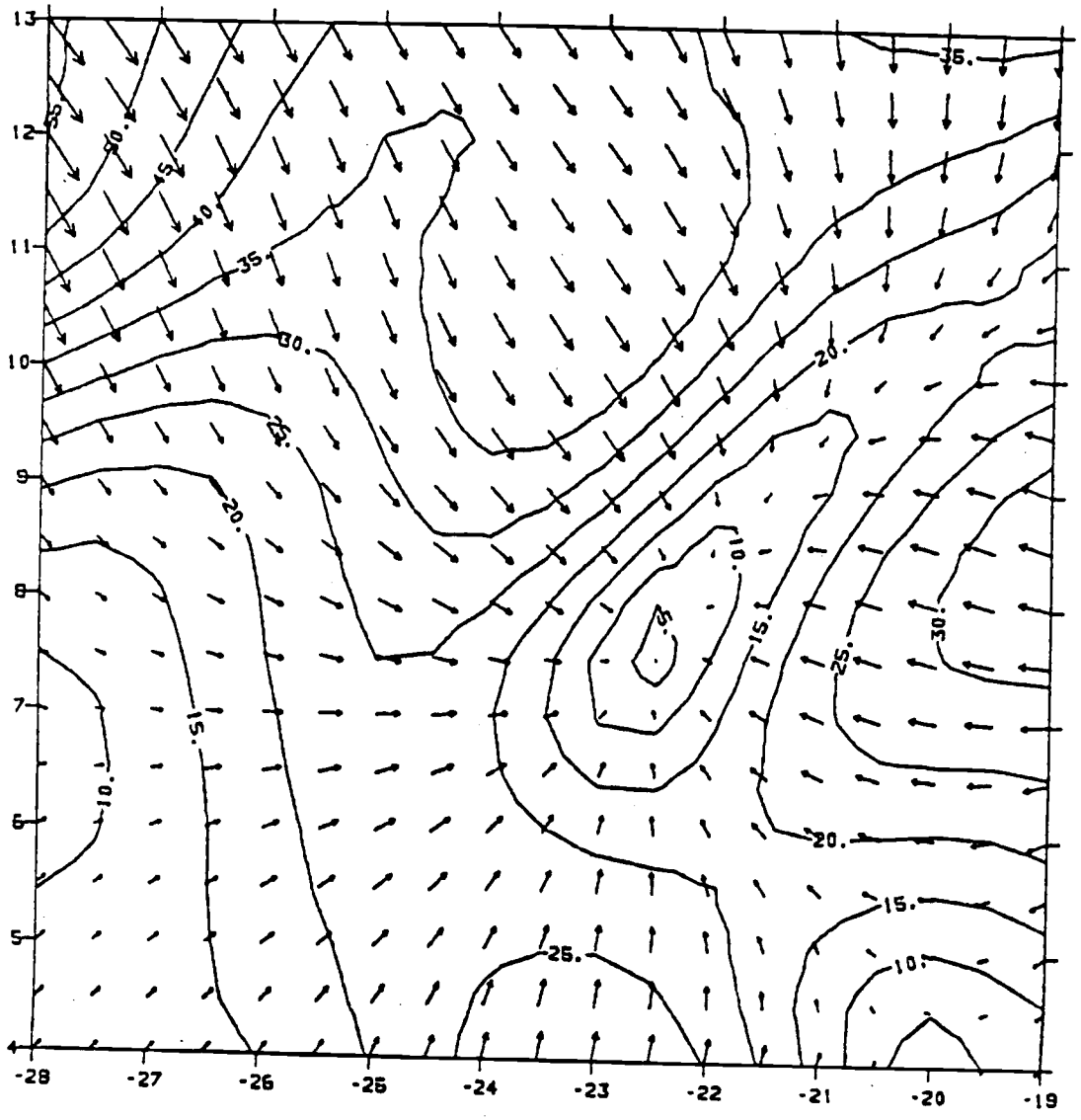

(b) mature, 705 mb

Figure 5.2 (continued)

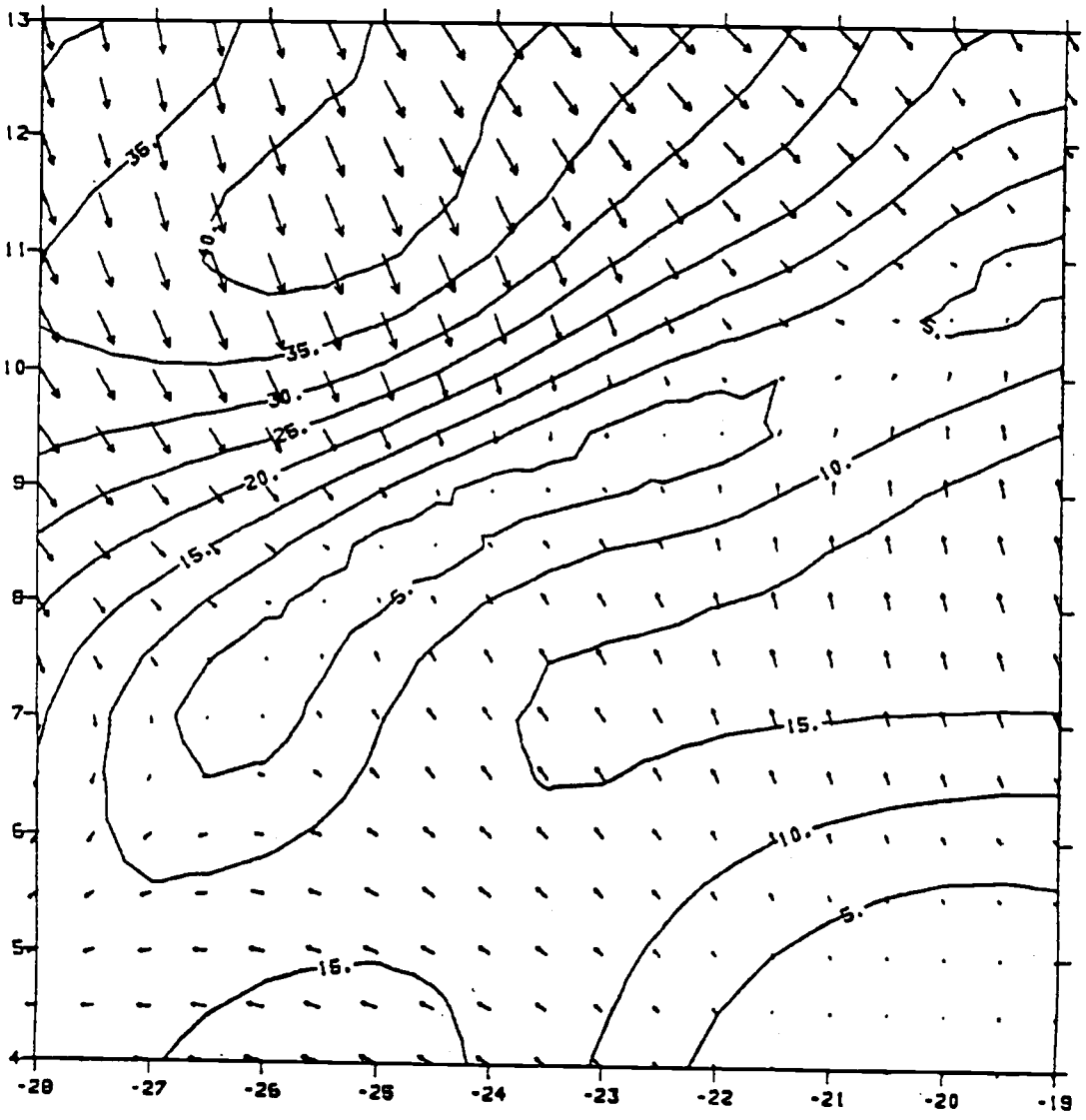

(c) dissipating, 705 mb

Figure 5.2 (continued)

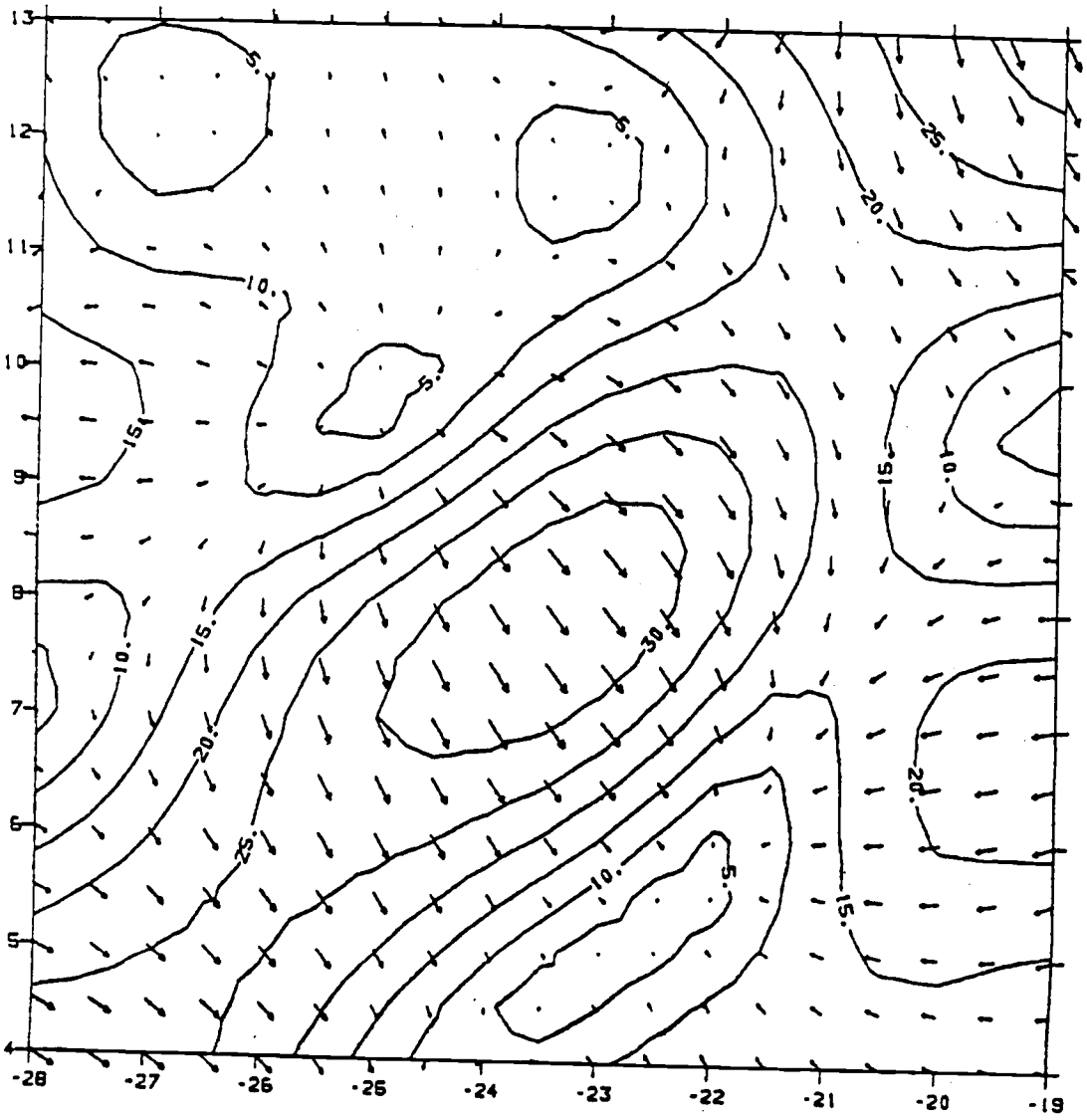

(d) growing, 227 mb

Figure 5.2 (continued)

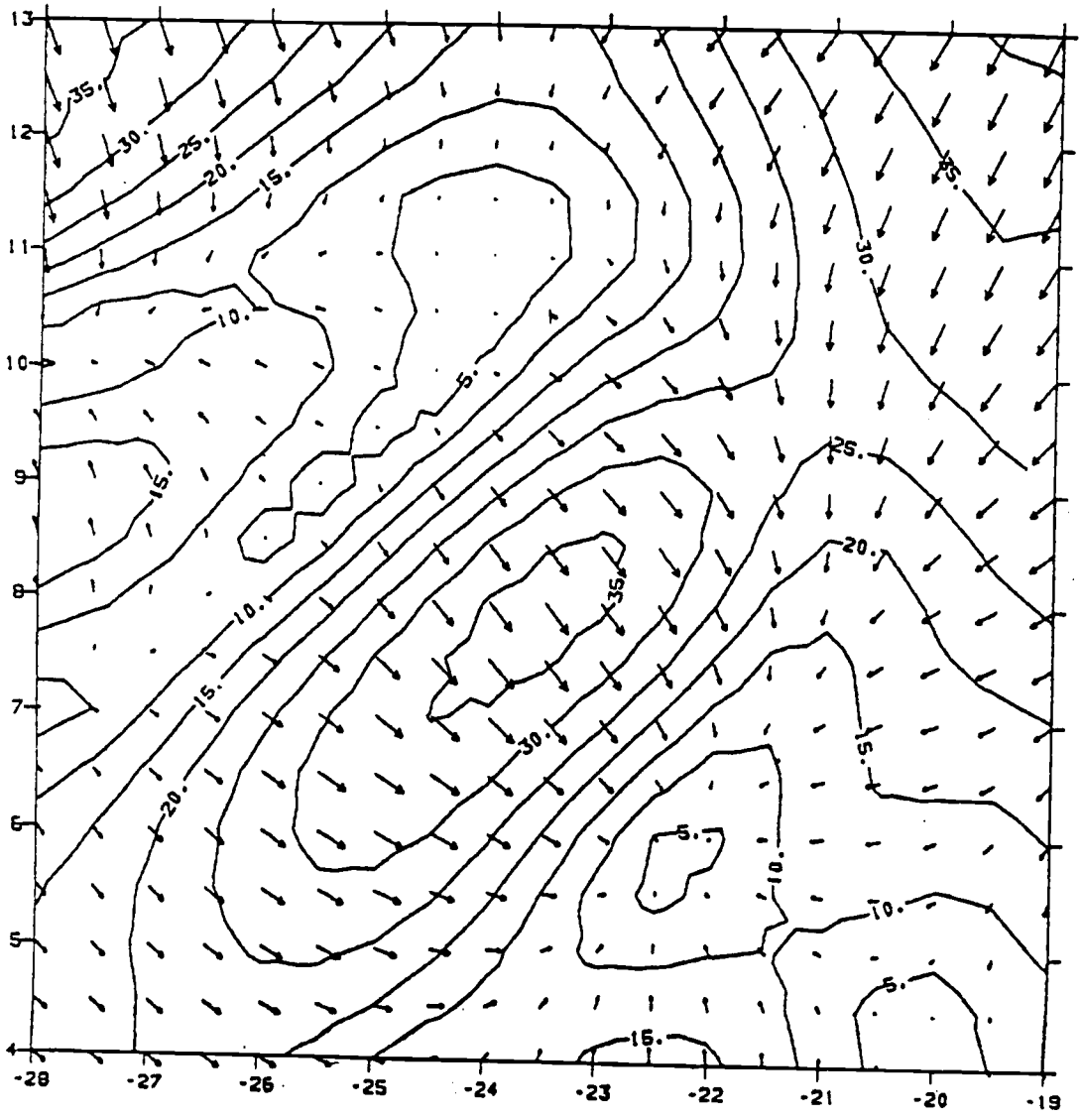

(e) mature, 227 mb

Figure 5.2 (continued)

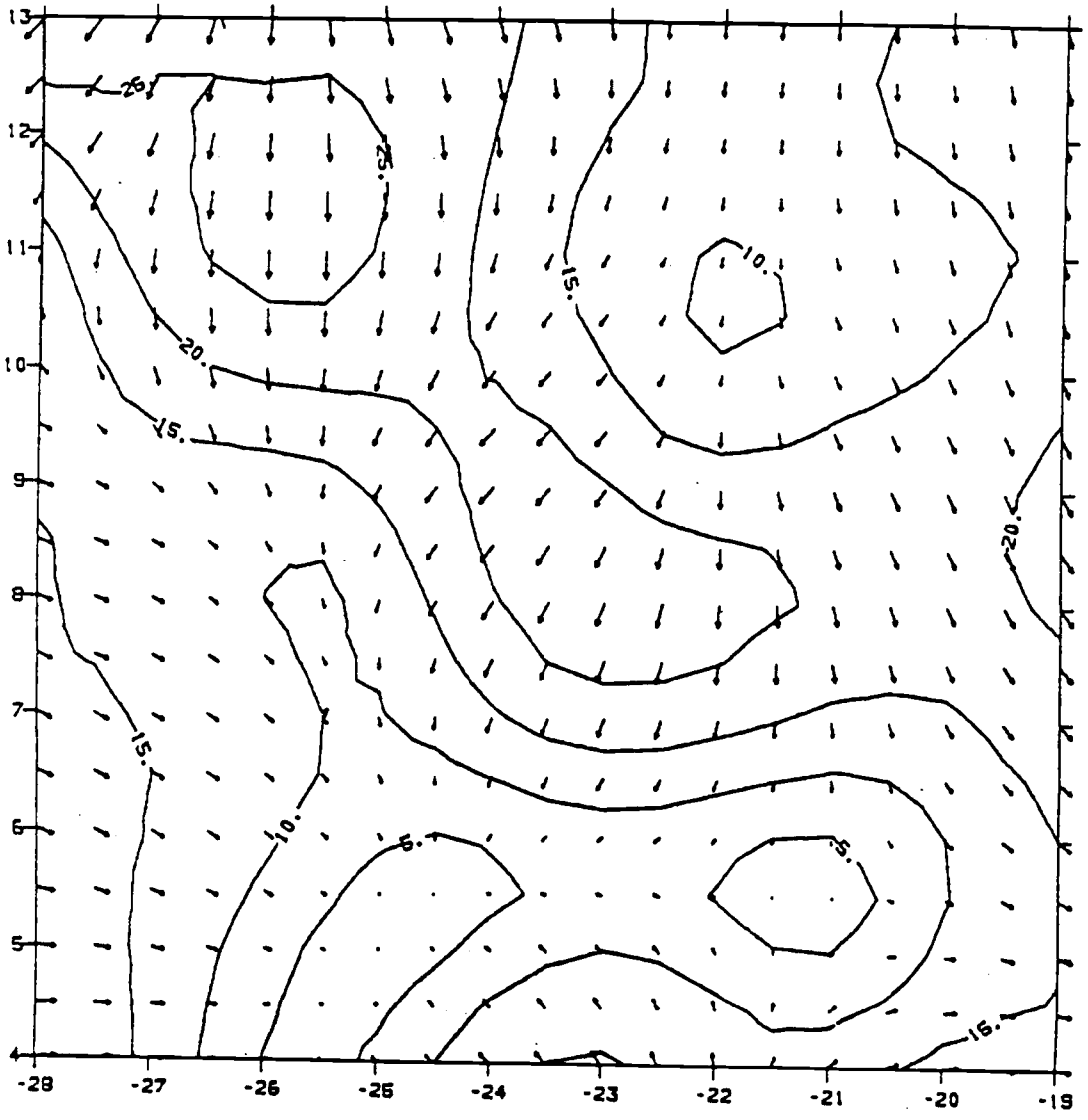

(f) dissipating, 227 mb

Figure 5.2 (continued)

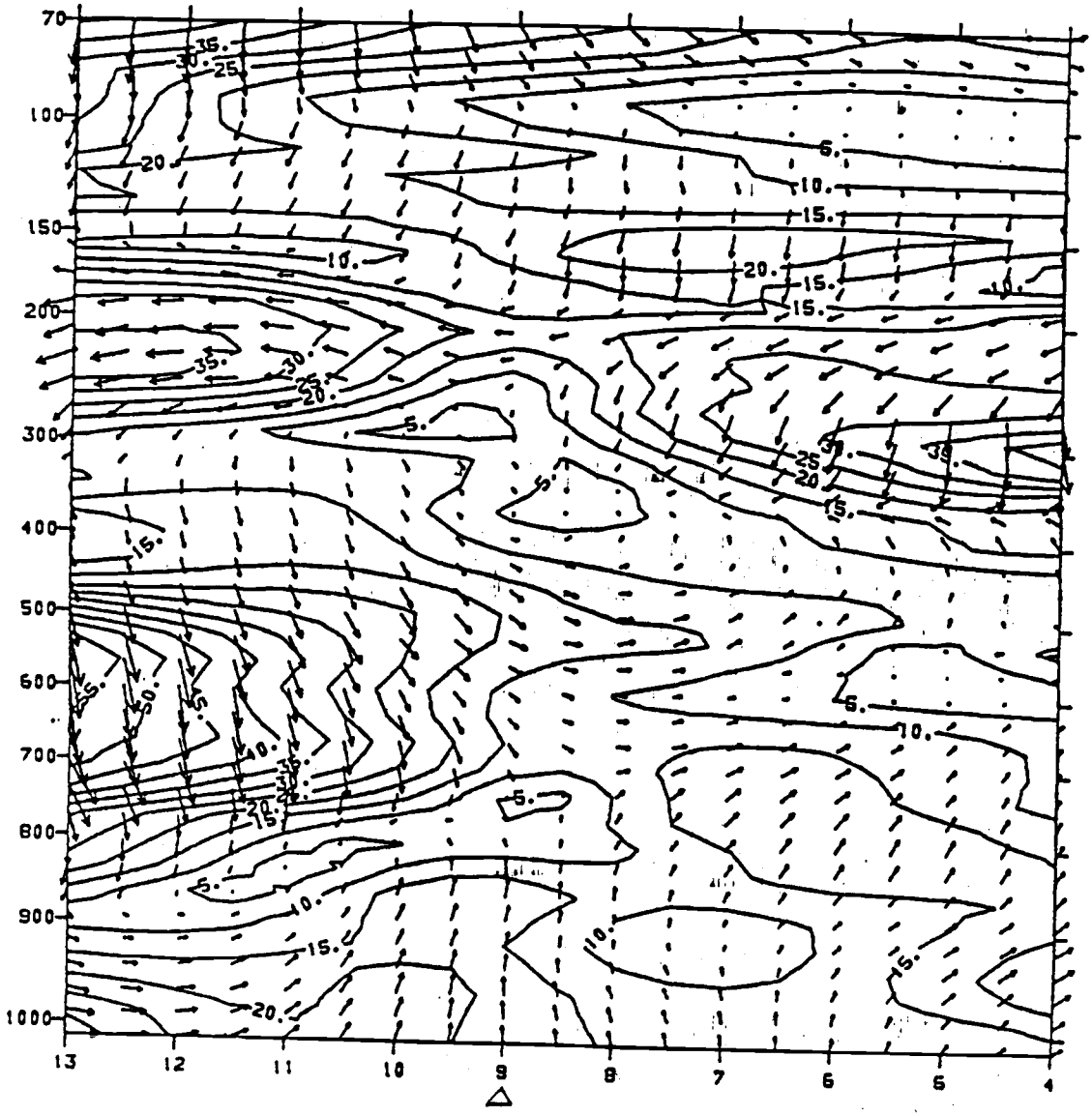

(a) growing

Figure 5.3. As in Fig. 5.1 except for the sum of total change and the Coriolis force.

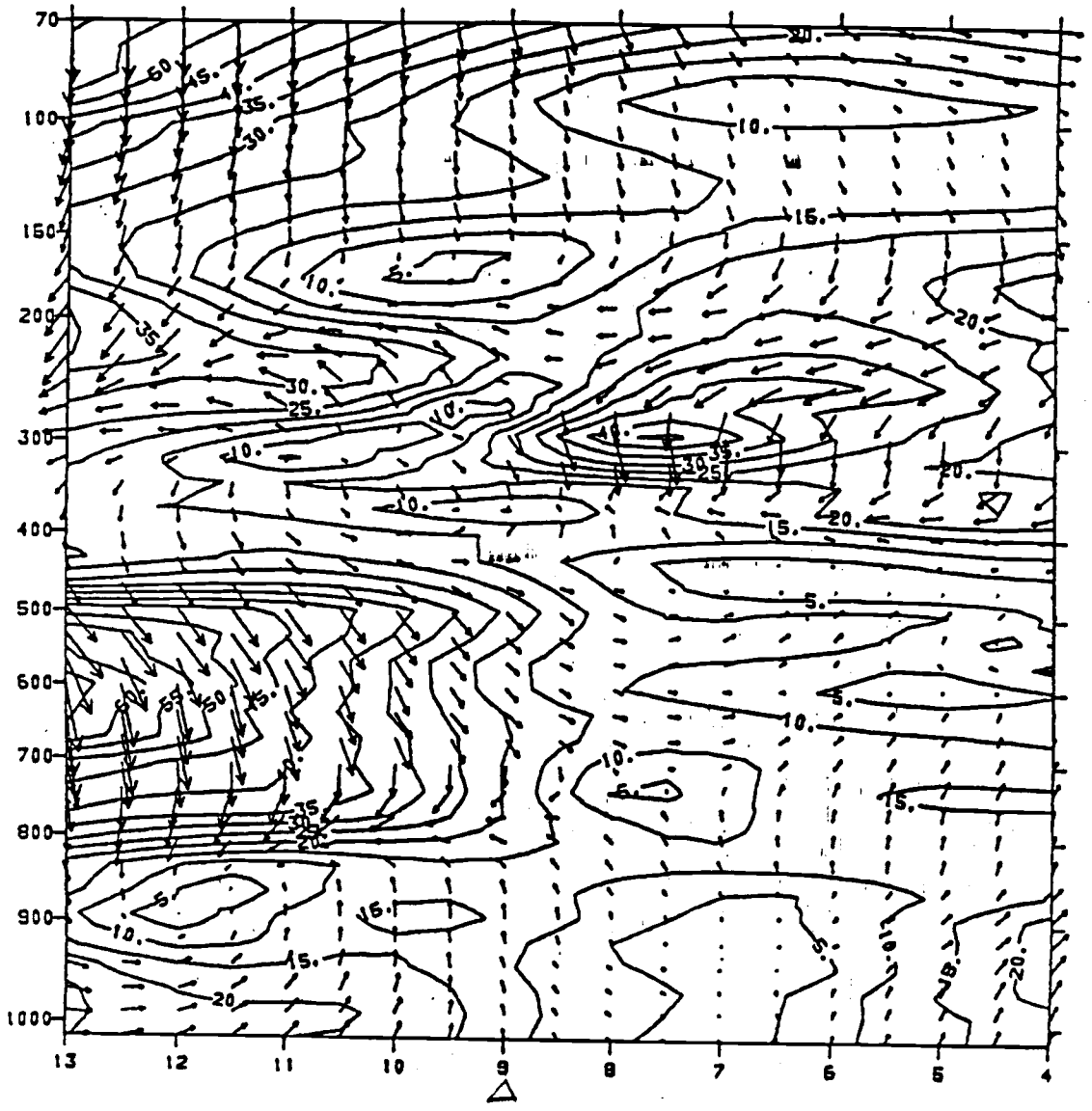

(b) mature

Figure 5.3 (continued)

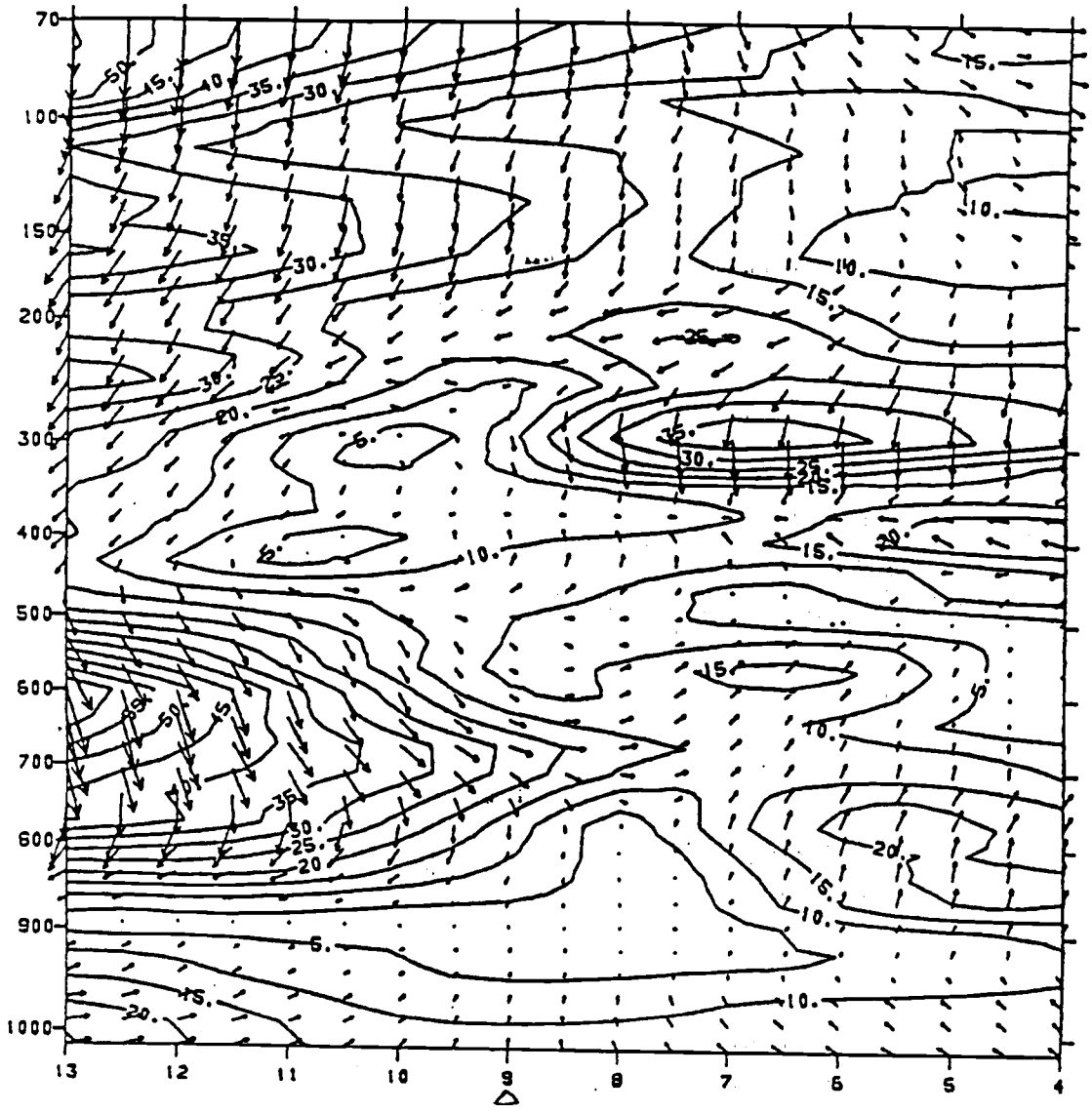

(c) dissiapting

Figure 5.3 (continued)

northern part of the array in the growing and mature stages. By comparison with the Fig. 5.1, it is found that this layer is very close to geostrophic balance. In the dissipating stage, northerly (southerly) accelerations dominate in more of the region than the westerly (easterly) accelerations.

The corresponding momentum residuals are shown in Fig. 5.4. The residuals here are computed as the difference between the total momentum change, the Coriolis force and the PGF [as in Eqs. (5.3) and (5.4)]. Easterly acceleration dominates in the growing stage. At the lower levels, this residual tends to induce a convergent circulation around the cluster center, with southerly (northerly) accelerations to the south (north) of the cluster center. Around the cluster center the easterly acceleration extends from the surface to 200 mb. Thus the residual effect will produce a net increase of easterly momentum in the vertical column. This is consistent with the easterly drag forces induced by the surface westerly flow. In the upper layer, the easterly accelerations are at a minimum near the cluster center.

In the mature stage, the cluster center possesses a minimum of accelerations in the 150-700 mb layer. Large easterly accelerations are found around the 700 mb level in the cluster center. While this lower level acceleration pattern still induces a convergent circulation around the cluster center, the residual in the upper layer will build up a divergent circulation in the 200-300 mb layer by forcing northeasterly (southeasterly) flow to the south (north) of the cluster center. In the dissipating stage,

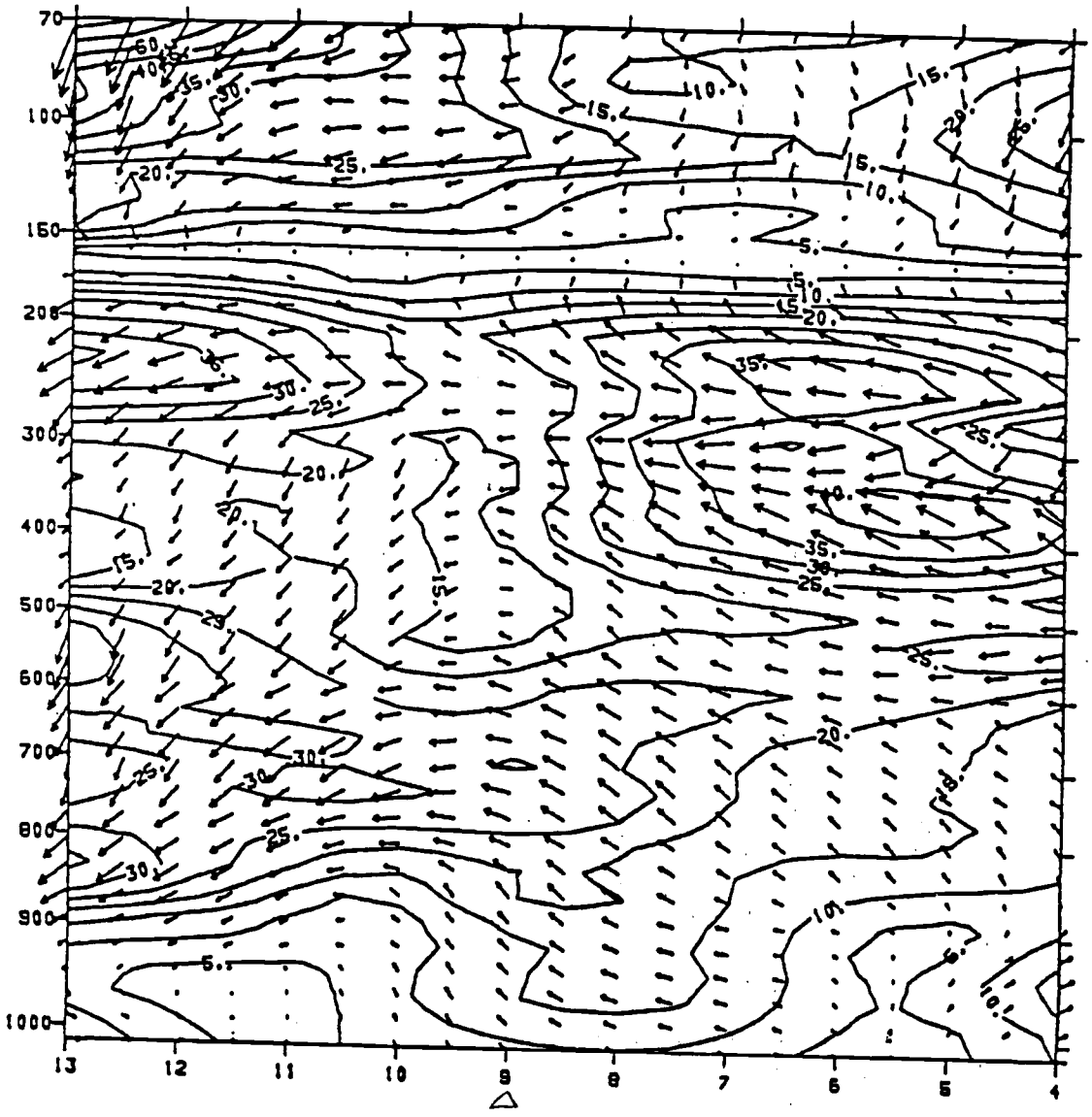

(a) growing

Figure 5.4. As in Fig. 5.1 except for the momentum budget residuals.

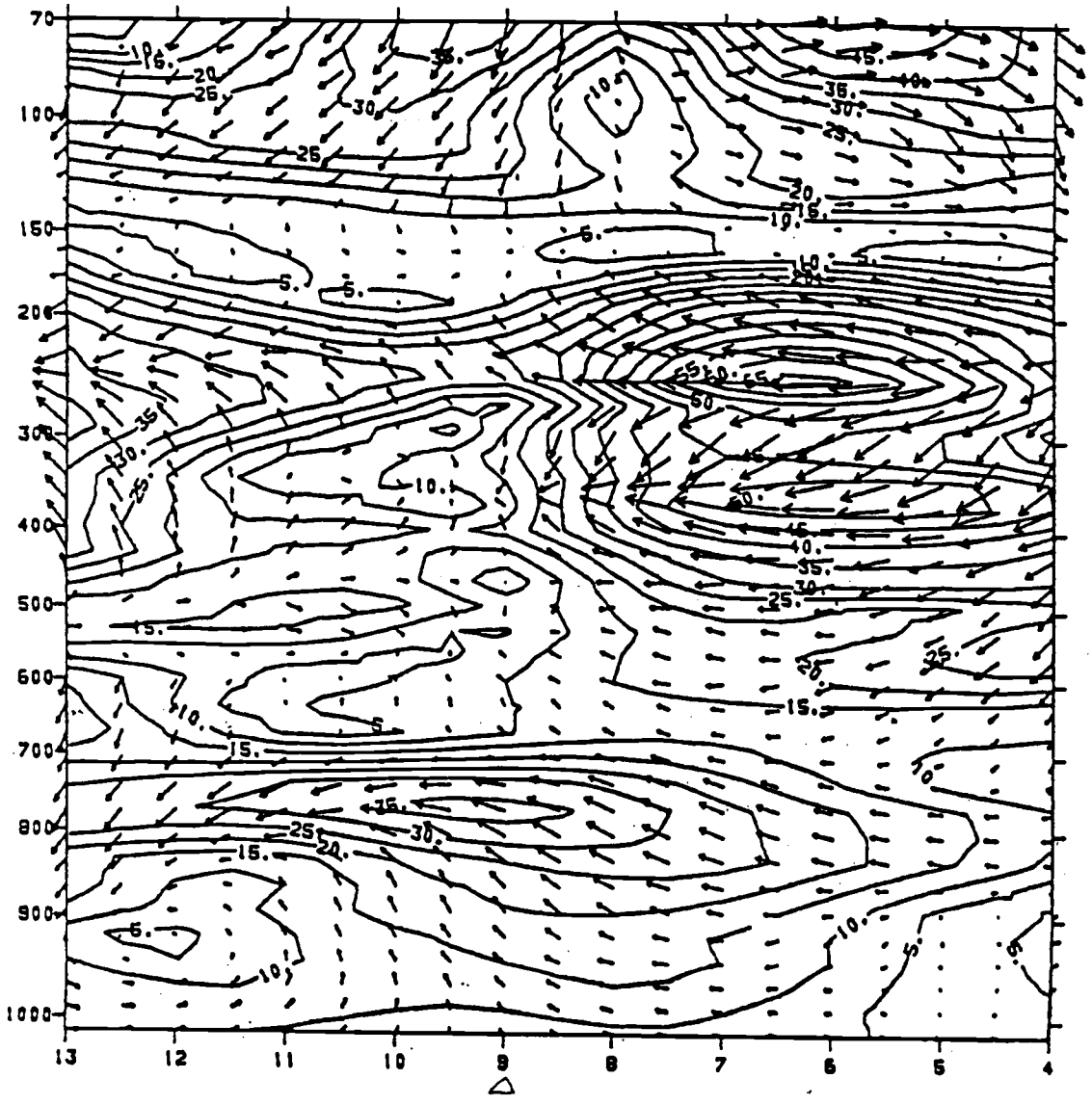

(b) mature

Figure 5.4 (continued)

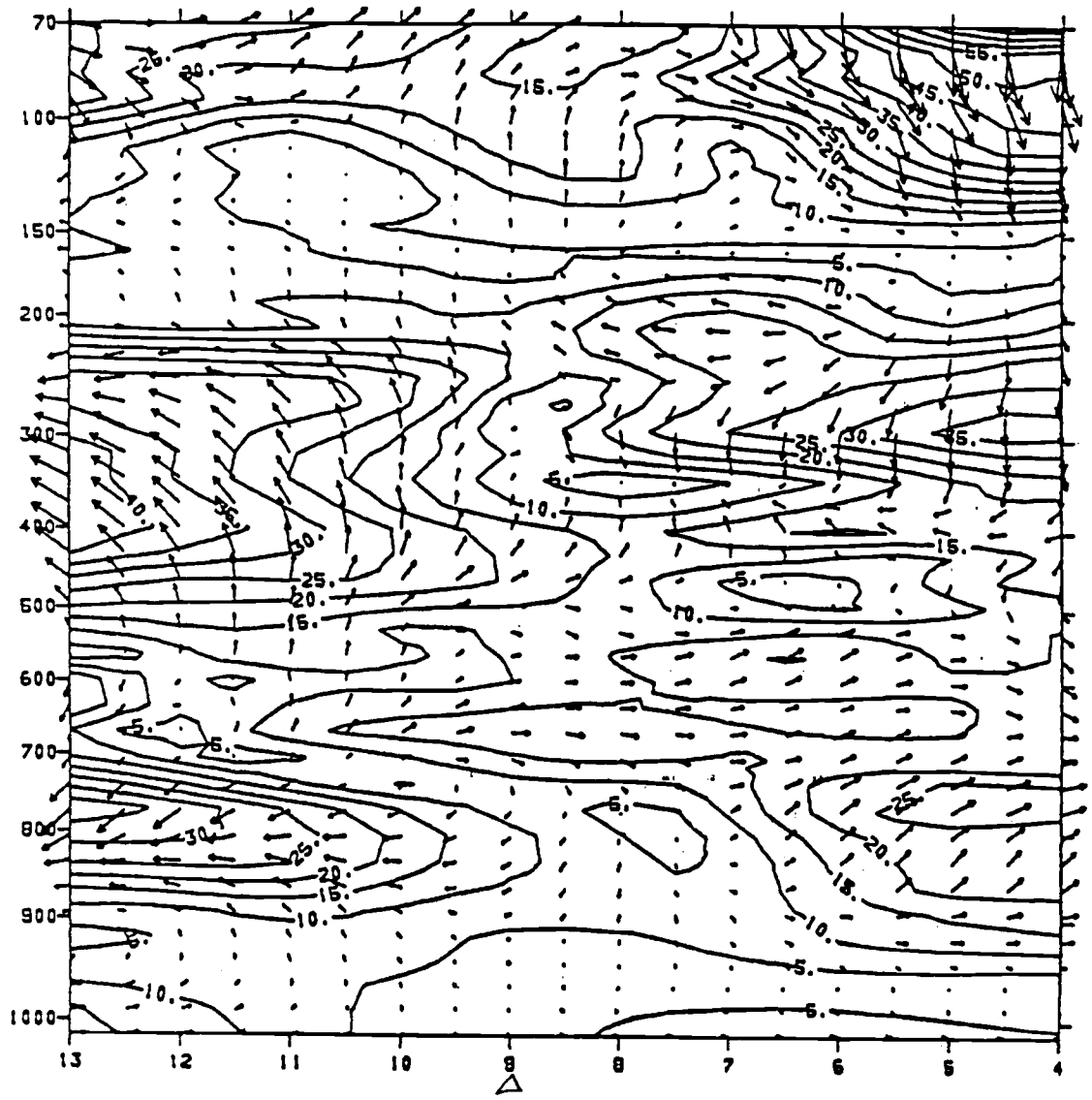

(c) dissipating

Figure 5.4 (continued)

residual effect no longer produces the convergent circulation, while the induced upper-level divergent circulation is still active. The vertical structure of residuals at this stage is quite different than that in the growing stage.

The momentum budget residual during the period when there is no convective disturbance is about one-third to one-half of the values at the disturbed periods. As pointed out in Tollerud (1983), the vorticity budget residual at the undisturbed period is one-third as large as those at the disturbed periods. Thus, the relative magnitudes of the momentum budget residuals in disturbed and undisturbed periods are consistent with the estimates of the vorticity budget residuals and probably contain a physically meaningful signal.

5.2.2 Composite results

In Chapter 4, it was found that the heat and moisture budgets of the five non-squall cloud clusters were quite similar. The compositing scheme may thus be viewed as summarizing the important features of individual clusters. This is not the case for the momentum budget. The momentum budgets in the vicinity of the five clusters have some similarities, but also some significant differences. This has to be kept in mind in the discussion of the composite results on the momentum budget.

Fig. 5.5 show the composite north-south cross-section through the center for the PGF (in vector form) in the growing, mature and dissipating stages. In the growing stage, the zonal PGF is

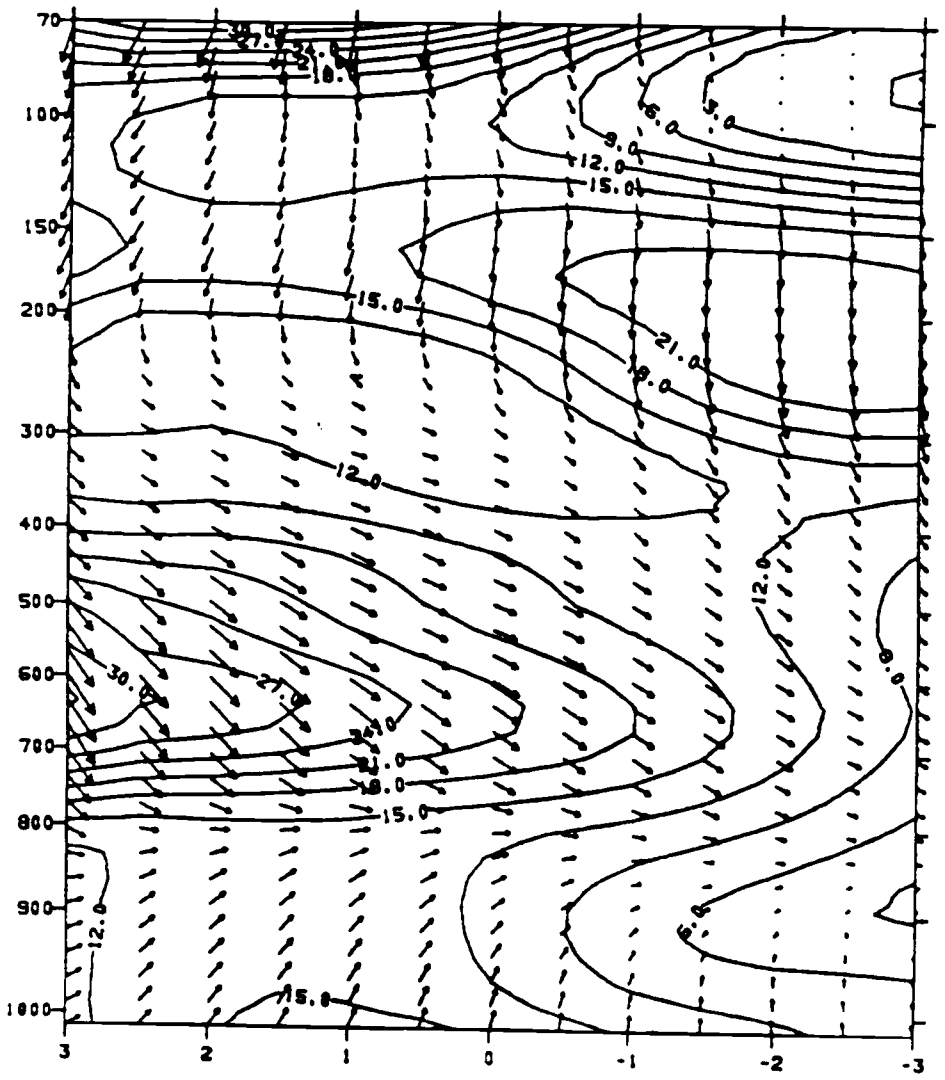

(a) growing

Figure 5.5. Meridional cross-section of pressure gradient force (in vector form) during the (a) growing, (b) mature, (c) dissipating stages of the composited cluster. Units are 10^{-5} m/s^2; contour interval is 3×10^{-5} m/s^2.

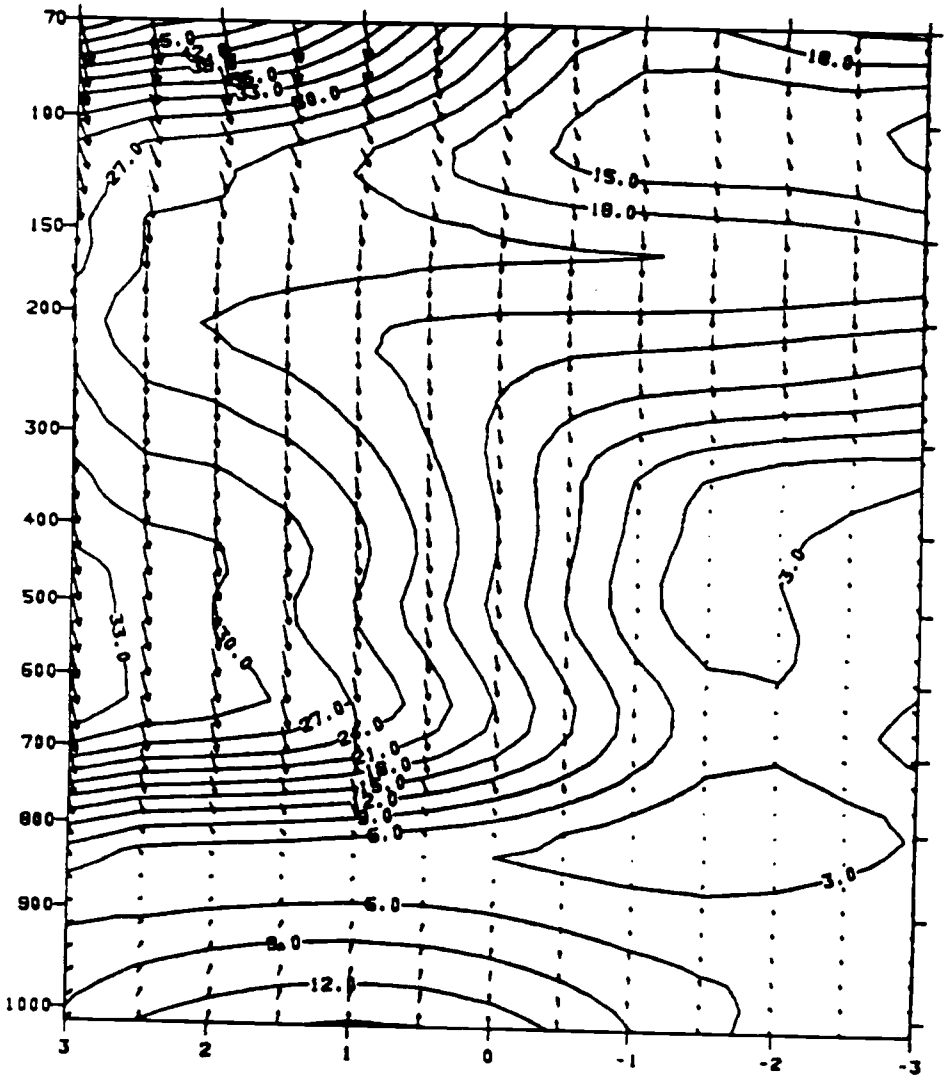

(b) mature

Figure 5.5 (continued)

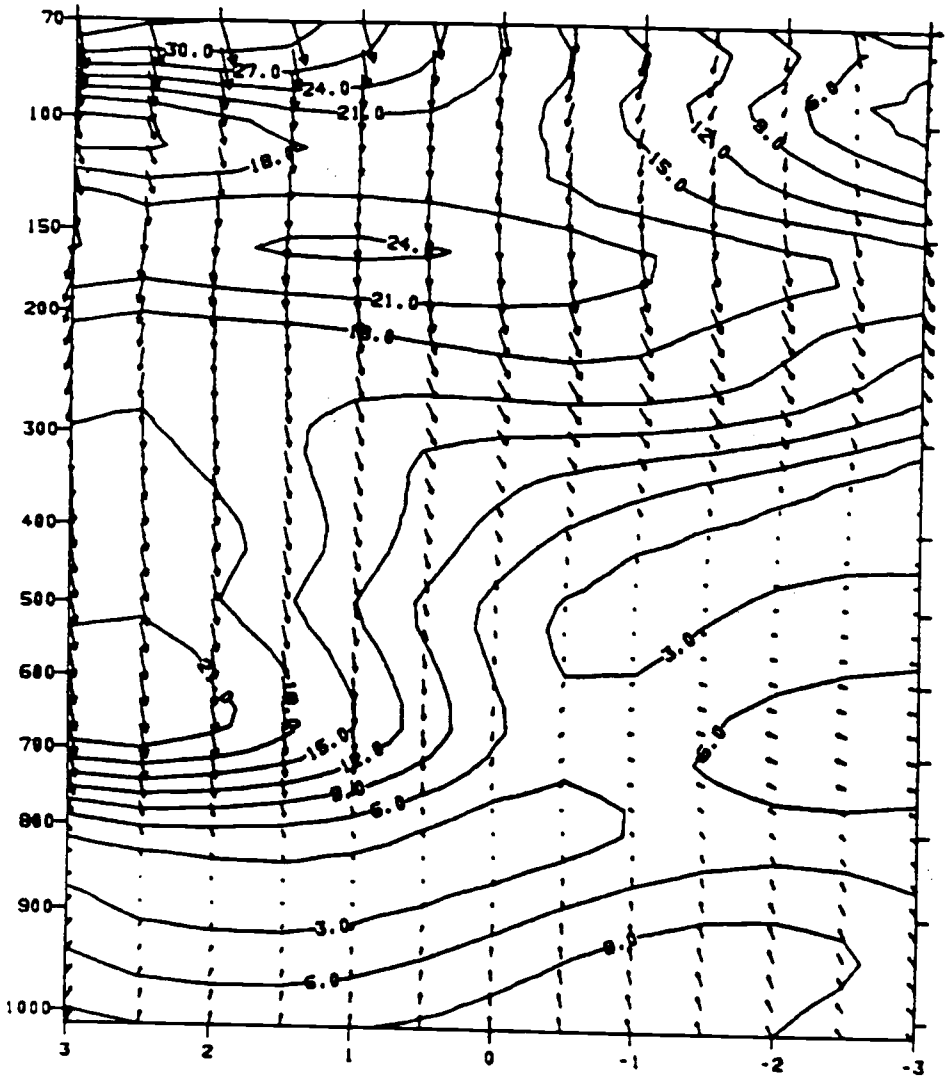

(c) dissiapting

Figure 5.5 (continued)

characterized by westerly acceleration from the surface to around 220 mb, with the maximum values on the order of $20*10^{-5}$ m/s^2 at 625 mb. The corresponding values are much smaller in the mature and dissipating stages. The lower level zonal PGF is highly influenced by the movement of the easterly wave trough. In the mature stage, the zonal pressure gradient force has a westerly acceleration in the northern part of the A/B array and an easterly acceleration in the southern part; in the dissipating stage, the upper layer has westerly acceleration on the order of $5*10^{-5}$ m/s^2.

Weak southerly acceleration in the lower layer (up to 850 mb) and northerly acceleration in the upper layer (from 850 mb and up) are found throughout the life cycle of the cluster. In the growing stage, maximum northerly acceleration of meridional MPF is found to the south of the cluster center around the 200 mb level. In the mature and dissipating stages, the maximum northerly acceleration shifts to the north of the cluster center with a magnitude on the order of $20*10^{-5}$ m/s^2.

In his momentum budget study with the easterly wave composite, Stevens (1979) found a zonal PGF maximum on the order of $15*10^{-5}$ m/s^2, with the trough region showing an westerly acceleration on the order of $5*10^{-5}$ m/s^2 from the surface to upper levels. That is quite comparable with the present result, although the present result shows larger acceleration. For the meridional PGF, Stevens (1979) showed southerly accelerations on the order of $5*10^{-5}$ m/s^2 from the surface to 400 mb, with northerly acceleration above. That is different from the present result, which shows

southerly acceleration in the lowest layer and northerly acceleration from 800 mb and up. This difference indicates that the study of the cluster events based on a point (the center of the array in Stevens, 1979), is potentially different from momentum budgets centered on the clusters.

Fig. 5.6 is the composite north-south cross-sections through the cluster center of the momentum budget residuals in vector form. Fig. 5.6 reveals that in the growing stage easterly accelerations are enhanced in the lower layer, while a relative minimum of easterly accelerations accompanies the relative large easterly accelerations to the south and north of the center at upper layers. From the surface to 200 mb, there is a sink of westerly momentum in most of the area at this stage. Stevens (1979) found that cumulus clouds apparently were not simply removing momentum from one level and transporting it to another; rather, cumulus friction may provide a vertically integrated net source/sink of westerly momentum for different wave categories. In the mature stage, the low level easterly acceleration is capped by the westerly acceleration above from 700 mb to 450 mb. The upper layer at the cluster center is a relative minimum of easterly acceleration. Thus, the momentum residual effect is capable of generating a vorticity couplet pattern with positive (negative) vorticity to the north (south) of the cluster center in the upper layer on the order of $5*10^{-10}\,s^{-2}$. This result is consistent with the formation of the horizontal vorticity couplet reported by Tollerud and Esbensen (1983). In the dissipating stage, the lower

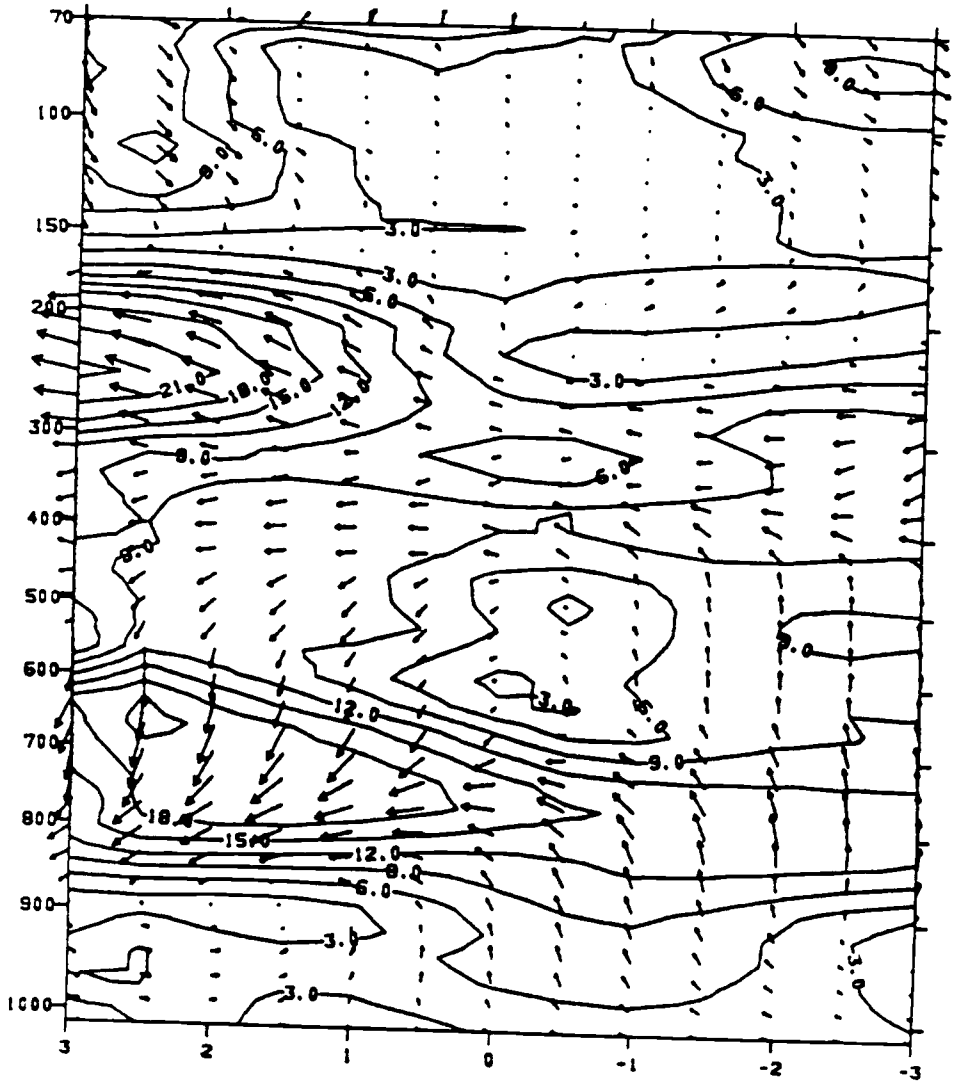

(a) growing

Figure 5.6. As in Fig. 5.5 except for the momentum budget residual.

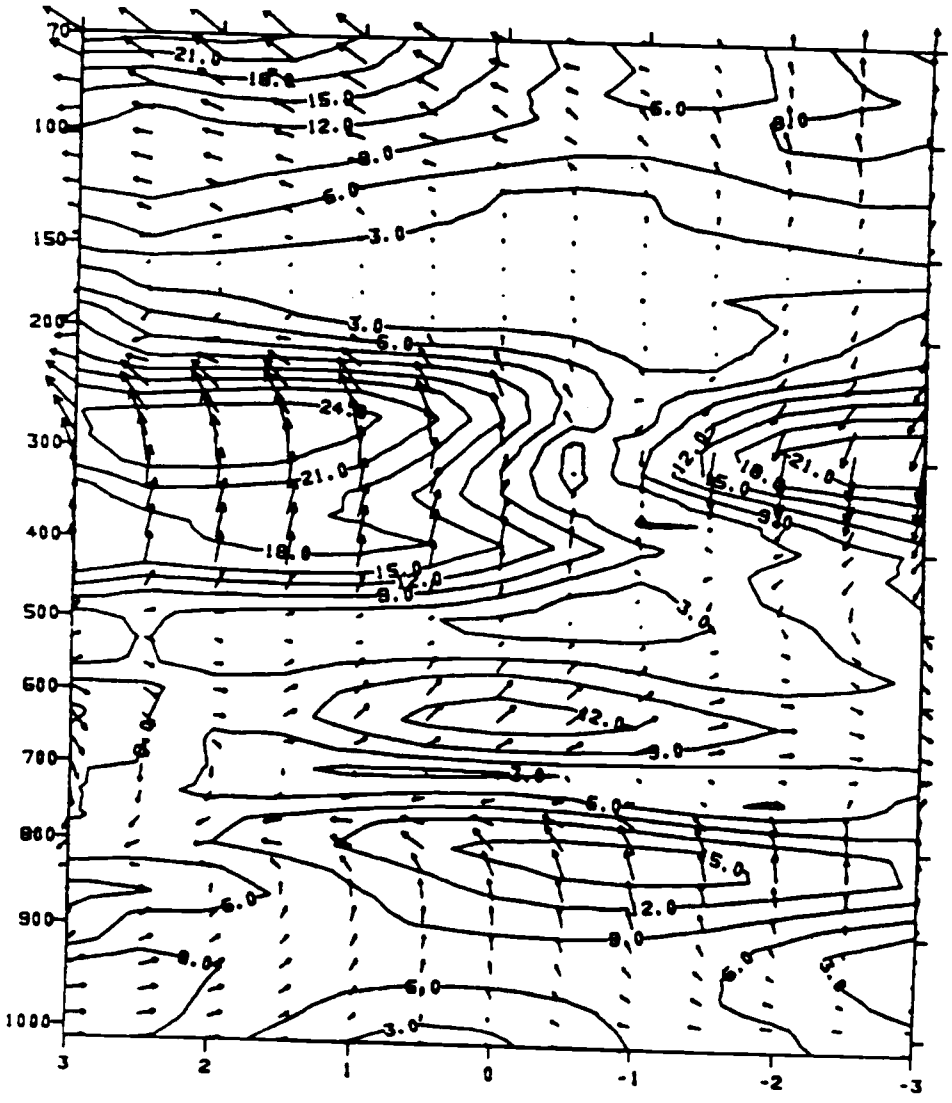

(b) mature

Figure 5.6 (continued)

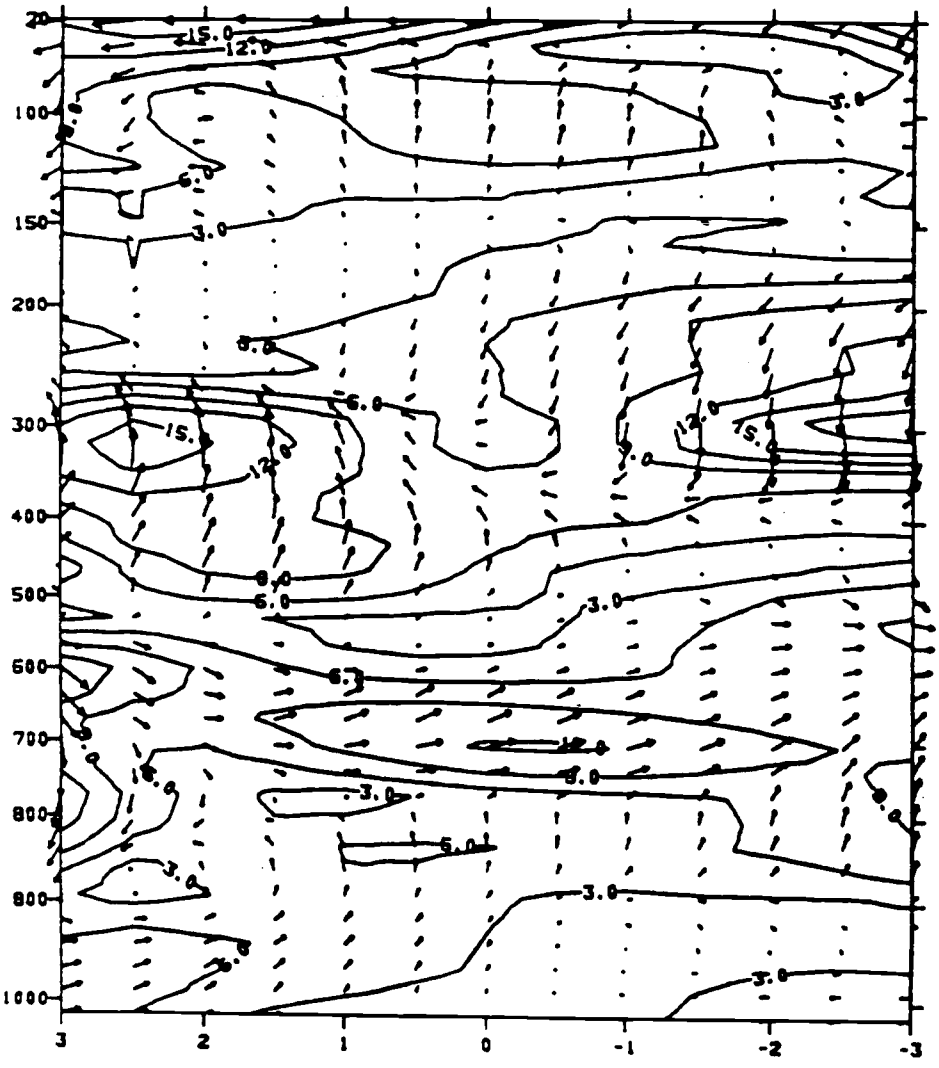

(c) dissipating

Figure 5.6 (continued)

layer is dominated by weak westerly accelerations, while weak easterly accelerations are found in the upper layer.

In the growing stage, the meridional momentum residual at 700 mb is characterized by near zero accelerations at the center with southerly (northerly) accelerations to the south (north) of the center. This will induce a convergent flow and further strengthen the existing large scale convergence in the lower layer. The upper layer is dominated by weak southerly acceleration from 320 mb to 160 mb. Again, except in a shallow layer at 320-360 mb, all levels through the cluster center tend to have a southerly momentum residual. In the mature stage, the residuals have a layered structure from the surface to 500 mb, with southerly acceleration from the surface to 800 mb and in the 500-650 mb layer, with very weak northerly acceleration in between. The upper layer is associated with the divergent circulation caused by the northerly (southerly) acceleration to the south (north) of the center, with minimum acceleration at the center. This upper layer residual structure is very similar to the composite meridional wind as shown in Fig. 5.7 from Tollerud (1983). This result suggests that at least part of the divergence in the upper layer is influenced by the cumulus scale or mesoscale effects as seen in the meridional momentum budget residuals.

In the dissipating stage, the results show relatively weaker southerly accelerations in the lower layer, and a weak northerly acceleration to the north of the cluster center. This will result in a much weaker divergent circulation than in the mature stage at

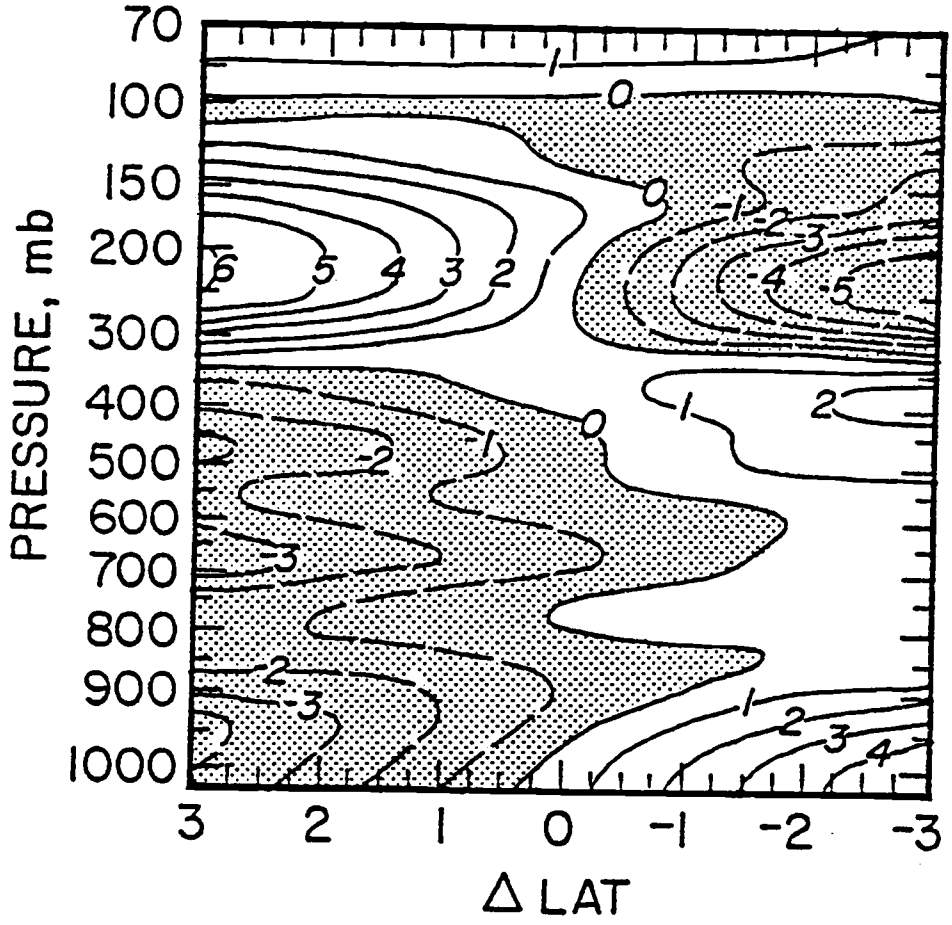

Figure 5.7. Meridional cross-section of the meridional velocity at mature stage through the composited cluster center. Units are m/s; contour interval is 1 m/s.

the upper layer. At the 400 mb level to the north of the cluster center, there is now a relatively strong southerly acceleration.

If we attribute the momentum residuals as mainly due to the sub-grid scale contribution, which in this study means the contribution from the meso- or convective- scale effect, then some conclusions can be drawn from the present results. The most important conclusions are that in the growing stage, the mesoscale and cumulus scale effect tends to: 1) provide a vertically integrated net sink for westerly momentum and a net source for easterly momentum around the cluster center; 2) induce a convergent circulation in the lower layer; and 3) cause a relatively weak easterly acceleration in the upper layer around the center, enhancing the production of a large-scale vorticity couplet.

In the mature stage, the effects are to: 1) cause a layered vertical structure in the westerly (southerly) acceleration, in contrast with the growing stage; 2) induce a divergent circulation in the upper layer and maintain a vorticity couplet pattern; 3) maintain a convergent circulation in the lower layer, although weaker at this stage.

In the dissipating stage, the corresponding effects are to: 1) induce layered vertical structures; and 2) maintain a weaker divergent circulation aloft.

Although the composite result seems to indicate the importance of the cumulus momentum effect, the conclusions have to be examined with caution, since not every case included in the composite shows qualitatively the same result. For example, in the case of day

245, the momentum residual in the growing stage tends to provide a westerly momentum source to the system instead of the sink described here. However, the tendency to provide a net source or sink still exists.

5.2.3 The interpretation of the cumulus momentum effects

From the composite momentum budget results, the momentum residual pattern showed that the cumulus momentum effects were quite complicated. They certainly cannot be explained by a simple mixing theory or a Rayleigh drag formulation.

The divergent circulation caused by the momentum residuals is supported by the finding of Maddox et al. (1981) for middle latitude convective system. They analyzed the upper tropospheric momentum features during a period in which an intense mesoscale convective complex developed, and found large changes in the wind and geopotential height fields over a six hours interval. A divergent circulation associated with a mesohigh around the convective region was identified in the upper layer. Rotunno and Klemp (1982) used the concept of obstacle flow to illustrate this nonhydrostatic effect. They demonstrated through a linear theory that an axisymmetric updraft in a vertically sheared environment would result in a PGF aligned parallel to the shear vector. The direction of the momentum generated through this effect depends on the vertical wind shear. This relationship might be the cause of the differences of the five individual cases involved in the compositing process.

So it is hypothesized that the first contribution from the cumulus scale in modifying the upper troposphere large-scale momentum field is through the PGF induced by the mesoscale divergent outflows. The second contribution from the cumulus scale is the horizontally varying detrainment of environmental momentum by the convective cells. The process to generate this induced PGF deserves some explanation. It is postulated that the horizontal flow around the mesohigh at the upper layer resembles the flow around an obstacle. The interaction between the updrafts which are associated with the convective and mesoscale ascent, and the mean shear vector will produce a pressure gradient in the horizontal as demonstrated by Rotunno and Klemp (1982). This pressure gradient across the updrafts is in the direction of the environmental wind shear. In the GATE region, the vertical wind shears at the easterly jet level are mostly easterly, and easterly accelerations are thus produced by the cumulus induced pressure gradient effects. The mixing processes would tend to generate a relative maximum of westerly momentum within the center of cloud cluster. The combination of these two hypothesized effects could account for the momentum residuals pattern seen in the mature stage of the momentum budget computed on the cloud-cluster-scale.

Tollerud and Esbensen (1983) used this horizontally-varying vertically-mixing process to explain the role of cumulus clouds in the development of an observed vorticity couplet at upper levels. The concept involved in this mixing process is that the environment momentum is modified through the detrainment of the in-cloud

momentum, and the modification of the large-scale vorticity will result from spatial variations of this process. On the other hand, the diagnostic analysis of Cho and Cheng (1980) and others stated that the large-scale vorticity was modified directly through the detrainment of the in-cloud vorticity. The formulation of the cumulus dynamic effect based on this concept [as in Eq. (1.1)], however, is unable to explain the observed horizontal vorticity residuals. The concept of the detrainment of in-cloud vorticity is not physically sound, as pointed out by Tollerud and Esbensen (1984).

These two cumulus effects can also be used to interpret the results of Zipser et al. (1981) or LeMone (1983). The net cumulus momentum effect is the sum of the mixing process and the induced pressure effect. Whether the net cumulus momentum is down or against the mean vertical momentum gradient depends on the induced pressure effect. The mixing process alone will produce a down-gradient transport. The net transport, however, can be either way. It is found that a net increase of easterly momentum in the vertical column by the convective effects. This result is consistent with the estimation from the bulk aerodynamic formula. Easterly drag force is induced by the surface westerly flow.

Based on a vorticity budget study in the upper troposphere from the GFDL model, Sardeshmukh and Held (1984) argued that nonlinear advective process may be the mechanism needed to explain the required damping discussed in Holton and Colton (1972), instead of the cumulus momentum effect. They pointed out that the damping

term needed in Holton and Colton (1972) might be due to the adoption of a linear model in that study. If that model had nonlinearity, there would have been a much better vorticity balance. However, from the present study, the momentum residuals on the scale of the cloud cluster are too large to be ignored. The largeness of the momentum residuals suggests the importance of the cumulus scale motion. In the GFDL model, a bi-harmonic function is used to represent the sub-grid scale effects, both thermodynamically and dynamically. So the study by Sardeshmukh and Held (1984), instead of suggesting that cumulus effects were of secondary importance, should be interpreted as suggesting that the location of the cumulus mass flux is not important to the large-scale or planetary-scale dynamics. The bi-harmonic diffusivity in their study can still be interpreted as a representation of the cumulus effect; only the sporadic nature of the cumulus mass flux is removed.

In summary, the vertical mixing processes can only represent the cumulus effects vertically. The horizontally varying aspects of the mixing processes and the source/sink generated by the induced pressure gradient force may make a significant contribution to the large-scale momentum budget.

In the next Chapter I will examine how these horizontal momentum patterns affect the larger-scale energetics.

5.3 Kinetic energy budget results

The momentum budget results were presented in Sec. 5.2, where

the cumulus momentum effects were discussed on the basis of momentum budget residuals. In this section, the kinetic energy budget results will be presented. The consistency between the momentum residuals and the kinetic energy residuals will also be discussed.

The kinetic energy budget equation Eq. (5.5) may be rewritten as

$$\frac{\partial \bar{K}}{\partial t} = - \underset{\sim}{\bar{V}} \cdot \nabla \bar{K} - \bar{\omega} \frac{\partial \bar{K}}{\partial p} - \underset{\sim}{\bar{V}} \cdot \nabla \bar{\phi} + \bar{u} X + \bar{v} Y \qquad (5.6)$$

This equation states that the local change of kinetic energy is due to the processes of horizontal and vertical advection of kinetic energy, work done by the PGF and the sub-grid scale effects.

5.3.1 5 September 1974 cluster

Fig. 5.8 presents the five components of the kinetic energy equation in the growing stage through the cluster center for the 5 September case. The local change of kinetic energy increases in the upper layer and decreases in most of the lower layer. A large decrease of kinetic energy appears at the easterly wave level. Horizontal advection of kinetic energy is quite large at 150 mb and is a source of the kinetic energy increase at that layer; while the contribution is quite small and negative in the middle layer. The major effect of vertical advection of kinetic energy is a kinetic energy sink at 700 mb, associated with the strong easterly wave motion. The work done by the PGF is generally one order of magnitude larger than the advective processes. The kinetic energy

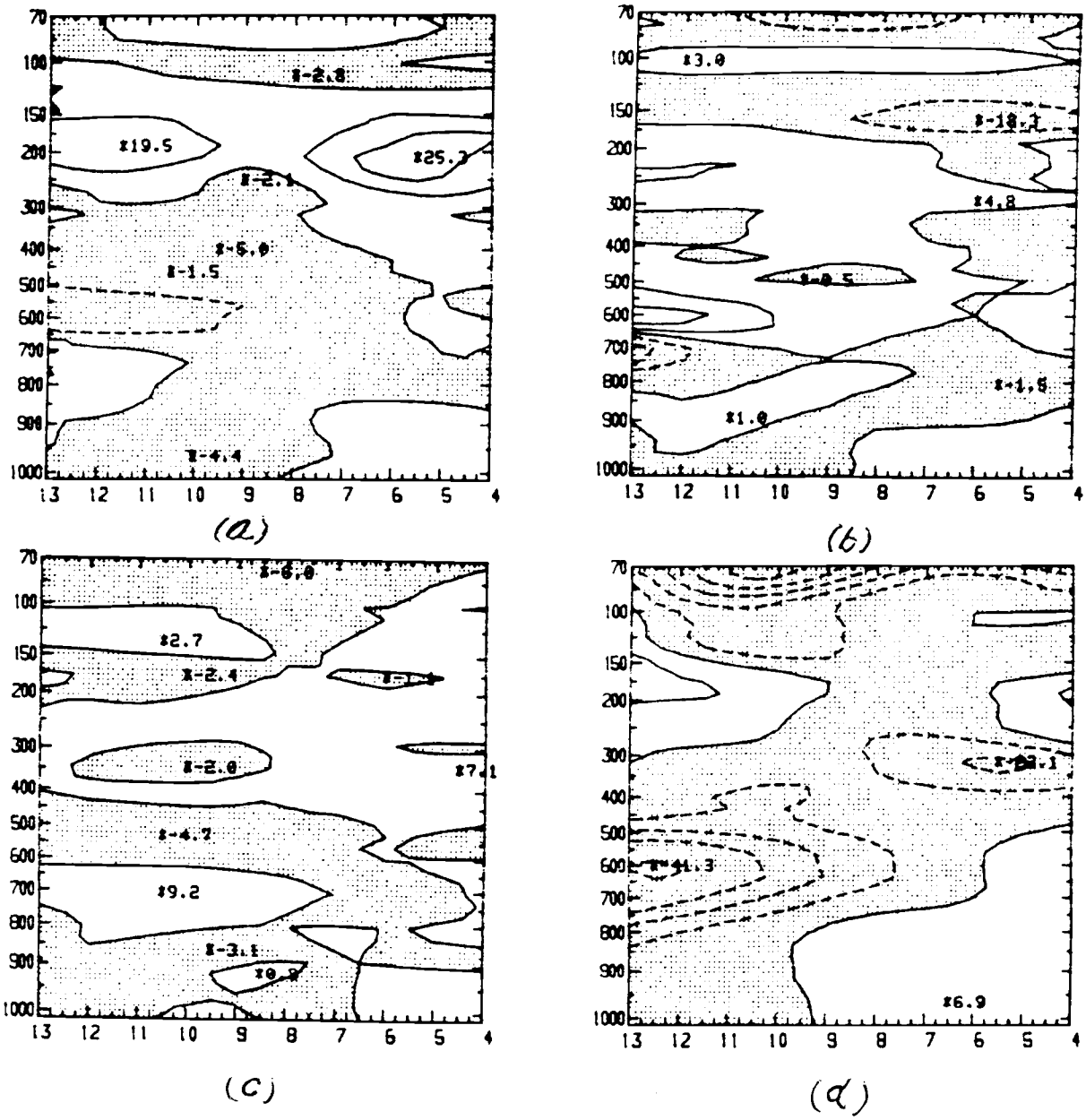

Figure 5.8. Meridional cross-section of kinetic energy budget components through the center during the growing stage of 5 September cluster. (a) the local change term, (b) the horizontal advection ($\bar{v}\cdot\bar{\nabla}\bar{k}$), (c) the vertical advection ($\bar{\omega}\,\partial\bar{k}/\partial p$), (d) the work done by pressure gradient force ($-\bar{v}\cdot\bar{\nabla}\bar{\phi}$), (e) the kinetic energy residuals. Units are $10^{-4}\,m^2/s^3$; contour interval is $10^{-3}\,m^2/s^3$.

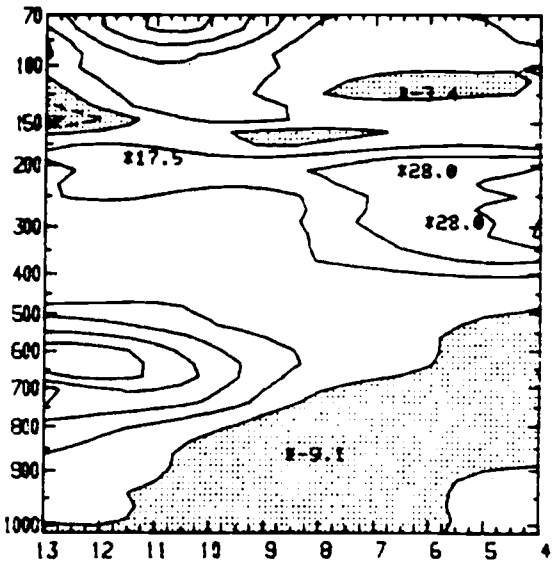

(e) the ke residual

Figure 5.8 (continued)

decreases in the middle troposphere through this ageostrophic process. In the southern part of the lower layer and northern part of upper layer, the contribution from this ageostrophic process is to increase the kinetic energy.

The residual of the kinetic energy budget, which may be regarded as the contribution from sub-grid scale processes, contributes to the increase of kinetic energy in the upper layer. That means the kinetic energy on the scale of clusters is increased by sub-grid scale processes. In the lower layer, the sub-grid scale processes cause consumption of kinetic energy from the surface up to the 600 mb level. At 700 mb the maximum contribution to the increase of kinetic energy is on the order of $30*10^{-4}$ m^2/s^3 to the north of the cluster center. In short, the major balance of the kinetic energy in this stage is the destruction of kinetic energy through the cross-isobaric flow (the work done by the PGF) and the supply of kinetic energy to the system through the sub-grid scale processes; advective processes play only a secondary role in the vicinity of the cluster. The advective processes, however, are on the same order of magnitude as the other processes in the upper layer. The tendency for large kinetic energy increases in the upper layer to the south of the center is mostly due to the horizontal advective process.

In the mature stage, Fig. 5.9 reveals that there has been a large decrease of kinetic energy over the northern part of the array, with an increase of kinetic energy to the south in the upper layer. A large increase of kinetic energy is also found at the

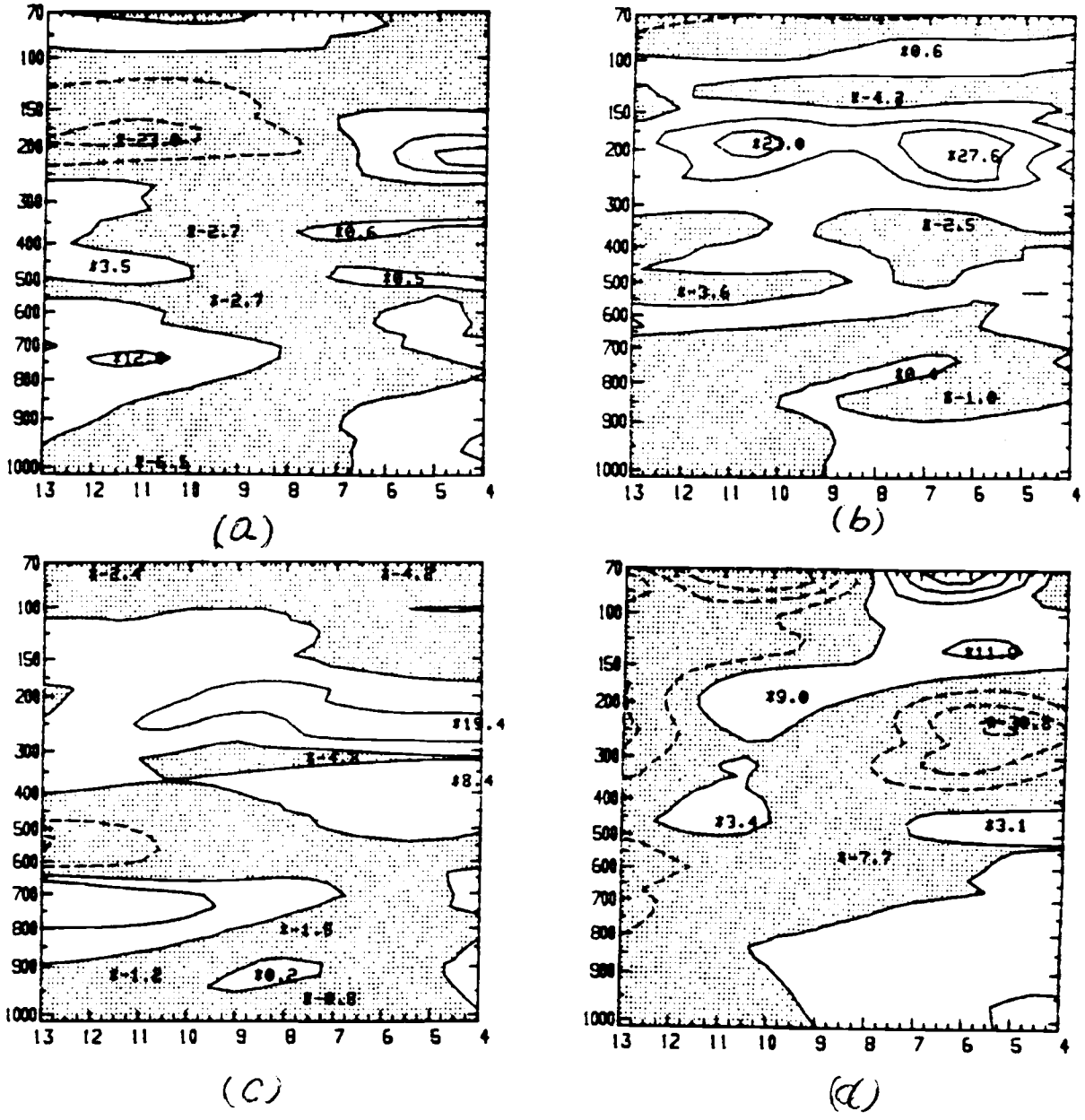

Figure 5.9. As in Fig. 5.8 except for the mature stage.

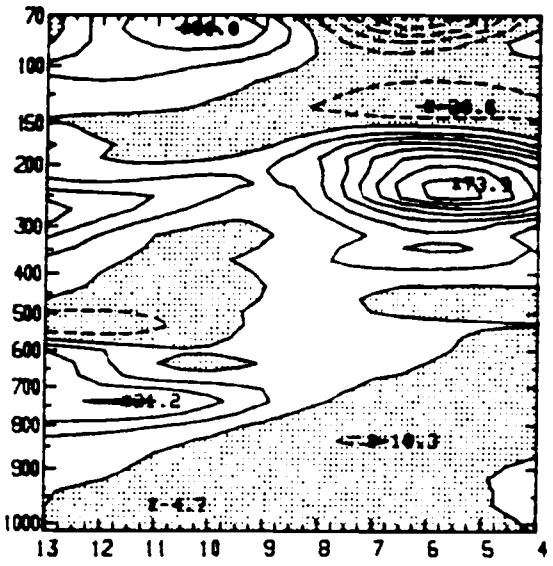

(e) the ke residual

Figure 5.9 (continued)

easterly wave level. Horizontal advection in the upper layer tends to decrease the kinetic energy with maxima to the north and south of the cluster center. The contribution from vertical advective processes is large only at the easterly wave level and constitutes a sink of kinetic energy for the upper layer. The kinetic energy tends to decrease through cross-isobaric processes in the upper layer to the south of the cluster center and to increase in a small area to the north of the cluster center. The situation is reversed in the lower layer with kinetic energy decreasing (increasing) to the north (south) of the center. The contribution at the easterly wave level is much weaker, but stronger in the upper layer to the south in comparison with the growing stage results. Again the sub-grid scale processes supply kinetic energy to the system, with the largest contribution in the upper layer with another maximum near the 750 mb level. The surface and lower layer acts as a kinetic energy sink for cloud-cluster-scale motion.

In the dissipating stage (Fig. 5.10), the magnitude of local kinetic energy change is smaller than in the mature stage, even though a relatively large tendency of change is still evident in the upper layer. Advective processes are a sink of kinetic energy for the upper layer. The cross-isobaric process at this stage is an energy source, instead of the energy sink found in the previous stage. The sub-grid scale processes still act, but with a smaller magnitude. The upper layer, however, still shows a kinetic energy source form the sub-grid scale process. In only a small region near 600 mb is kinetic energy decreased through these process.

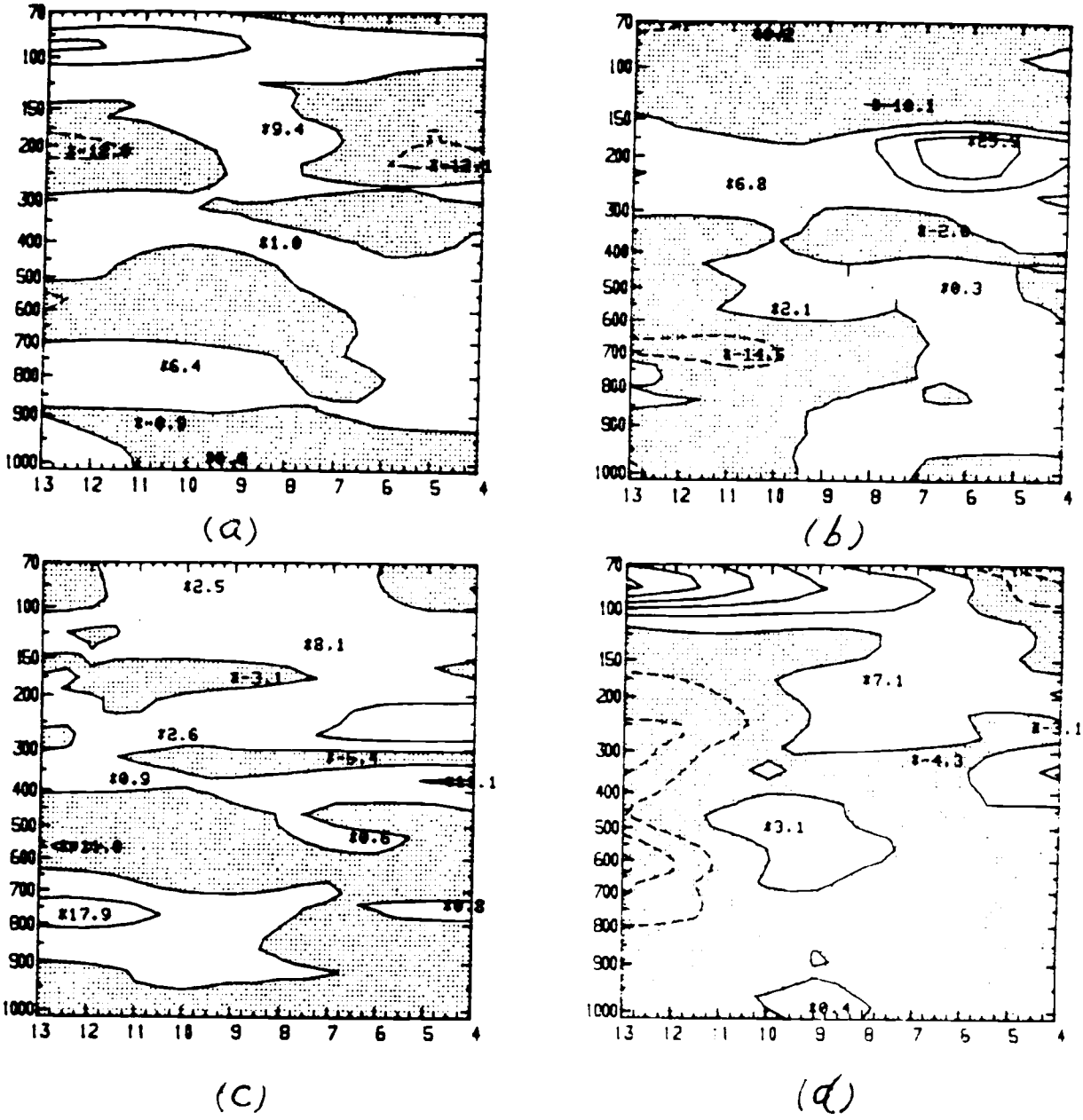

Figure 5.10. As in Fig. 5.8 except for the dissipating stage.

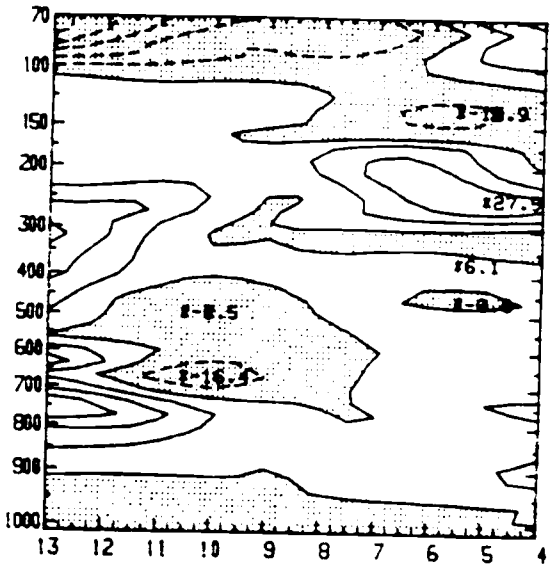

(e) the ke residual

Figure 5.10 (continued)

Since the kinetic energy budget was computed by multiplying the momentum budget quantities by the environmental wind fields, the directional dependence of the kinetic energy budget quantities must have significant differences in different convective cases. Thus no attempt is made to study the composite kinetic energy budget.

Although only a single kinetic energy budget is presented here, the kinetic energy residuals pattern is quite consistent with the physical processes implied by momentum residuals. These aspects will be discussed further in the next Section.

5.3.2 Discussion

As suggested in Sec. 5.2.3, the cumulus momentum effects might be hypothesized as 1) the vertical mixing process, and 2) the induced PGF. The kinetic energy residuals computed here are consistent with these proposed mechanisms. From the mixing process viewpoint, the momentum is transported in the direction to reduce the mean wind shear. In the 5 September case, the vertical shear is dominated by easterly flow. Thus, the westerly momentum has to be transported upward as dictated by the mixing process. By multiplying the momentum residual generated by mixing process by the environmental wind, the upper (lower) layer should be a kinetic energy sink (source). That is to suggest that by the vertical mixing process, the kinetic energy is transported downward to compensate the surface kinetic energy dissipation.

However, as indicated in Sec. 5.2.3, one must consider the

contribution from the nonhydrostatic PGF induced by convective scale motion in evaluating the kinetic energy residuals. From the momentum budget of 5 September case, we deduced that the non-hydrostatic pressure effect would generate an easterly acceleration, and hence be a kinetic energy source in the upper layer. The combination of these two effects produced a kinetic energy source in the upper layer.

So the net sub-grid scale processes in the upper layer of this event are an up-scale transport processes, which means the kinetic energy is moved from the sub-grid scale to the grid scale. Fuelberg and Jedlvec (1982) studied the kinetic energy budget in mid-latitude for a meso-α scale convective event. They found the vertically integrated area-averaged dissipation is a positive quantity, which implied the up-scale transport of kinetic energy.

A different horizontal scale for the compositing would lead to different conclusions on the effects of sub-grid processes. A kinetic energy budget constructed by Frank (1983a) in the eastern Atlantic ITCZ on the scale of ITCZ revealed that strong generation of kinetic energy through the work done by the pressure gradient force occurred below 900 mb south of the maximum convection. Flow up the pressure gradient (consuming the kinetic energy of the system) was found in the upper troposphere on the northern portion of the maximum convection. No evidence of major generation of kinetic energy by subgrid scale processes on the scale of ITCZ composite was found. The residual effect caused a net sink of kinetic energy.

Other studies using synoptic scale data found that the dissipation of kinetic energy through the sub-grid scale process is the most common feature of the kinetic energy budget (Robertson and Smith, 1980; Newell et al., 1972). Thus, the time scale of the disturbances have a great impact to the large-scale momentum fields. Present study of the sub-grid scale effects is focussed on the scale of cloud cluster, the up-scale transfer of kinetic energy by sub-grid scale processes being regarded as a characteristic feature. More discussion on this aspect will be presented in the next Chapter.

CHAPTER 6. NUMERICAL MODELING OF THE CUMULUS MOMENTUM EFFECT

6.1 General description

Chapter 5 has discussed the momentum and kinetic energy budgets on the cloud-cluster-scale in the GATE region. The momentum budget at the mature stage of the cloud-cluster life cycle showed that large momentum budget residuals were found at lower and upper levels. The vertical structure of the residual fields in the mature stage through the cluster center should be a relatively large (small) westerly momentum sink in the lower (upper) levels. At the upper levels, the horizontal structure of the momentum residuals revealed that there was a relative maximum of westerly acceleration around the cluster center and a southerly (northerly) acceleration toward the north (south) of the cluster center.

These residual structures tend to generate a vorticity couplet pattern having positive (negative) vorticity to the north (south) of the cluster center, while the southerly (northerly) momentum budget residual would generate a divergent circulation around the cluster center; this is consistent with the vorticity residuals computed by Tollerud and Esbensen (1983). The horizontal structure of the residual fields at the upper level suggests that meso-scale and cumulus scale circulation are important in influencing the large-scale momentum budget.

The divergent circulation caused by the momentum residuals were supported by the findings of Maddox et al. (1981). They analyzed the upper troposphere momentum features during a period

when an intense mesoscale convective complex developed and found strong changes in the wind and geopotential height fields over a six-hour interval. A divergent circulation associated with a mesohigh around the convective regions was identified. They hypothesized that the convective system was responsible for these changes. Present results seem to be consistent with that hypothesis. The contribution of the meso-scale or convective scale features to the environmental momentum field may thus be needed in parameterization schemes for large-scale dynamical models.

It was hypothesized in Chapter 5 that the cumulus momentum contributes to the larger-scale environment through two effects. They are the horizontally varying mixing process and the induced pressure gradient. It is desirable to formulate an exact form of these cumulus momentum effects for the inclusion in the large-scale model.

The recent study by Sardeshmukh and Held (1984), however, has given a new perspective on the cumulus momentum problem. As stated in Chapter 5, based on a vorticity budget study in the upper troposphere from the GFDL model, Sardeshmukh and Held (1984) argued that nonlinearity may be the potential mechanism needed for the required damping discussed in Holton and Colton (1972), instead of the cumulus momentum effect. They pointed out that the damping term needed in Holton and Colton (1972) might be due to the adoption of a linear model in that study. If that model had nonlinearity, there might have been a much better balance.

But the study by Sardeshmukh and Held (1984) is not conclusive. In the GFDL model, a bi-harmonic function is used to represent the sub-grid scale effects, both thermodynamically and dynamically. Instead of suggesting that cumulus effects are of secondary importance, their results may simply show that the sporadic nature of the cumulus mass flux is not important to the large-scale or planetary-scale dynamics. The bi-harmonic diffusivity can still be interpreted as a representation of the cumulus effect, with the sporadic nature of the cumulus mass flux removed.

It was also suggested that the kinetic energy source in the upper troposphere generated by the momentum residuals can be explained physically by the hypothesized cumulus momentum effects. This indicates an up-scale transfer of the kinetic energy is acting within the cloud cluster system. This result for the kinetic energy budget also supports the hypothesis by Gage (1979) and Lilly (1983), in which they stated that the small scale convective forcing is responsible for the setting up of the mesoscale wavenumber energetics through the up-scale transfer embedded in the two-dimensional turbulence dynamics. It is interesting therefore to understand the large-scale response to the hypothesized cumulus momentum forcing, and whether the sporadic nature of the cumulus mass flux will make a difference in affecting the large-scale momentum field.

The issue may come down to asking the following question. What are the physical mechanisms by which convective systems affect the large-scale momentum fields. There are at least two different

routes to approach the cumulus momentum problem. One way is to diagnostically determined a proper mathematical form to represent the cumulus momentum effects and to verify the formulation through observational studies. Another approach is to understand fundamentally the interaction of the cumulus cloud and their environment. Within these two categories, several different methods can be adopted. In this Chapter, the latter approach will be followed to further study the cumulus dynamical effect on the large-scale environmental fields.

In this Chapter, I will develope a simple numerical model to study the scale interaction problem. The cloud detrainment/ entrainment processes will be regarded as a representation of the sub-grid scale contribution to the large-scale upper tropospheric flow. The cloud activity associated with the deep convection is quite complicated and behaves in a three dimensional manner. In such a complicated system, it would be difficult to represent all aspects of the sub-grid scale momentum effect upon the large scale flow. Instead of constructing a complicated model, a dynamically simple model will be used.

A two-dimensional barotropic nondivergent model is chosen to investigate the cumulus momentum effect on the large-scale flow. The dynamical mechanism involved in this simple model is the horizontal nonlinear interaction process. The two-dimensional nonlinear upscale cascade process was proposed as a mechanism to set up the planetary scale wavenumber energetics through the synoptic baroclinic unstable wave forcing by Kraichan (1967). A

similar perspective has been adopted by Gage (1979) and Lilly (1983). The observed mesoscale kinetic energy spectrum shows a $K_h^{-5/3}$ law (where K_h is the wavenumber). One of the hypotheses postulated to explain this $K_h^{-5/3}$ law is the upscale transfer of kinetic energy by two-dimensional turbulence. The small scale sporadic horizontal forcing needed to establish that relationship is hypothesized as coming from convective events.

Before discussions of the objectives of this Chapter, some related topics concerning the mesoscale energy spectrum and a review of the two-dimensional turbulence will be presented.

6.1.1 Mesoscale spectrum

The statistical structure of atmospheric variables has been observed and studied rather extensively for large scales (planetary and synoptic scales) and more selectively for scales of a few kilometers and less. The mesoscale range from a few to about a thousand kilometers in wavelength has been somewhat neglected, due to the scarcity of appropriate measurement techniques. From the mid 1970's, however, aircraft data of appropriate quality have been available to help fill this gap. A variety of observational evidence leads to the conclusion that much more mesoscale energy exists than predicted by the decay of geostrophic turbulence. A spectral slope of $K_h^{-5/3}$ has been suggested by various researchers (Vinnichenko, 1970; Brown and Robinson, 1979; Gage, 1979). Recently, Balsley and Carter (1982) have found from Doppler radar measurements further evidence of a well-defined $K_h^{-5/3}$

range in both the troposphere and the mesosphere. Lilly and Petersen (1983) and Nastrom and Gage (1983) carried out spectral analyses of the horizontal velocities measured by commercial aircraft. Fig. 6.1 from Lilly and Petersen (1983) shows the horizontal energy spectra over the wavelength range from 5 km to the earth's circumference. A power spectrum with a $K_h^{-5/3}$ slope for the spatial scale ranging from 100 km to about 400-700 km can be identified.

As suggested by Lilly (1983), a possible explanation for the observed mesoscale spectrum is simply that the net effects of a variety of intermittent mesoscale phenomena, such as large mountain waves, squall lines, sea breezes, mesoscale convective complexes, etc., produce it somewhat accidentally. Van Zandt (1982) suggested that the atmospheric spectrum is produced largely by internal gravity and inertial-gravity waves. Gage (1979) proposed, however, that the atmospheric mesoscale kinetic energy spectrum is produced by the upscale transfer of small-scale turbulence through the energy transfer processes originally proposed by Kraichnan (1967) for two-dimensional flow. By this process, a $K_h^{-5/3}$ spectrum develops for wavenumbers smaller than those being forced.

6.1.2 Brief review of 2-D turbulence theory

Several theoretical models have been used to describe the behavior of atmospheric turbulence. These include the three-dimensional inertial range model ($K_h^{-5/3}$ law), the two-

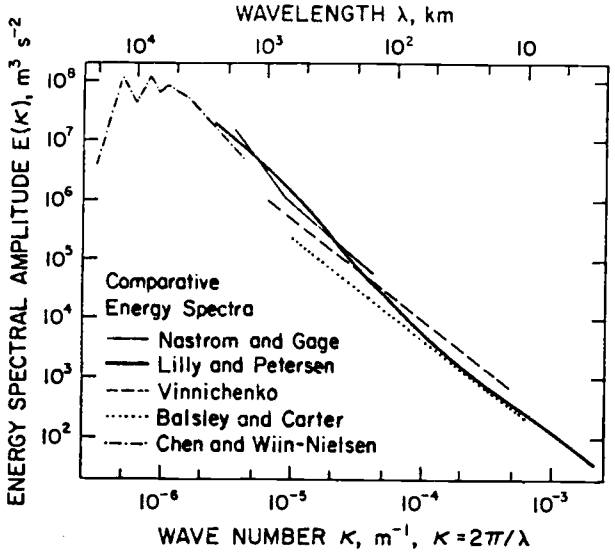

Figure 6.1. Horizontal energy spectra over the wavelength range from 5 km to the earth's circumference (from Lilly and Peterson, 1983).

dimensional energy inertial range ($K_h^{-5/3}$ law), and the two-dimensional enstrophy inertial range model (K_h^{-3} law).

The three-dimensional inertial range theory is the original theoretical model considered by Kolmogoroff (1941) to describe the statistical small-scale behavior of locally isotropics homogeneous turbulence. Its relevance is limited to spatial scales typically on the order of 100 m or less.

Theoretical studies of two-dimensional turbulence (Kraichnan,-1967; Leith, 1968) have shown that a source of energy and enstrophy isolated at wavenumber Ki leads to a wavenumber spectrum with a discontinuity at K_i. For $K \ll K_i$, energy is cascaded to smaller wavenumbers (large spatial scale), while for $K \gg K_i$, enstrophy is cascaded to larger wavenumbers (smaller spatial scale). The net result is a spectrum with $K_h^{-5/3}$ behavior at the lower wavenumber end and K^{-3} behavior at higher wavenumber. These theoretical expectations were confirmed numerically by Lilly (1969, 1972) in a two-dimensional numerical model. Observations (Wiin-Nielsen, 1967; Julian et al., 1970; Chen and Wiin-Nielsen, 1978) indicate an approximate K_h^{-3} dependence of the kinetic energy on the longitudinal wavenumbers roughly between 10 and 30 (wavelengths between 1000 and 3000 km). In applying the two-dimensional turbulence theory to the atmosphere from the large-scale end, injected forcing at longitudinal wavenumber 6 (which presumably is provided by the baroclinic instability as a continuous source of energy and enstrophy) will generate a kinetic energy spectrum of K_h^{-3} for the wavenumbers larger than 6. This is a

plausible explanation for the large-scale atmospheric spectrum in the wavelengths between 1000 and 3000 km.

Charney (1971) investigated the characteristic of three-dimensional quasi-geostrophic flow and concluded that all the theorems pertaining to energy exchange among spectral components in two-dimensional flow may be applied to three-dimensional quasi-geostrophic flow as well, and in that case (geostrophic turbulence) it is the geostrophic constraint, not the two-dimensionality, that prevents the downscale energy cascade.

In the limit of a purely two-dimensional cascade, energy accumulates at the lowest possible wavenumber, i.e, eddies grow to the size of the domain. Such an end state does not occur when surface drag (Lilly, 1972) or planetary wave propagation (Rhines, 1975) also operate. The planetary scales are strongly modulated by these processes.

6.1.3 Gage's hypothesis

There are two formal inertial ranges discussed in the work of Kraichnan (1967) concerning the two-dimensional turbulence theory. Attention has been focused on the K_h^{-3} law enstrophy range, and substantial evidence had been provided for the relevance of the K_h^{-3} law on the planetary and synoptic scales.

For the mesoscale or the intermediate scale, evidence showed the existence of a $K_h^{-5/3}$ law range. That lead Gage (1979) to propose that the horizontal kinetic energy spectrum at mesoscale wavelengths was produced by upscale energy transfer through quasi-

two-dimensional turbulence. And the source of the forcing was related to the small scale where microscale turbulence was generated. In his view, microscale turbulence was usually thought to lose its energy by dissipation by means of a three-dimensional cascade of energy into the higher wavenumber end of spectrum. However, the existence of a $K_h^{-5/3}$ law inertial range extending to the mesoscale implied that some of the microscale turbulent kinetic energy is being cascaded to lower wavenumbers as predicted by the upscale cascade of two-dimensional turbulence theory.

Lilly (1983) reexamined Gage's hypothesis and suggested that the principal source associated with the forcing in creating the mesoscale spectrum can be found in decaying convective clouds and thunderstorm anvil outflows. Following the scale analysis by Riley et al. (1981), he argued that in the presence of strong stratification, initially three-dimensional isotropic turbulence divides roughly equally into gravity waves and stratified (quasi-two-dimensional) turbulence. The former then propagates away from the generation region on the time scale of (1/buoyancy frequency), while the latter propagates in spectral space to larger scales, forming the $K_h^{-5/3}$ upscale transfer spectrum predicted by Kraichnan. Part of the energy of the stratified turbulence is recycled into three-dimensional turbulence by shearing instability, but the upscale escape of only a few percent of the total energy released by convective activity is apparently sufficient to explain the observed mesoscale energy spectrum of the troposphere.

6.1.4 The proposed experiments

As we know, convective activity is usually associated with full three dimensional disturbance. A primitive system is necessary in order to investigate the interaction between the large-scale and cumulus scale motion. However, as suggested by Lilly (1983), an initial three-dimensional turbulence will become stratified turbulence when the faster time scale of gravity waves disperse some of the perturbation energy away and leave the quasi-two-dimensional motion behind. Stratification plays an important role in modifying the inertial range spectrum. The existence of the stratification creates a buoyancy subrange within the inertial range spectrum distribution. At this moment, we are only concerned with the effects of the cumulus momentum associated with the quasi-two-dimensional motion on the large-scale environment flow. It is in this context that a numerical model is constructed. The system chosen for the study is a barotropic non-divergent system.

The scale interaction processes investigated by this barotropic non-divergent system are limited by its dynamical mechanism. The dynamical mechanism contained in this system is the nonlinear interaction process between different scales. The situation envisioned here is that in the tropical upper troposphere, where deep cumulus activity is abundant and the stratification is large, the convective cloud detrainment process dominates the momentum budget (as indicated by cumulus momentum residuals in Chapter 5). What is the large-scale response with respect to this large momentum forcing in a system which has only one simple

dynamical mechanism? Does the sporadic nature of convective mass flux will make any difference to the large-scale dynamics compared to a parameterized quasi-equilibrium form of convective mass flux?

6.2 The barotropic non-divergent vorticity equation

The barotropic non-divergent vorticity equation is used to study the large-scale response to with respect to cumulus momentum forcing. The equation may be written as

$$\frac{\partial \zeta}{\partial t} = - \underset{\sim}{V} \cdot \underset{\sim}{\nabla} \zeta - \beta v + F + \nu \underset{\sim}{\nabla}^2 \zeta \qquad (6.1)$$

$$\underset{\sim}{V} = u \underset{\sim}{i} + v \underset{\sim}{j} = - \frac{\partial \psi}{\partial y} \underset{\sim}{i} + \frac{\partial \psi}{\partial x} \underset{\sim}{j} \ , \quad \zeta = \underset{\sim}{\nabla}^2 \psi$$

where ζ is the vorticity and is equal to two-dimensional Laplacian of a stream function ψ, $\underset{\sim}{V}$, β, ν, are the horizontal velocity, the gradient of Earth vorticity and the viscosity coefficient. F is the vorticity forcing function (actually the curl of an applied force per unit mass). This applied force represents a momentum effect from a given scale of disturbance, and will be set up so as to represent the cumulus momentum effect.

Lilly (1969) used the same set of equations to study the planetary scale wavenumber spectra, with the forcing F constructed to represent synoptic-scale disturbances. Since the present study has some aspects similar to the study of Lilly (1969), this section will review Lilly's experiment which focussed on the planetary scale aspects of the problem. Sec. 6.3 and Sec. 6.4 will focus on the cumulus scale forcing as proposed in Sec. 6.1.4.

6.2.1 Lilly's experiment

Lilly's studies focused on the relationships between the planetary wavenumber spectrum and the synoptic scale forcing. A rectangular domain of 64 by 64 points was used by Lilly, which allows Fourier components up to wavenumber 32 in each direction. Time integration was performed by the second order Adams-Bashforth scheme. The numerical space-differencing method used for the nonlinear term of Eq. (6.1) was the second order scheme developed by Arakawa (1966). The boundary conditions are chosen to be cyclic in both x and y directions. Initially the fluid was at rest. The continuous forcing was constructed from a randomly varying set of Fourier modes lying within a narrow spectral band near a chosen scalar wavenumber K_e. The solution of the Poisson equation for the stream function is performed by a fast Fourier transform method [see Lilly (1969) for more detail].

Our method essentially follows Lilly's formulation and procedures, except that a different algorithm is used in solving the Poisson equation. Fig. 6.2 shows one example of the vorticity forcing field at a given scalar wavenumber 8. Forcing is continuously injected into the domain by setting the mean amplitude of the forcing constant and allowing the phase and Fourier component structure to vary randomly with time (see Appendix B for more model detail).

In the early stages of the integration, there is a linear growth of an almost monochromatic field with slight viscous damping. After some time, the nonlinear terms become dominant and

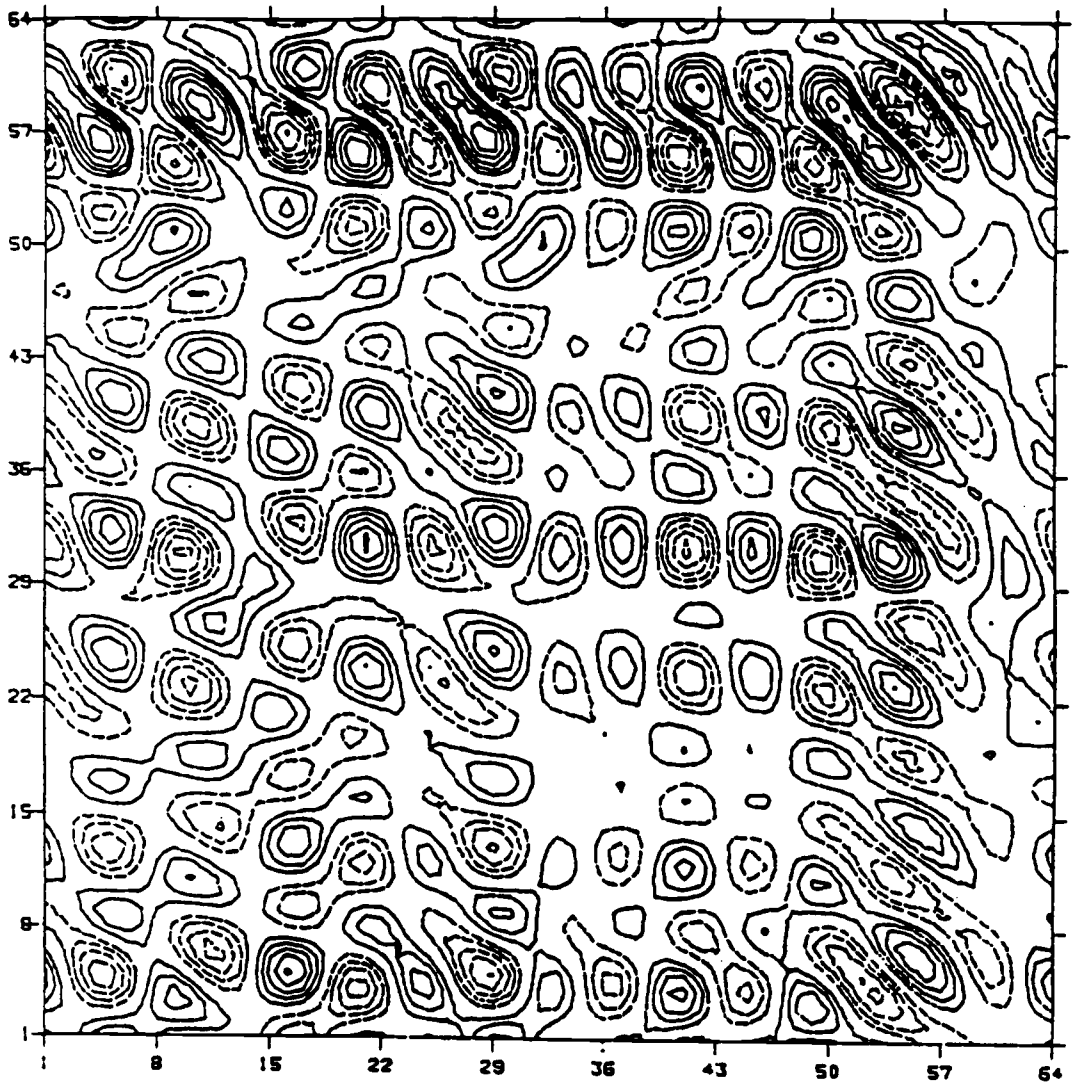

Figure 6.2. One example of the forcing field in Lilly's experiment (wave number 8 forcing in this case).

rapid energy dispersion in wave-number space occurs. Fig. 6.3 presents the kinetic energy spectrum at every 400 time steps up to the 2800th time step. Initially, there is no motion, energy is injected through a specified scalar wavenumber (K_e = 8 in this experiment). At the 400th time step, although energy dispersion in wavenumber space is occurring, the dominant mode still is at the forcing scale. As time increases, the smaller wavenumbers increase their kinetic energy dramatically. At the 2800th time step, wavenumber 1 dominates. Two distinct spectral ranges exist and are separated by the wavenumber of the forcing. The kinetic energy spectrum for large wavenumbers becomes virtually saturated after the 400th time step. In Fig. 6.4 we see that a clear wavenumber 1 pattern is manifested by the 2800th time step. This is the lowest mode possible in the system, although the particular cell orientation is arbitrary.

Fig. 6.5 shows the vorticity field at the 2800th time step. The small scale vorticity fields dominate. These numerical results are consistent with the prediction postulated from the two-dimensional turbulence theory.

6.2.2 The boundary conditions and beta effect

This section will examine the effects of boundary conditions and beta effects on the simulation results. Cyclic boundary conditions in x and y directions are used in Lilly's experiment. Fig. 6.6 shows the kinetic energy spectrum for an experiment exactly the same as the one in Sec. 6.2.1 except that a no normal flow boundary

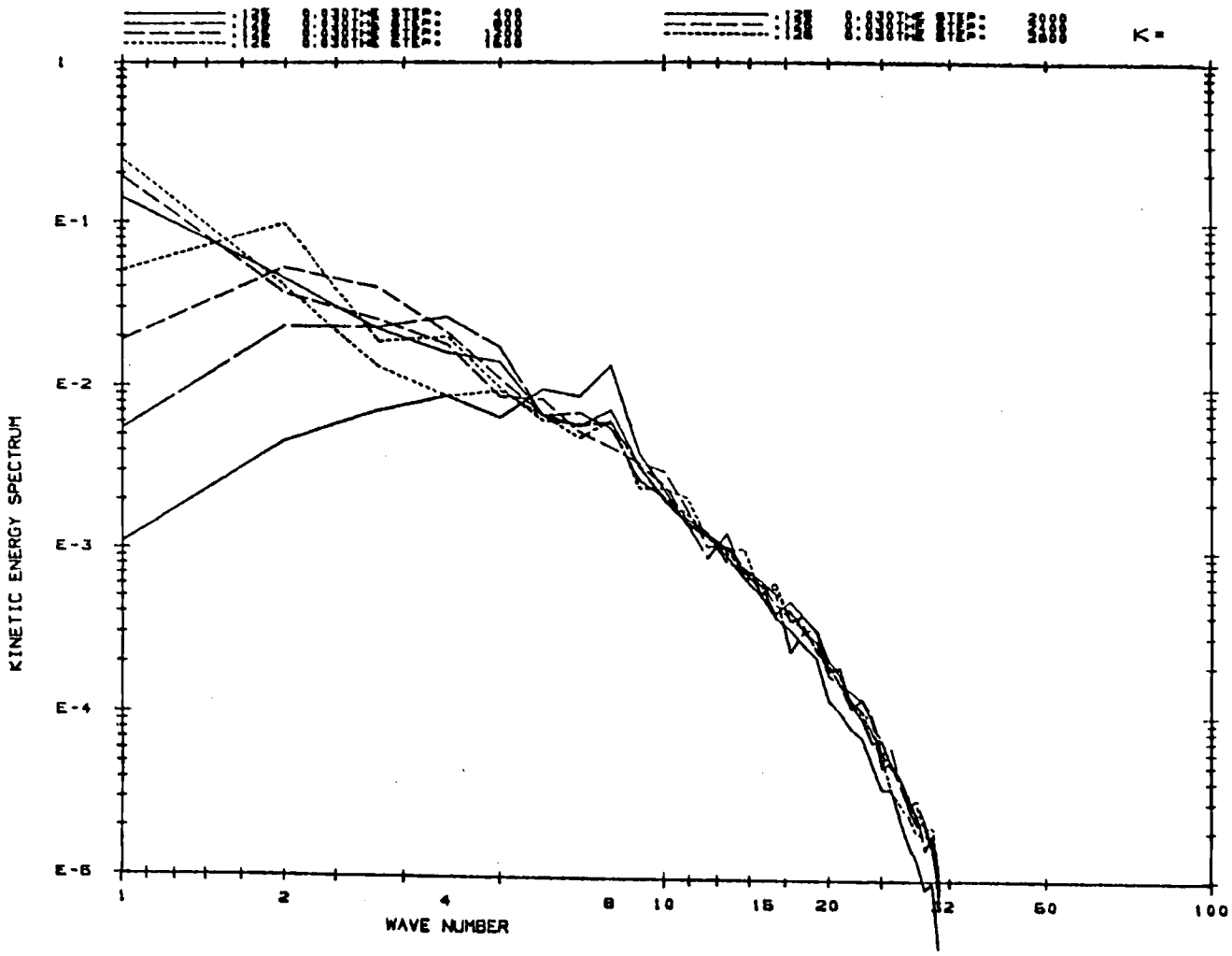

Figure 6.3. The kinetic energy spectrum in various stages of the integration with random forcing and cyclic boundary condition.

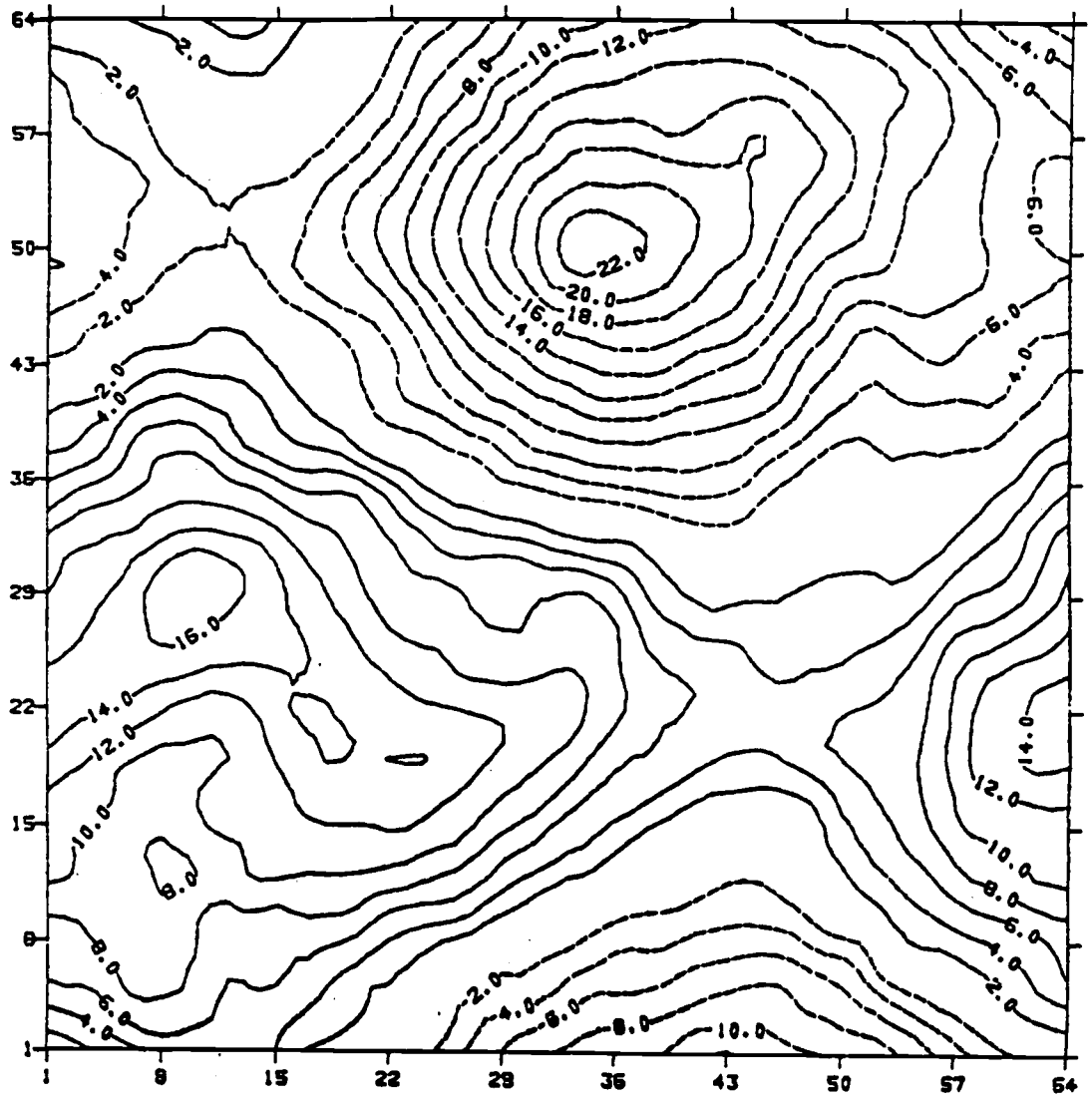

Figure 6.4. The stream function at the 2800th time step of the integration with random forcing and cyclic boundary condition.

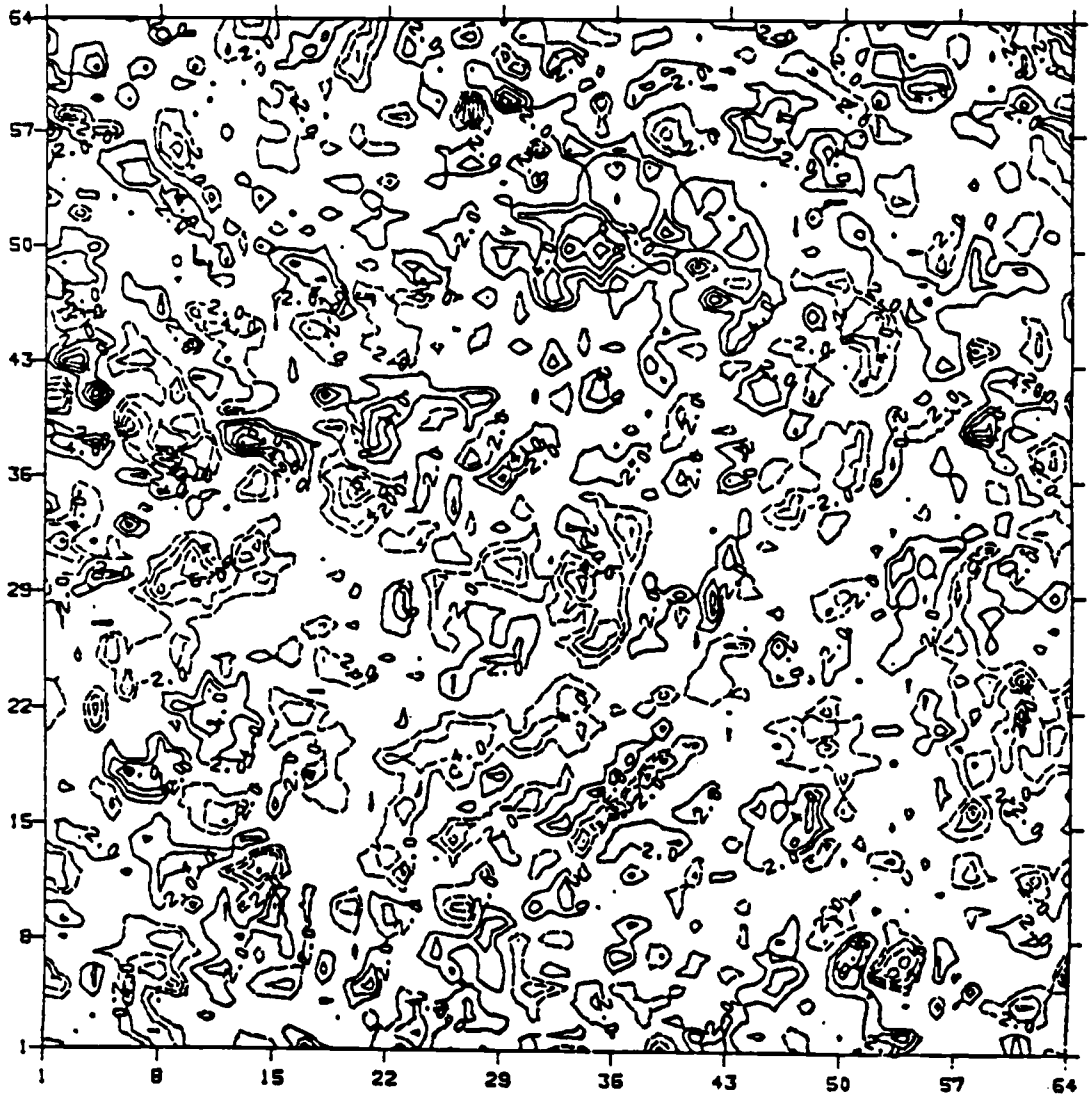

Figure 6.5. As in Fig. 6.4 except for vorticity field.

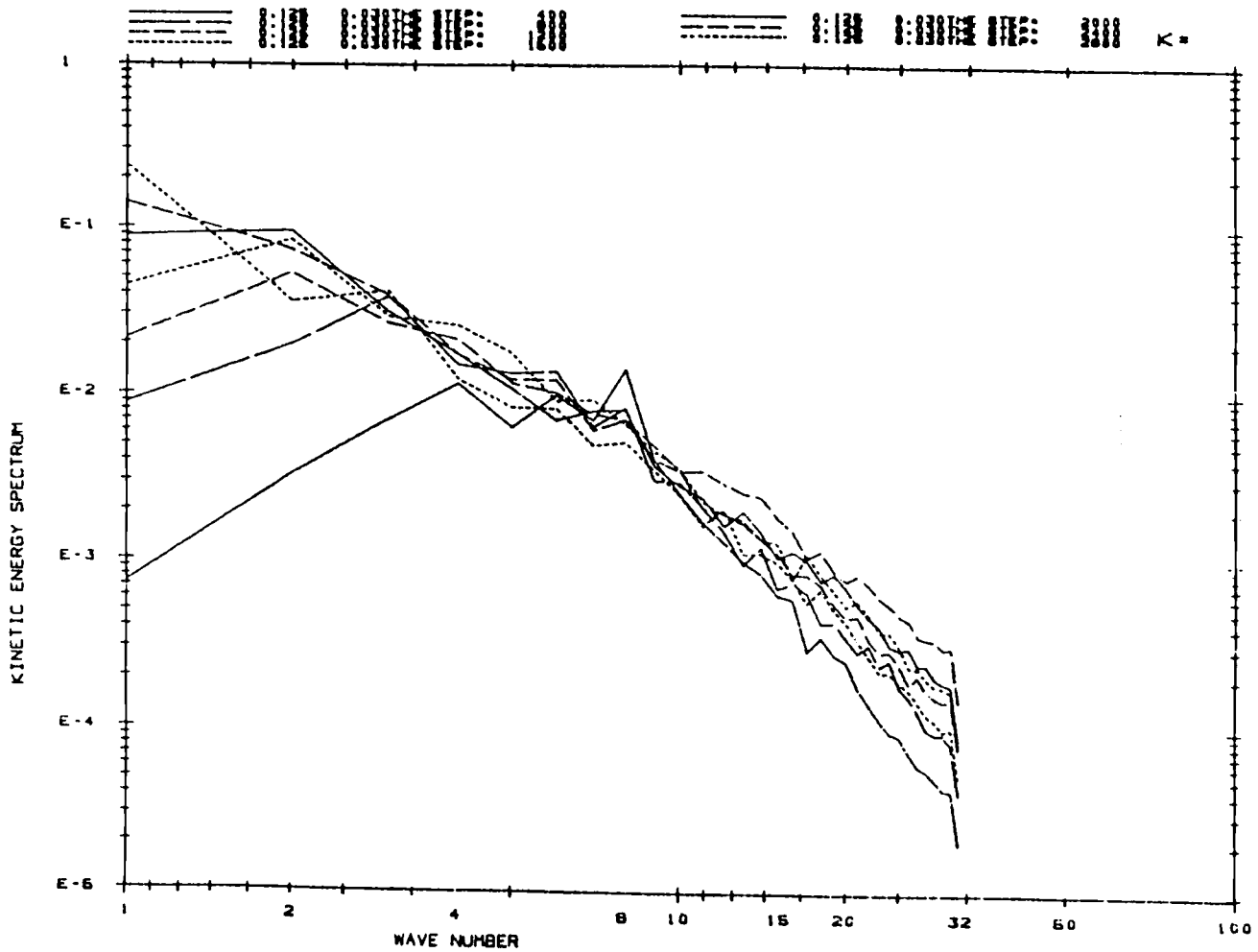

Figure 6.6. As in Fig. 6.3 except for the fixed N-S boundary condition.

condition is imposed on the N-S boundary instead of a cyclic condition. The kinetic energy spectrum at smaller wavenumbers is similar to that in Fig. 6.2. At the large wavenumber end, however, the kinetic energy is more spread to the large wavenumber end as time progresses. This effect might be caused numerically by the false reflection of shorter waves at the solid boundary as pointed out by Matsuno (1966). Figs. 6.7 and 6.8 show the stream function and vorticity field at the 2800th time step.

Rhines (1975) showed that the β effect strongly modulates the processes of upscale energy cascade on the planetary scale. Fig. 6.9 is the kinetic energy spectrum of a dimensional run with the β effect (dx = dy = 50 km, dt = 1000 second, $\beta = 1.1*10^{-11}/(m*s)$, in a 64 by 64 grid). The upscale transfer of kinetic energy is limited by the balance between two-dimensional energy cascade and the Rossby wave dispersion below a critical wavenumber. The dispersive character of the Rossby waves inhibits the nonlinear transfers in the sense that the wave packets disperse energy before the nonlinearity dispersion becomes important. Fig. 6.10 shows the stream function at the 2800th time step. A wavenumber 2 or 3 pattern dominates, rather than the wavenumber 1 pattern shown in Figs. 6.2 and 6.7.

6.2.3 The effect of initial flow

The kinetic energy equation derived from the two-dimensional nondivergent vorticity equation is

$$\frac{\partial}{\partial t} K = \iint - \psi F \, dA - \iint \psi \nu \nabla \zeta \, dA \qquad (6.2)$$

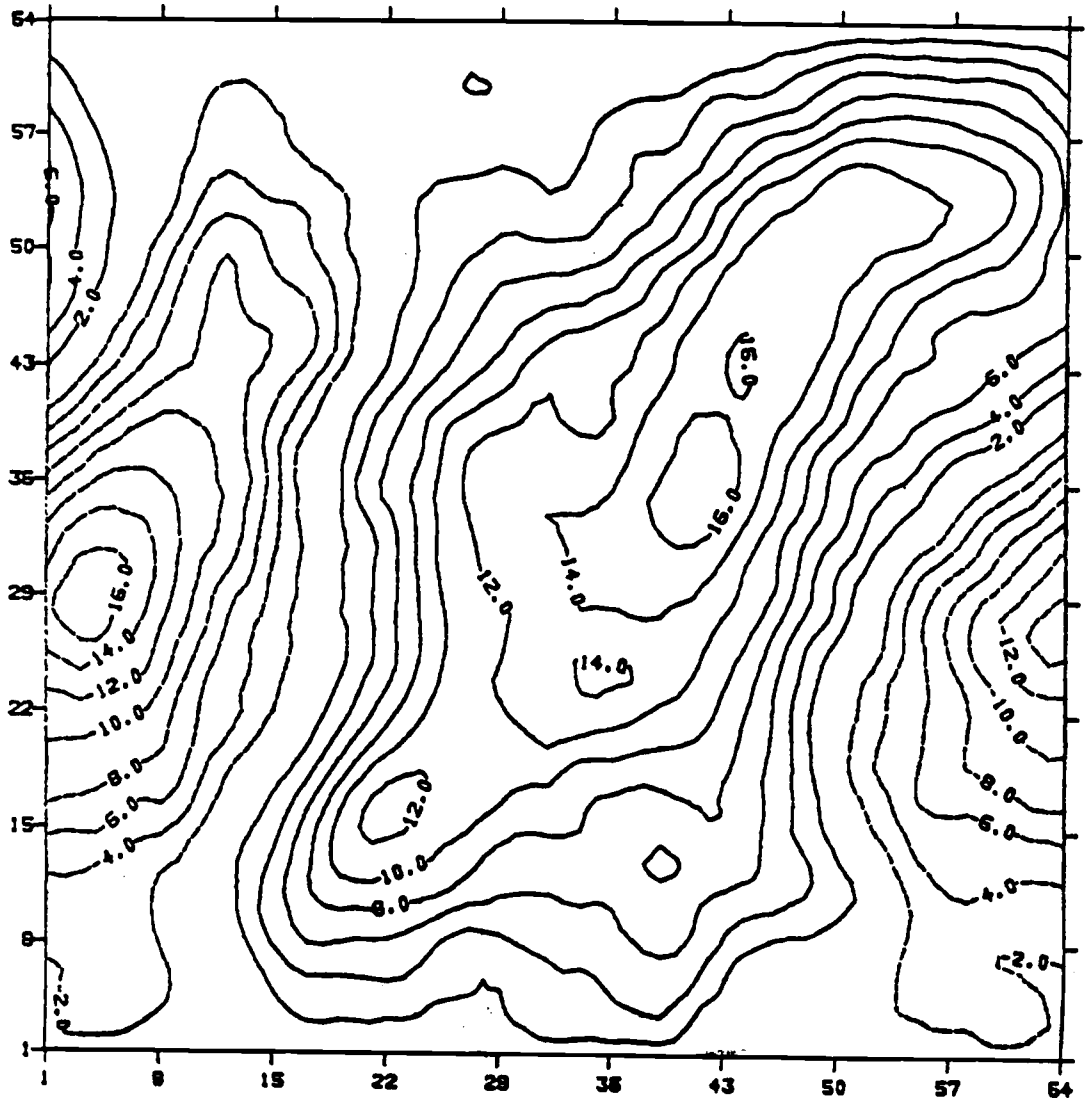

Figure 6.7. The stream function at the 2800th time step of the integration with fixed N-S boundary condition and random forcing.

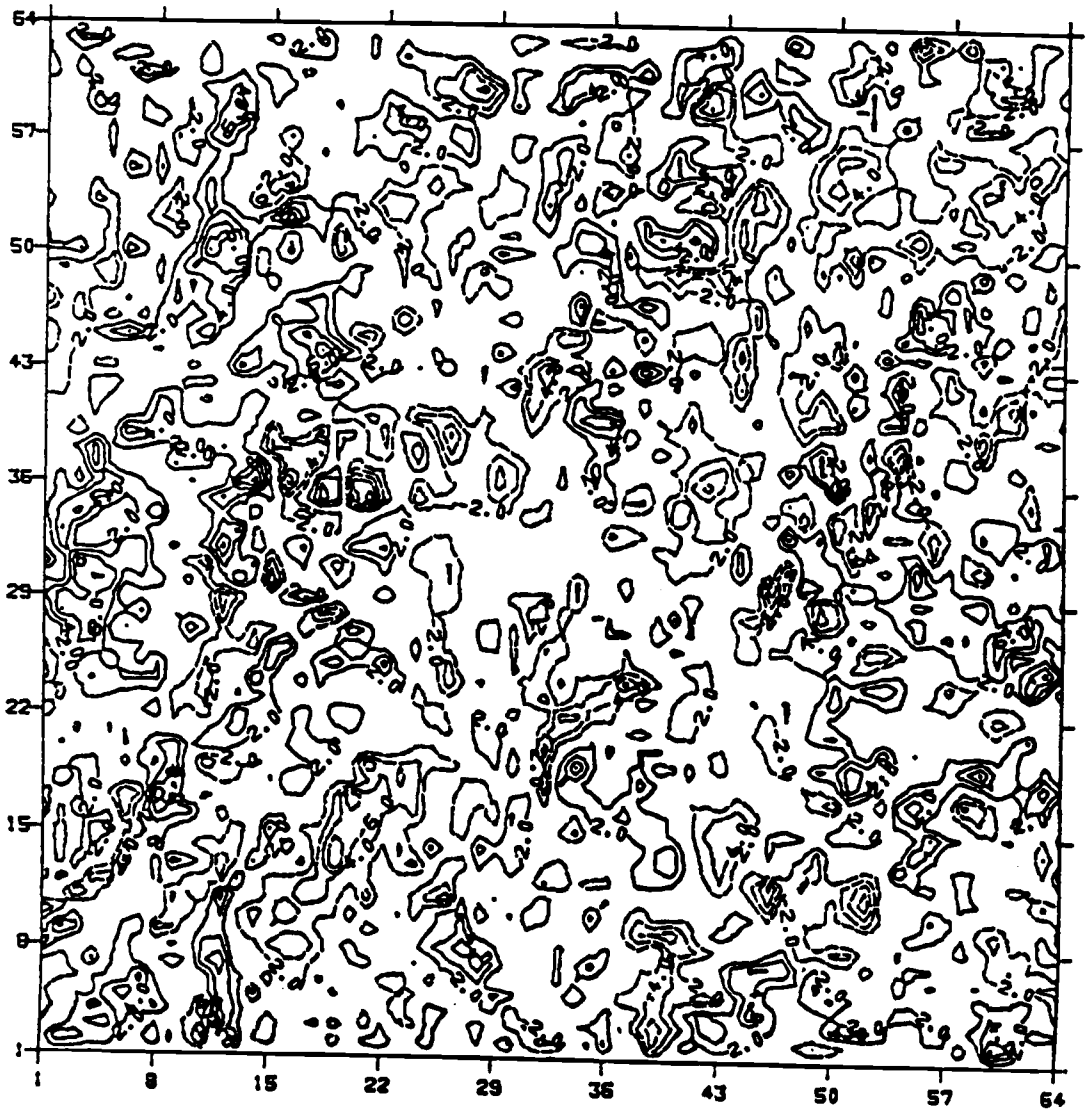

Figure 6.8. As in Fig. 6.7 except for the vorticity field.

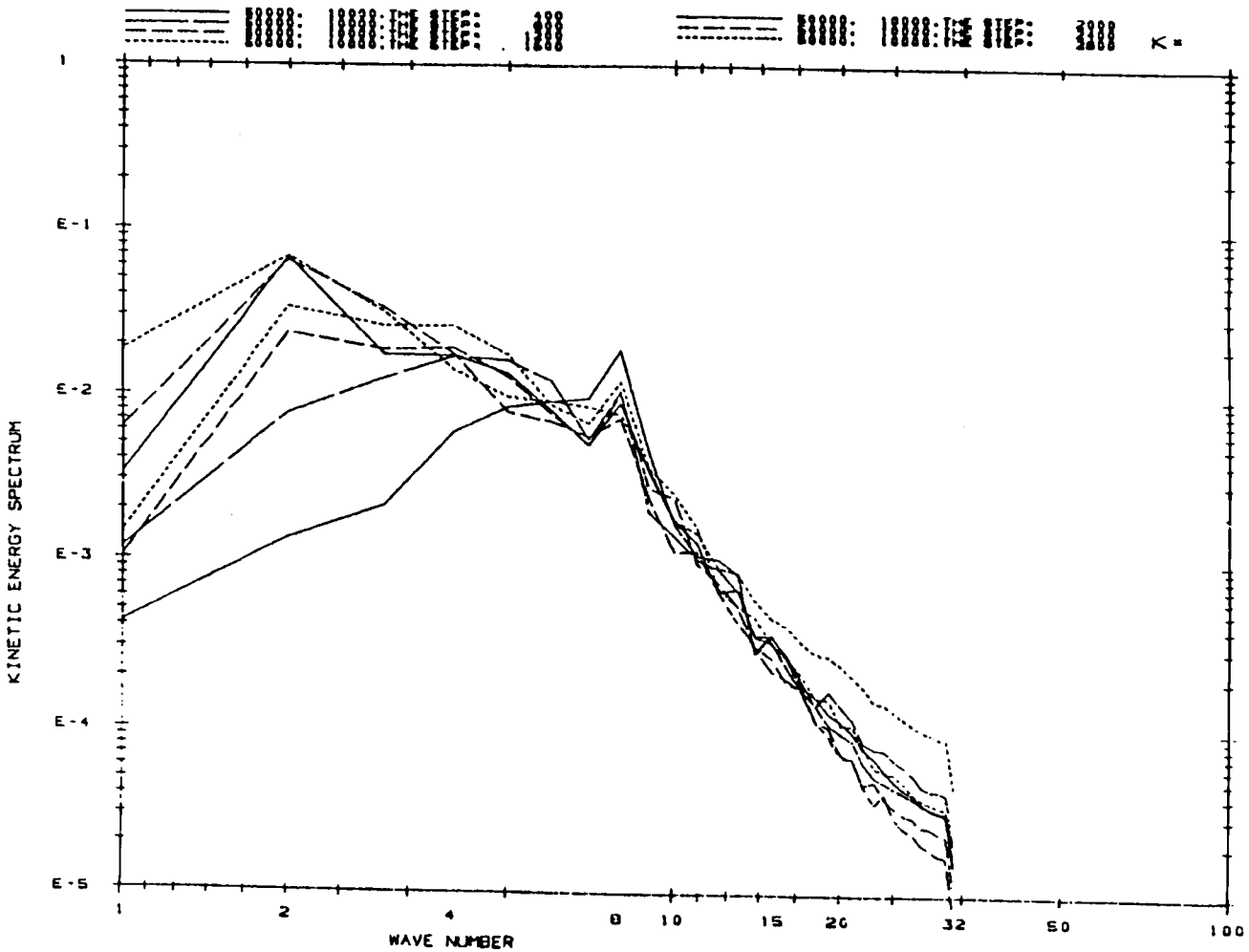

Figure 6.9. The kinetic energy spectrum with beta effect with fixed N-S boundary condition and random forcing, in a dimensional experiment.

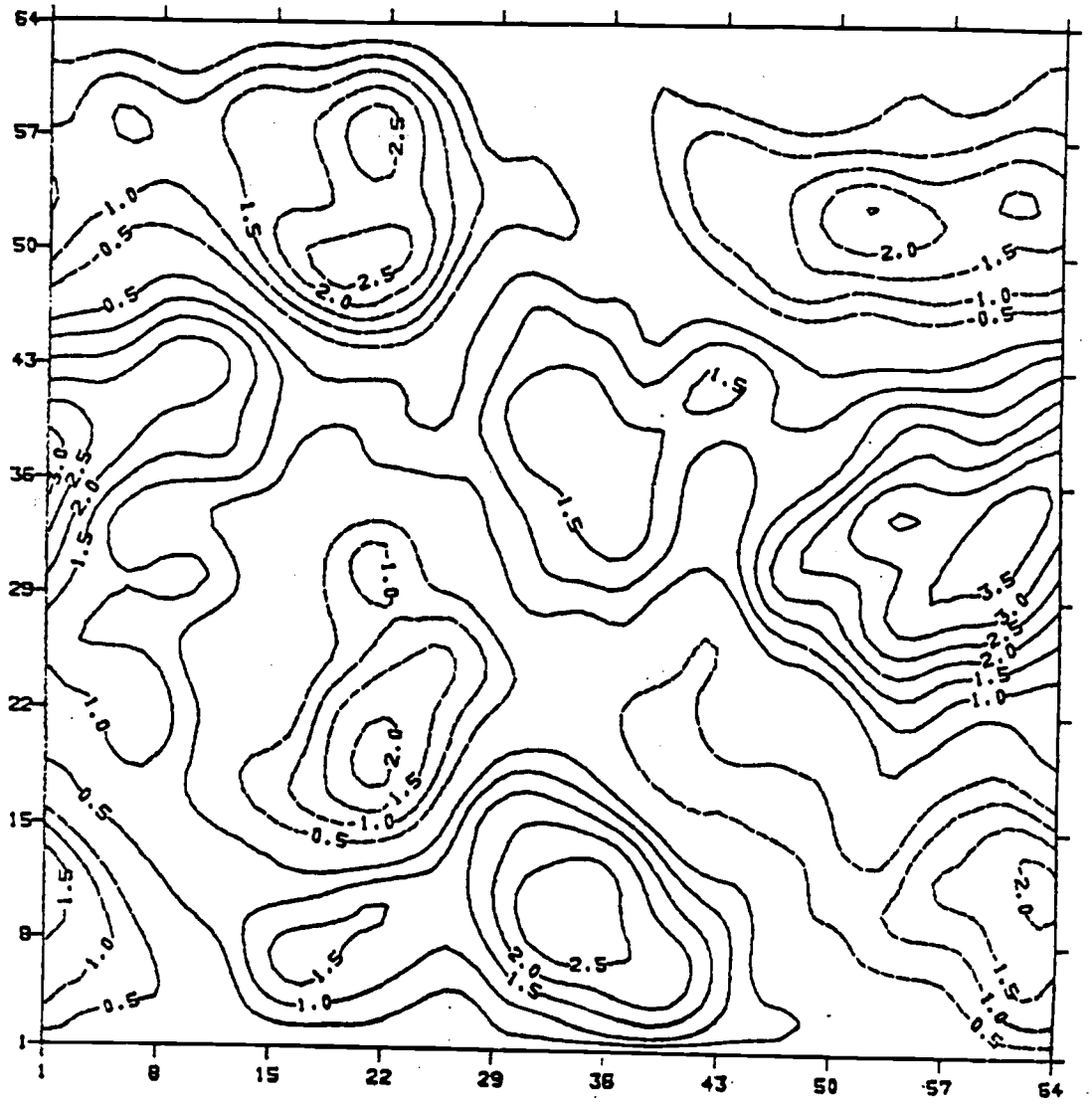

Figure 6.10. The stream function at the 2800th time step with beta effect in the experiment discussed in Fig. 6.9.

where $K = \iint \frac{1}{2}(\nabla\psi)^2 dA$, dA is the unit area. This means that the kinetic energy of the system can only be changed either through the generation by specified forcing or through dissipation by viscosity. Fig. 6.11 shows the time series of total kinetic energy, the rate of kinetic energy generation and rate of kinetic energy dissipation. The kinetic energy shows large increases in the initial 1000 time steps or so, following by a decay for about several hundred time steps with increases again toward the end of the integration. The dissipation rate tends to decrease the kinetic energy of the system. (Positive here means the decrease of the kinetic energy.) The generation rate is fluctuating, although most of the time this process contributes to an increase of the kinetic energy.

If the system has an initial mean flow, then the initial mean flow and the perturbed flow will interact through the linear barotropic conversion process, and the system is governed by a different set of kinetic energy equations:

$$\frac{\partial}{\partial t} K_Z = -\iint \bar{u} \frac{\partial}{\partial y}(\overline{u'v'})dA - \iint \nu\left(\frac{\partial \bar{u}}{\partial y}\right)^2 dA + \iint \bar{u}\,\bar{S}\, dA \qquad (6.3)$$

$$\frac{\partial}{\partial t} K_E = \iint \bar{u} \frac{\partial}{\partial y}(\overline{u'v'})dA - \iint \psi'(\nu\nabla^2\zeta')dA - \iint \psi' F' dA \qquad (6.4)$$

where $K_Z = \frac{1}{2}\iint \bar{u}^2 dA$, $K_E = \frac{1}{2}\iint (\nabla\psi')^2 dA$. '-' and "'" are the zonal mean and zonal departure, respectively. $\bar{S}$ is the zonal mean momentum forcing which $\bar{F} = -\underset{\sim}{k}\cdot\nabla\times\bar{\underset{\sim}{S}}$. Figure 6.12 shows the eddy kinetic energy of the system with initial uniform easterly flow

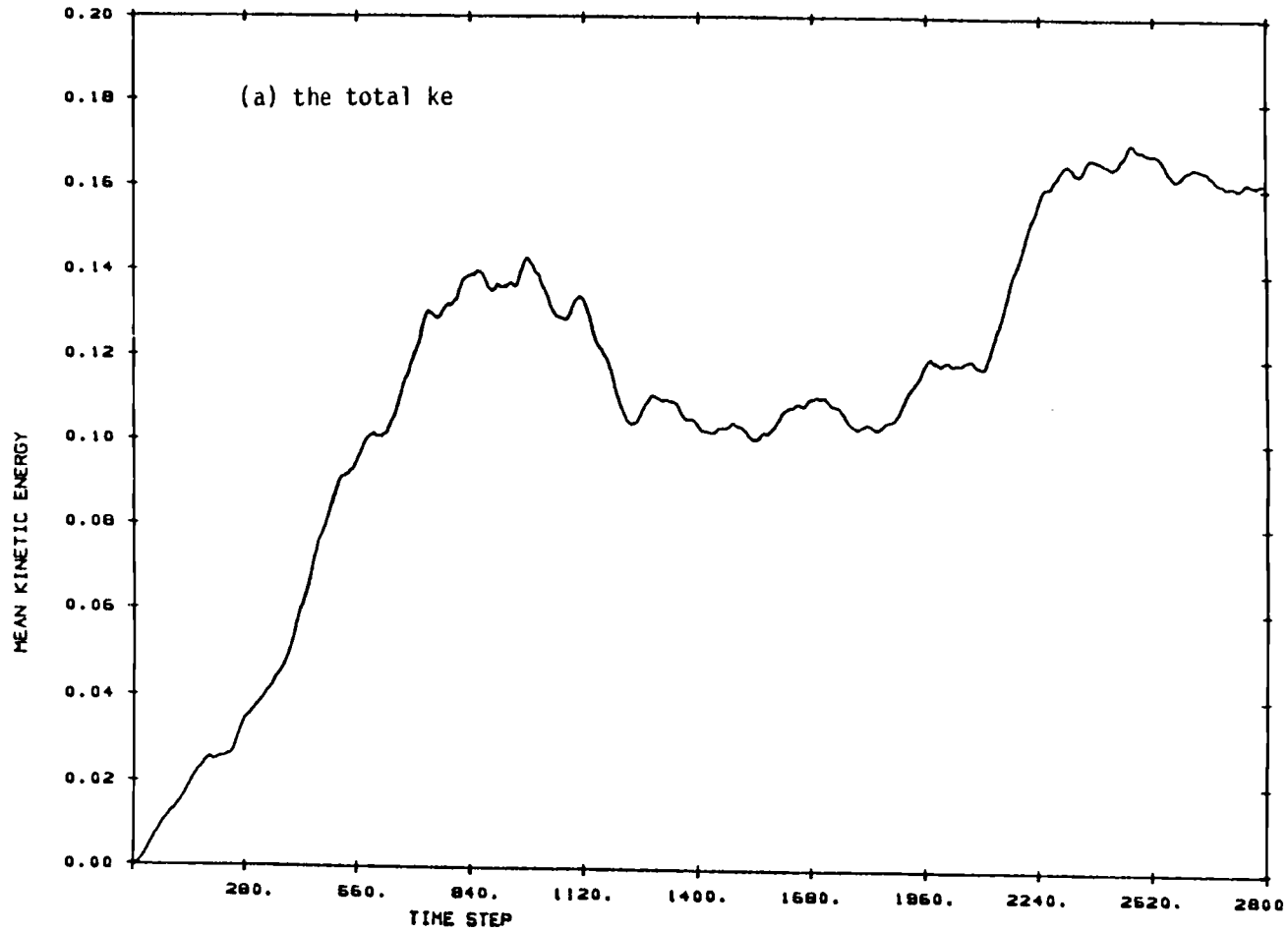

Figure 6.11. The time series of the kinetic energy budget component in Lilly's experiment. (a) the total kinetic energy, (b) the generation rate, (c) the dissipation rate.

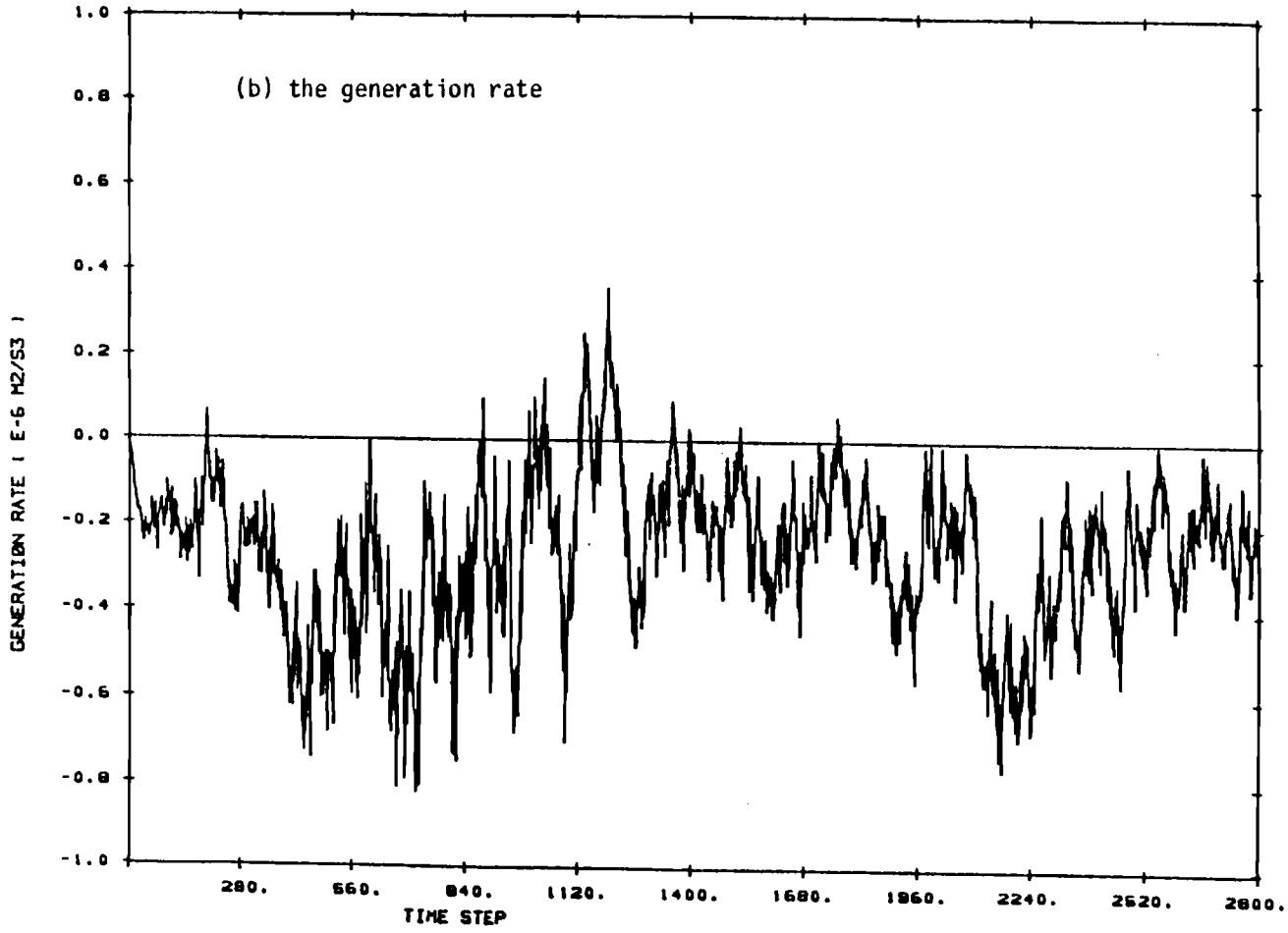

Figure 6.11 (continued)

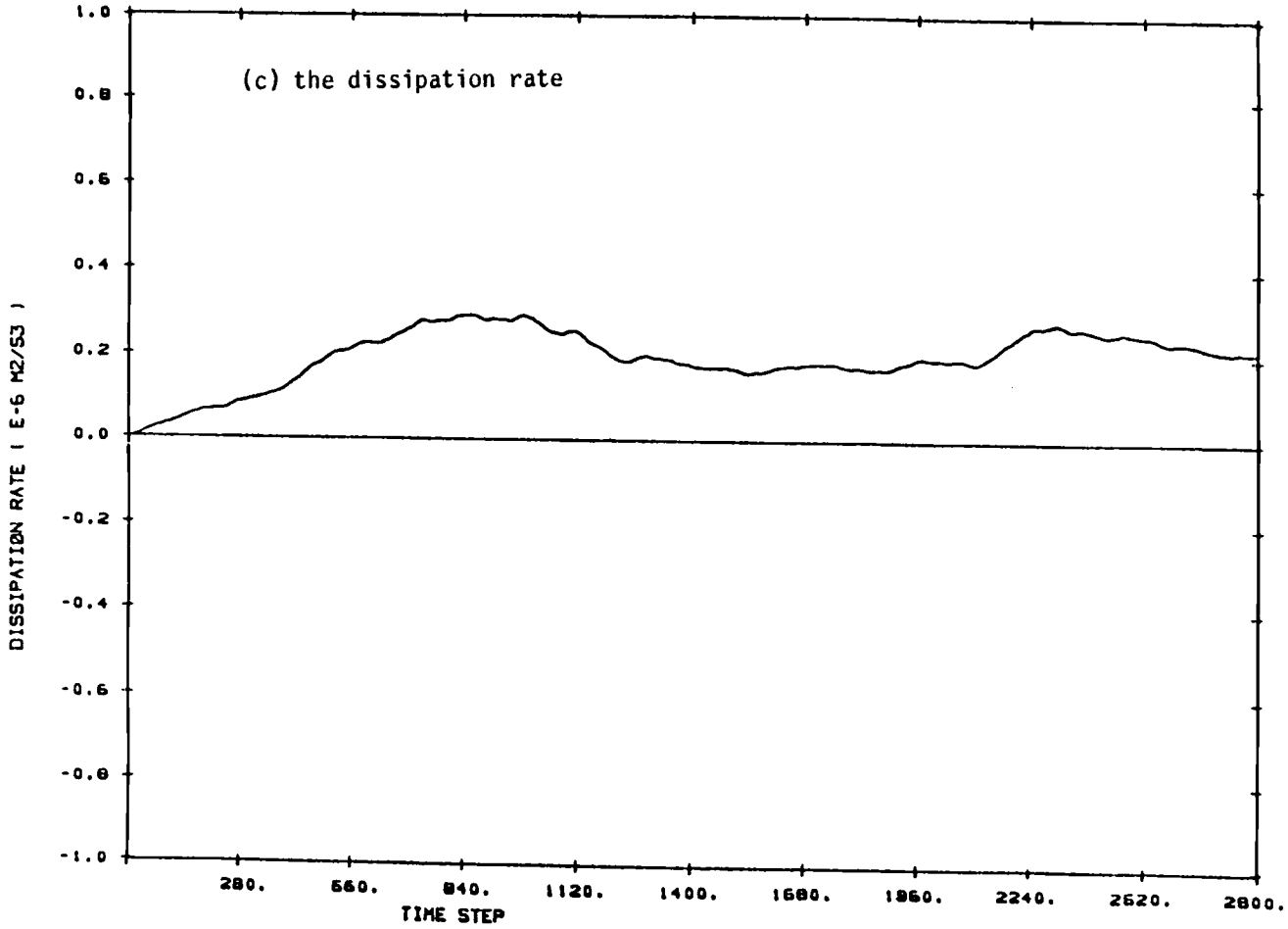

Figure 6.11 (continued)

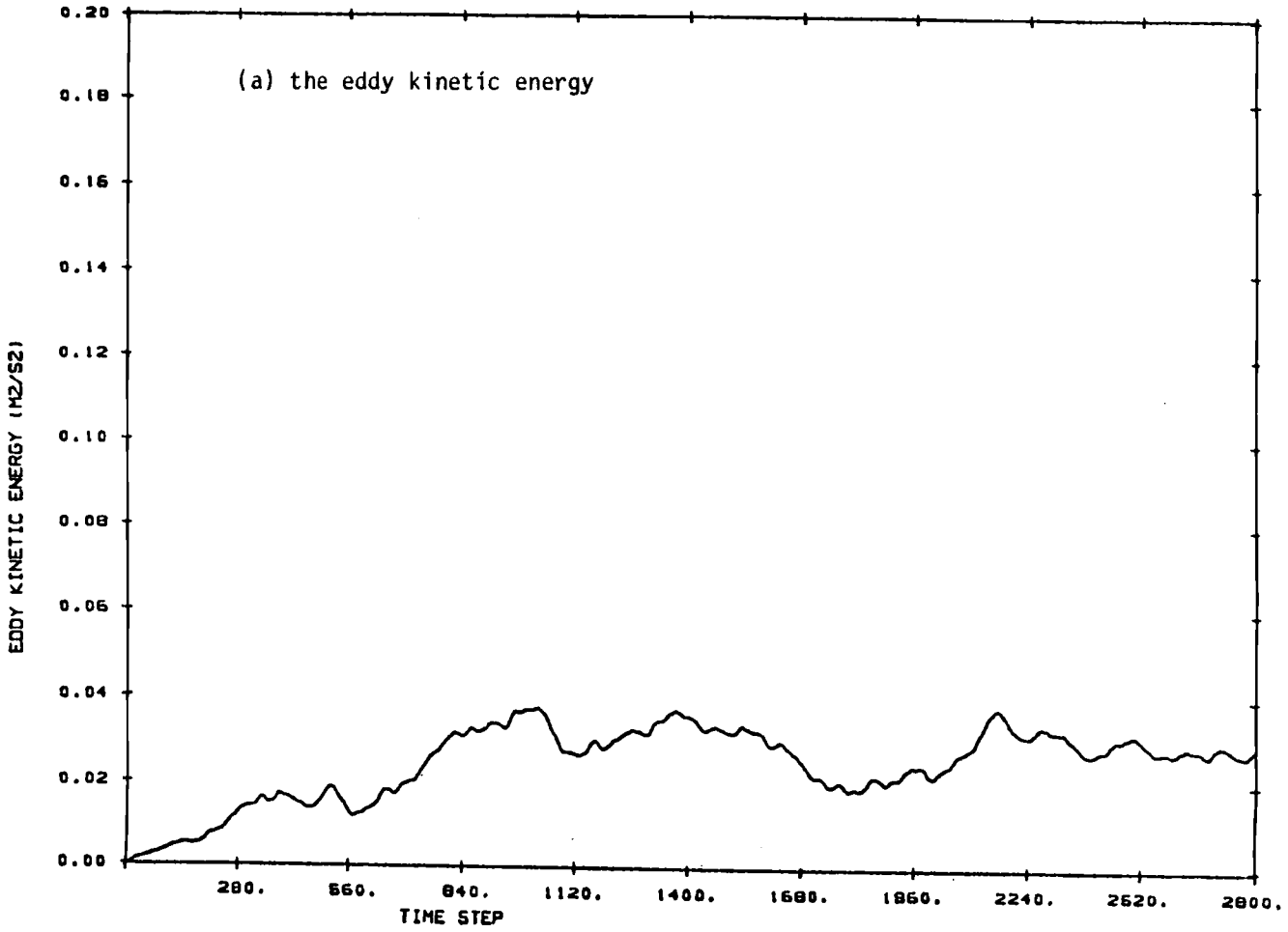

Figure 6.12. The time series of the kinetic energy budget components with the initial flow. (a) the eddy kinetic energy, (b) the eddy generation rate, (c) the eddy dissipation rate, (d) the conversion rate between the zonal and eddy flow.

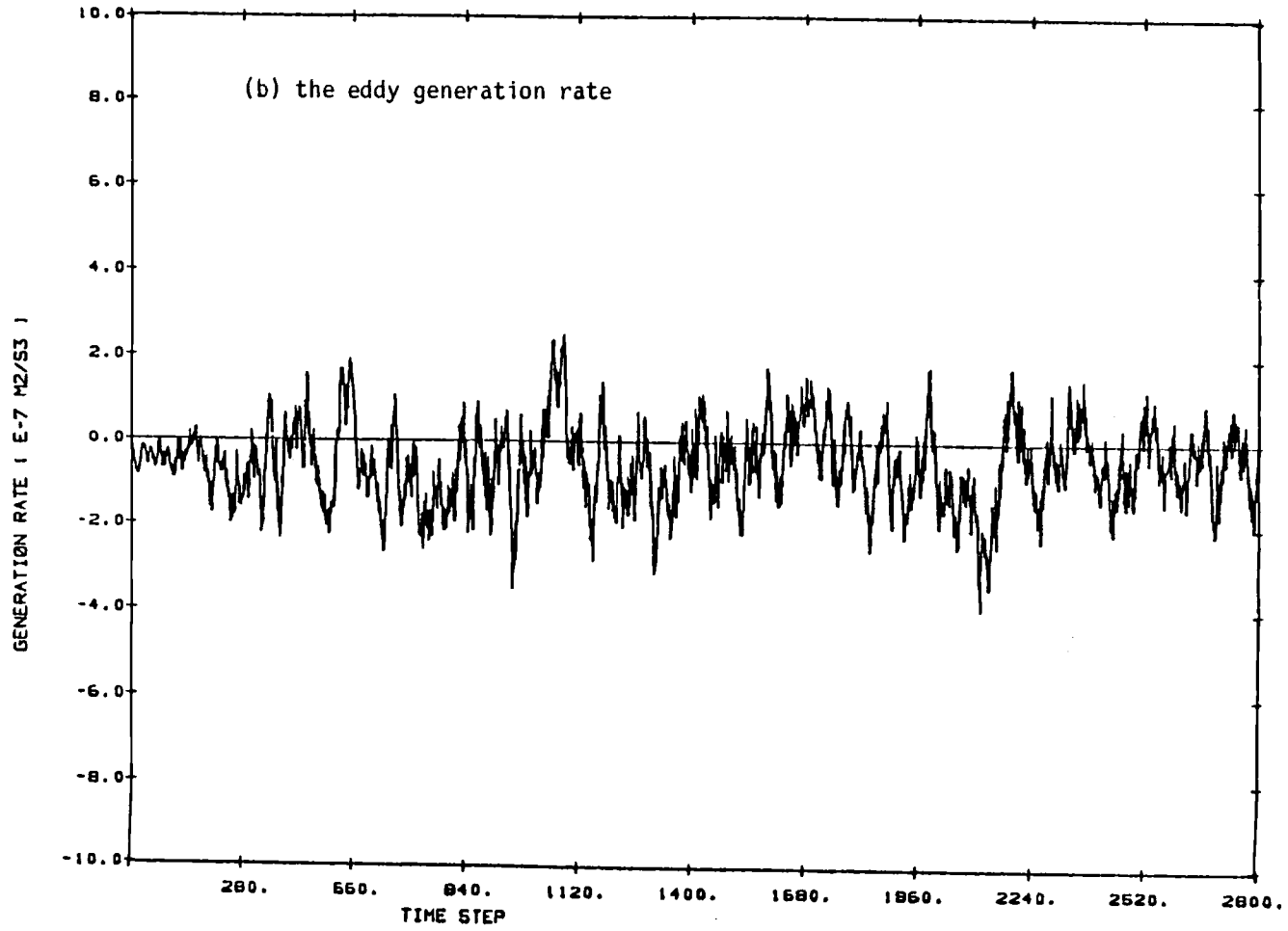

Figure 6.12 (continued)

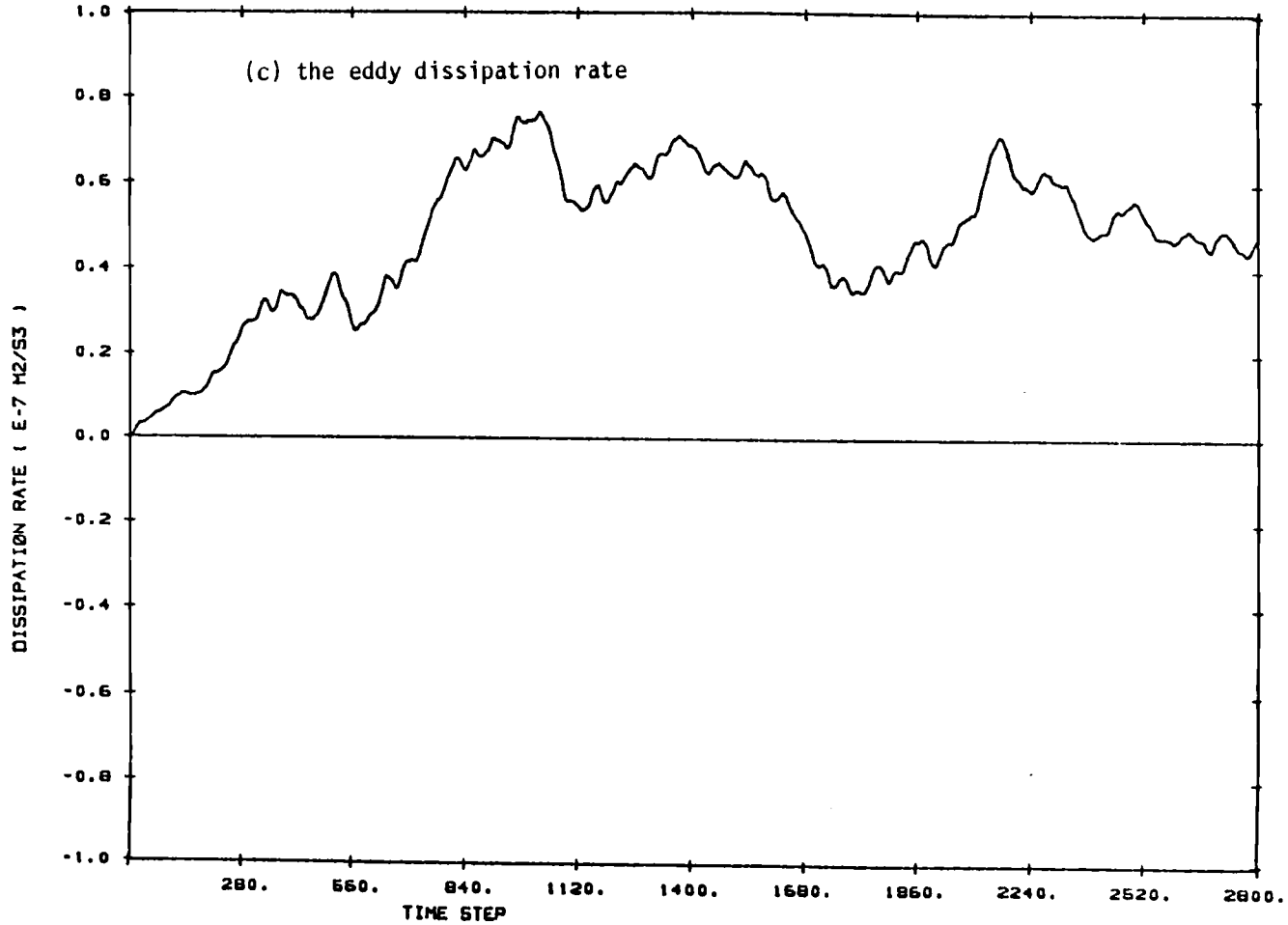

Figure 6.12 (continued)

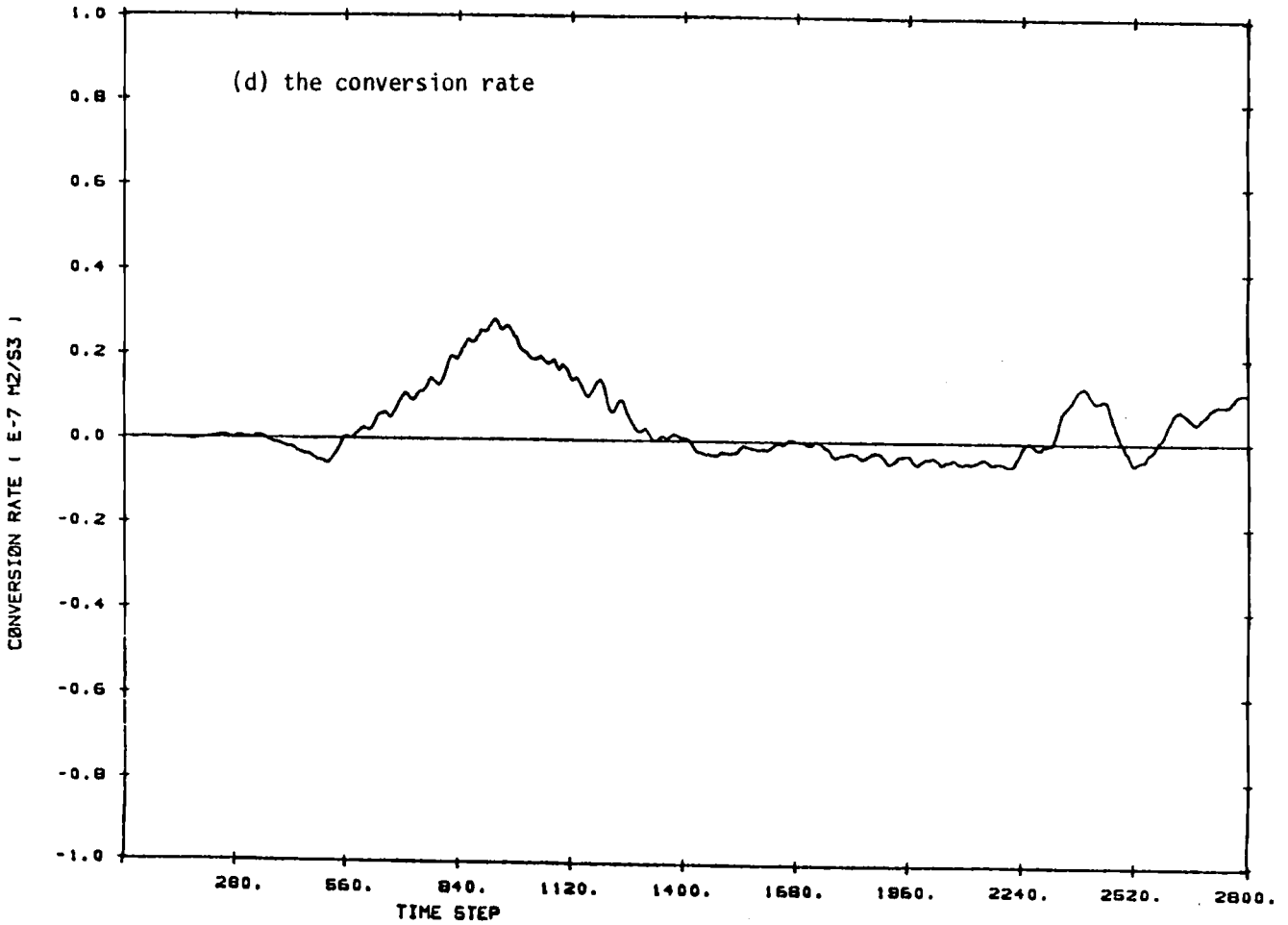

Figure 6.12 (continued)

(-5 m/sec), and the corresponding generation, dissipation and conversion rates. The kinetic energy in the system increases at a slower rate and there is fluctuation in the energy time series. The eddy generation rate is smaller and in a different phase relationship. The eddy dissipation rate also is weak. The conversion rate (positive means the increase of the eddy kinetic energy at the expense of the mean kinetic energy) is on the same order of magnitude as the dissipation rate, with large positive conversion occurring in between time steps 600 and 1200 and in the final stage, with some small negative conversion occurring at other times. The time mean contribution of generation is one order of magnitude larger than the conversion. This suggests that in the isotropic forcing situation, nonlinear process (associated with the generation) are more dominant in producing the eddy kinetic energy than the linear (conversion) process.

6.3 Sporadic cumulus momentum forcing

This section will study the large-scale response in which the momentum forcing is introduced on the scale of large cloud clusters. The experiment discussed in Sec. 6.2 was mainly focused on the understanding of the planetary-scale wavenumber energetics. It was shown that nonlinear transfer within two-dimensional turbulence may be an important process in setting up the kinetic energy spectrum of planetary-scale waves. As the forcing supplied energy through the synoptic scale disturbances (the baroclinically unstable waves at hemispheric wavenumbers 6-8), the energy at those

scales propagates upscale through the 2-D nonlinear interaction and reaches the scale of the domain (wavenumber 1). The dispersion of the planetary-scale Rossby waves inhibits the transfer of the energy to the largest scale through nonlinear interaction.

Gage (1979) hypothesized that some of the energy associated with mesoscale wavenumber spectrum was established through the upscale transfer of energy by the convective scale forcing under the constraint of 2-D turbulence. To represent the convective scale forcing, the physical conditions within the numerical model used in Sec. 6.2 have to be modified. In contrast to Lilly's experiment, the forcing appears only in a limited latitudinal domain instead of being globally distributed. This forcing should have a shorter time scale, and the integration time of this physical system has to be much shorter. Since Lilly's experiment investigates the planetary scale part of disturbance, it is appropriate to start the system from rest and have a longer integration. However, a mean (or initial) flow has to be included in the present model and the integration time has to be shorter in order to represent more suitable physical conditions.

The horizontal momentum residuals estimated in Chapter 5 in the upper troposphere were used as a guideline for constructing the small scale forcing. As described in Chapter 1, the interaction of the cumulus cloud and the large scale environment is thermodynamically qualitatively understood. However, it is not clear how the cumulus cloud interacts with the large-scale flow dynamically. From the study of Tollerud and Esbensen (1983), it was identified

that the detrainment of excessive in-cloud momentum is a plausible process to represent the cumulus dynamical effect, in contrast to the concept of detrainment of in-cloud vorticity to represent the cumulus dynamical effect. The experiments performed here will use the detrainment process formulation as a representation of the cumulus momentum effect.

Except for the forcing, the model used in this section is mainly the same as that described in Sec. 6.2. The grid distance is reduced to dx = dy = 20 km and dt = 500 sec in a 64 by 64 domain. The stream function is solved by a Fourier direct method in a rectangular domain. Two types of forcing and three types on initial flow are investigated. Table 6.1 describes the physical conditions of the experiments. The first type of forcing is termed the sporadic momentum forcing, which is given as $[M_c(U_c - U)]/Dp$, a representation of cumulus momentum effects given by Ooyama and others as $\frac{\partial}{\partial p}[M_c(\underset{\sim}{V}_c - \underset{\sim}{\bar{V}})]$, U_c and U are the assumed in cloud zonal momentum and the environmental mean momentum, respectively, and Dp is the assumed pressure difference (=100 mb). Mc, the convective mass flux, is assumed to have a half sine wave structure with a maximum intensity of 10^{-3} mb/s around the center of the domain. This forcing is set to have an influence region of about 320 km. The horizontal occurrence of this forcing is limited to 10 groups only, and the horizontal positions are determined randomly. Each forcing event has a horizontal extent of 80 km, and the corresponding vorticity forcing is computed from

Table 6.1. Classification of the experiments.

	Sporadic momentum forcing	Zonal momentum forcing
uniform flow (-5 m/s)	M1	Z1
shear flow	M2	Z2
unstable flow (-10*tanh y)	M3	Z3

this momentum forcing. The M_c is assumed to grow and decay within 2.5 hours (see Appendix B for more detail).

Another type of forcing is termed the zonal mean momentum forcing, which is constructed as the zonal mean of the vorticity forcing estimated from the sporadic momentum forcing just described. These two types of forcing have a couplet structure in the vorticity field with positive (negative) vorticity forcing to the north (south) of the center of the domain.

The sporadic momentum forcing in the horizontal plane is intended to represent the modification of the large-scale momentum through the random detrainment of in-cloud momentum. The zonal mean momentum forcing (its magnitude is the same as the zonal mean of the sporadic momentum forcing), on the other hand, is intended to represent the modification of the large-scale momentum through the zonal mean type of forcing. The sporadic momentum forcing experiment can serve to identify the large-scale response to the cumulus momentum forcing, since the forcing is randomly deposited in a horizontal plane. The zonal mean momentum forcing, on the other hand, can serve to investigate whether the sporadic nature of the convective forcing is an essential effect on the large-scale flow. The difference in response may reveal how in this system the forcing pattern affects the large-scale flow under the governing dynamical mechanism.

Three types of initial flow are incorporated with these two types of forcing. The horizontal uniform flow is assumed to be -5 m/s easterly; the shear flow is assumed to be linearly in the N-S

direction with easterly flow at the center of -5 m/s (-10 m/s at the southern boundary); and the unstable initial flow U = (-10.*tanh y) m/s.

Fig. 6.13 shows the time series of the mean flow pattern every 100 time steps of integration up to 800 time steps (~4 days) of the experiments M1 and Z1. Both experiments have a similar mean flow pattern. The eddy stream function of the experiment M1 after 800 time steps of integration is shown in Fig. 6.14. The eddy stream function possesses a wavenumber 1 structure. Fig. 6.15 is the same as Fig. 6.13, except for experiments M2 and Z2 which are for shear flow. The mean flow patterns are quite similar in both sets of experiments (M1 and Z1, M2 and Z2). The mean flow response is mainly within the forcing region. The sporadic momentum forcing and the zonal mean momentum forcing do not differ much in terms of the mean flow energetics, under this barotropic nondivergent system. Eddies pick up energy only from the sporadic type of forcing, not in the zonal mean type of forcing. Fig. 6.16 shows the eddy stream function after 800 time steps of integration for experiment M2. The eddy again contains its energy at the largest scale of the system. Eddy kinetic energy is larger in experiment M2 than experiment M1.

Fig. 6.17 is the same as Fig. 6.13, except for experiments M3 and Z3, in which the initial flow is U ≡ (-10.*tanh y) m/s. The two different forcings don't contribute to any significant difference in the mean-flow pattern. The eddy stream function at 800 time steps for experiment M3 is shown in Fig. 6.18. Although

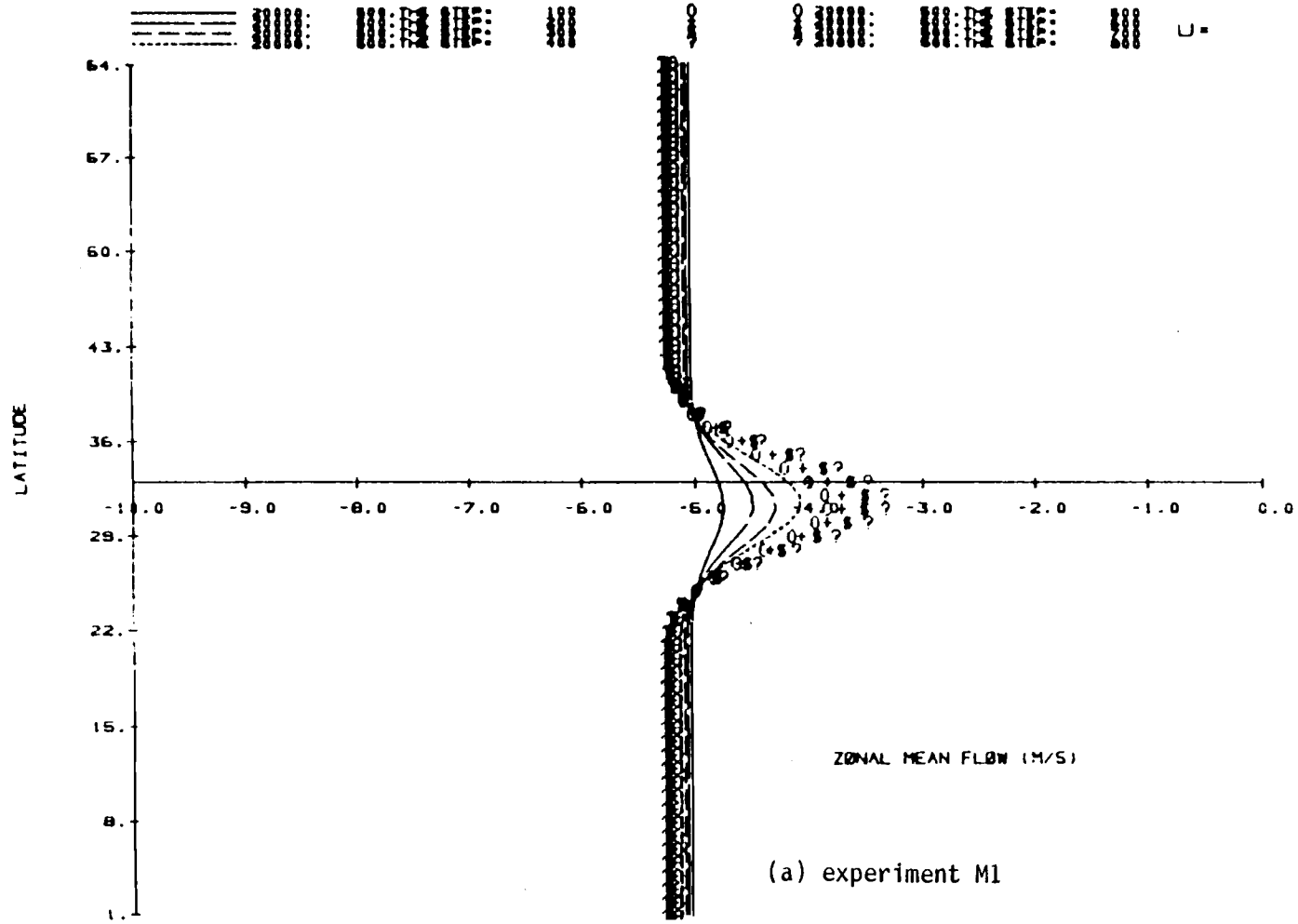

Figure 6.13. The time series of the mean flow pattern every 100 time steps of the integration up to 800 time steps for experiments (a) M1 and (b) Z1. Units are m/s.

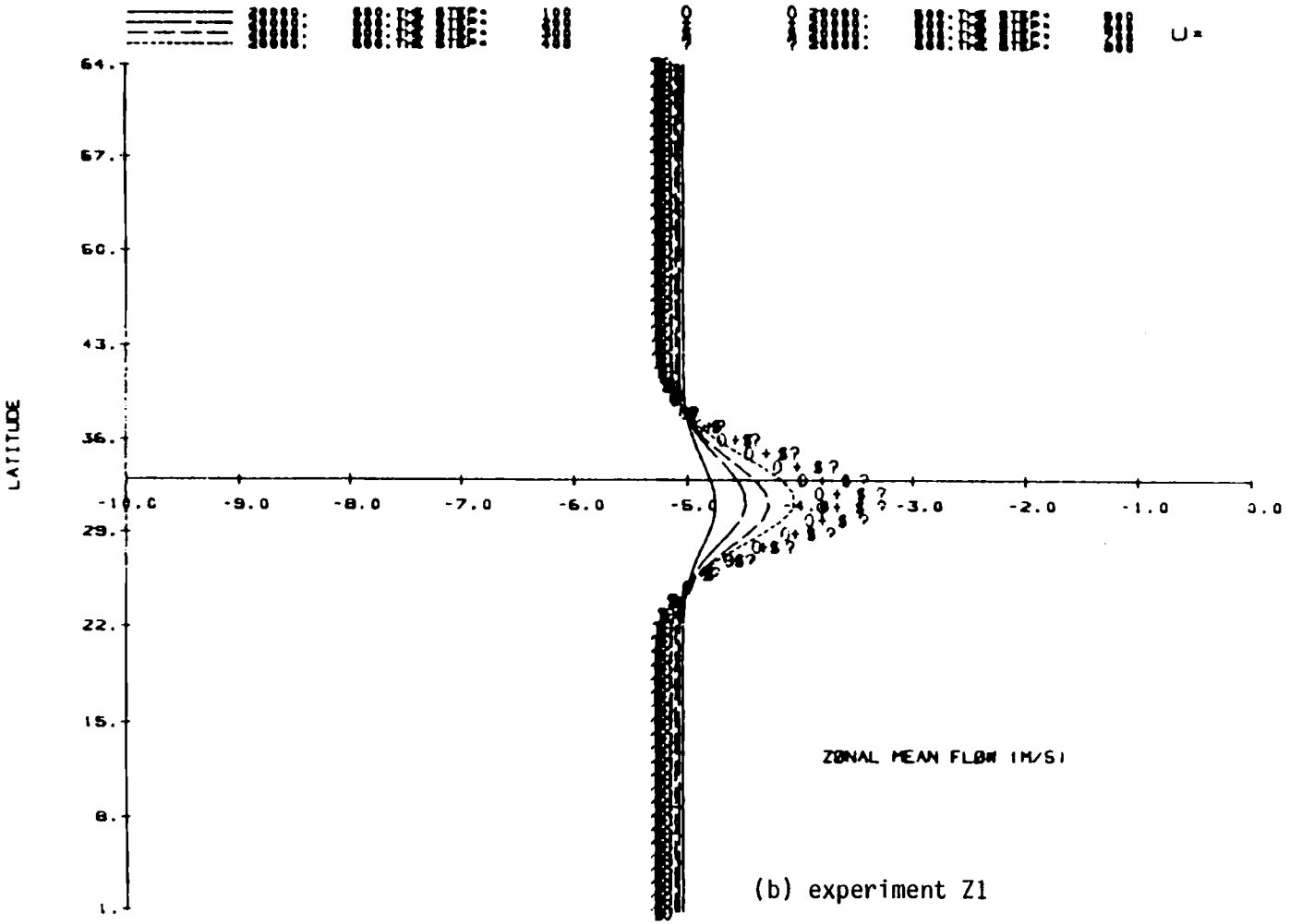

(b) experiment Z1

Figure 6.13 (continued)

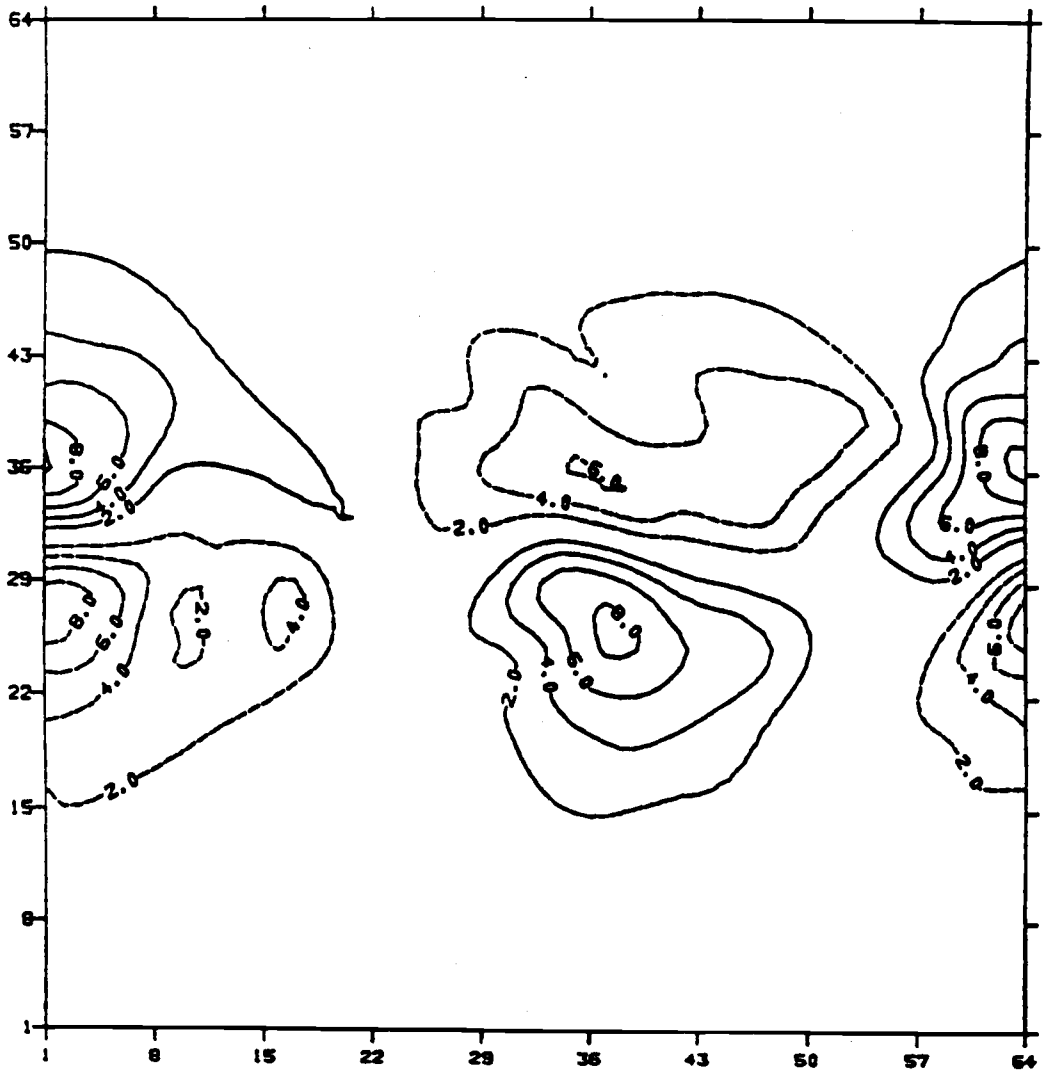

Figure 6.14. The eddy stream function at the 800th time step of the integration of experiment M1. Units are $10^3 m^2/s$.

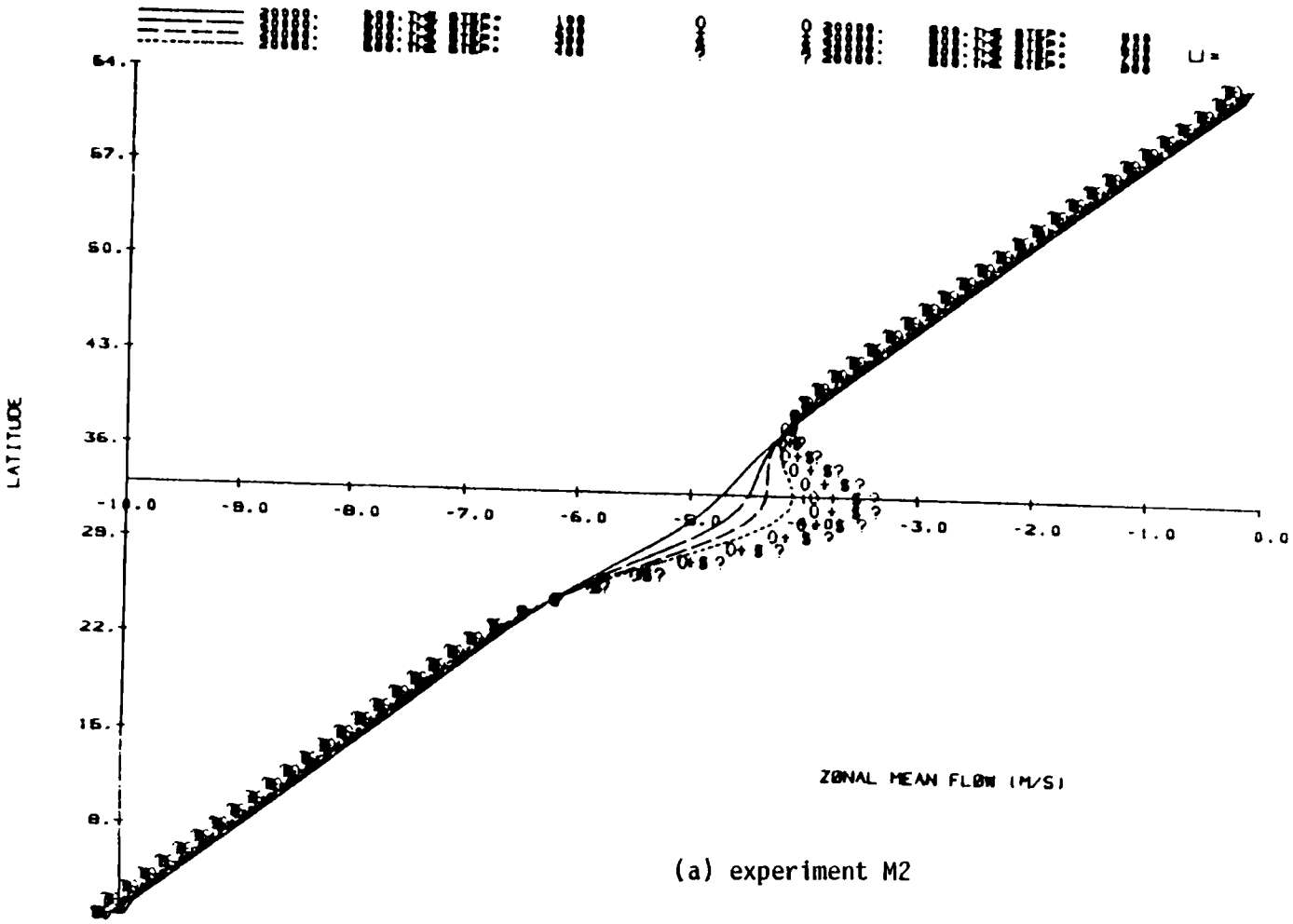

(a) experiment M2

Figure 6.15. The same as Fig. 6.13 except for experiments (a) M2 and (b) Z2.

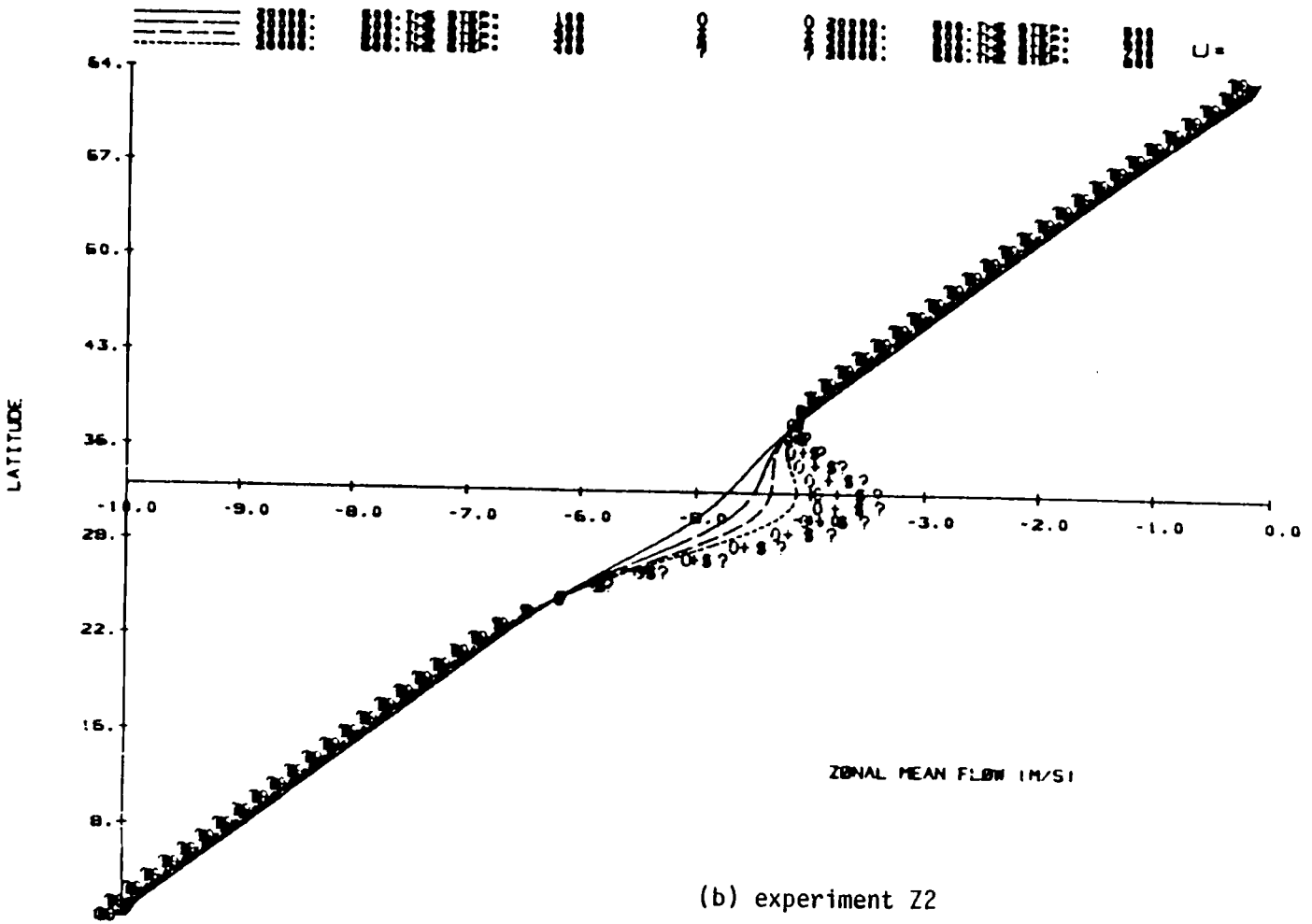

(b) experiment Z2

Figure 6.15 (continued)

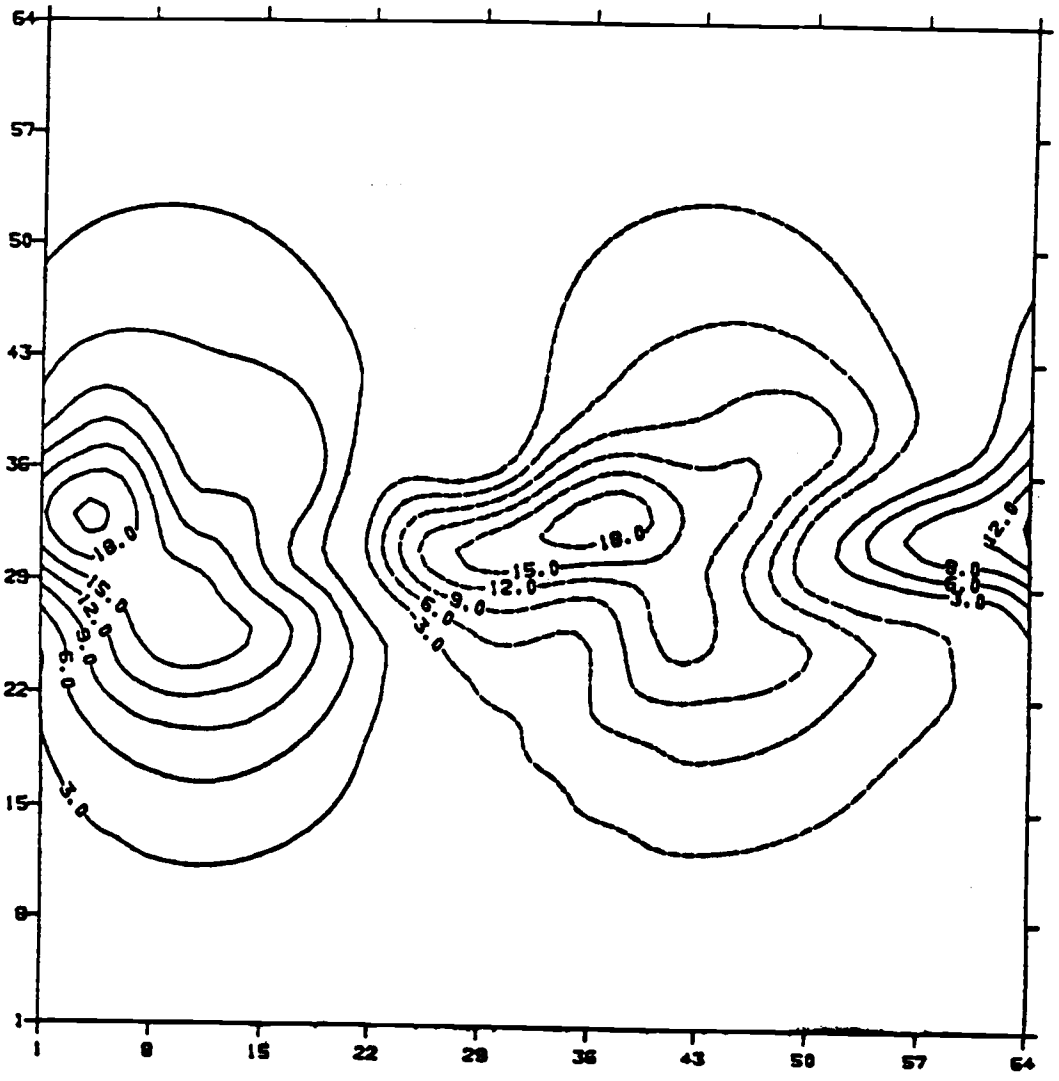

Figure 6.16. The same as Fig. 6.14 except for experiment M2.

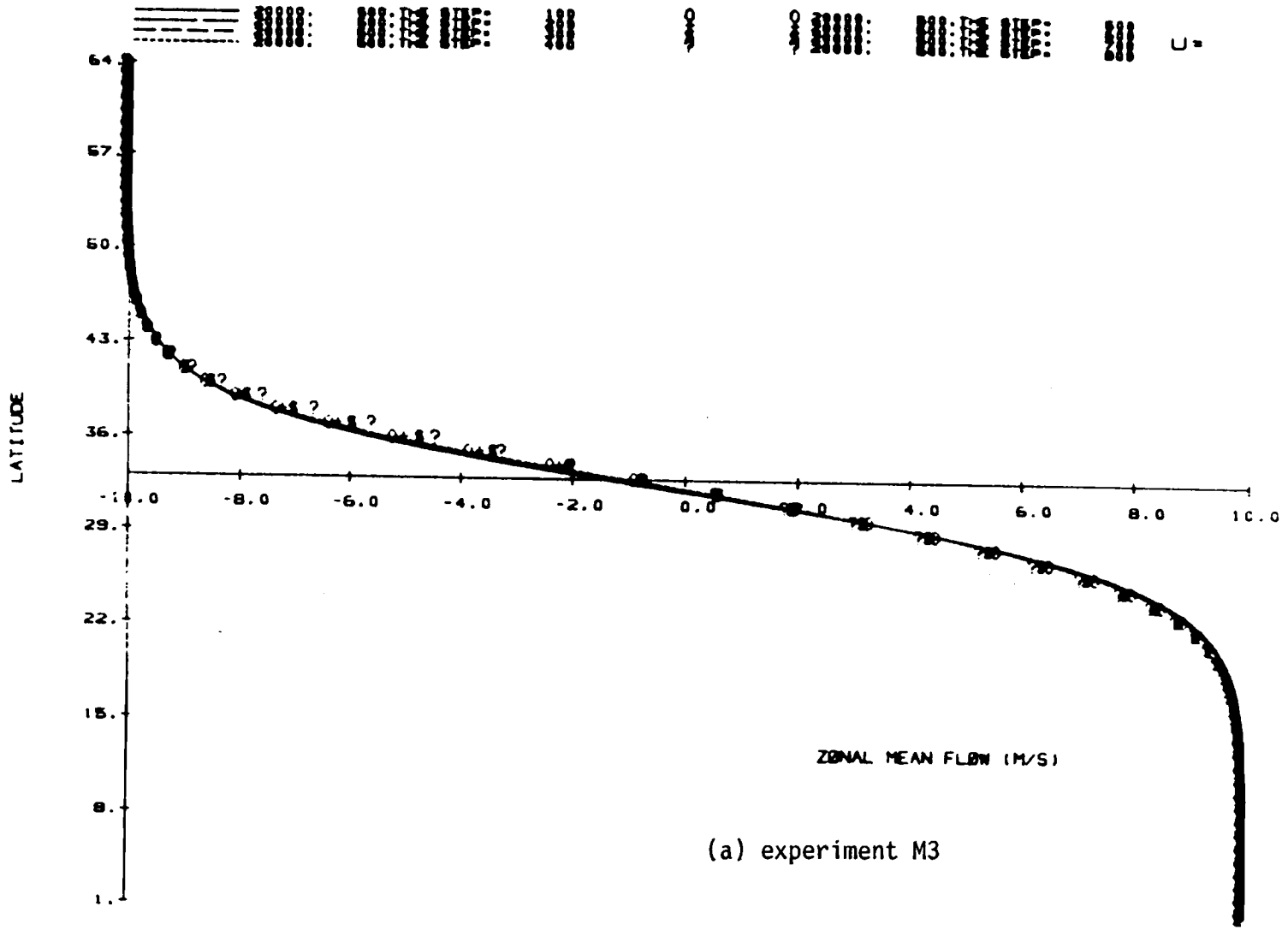

(a) experiment M3

Figure 6.17. The same as Fig. 6.13 except for experiments (a) M3 and (b) Z3.

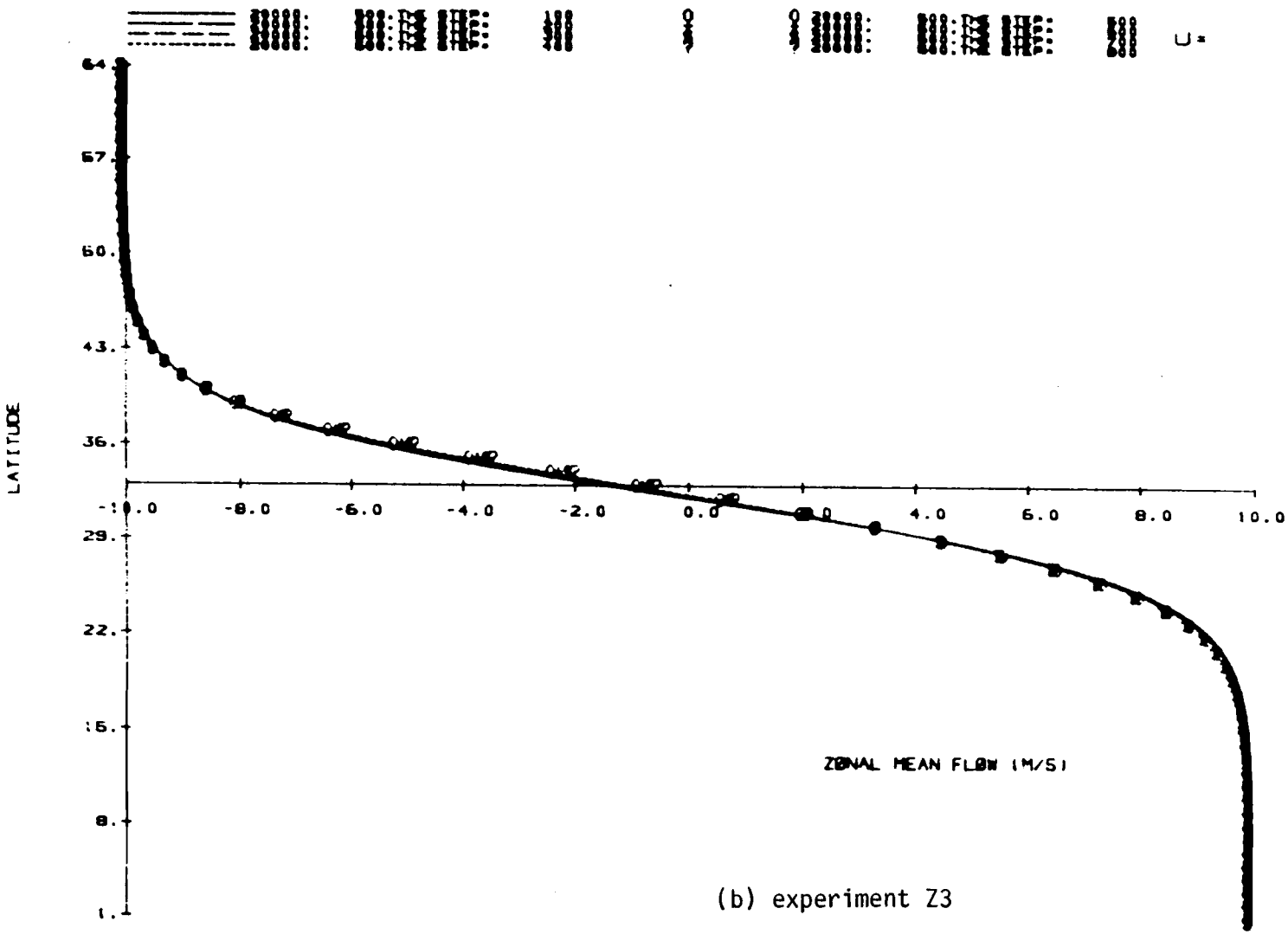

(b) experiment Z3

Figure 6.17 (continued)

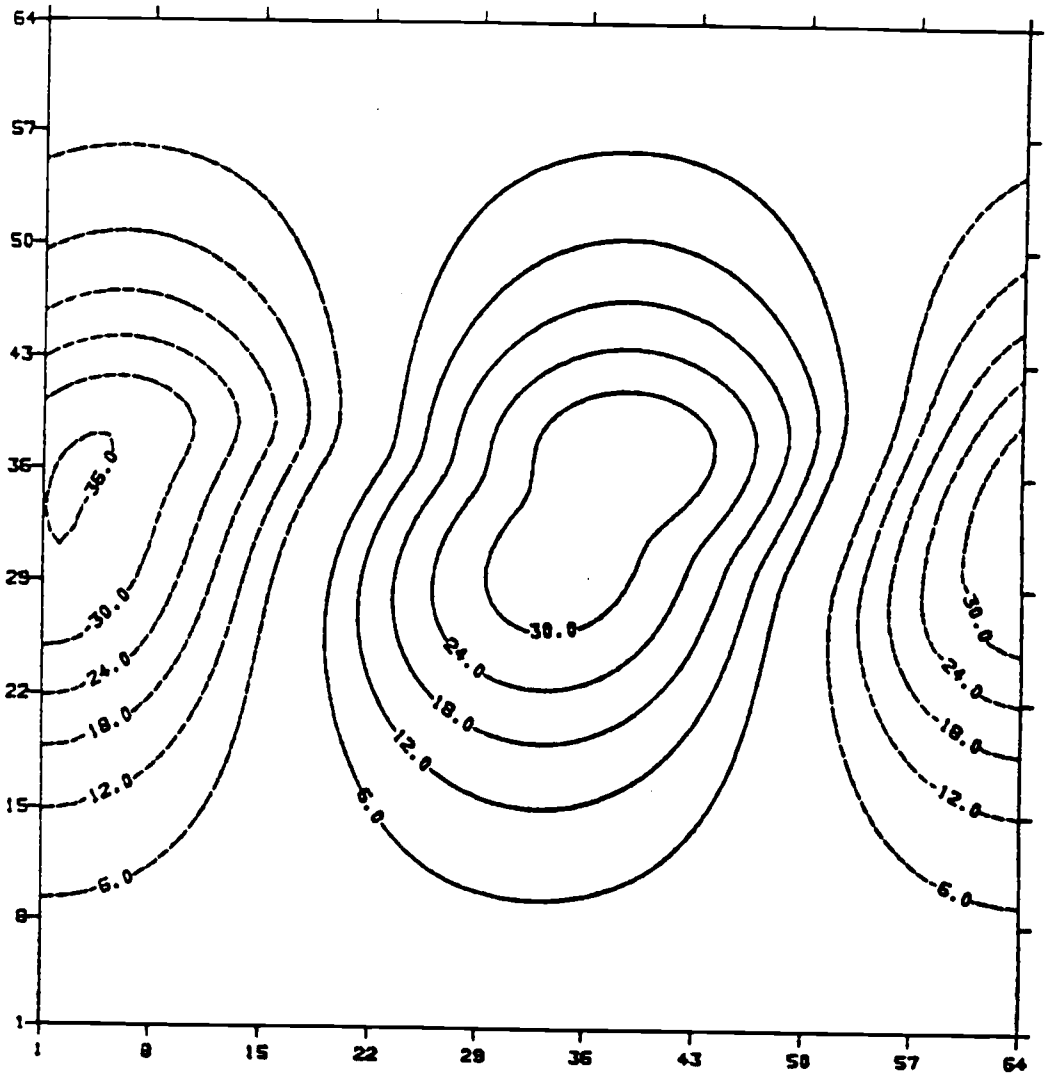

Figure 6.18. The same as Fig. 6.14 except for experiment M3. Units are $10^4 m^2/s$.

the wavenumber 1 pattern is reached as in other experiments, the energetics are totally different. Table 6.2 summarizes the energetics of these experiments. The eddy kinetic energy gains its energy mostly through the nonlinear generation as in the experiments M1 and M2. However, the linear barotropic conversion process in this unstable flow experiment (M3) dominated the production of the eddy kinetic energy. This suggests that in a barotropically unstable atmosphere, the growth of the eddy kinetic energy mainly depends on the linear conversion from the mean flow.

The eddy kinetic energy growth in the zonal mean momentum forcing experiments (Z1, Z2 and Z3) are all negligibly small. The forcing only contributes to the modification of the mean state energetics.

The generation of mean kinetic energy through the forcing is estimated as $\iint \overline{u}\ \overline{S}\ dA$, as in Eq. (6.3). As indicated in Table 6.2, different forcings in the experiment have a similar mean kinetic energy generation for given initial flow. This is due to the constraint under which the forcing was set up. The zonal mean of these two types of forcing have the same magnitude. From the kinetic energy equation of this system [Eqs. (6.3) and (6.4)], it is reasonable to have similar mean generation in the experiments of M1 and Z1, M2 and Z2, and M3 and Z3, within the framework of the present dynamical system.

Table 6.2. Generation and conversion rates of experiments [$(m/s)^2$/day].

	Mean generation	Eddy generation (nonlinear)	Conversion† (linear)
M1	0.255	2.55×10^{-4}	3.24×10^{-6}
Z1	0.255	10^{-14} *	10^{-14} *
M2	0.266	2.90×10^{-4}	1.50×10^{-4}
Z2	0.260	10^{-14} *	10^{-14} *
M3	0.071	7.02×10^{-4}	0.085
Z3	0.073	10^{-14} *	10^{-14} *

†: positive means the conversion from mean flow to eddy.
*: indicates very small number.

6.4 Interpretation and discussion

The numerical results from Sec. 6.3 revealed that the structure of the environmental flow plays an important role in determining the energy of the perturbed flow under the sporadic momentum forcing. In the barotropically stable initial flow with sporadic momentum forcing, the kinetic energy of the largest eddy obtained its energy from the upscale (nonlinear) transfer from the forcing scale. And the eddy kinetic energy in the shear flow case is stronger than in the uniform flow situation. However, with barotropically unstable initial flow, the largest eddies gained most of their energy from the linear process (barotropic linear conversion) and the nonlinear upscale transfer in the unstable environment is only of secondary importance, at least in the initial four days of integration.

The most important conclusions one can draw from the above are 1) in a barotropically stable atmosphere, the mesoscale wavenumber energetics may be established through the nonlinear energy cascade from smaller scales, with the forcing supplied through convective activity; 2) in a barotropically unstable atmosphere, the mesoscale wavenumber spectrum are established mainly by barotropic linear conversion; 3) the eddy kinetic energy grows only under the sporadic momentum forcing, while for the zonal momentum forcing the eddy kinetic energy in the system is negligibly small; although the eddy kinetic energy is generated through the nonlinear process, generation of mean kinetic energy by the forcing is more effective than the generation of eddy kinetic energy under the barotropic

non-divergent dynamical system; 4) the large scale (or mean flow) response is not affected by these two types of forcing in the barotropic non-divergent system, which only has nonlinearity as the governing dynamics, provided that the zonal means of these two types of forcings are the same. This implies that whether the occurrence of the convective mass flux is random or zonally distributed, the large-scale momentum fields will be the same under this dynamical system.

The discussions in Haynes and McIntyre (1986) can be used to interpret this result. To make local vorticity dynamics relevant to the large-scale flow, the forcing has to create horizontal inhomogeneities of the transported properties. When an intermittant forcing event occurs, horizontal eddies will be generated. The large-scale advective processes then spread the kinetic energy of the eddies over a large area with time. However, the rate of energy transfer to the large-scale flow is very small and the response of the large-scale flow does not vary significantly on the time scale of eddies. Under the barotropic nondivergent system, the eddies can only gain energy through nonlinear interaction. This nonlinear interaction mechanism is a slow process, hence most of the energy associated with forcing is transferred to mean flow directly. The sporadic nature of the forcing thus becomes irrelevant to the large-scale dynamics. This is also consistent with the interpretations of Sardeshmukh and Held (1984).

In summary, this Chapter has used a simple dynamic system to

investigate some aspects of the dynamical interaction between convection and the large-scale flow. In the barotropically non-divergent system, sporadic momentum forcing provides an energy source to make up the mesoscale kinetic energy spectrum of the system through the nonlinear upscale cascade of energy as proposed by Gage (1979). In this study, only the barotropically non-divergent system is used. It is obvious that in a barotropic divergent system, there will be an additional dynamical process to affect the mean flow and the eddies, namely, the gravity wave excitation in the divergent system. The dispersive nature and relatively large group velocity of the inertial gravity wave within a divergent system is capable of transferring the kinetic energy to different wavenumbers in a relatively short period. The inclusion of the inertial gravity wave dynamics in a system may thus alter the mean flow response to the sporadic momentum forcing.

In Chapter 5, the pressure gradient forces induced by the convective cells were identified as an important cumulus effect in generating or modifying the environment momentum. It takes a divergent or a baroclinic system to represent this pressure effect. The pressure effect will then be involved in the generation of the mean or eddy kinetic energy and contribute to the energetics of the system. It is a reasonable extension of the present study to use a system which contains gravity wave dynamics (barotropic divergent system), or a system which contains the pressure effect (some divergent or baroclinic system) to investigate the interaction between sub-grid scale disturbances and

large-scale flow. These aspects will be a topic for further research.

CHAPTER 7. CONCLUSIONS AND SUGGESTIONS FOR FURTHER RESEARCH

This thesis has studied the thermodynamic and dynamical aspects of cloud clusters in GATE region. The data used in this study were a three-dimensional gridded dataset constructed by Ooyama and Chu (Hurricane Research Division, AOML/NOAA and SSEC-University of Wisconsin) for wind data and Esbensen (Oregon State University) for thermodynamic data. From the budget studies, the characteristics of the cloud-cluster-scale circulation were identified.

The contributions from the sub-grid scale motion to the large-scale thermodynamic and dynamical environment were discussed. This Chapter will summarize some of the important conclusions and discuss some suggestions for further research.

7.1 Conclusions

The conclusions from this study on the thermodynamic aspects of the cloud-cluster-scale and the sub-grid scale effects are as follows.

Warming and moistening occur in the 250-450 mb layer, with cumulus cloud effects and radiative effects (through the diurnal cycle) contributing to the warming. Moistening is due to the water vapor transport from the lower layer, with the detrainment of cloud water substance or the transport associated with the cloud cluster scale ascent being the two possible mechanisms. In the lowest layer, cooling and drying dominate. This is related to the

activity of the mesoscale downdraft in the convective event. In between, the easterly wave has a large influence on the change of the temperature and moisture fields through the advancement of the wave itself.

Through the horizontal structure of the budget, we can identify that large Q_1 and Q_2 are associated with the cloud cluster center, not in the center of the A/B ship array. A strong upper-tropospheric heat source and the middle-tropospheric drying in the mature stage, as well as the sudden collapse of the drying at lower levels in the dissipating stage, are found to be characteristic features of the cloud cluster scale budget.

The Q_1, Q_2 and F_h* values are larger than the easterly wave composite result, indicating that the disturbances which dominated in the GATE A/B area are below the scale of the easterly wave. The budget based on the cloud cluster life cycle will not go through a cycle of significant change within the time span of cloud-cluster activity if the cloud-cluster-scale motion in weak or nonexistent. Large surface precipitation is found near the cluster center in the mature stage, while small surface evaporation found in the dissipating stage indicates a recovery of the boundary layer. On both the cloud cluster scale and easterly wave scale, the unresolved processes, namely the convective effects, always have a stablizing effect on the large-scale environment.

Chapter 5 discussed the momentum and kinetic energy budget in the vicinity of the cloud clusters. Residuals of the momentum and the kinetic energy were computed. It is concluded that the physi-

cal processes associated with the unresolved scale motions (mesoscale and convective scale) are producing the residuals. The major effects are summarized here.

In the growing stage, the mesoscale and cumulus scale effect tends to: 1) provide a vertically integrated net sink for the westerly momentum and a net source for easterly momentum around the cluster center; 2) induce a convergent circulation in the lower layer; 3) cause a relatively large westerly acceleration in the upper layer around the center, hence enhancing the production of a vorticity couplet.

In the mature stage, the effects are to: 1) cause a layered vertical structure in the westerly and southerly acceleration, in contrast with the growing stage; 2) induce a divergent circulation in the upper layer, and maintain a vorticity couplet pattern; 3) still maintain a convergent circulation in the lower layer, although weaker at this stage.

In the dissipating stage, the effects are to: 1) induce layered vertical structures; and 2) maintain a weaker divergent circulation aloft.

From the momentum budget residual, it is hypothesized that the first contribution from cumulus scales in modifying the upper tropospheric large-scale momentum field is through the pressure gradient forces induced by the perturbed pressure field associated with the divergent flow. The second contribution from the cumulus scale is the horizontally varying detrainment of environment momentum by the convective mass flux. The induced PGF may be

regarded as an interaction between the updrafts and the vertical mean shear. The hypothesized pressure gradient across the updrafts is in the direction of the environmental wind shear. In the GATE region, the vertical wind shear at the easterly jet level is mostly easterly, and easterly accelerations are thus produced by the cumulus induced pressure gradient effects. The mixing processes would generate a relative maximum of westerly momentum within the center of cloud cluster. The combination of these two hypothesized effects could account for the momentum residuals pattern seen in the mature stage of the momentum budget computed on the cloud-cluster-scale.

The postulation of these two cumulus effects can also be used to interpret the conclusions drawn by Zipser et al. (1981) or LeMone (1983). The net cumulus momentum effect is the sum of the mixing process and the induced pressure effect. Whether the net cumulus momentum is down or against the mean vertical momentum gradient depends on the induced pressure effect. The mixing process alone will produce a down-gradient transport, although the net transport can be either way.

The kinetic energy residuals computed for 5 September can be interpreted by these hypothesized convective momentum effects. From the mixing process viewpoint, the momentum is transported in the direction to reduce the mean wind shear. In the 5 September case, the vertical shear is dominated by easterly flow. Thus, the westerly momentum has to be transported upward as dictated by the mixing process. By multiplying the environmental wind with the

momentum residual generated by mixing process, the upper (lower) layer should be a kinetic energy sink (source). That is to suggest that by vertical mixing process, the kinetic energy is transported downward to compensate the surface kinetic energy dissipation. However, one must also consider the contribution from the nonhydrostatic pressure gradient forces induced by convective scale motion in evaluating the kinetic energy residuals. From the momentum budget of the 5 September case, we deduced that the induced nonhydrostatic pressure effect would be necessary to generate the observed easterly acceleration and hence the kinetic energy source in the upper layer.

To better understand the mechanisms of interaction, Chapter 6 focussed on the effects of sporadic momentum forcing from the cumulus scale on barotropic non-divergent large-scale flow. It was hypothesized that this horizontal momentum forcing from sub-grid scale features interacts with the large-scale flow through a nonlinear cascade of energy from smaller to larger scales of motion and that the interaction of the clouds and the large-scale flow may be strongly dependent on the nature of the nonlinear effect.

The numerical experiment results did support this hypothesis in part. In the upper troposphere, a portion of the energy on the convective scale is transported nonlinearly through wavenumber space to mesoscale wavenumbers. In a stable environment, this nonlinear process is a dominant factor in the supply of eddy kinetic energy. The eddy kinetic energy grows only under the sporadic momentum forcing, while for the zonally constant momentum

forcing, the growth of eddy kinetic energy in the system is negligibly small. Although the eddy kinetic energy is generated through the nonlinear process, generation of mean kinetic energy by the forcing is more effective than the generation of eddy kinetic energy under this dynamical system.

The large scale (or mean flow) response, however, is not affected by these two types of forcing in the barotropic non-divergent system, which only has nonlinearity as the governing dynamics. This implies tha the sporadic nature of convective activity does not have a significant effect on the large-scale flow through barotropic processes.

7.2 Suggestions for further research

At present, several large-scale general circulation models include the thermodynamic effects of convective scale motions through a variety of parameterization schemes (Louis, 1982; Shukla et al., 1981; Ghan et al., 1982; Hansen et al., 1983).

In view of the definite mesoscale organization of the cloud-cluster system, the parameterizations of the contributions from the mesoscale as well as the convective scale may have to be included in the large-scale models (Ooyama, 1982; Frank, 1983b). However, the behavior of mesoscale characteristics of the cluster system cannot be described adequately by an ensemble model of cumulus clouds. It is still an open question how to parameterize these mesoscale features. A diagnostic cloud model with mesoscale and convective scale features must be constructed and tested based on

more observational evidence before any improvement in the parameterization of the large-scale model can be expected.

The parameterization of the cumulus momentum effect within the large scale model is in its beginning stages, in comparison with the cumulus thermodynamic effects. It was found that a net increase of the easterly momentum in the vertical column by the convective effects. This result is consistent with the easterly drag forces induced by the surface westerly flow. Whether this net source of the momentum should be parameterized in the large-scale model certainly deserves more study. The mesoscale organization of the cluster system as investigated in this study suggests that nonhydrostatic pressure gradient forces in the upper troposphere must be included. But more observational evidence is needed to support this result.

This study also investigated the dynamical mechanism connecting the sub-grid scale processes to the large-scale flow. Although a simple barotropic non-divergent model indicates that the sporadic nature of convection has little effect on the resulting large-scale momentum fields, the inclusion of divergence might change the result through the energy and momentum transports by gravity waves.

To examine the effects of the pressure gradient forces induced by the mesoscale outflow, a baroclinic model will be necessary. The pressure effect may then generate the mean or eddy kinetic energy of the system. The examination of systems which contain gravity-wave dynamics as well as baroclinic pressure effects to investigate the interaction between sub-grid scale disturbances is an interesting area for further research.

BIBLIOGRAPHY

Albright, M.D., D.R. Mock, E.E. Recker, and R.J. Reed, 1981: A diagnostic study of the diurnal rainfall variations in the GATE B-scale area. J. Atmos. Sci., 38, 1429-1445.

Arakawa, A., 1966: Computational design for long-term numerical integration of the equations of fluid motion: Two-dimensional incompressible flow. Part I. J. Comput. Phy., 1, 119-143.

Arakawa, A., and W.H. Schubert, 1974: Interaction of a cumulus cloud ensemble with the large-scale environment: Part I. J. Atmos. Sci., 31, 674-701.

Balsley, B.B., and D.A. Carter, 1982: The spectrum of atmospheric velocity fluctuations at 8 Km and 86 Km. Geophys. Res. Lett., 9, 465-468.

Betts, A.K., R.W. Grover, and W.M. Moncrieff, 1976: Structure and motion of tropical squall-lines over Venezuela. Quart. J. Roy. Meteor. Soc., 102, 395-404.

Brown, R.S., and G.D. Robinson, 1979: The variance spectrum of tropospheric winds over eastern Europe. J. Atmos. Sci., 36, 270-286.

Byrd, G.P., and S.K. Cox, 1984: A case study of radiative forcing upon a tropical cloud cluster system. Mon. Wea. Rev., 112, 173-187.

Chan, J.C.L., 1985: Tropical cyclone activity in the northwest Pacific in relation to the El-Nino/Southern Oscillation phenomenon. Mon. Wea. Rev., 113, 106-116.

Chang, C.-P., 1970: Westward propagating cloud patterns in the tropical Pacific as seen from time-composite satellite photography. J. Atmos. Sci., 27, 133-138

Chang, C.-P., and K.-M. Lau, 1980: Northeasterly cold surge and near equatorial disturbances. Part II: Planetary-scale aspects. Mon. Wea. Rev., 108, 298-312.

Chang, C.-P., and K.-M. Lau, 1982: Short-term planetary scale interactions over the tropics and mid-latitudes. Part I: Contrast between active and inactive periods. Mon. Wea. Rev., 110, 933-946.

Charney, J.G., 1971: Geostrophic turbulence. J. Atmos. Sci., 28, 1087-1095.

Chen, T.-C., and A. Wiin-Nielsen, 1978: On nonlinear cascades of atmospheric energy and enstrophy in a two-dimensional spectral index. Tellus, 30, 313-322.

Chen, Y.-L., 1985: Diagnosis of the net cloud mass flux in GATE. J. Atmos. Sci., 42, 1757-1769.

Cheng, C.-P., and R.A. Houze, Jr., 1979: The distribution of convective and mesoscale precipitation in GATE radar echo patterns. Mon. Wea. Rev., 107, 1370-1381.

Cheng, C.-P., and R.A. Houze, Jr., 1980: Sensitivity of diagnosed convective fluxes to model assumptions. J. Atmos. Sci., 37, 774-783.

Cho, H.-R., 1977: Contribution of cumulus cloud life-cycle effects to the large-scale heat and moisture budget equations. J. Atmos. Sci., 34, 87-97.

Cho, H.-R., and L. Cheng, 1980: Parameterization of horizontal transport of vorticity by cumulus convection. J. Atmos. Sci., 37, 312-326.

Chu, J.-H., M. Yanai, and C.-H. Sui, 1981: Effects of cumulus convection on the vorticity field in the tropics. Part I: The large-scale budget. J. Meteor. Soc. Japan, 59, 535-546.

Cox, S.K., and K. Griffith, 1979a: Estimate of radiative divergence during Phase III of GARP Atlantic Tropical Experiment: Part I. Methodology. J. Atmos. Sci., 36, 576-585.

Cox, S.K., and K. Griffith, 1979b: Estimate of radiative divergence during Phase III of GARP Atlantic Tropical Experiment. Part II: Analysis of Phase III results. J. Atmos. Sci., 36, 586-601.

Esbensen, S.K., and K.V. Ooyama, 1983: An objective analysis of temperature and relative humidity data over the B and A/B ship arrays during Phase III of GATE. (Unpublished manuscript).

Esbensen, S.K., and E.I. Tollerud, and J.-H. Chu, 1982: Cloud-cluster-scale circulations and the vorticity budget of synoptic-scale waves over the eastern Atlantic intertropical convergence zone. Mon. Wea. Rev., 110, 1677-1692.

Esbensen, S.K., L.J. Shapiro, and E.I. Tollerud, 1986: The consistent parameterization of the effects of cumulus clouds on the large-scale momentum and vorticity fields (submitted to Mon. Wea. Rev.).

Frank, W.M., 1978: The life cycle of GATE convective systems. J. Atmos. Sci., 35, 1256-1264.

Frank, W.M., 1983a: The structure and energetics of the east Atlantic intertropical convergence zone. J. Atmos. Sci., 40, 1916-1929.

Frank, W.M., 1983b: The cumulus parameterization problem. Mon. Wea. Rev., 111, 1859-1871.

Fuelberg, H.E., and J. Jedlovec, 1982: A subsynoptic scale kinetic energy analysis of the Red River valley tornado outbreak. Mon. Wea. Rev., 110, 2005-2024.

Gage, K.S., 1979: Evidence of a $K^{-5/3}$ law inertial range in mesoscale two-dimensional turbulence. J. Atmos. Sci., 36, 1950-1954.

Gamache, J.F., and R.A. Houze, Jr., 1982: Mesoscale air motions associated with a tropical squall line. Mon. Wea. Rev., 110, 118-135.

Gandin, L.S., 1963: Objective Analysis of Meteorological Fields. Gidrometeor. Isdat., Leningrad. (Translated from Russian, Israel Program for Scientific Translations, Jerusalm, 1965, 242 pp.)

Ghan, S.J., J.W. Lingaas, M.E. Schlesinger, R.L. Mobley, and W.L. Gates, 1982: A documentation of the OSU two-level atmospheric general circulation model. Report No. 35, Climatic Research Institute, Oregon State University, Corvallis, OR, 395 pp.

Gray, W.M., 1973: Cumulus convection and large-scale circulations. Part I: Broadscale and mesoscale considerations. Mon. Wea. Rev., 101, 839-853.

Hansen, J., G. Russel, D. Rind, P. Stone, A. Lacis, S. Lebedeff, R. Ruedy, and L. Travis, 1983: Efficient three-dimensional global models for climatic studies: Models I and II. Mon. Wea. Rev., 111, 609-662.

Haynes, P.H., and M.E. McIntyre, 1986: On the evolution of vorticity and potential vorticity in the presence of diabatic heating and frictional or other forces. J. Atmos. Sci., (in press).

Holton, J.R., and D.E. Colton, 1972: A diagnostic study of the vorticity balance at 200 mb in the tropics during the northern summer. J. Atmos. Sci., 29, 1124-1128.

Houze, R.A., Jr., 1977: Structure and dynamics of a tropical squall-line system observed during GATE. Mon. Wea. Rev., 105, 1540-1567.

Houze, R.A. Jr., and A.K. Betts, 1981: Convection in GATE. Rev. Geophys. Space Phys., 19, 541-576.

Johnson, R.H., 1976: The role of convective-scale precipitation downdrafts in cumulus and synoptic-scale interactions. J. Atmos. Sci., 33, 1890-1910.

Johnson, R.H., 1980: Diagnosis of convective and mesoscale motions during phase III of GATE. J. Atmos. Sci., 733-753.

Johnson, R.H., 1984: Partitioning tropical heat and moisture budgets into cumulus and mesoscale components: Implications for cumulus parameterization. Mon. Wea. Rev., 112, 1590-1601.

Johnson, R.H., and M.E. Nicholls, 1983: A composite analysis of the boundary layer accompanying a tropical squall line. Mon. Wea. Rev., 111, 308-319.

Julian, P., W. Washington, L. Hembree, and C. Ridley, 1970: On the spectral distribution of large-scale atmospheric kinetic energy. J. Atmos. Sci., 27, 376-387.

Kolmogoroff, A.N., 1941: The local structure of turbulence in incompressible viscous fluids for very large Reynolds number. C.R. Acad. Sci. URSS, 30, 301-305.

Kraichnan, R.H., 1967: Inertial ranges in two-dimensional turbulence. Phys. Fluids, 10, 1417-1423.

Leary, C.A., 1979: Behavior of the wind field in the vicinity of a cloud cluster in the intertropical convergence zone. J. Atmos. Sci., 36, 631-639.

Leary, C.A., and R.A. Houze, Jr., 1979: The structure and evolution in a tropical cloud cluster. J. Atmos. Sci., 36, 437-457.

Leary, C.A., and R.A. Houze, Jr., 1980: The contribution of mesoscale motions to the mass and heat fluxes of an intense tropical convective system. J. Atmos. Sci., 37, 784-796.

Leith, C.E., 1968: Diffusion approximation for two-dimensional turbulence. Phys. Fluids, 11, 671-673.

LeMone, M.A., 1983: Momentum transport by a line of cumulonimbus. J. Atmos. Sci., 40, 1815-1834.

LeMone, M.A., and G.M. Barnes, and E.J. Zipser, 1984: Momentum flux by lines of cumulonimbus over the tropical oceans. J. Atmos. Sci., 41, 1914-1932.

Lilly, D.K., 1969: Numerical simulation of two-dimensional turbulence. High Speed Computing in Fluid Dynamics. Phys. Fluids Suppl. II, 240-249.

Lilly, D.K., 1972: Numerical simulation studies of two-dimensional turbulence. Part II: Stability and predictability studies. Geophys. Fluid Dyn., 4, 1-28.

Lilly, D.K., 1983: Stratified turbulence and the mesoscale variability of the atmosphere. J. Atmos. Sci., 40, 749-761.

Lilly, D.K., and E. Petersen, 1983: Aircraft measurements of atmospheric kinetic energy spectra. Tellus, 35A, 379-382.

Louis, J.F. (Ed.), 1982: ECMWF Forecast Model Documentation Manual Volume 1, Theoretical Bases. European Centre for Medium Range Weather Forecasts, Reading, United Kingdom, 155 pp.

Maddox, R.A., D.J. Perkey, and J.M. Fritsch, 1981: Evolution of upper tropospheric features during the development of a mesoscale convective complex. J. Atmos. Sci., 38, 1664-1674.

Malkus, J.S., 1960: Recent development in studies of penetrative convection and an application to hurricane cumulonimbus towers. Cumulus Dynamics, 65-85, Pergamon Press, New York.

Martin, D.W., and A.J. Schreiner, 1981: Characteristics of west African and east Atlantic cloud clusters: A survey from GATE. Mon. Wea. Rev., 109, 1671-1688.

Matsumoto, S., K. Ninomiya, and T. Akiyama, 1967: Cumulus activities in relation to the mesoscale convergence field. J. Meteor. Soc. Japan, 45, 292-305.

Matsuno, T., 1966: False reflection of waves at the boundary due to the use of finite differences. J. Meteor. Soc. Japan, Ser. 2, 44, 145-157.

McBride, J.L., and W.M. Gray, 1980: Mass divergence in tropical weather systems: Paper I. Diurnal variation. Quart. J. Roy. Meteor. Soc., 106, 501-516.

McGarry, M.M., and R.J. Reed, 1978: Diurnal variations in convective activity and precipitation during phase II and III of GATE. Mon. Wea. Rev., 106, 101-113.

Nastrom, G.D., and K.S. Gage, 1983: A first look at wavenumber spectra from GASP data. Tellus, 35A, 383-388.

Newell, R.E., J.W. Kidson, D.G. Vincent, and G.J. Boer, 1972: The General Circulation of the Tropical Atmosphere and Interactions with Extratropical Latitudes. Vol. 1, MIT press, 258 pp.

Nitta, T., 1977: Response of cumulus updrafts and downdrafts to GATE A/B scale motion systems. J. Atmos. Sci., 34, 1163-1186.

Nitta, T., 1975: Observational determination of cloud mass flux distributions. J. Atmos. Sci., 32, 73-91.

Nitta, T., and S.S. So, 1980: Structure and heat, moisture and momentum budgets of a convective mixed layer during AMTEX'75. J. Meteor. Soc. Japan, 58, 378-393.

Ogura, Y., and H.-R. Cho, 1973: Diagnostic determination of cumulus cloud population from large-scale variables. J. Atmos. Sci., 30, 1276-1286.

Ogura, Y., and Y.-L. Chen, J. Russell, and S.-T. Soong, 1979: On the formation of organized convective systems observed over the eastern Atlantic. Mon. Wea. Rev., 107, 426-441.

Ooyama, K.V., and S.K. Esbensen, 1977: Rawinsonde data quality. Report of the GATE Central Program Workshop, 25 July - 12 August 1977, NCAR, 131-164. [GATE Project Office, NOAA, Rockville, MD 20852.]

Ooyama, K.V., 1971: A theory of parameterization of cumulus convection. J. Meteor. Soc. Japan, 49, 744-756.

Ooyama, K.V., 1982: Conceptual evolution of the theory and modeling of the tropical cyclones. J. Meteor. Soc. Japan, Special Issue, 60, 369-379.

Palmen, E., and C.W. Newton, 1969: Atmospheric Circulation Systems. International Geophysics Series, Volume 13, Academic Press, 603 pp.

Rasmusson, E.M., and T.H. Carpenter, 1982: Variations in tropical sea surface temperature and surface wind fields associated with the Southern Oscillation/El Nino. Mon. Wea. Rev., 110, 354-384.

Reed, R.J., D.C. Norquist, and E.E. Recker, 1977: The structure and properties of African wave disturbances as observed during phase III of GATE. Mon. Wea. Rev., 105, 317-342.

Reed, R.J., and E.E. Recker, 1971: Structure and properties of synoptic-scale wave disturbances in the equatorial western Pacific. J. Atmos. Sci., 28, 1117-1133.

Reeves, R.W., S. Williams, E. Rasmusson, D. acheson, and T. Carpenter, 1976: GATE Convection Subprogram Data Center - analysis of rawinsonde intercomparison data. NOAA Tech. Report EDS 20, Washington, D.C., 75 pp.

Rhines, P.B., 1975: Waves and turbulence on a β-plane. J. Fluid Mech., 69, 417-443.

Riehl, H., and J.S. Malkus, 1958: On the heat balance in the equatorial trough zone. Geophysica, 6, 503-538.

Riley, J.J., R.W. Metcalfe, and M.A. Weissman, 1981: Direct numerical simulations of homogeneous turbulence in density stratified fluids. Proc. AIP Conf., Nonlinear Properties of Internal Waves, B.J. West, Ed., 79-112.

Roache, P.J., 1972: Computational Fluids Dynamics. Hermosa Publ., 434 pp.

Robertson, F.R., and P.J. Smith, 1980: The kinetic energy budgets of two severe storms producing extratropical cyclones. Mon. Wea. Rev., 108, 127-143.

Rotunno, R., and J.R. Klemp, 1982: The influence of a shear-induced pressure gradient on thunderstorm motion. Mon. Wea. Rev., 110, 136-151.

Sardeshmukh, P.D., and I.M. Held, 1984: The vorticity balance in the tropical upper troposphere of a general circulation model. J. Atmos. Sci., 41, 768-778.

Schneider, E.K., and R.S. Lindzen, 1976: A discussion of the parameterization of momentum exchange by cumulus convection. J. Geophys. Res., 81, 3158-3160.

Shapiro, L.J., 1978: The vorticity budget of a composite African tropical wave disturbance. Mon. Wea. Rev., 106, 806-817.

Shapiro, L.J., and D.E. Stevens, 1980: Parameterization of convective effects on the momentum and vorticity budgets of synoptic-scale Atlantic tropical waves. Mon. Wea. Rev., 108, 1816-1826.

Shukla, J., D. Straus, D. Randall, Y. Sud, and L. Marx, 1981: Winter and summer simulations with the GLAS climate model. Technical Memorandum 83866. Laboratory for Atmospheric Sciences, Modeling and Simulation Facility, NASA Goddard Space Flight Center, Greenbelt, MD, 282 pp.

Soong, S.-T., and W.-K. Tao, 1984: A numerical study of the vertical transport of momentum in tropical rainband. J. Atmos. Sci., 41, 1049-1061.

Stevens, D.E., 1979: Vorticity, momentum and divergence budgets of synoptic-scale wave disturbances in the tropical eastern Atlantic. Mon. Wea. Rev., 107, 535-550.

Sui, C.-H., and M. Yanai, 1984: Vorticity budget of the GATE A/B area and its interpretation. Postprints, 15th Conference on Hurricanes and Tropical Meteorology, Miami, FL, American Meteorological Society, Boston, MA, pp 465-472.

Thompson, R.M., Jr., S.W. Payne, E.E. Recker, and R.J. Reed, 1979: Structure and properties of synoptic-scale wave disturbances in the intertropical covergence zone of the eastern Atlantic. J. Atmos. Sci., 36, 53-72.

Tollerud, E.I., 1983: An observational study of the wind fields associated with GATE cloud clusters. Ph.D. Thesis, Department of Atmospheric Sciences, Oregon State University, 215 pp.

Tollerud, E.I., and S.K. Esbensen, 1983: An observational study of the upper-tropospheric vorticity fields in GATE cloud clusters. Mon. Wea. Rev., 111, 2161-2175.

Tollerud, E.I., and S.K. Esbensen, 1984: A note on the production of vorticity by parameterized cumulus clouds in general circulation models. Report No. 59, Climatic Research Institute, Oregon State University, Corvallis, OR, 42 pp.

Van Zandt, T.E., 1982: A universal spectrum of buoyancy waves in the atmosphere. Geophys. Res. Lett., 9, 575-578.

Vinnichenko, N.K., 1970: The kinetic energy spectrum in the free atmosphere - 1 second to 5 years. Tellus, 22, 158-166.

Wiin-Nielsen, A., 1967: On the annual variation and spectral distribution of atmospheric energy. Tellus, 19, 540-559.

Williams, K.T., and W.M. Gray, 1973: Statistical analysis of satellite-observed trade wind cloud clusters in the western north Pacific. Tellus, 25, 313-336.

Yanai, M., S.K. Esbensen, and J.-H. Chu, 1973: Determination of bulk properties of tropical cloud clusters from large-scale heat and moisture budgets. J. Atmos. Sci., 30, 611-627.

Yanai, M., C.-H. Sui, and J.-H. Chu, 1982: Effects of cumulus convection on the vorticity field in the tropics. Part II: Interpretation. J. Meteor. Soc. Japan, 60, 411-424.

Zipser, E.J., 1969: The role of unsaturated convective downdrafts in the structure and rapid decay of an equatorial disturbance. J. Appl. Meteor., 8, 799-814.

Zipser, E.J., 1977: Mesoscale and convective scale downdrafts as distinct components of squall-line circulation. Mon. Wea. Rev., 105, 1568-1589.

Zipser, E.J., R.J. Meitin, and M.A. LeMone, 1981: Mesoscale motion fields associated with a slowly moving GATE convective band. J. Atmos. Sci., 38, 1725-1750.

APPENDICES

APPENDIX A. THE CONSTRUCTION OF GEOPOTENTIAL HEIGHT

The geopotential gradient is a difficult quantity to measure in the tropical region. In most cases, the geopotential analysis is derived from the observed temperature fields with some assumptions. Stevens (1979) constructed the geopotential fields by integrating the hydrostatic equation upward from the surface. The surface geopotential field is independently determined through the observed surface pressure field. In this study, the geopotential fields will be constructed slightly differently.

The geopotential field is constructed from the temperature fields through the hydrostatic approximation. The hydrostatic equation is

$$\frac{\partial \phi}{\partial p} = -\alpha = -\frac{R_d T_v}{P} \qquad (A.1)$$

$$\phi \text{ (any level)} - \phi(\text{sfc}) = \int_{\text{sfc}}^{\text{any level}} -R_d * T_v \, d \ell n \, p \qquad (A.2)$$

where ϕ and T_v represent the geopotential field and virtual temperature, respectively. R_d is the dry air gas constant.

If we can estimate the geopotential field at the surface, the other levels of geopotential fields can be determined through Eq. (A.2). There are quite a few methods to estimate the surface geopotential field. Here the surface (1012 mb) geopotential field is estimated by the constant flux approximation for the lowest layer. With the use of wind data, the horizontal structure of ϕ at

the surface can be obtained through the momentum equation.

Because of the diurnal effect, the temperature fields have the tendency to become warmer (cooler) in the upper-layer in the afternoon (early morning). The constructed ϕ field had a large noise component from 150 mb and up to where the diurnal effect is most significant. In order to make this diurnal influence a minimum, another approximation with a dynamic constraint to produce a new geopotential field at the upper troposphere was introduced, and the analyzed field was modified subsequently.

Generally, it was regarded that the upper tropospheric wind fields were more accurately measured than was the temperature field. And it was found that the wind at 160 mb was above the tops of most convective elements, but was well below the tropopause. Frank (1983a) suggested from a scale analysis of the zonal momentum equation that the mean winds at the 150 mb level were close to geostrophy. In the present analysis, instead of assuming geostrophy, a constant eddy flux layer was assumed to exist at the 160 mb level. The geopotential field at 160 mb level thus could be estimated through the momentum equation and the observed wind data with the frictionless approximation at that layer. The geopotential height difference between the newly analyzed and the originally analyzed 160 mb level was used as a correction guideline. It was assumed that the height corrections resulted from virtual temperature errors which were constant with height. Thus

$$\Delta\phi = R_d * \Delta T_v^* * \ln(P_0/P_1) \qquad (A.3)$$

where $\Delta\phi$ is the geopotential height correction, P_1 and P_0 are the pressures at the top and bottom of a layer, and ΔT_v^* is the virtual temperature correction.

The final geopotential heights were reconstructed from the thickness equation. Fig. A.1 shows the perturbation geopotential field (E+D band only) at 705 mb, which was dominated by easterly waves at that time. The estimated geopotential field seemed to be able to resolve the easterly wave pattern at the 700 mb level quite well. It is comparable to the stream line study by Leary (1979). Fig. A.2 from Leary (1979) based on the stream line analysis at 700 mb also identifies a wave trough in the southeast region of the array.

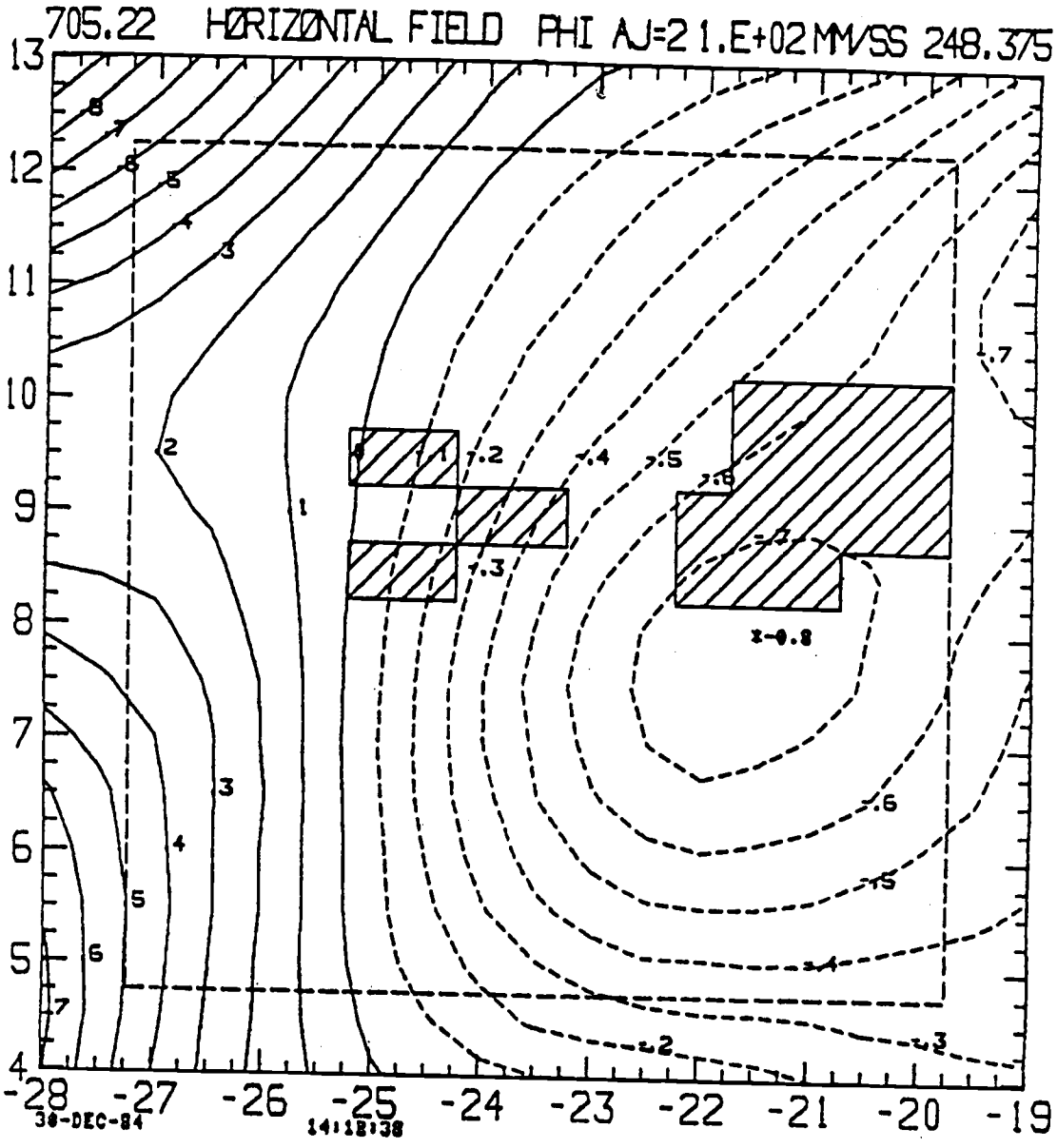

(a) growing

Figure A.1. Horizontal plot of the perturbed geopotential field during (a) growing, (b) mature stages of 5 September cluster. Units are 10 m^2/s^2; contour interval is 10 m^2/s^2.

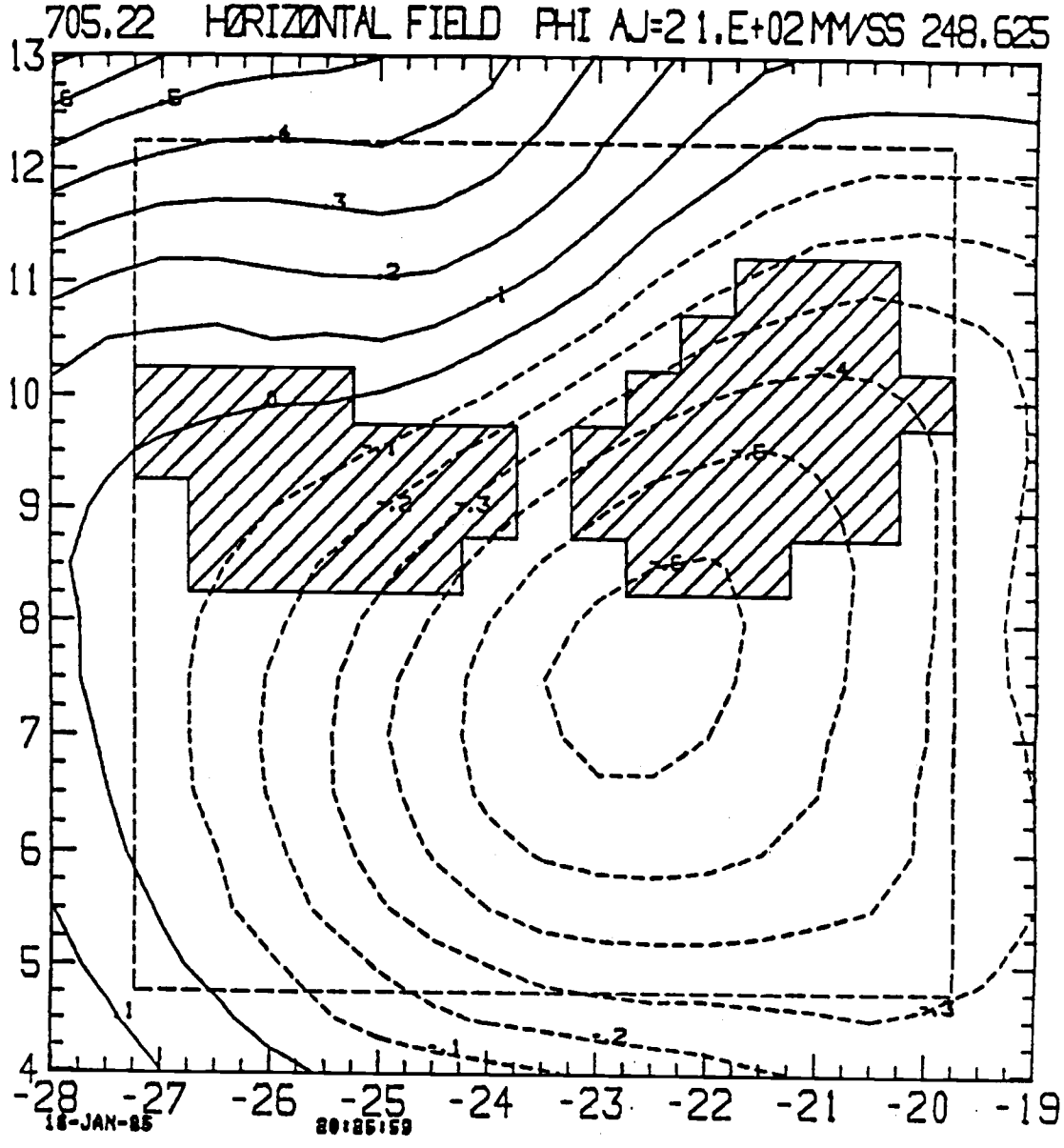

(b) mature

Figure A.1 (continued)

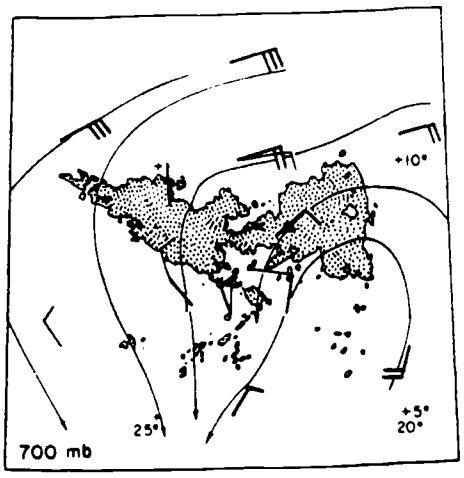

(a) 1200 GMT

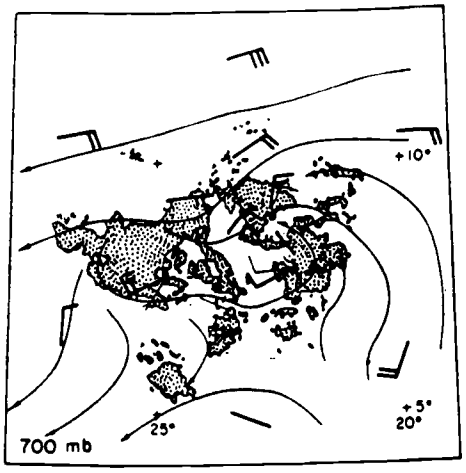

(b) 1800 GMT

Figure A.2. Streamline analysis of 700 mb from Leary (1979) for the 5 September 1974 cloud cluster. (a) 1200 GMT and (b) 1800 GMT.

APPENDIX B. THE BAROTROPIC NON-DIVERGENT MODEL

The barotropic non-divergent vorticity equation may be written as

$$\frac{\partial \zeta}{\partial t} = - \underset{\sim}{V} \cdot \underset{\sim}{\nabla} \zeta - \beta v + F + \nu \underset{\sim}{\nabla}^2 \zeta \qquad (B.1)$$

and

$$\underset{\sim}{V} = u \underset{\sim}{i} + v \underset{\sim}{j} = - \frac{\partial \psi}{\partial y} \underset{\sim}{i} + \frac{\partial \psi}{\partial x} \underset{\sim}{j}, \quad \zeta = \underset{\sim}{\nabla}^2 \psi$$

where all the notations are traditional. F and ν are the cumulus momentum forcing and viscosity coefficient, respectively. This dynamic set can be regarded as having one prognostic variable (stream function ψ) and one equation.

This equation is integrated forward in time using the second order Adams-Bashforth method with diffusion. Equation (B.1) can be rewritten as

$$\frac{\partial \zeta}{\partial t} = G + \nu \underset{\sim}{\nabla}^2 \zeta$$

where G represents the sum of $-\underset{\sim}{V} \cdot \underset{\sim}{\nabla} \zeta - \beta v + F$. At time t = (n+1)* dt, the Adams-Bashforth method gives (Roache, 1972)

$$\zeta^{n+1} = \zeta^n + \nabla t \left(\frac{3}{2} G^n - \frac{1}{2} G^{n-1}\right) + \nu \underset{\sim}{\nabla}^2 \zeta^n \qquad (B.3)$$

A forward scheme is used for the first time step, and the Adams-Bashforth scheme follows. The stream function is solved from the predicted vorticity at every time by a Fourier direct method, which is very efficient for a rectangular domain.

The Arakawa Jacobian (Arakawa, 1966) was used to estimate the nonlinear advective term, in order to suppress nonlinear instability. β and ν are chosen as $1.1*10^{-11}/(m*s)$ and $10^3\ (m^2/s)$, respectively. The parameters used in Sec. 6.2.3 are dx = dy = 50 km, and dt = 1000 s, while the parameters used in Sec. 6.3 are dx = dy = 20 km, and dt = 500 s.

The cumulus momentum forcing needed in Sec. 6.3 is estimated from $M_c(U_c-U)/Dp$; M_c is assumed as

$$M_c(x,y) = 1.0 \times 10^{-3} \frac{mb}{sec} \times \sin(DST*3.14159/16.) \qquad (B.4)$$

where DST $\equiv$ SQRT($(X-X_0)^2+(Y-Y_0)^2$). When DST is larger than a prescribed value, M_c is set to zero. DP is set to 100 mb to represent the layer thickness. M_c has a maximum intensity approximated as 100 mb/day (or 10^{-3} mb/sec). The horizontal domain (X_0) of this M_c is limited to 10 groups only, and their positions are determined randomly. The meridional occurrence of this $M_c(Y_0)$ is also random and limited to 160 km (10 grid lengths) each side through the center of the domain. The horizontal extent of each group is limited to 80 km (4 grid lengths).

The cumulus momentum forcing is computed as

$$F_m(x,y,t) = \frac{M_c(x,y)}{DP} * \tau(t) * (U_c - U) \qquad (B.2)$$

where $\tau(t)$ is for $e^{-(MOD(n,15)*4./15)}$. The M_c is assumed to grow and decay in 2.5 hrs. U_c is in-cloud momentum (set to 5 m/sec westerly), and U is the zonal mean of the zonal velocity of the large-scale system. The zonal mean of this sporadic momentum

forcing is distributed in all the grids and regarded as the zonal mean forcing.

The corresponding vorticity forcing is computed from this momentum forcing, and is represented as F in Eq. (B.1).